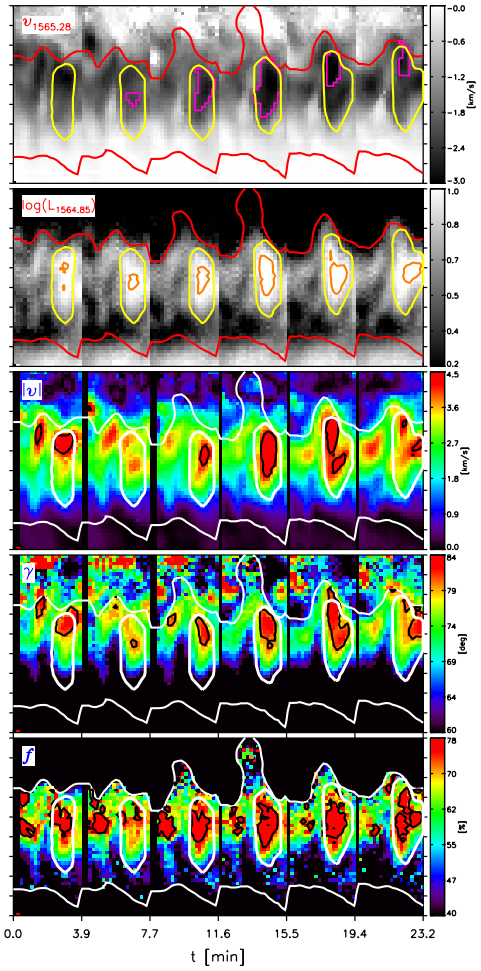

Temporal evolution of the Evershed flow and its magnetic properties

Daniel Cabrera Solana

INSTITUTO DE ASTROFÍSICA DE ANDALUCÍA
CONSEJO SUPERIOR DE INVESTIGACIONES CIENTÍFICAS

Editor: Editorial de la Universidad de Granada
Autor: Daniel Cabrera Solana
D.L.: Gr. 1120 - 2007
ISBN: 978-84-338-4335-7

DEPARTAMENTO DE FÍSICA APLICADA

Universidad de Granada

TEMPORAL EVOLUTION OF THE EVERSHED FLOW AND ITS MAGNETIC PROPERTIES

Memoria que presenta
D. Daniel Cabrera Solana
para optar al grado de
Doctor en Astrofísica.

INSTITUTO DE ASTROFÍSICA DE ANDALUCÍA
CONSEJO SUPERIOR DE INVESTIGACIONES CIENTÍFICAS
June 2007

Examination date : 2007 June 1
Thesis supervisors: Drs. Jose Carlos del Toro Iniesta and Luis Ramón Bellot Rubio

ISBN: XX–XXX–XXXX–X
Depósito Legal: GR–XXX/XX
Some of the figures included in this document have been previously published
in *The Astrophysical Journal* and *Astronomy & Astrophysics*

Abstract

In this thesis we study the physical nature of the Evershed flow by investigating its temporal evolution. The only way to derive the physical properties of the solar atmosphere is by means of inversions of spectropolarimetric measurements. In this context, one should carefully select the spectral lines that are going to be used to derive the atmospheric parameters. In order to understand the properties of the visible and infrared lines, we have developed a simple phenomenological model capable of describing the sensitivity of any weak line to magnetic field, velocity, and temperature in terms of simple line parameters. The results of this model demonstrated that due to the different sensitivities of visible and infrared lines to the atmospheric quantities is advantegous to combine them in order to obtain the physical properties of the solar atmosphere more reliably. Due to their simple Zeeman patterns and high sensitivity to the magnetic field we decided to observe the visible Fe I lines at 630 nm and the infrared Fe I lines at 1565 nm. We have inverted in terms of one-component models the Stokes profiles of these lines emerging from three sunspots located at different heliocentric angles. Although the results derived from the two spectral ranges esentially lead to similar physical parameters, a cross-talk between temperature and stray light affecting the visible lines is found. Our results demonstrate that simultaneous inversion of the visible and infrared lines minimize this problem and improves the determination of the atmospheric parameters.

The former arguments motivated us to investigate the temporal evolution of the physical properties of the Evershed flow by analyzing the polarization signals of visible (630 nm) and infrared (1565 nm) spectral lines. The Stokes profiles of such lines were recorded by the Polarimetric Littrow Spectrograph and the Tenerife Infrared Polarimeter during 236 min of observations in two consecutives days at the German Vacuum Tower Telescope in Tenerife. The good seeing conditions together with the Kiepenheuer Adaptive Optics System allowed us to reach diffraction-limited spatial resolution of the infrared observations ($0\farcs6$). Different degrees of sophistication have been used in order to interpret the observations. We perform a detailed characterization of the observational properties of Evershed clouds by means of simple line parameters. Their physical properties are derived from the simultaneous inversion of the visible and infrared lines by using two different semiempirical models: one-component model atmospheres, and uncombed models that take into account the fine structure of the penumbra. This allows us to propose a physical

mechanism that explains the formation of Evershed clouds in a natural way. The relation between the Evershed clouds and the origin of moving magnetic features around sunpots is also investigated. We observe the formation of two different types of moving magnetic features that are related with the uncombed structure of the penumbra. We propose qualitative geometrical models of ECs and MMFs that explain our observations. These models are consitent with the idea that the penumbra is formed by horizontal flux tubes channeling the Evershed flow embedded in a more vertical background in agreement with the uncombed model proposed by Solanki & Montavon (1993).

Contents

1

Introduction

1.1 Overall properties of the Sun

There is an indetermined number of stars in the universe with rather different physical properties. In spite of the fact that between them the Sun is an ordinary star of small size, its study is of vital relevance for several reasons. Obviously, the Sun is extremely important for our existence. Moreover, due to its proximity, the Sun is the only star that can be studied with high temporal, spectral, and spatial resolution. This allows us to investigate in detail many physical processes that are taking place in our star and are important not only for the understanding of other stars (Schüssler 2002) but also for many other branches of astrophysics (Blandford et al. 2002; Bellot Rubio 2004).

The Sun is mainly composed by hydrogen (74%) and helium (25%). The remaining 1% is made up of heavier elements such as oxygen, carbon, iron, etc. The heavy elements are found in the same proportions on Earth which suggests a common origin for the two celestial bodies. The presence of such heavy ele-

TABLE 1.1:— Comparison between the overall properties of the Sun and the Earth.

Property	Sun	Earth
Mass	1.99×10^{30} kg	5.97×10^{24} kg
Diameter	1.39×10^{6} km	1.27×10^{4} km
Surface gravity	274 m s^{-2}	9.8 m s^{-2}
Mean density	1.4 kg m^{-3}	5.5 kg m^{-3}
Rotation period	26 days	1 day

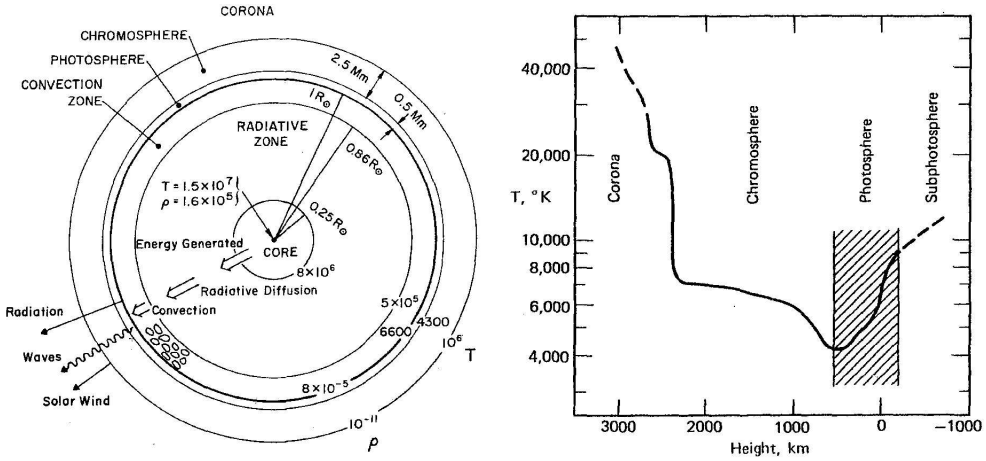

FIGURE 1.1:— *Left:* Illustration of the overall structure of the Sun [taken from Priest (1982)]. The different layers, temperatures, densities, and energy transport processes are indicated. *Right:* Thermal structure of the solar atmosphere [taken from Gray (1992)].

ments indicates that the formation of the Sun could has been triggered by shock waves from a nearby supernova. The age of the Sun (4.57×10^9 yr, i.e. a third of the age of the universe) indicates that is halfway through its main-sequence evolution. It contains approximately 99% of the mass of the entire solar system being 330000 times more massive than the Earth. Moreover, its diameter is around 109 times larger than that of the Earth, while the surface gravity is 28 times greater. The fact that the mean density on Earth is greater than that on the Sun is not surprising if one takes into account that the properties of the medium dramatically changes from the solar interior to the outer layers.

1.2 Structure of the Sun: from the interior to the atmosphere

"The Sun, like all stars, is such a massive ball of plasma that it is held together and compressed under its own gravitational attraction" Priest (1982). This compression leads to the plasma of the internal parts of our star (*core*) to densities ($\sim 10^5$ kg m^{-3}) and temperatures ($\sim 10^7$ K) high enough for thermonuclear fusion reactions to take place. This is the starting point where the photons begin their travel to the solar exterior (cf. left panel of Fig. 1.1). After the photons have been generated, they are in the *intermediate zone* (or *radiative*) of the solar interior where the opacity of the medium is large and the energy transport is carried out by means of radiative diffusion, i.e., processes in which the photons are continuously absorbed and re-emitted. In this way, the photons typically employ ten million years to reach the outer layers of

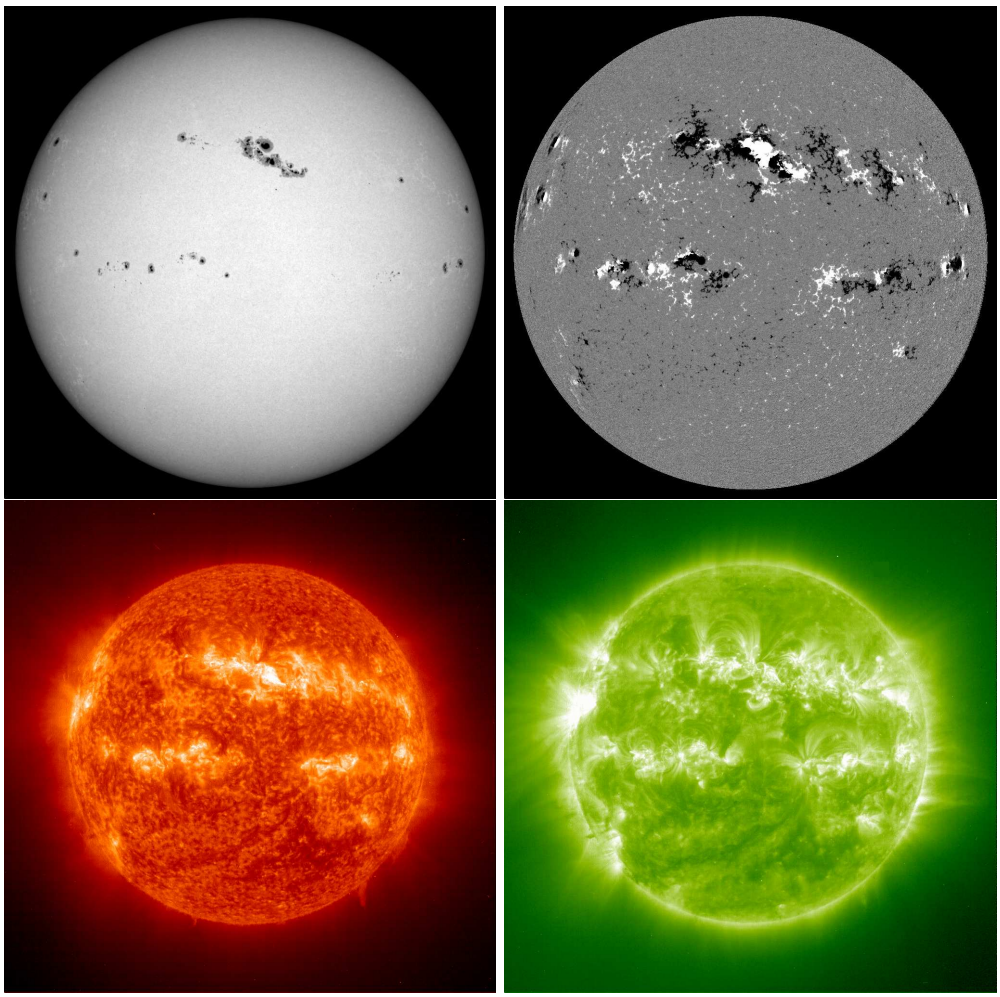

FIGURE 1.2:— Full disk continuum intensity at 676.8 nm (photosphere), magnetogram constructed from Ni I line at 676.78 nm (photosphere), He II emission line at 30.4 nm (chromosphere), and Fe IX emission line at 17.1 nm (low-corona) observed on 29 March 2001. Observations were taken by Michelson Doppler Imager (MDI) and Extreme ultraviolet Imaging Telescope (EIT) onboard of Solar and Heliospheric Observatory (SOHO; Domingo et al. 1995).[Data were taken from the public data archive on http://sohowww.nascom.nasa.gov/].

the Sun!. During this long journey, the wavelength of the radiation is increased from that of gamma rays to that of visible light. In the internal zone of the Sun, the strong interaction between the radiation field and the plasma takes place in thermodynamical equilibrium (ET) conditions. Leaving the solar interior, the photons arrive at layers where the presence of strong gradients of temperature and density make the energy transport by convection more efficient. This is the outer part of the solar interior (the *convective zone*) where hot plasma rises up, cools and then returns to deeper layers to receive more heat from the top of the radiative zone. At higher layers, the density and opacity of the medium dramatically decrease. This region is called the atmosphere and the physical conditions are such that opacity is so low so that radiation can freely escape from the star. The atmosphere is divided into three different regions that are known as the *photosphere*, the *chromosphere*, and the *corona* (cf. right panel of Fig. 1.1). The deepest of them, the *photosphere*, is a thin layer of 500 km which is relatively dense and opaque and emits most of the radiation emerging from the Sun. Above it is the chromosphere which is a rare and transparent layer of gas, while the corona extends from the end of the chromosphere until an undetermined boundary of the order of several astronomical units. Surprisingly, the temperature increases from the photosphere to higher layers (cf. right panel of Fig. 1.1). In fact, it is well known that it varies from $\sim$ 5700 K in the photosphere to 1-3 MK in the corona. The mechanism that produces such *coronal heating* still remains not fully understood. Nowadays, this is one of the major challenges that solar physicists have to face.

Unfortunately, due to the high opacity, the solar interior is not directly observable. This is the reason why the study of the internal structure of the Sun is performed by means of indirect measurements of the physical quantities derived from the oscillation modes of the Sun (heliosismology) and the number of neutrinos generated in the nuclear reactions. By contrast, since the opacity is small enough in the outer layers, a detailed study of the physical properties in the solar atmosphere can be performed by means of the analysis of spectral lines. The physical conditions of the medium determine the ionization state and the population of the atomic levels of the species that produce the spectral lines. In this way, depending on the physical properties, different spectral lines are formed. For example, photospheric lines are usually formed at visible wavelengths (cf. top left panel of Fig. 1.2) because they are produced by transitions of low ionized states of the atomic species. The higher temperatures of the chromosphere and corona produce highly ionized atomic species which lead to the formation of spectral lines at ultra-violet and X-ray wavelengths (cf. bottom left and bottom right panels of Fig. 1.2).

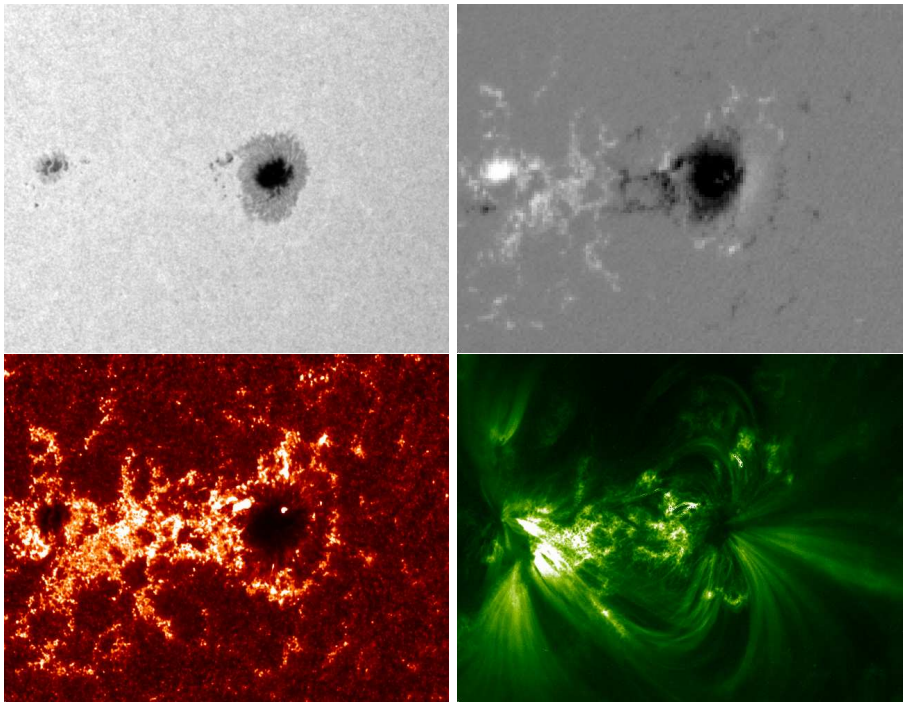

FIGURE 1.3:— Bipolar Active region 9017 as observed in continuum at 500 nm (photosphere), MDI magnetograms (photosphere), continuum at 160 nm (chromosphere), and Fe IX emission line at 17.1 nm (low-corona). The data were taken by the Transition Region and Coronal explorer (TRACE; Handy et al. 1999) and SOHO on June 2, 2000.

1.3 Sunspots as the manifestation of the solar magnetic fields

Sunspots are the most conspicuous features in the photosphere (cf. top left panel of Fig. 1.2). They exhibit a broad range of sizes that vary from 3500 km to more than 60000 km in diameter, i.e. they can be until six times larger than the Earth!. Many of them live for less than a day, although some have lifetimes longer than a week. Sunspots appear darker because are cooler than their surroundings. This does not mean that they are cold structures. In fact, they display temperatures at $\tau = 1$ in the range of 3500-6500 K. The lower temperature inside the spots is produced by the presence of intense vertical magnetic fields which block convection (Biermann 1941).

Although the underlying physics of the sunspot formation process is still a matter of debate, it is accepted that sunspots are produced by the intersection of magnetic flux tubes that emerge from the convective zone (Schüssler 2002). Since the total magnetic flux through the solar surface is zero, sunspots typically appear in pairs of different polarity (cf. top right panel of Fig. 1.2).

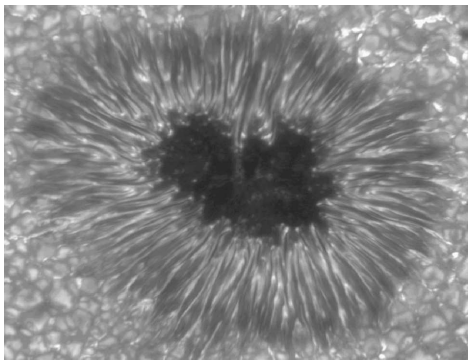

FIGURE 1.4:— Sunspot observed with a circular polarizer in the red wing of the Fe I line at 630.25 nm. The image was taken at the Swedish Solar Telescope and it was reconstructed using a phase diversity technique reaching a spatial resolution about 0.″12 (Spruit & Scharmer 2006).

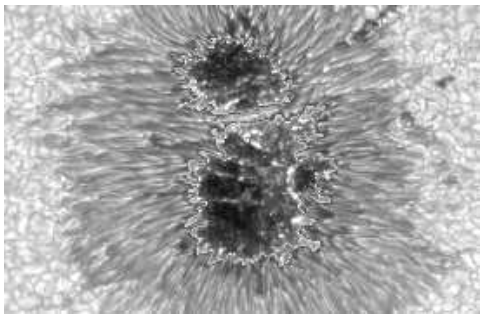

FIGURE 1.5:— Image of a sunspot observed at the TiO band at 705.5 nm with the SST by V. Zakharov and A. Gandorfer. The intensity scale of the umbra is artificially enhanced in order to show the umbral dots. [taken from Solanki et al. (2006)].

Figure 1.3 shows an example of a bipolar active region. Field lines emerging with positive polarity, i.e. pointing towards the observer, returns to the solar interior in the region with negative polarity (cf. top right panel of Fig. 1.3). This leads to the apparition of brilliant coronal loops between the regions of different polarities (cf. bottom right panel of Fig. 1.3). Most of coronal mass ejections and flares have their origin in the surroundings of such bipolar regions.

1.4 Sunspots in the photosphere

A typical sunspot observed in the photosphere (cf. Fig. 1.4) consists of a darker central area called the *umbra* surrounded by a brighter annular region known as the *penumbra*. The two regions display rather different properties as described in the following.

1.4.1 Umbra

The umbra is the region displaying the smallest temperatures ($T \sim 3500 - 5000$ K) and the strongest magnetic fields ($B \sim 2000 - 3500$ G) of the sunspot. Its magnetic field is approximately vertical to the local solar surface ($\gamma \sim 0°$;

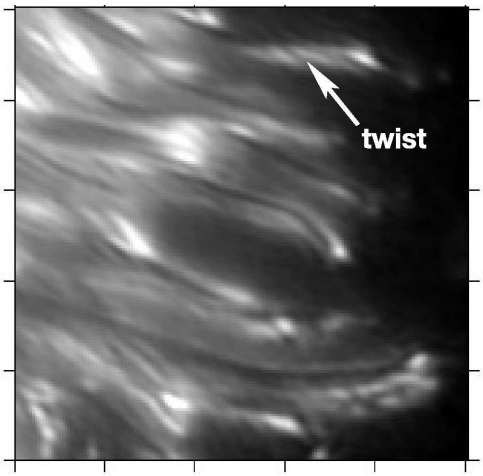

FIGURE 1.6:— Close up of dark cored penumbral filaments (DC) observed at the SST (Scharmer et al. 2002). Each tickmark represents 1.″4.

γ is the angle between the local vertical and the vector magnetic field) at the sunspot center becoming more horizontal ($\gamma \sim 20^{\circ}$) at the outer umbral boundary. It is well known that large sunspots are cooler and posses stronger magnetic fields in the umbra as compared to the small ones (Collados et al. 1994).

Excluding the presence of oscillations, the umbra is known to be at rest (Beckers 1977). There are small structures (0.″15-0.″60) called *umbral dots* (cf. Fig. 1.5), however, that are brighter than their surroundings and harbor small upflows (Socas-Navarro et al. 2004). Umbral dots possess weaker fields and larger temperatures than the umbral average.

As can be seen in Fig. 1.5, some spots show a bright lane which divides the umbra in two parts. This type of structures are called *light bridges* and can reach the same intensity as the quiet photosphere. They display significantly lower values of the field strength than the umbral average and could be produced by intrusion of field free material from deep layers of the photosphere (Leka 1997).

1.4.2 Penumbra

The sunspot penumbra shows up as a filamentary radial distribution alternating bright and dark filaments (cf. Figs. 1.4 and 1.5). Recent advances in instrumentation and the application of image restoration techniques have permitted to obtain images of sunspots with unprecedented spatial resolution 0.″12 ($\sim$ 90 km) at the Swedish Solar Telescope (SST). At this spatial resolution, the filaments show a *dark core* (DC) surrounded by two lateral brightenings (cf.

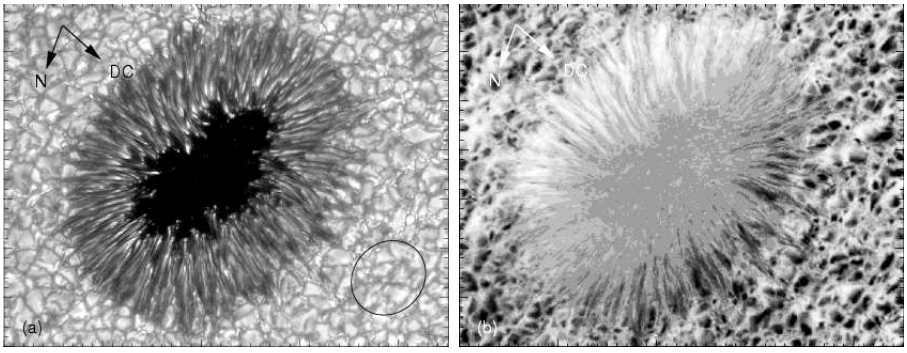

FIGURE 1.7:— Continuum intensity and Dopplergram of NOAA 10425 observed on August 9, 2003 (Langhans et al. 2005). White and black colours in the Dopplergram represent blueshifts and redshifts, respectively. Note the filamentary structure of the Evershed flow.

Fig. 1.6). The fact that DCs and the brightenings evolve and move together indicates that they are a single entity (Scharmer et al. 2002). The typical width of the filaments, as measured between the intensity maxima of the two lateral brightenings, is about $150 - 180$ km. Some of them are seen to cross the entire penumbra reaching a radial extension up of 1000 km. The footpoints of the filaments are usually located at structures brighter than its surroundings called *penumbral grains*. There are many cases where penumbral grains move radially inwards entering the umbra (Spruit & Scharmer 2006) and becoming peripheral umbral dots. Recent observations performed by Rimmele & Marino (2006) demonstrate that upflows occur at the penumbral grains. Despite of the very high spatial resolution reached by the observations taken at the SST, there is evidence that there are still unresolved structures inside the penumbral filaments (Rouppe van der Voort et al. 2004).

1.4.3 Evershed flow

The Evershed effect (Evershed 1909) is the most conspicuous dynamical phenomenon on sunspot penumbrae. It is observed as a redshift and a blueshift of the spectral lines on the center and limb sides of the penumbra, respectively. The magnitude of the effect is greater when the sunspot is located nearer of the solar limb. These solid observational results have been interpreted as the signature of a radial outflow of plasma propagating nearly parallel to the solar surface[1]. The Evershed effect is height dependent: the line shifts decrease in

[1]Bunte et al. (1993) explained the Evershed effect in terms of magneto acoustic surface gravity waves but Buente & Solanki (1995) realized that such waves produce opposite line shifts depending on the spectral lines. This is not observed and, consequently, the proposed

spectral lines formed at higher layers of the photosphere (St. John 1913a,b). Moreover, larger Doppler shifts are observed in the line wings than in the line cores leading to asymmetric line profiles. The magnitude of the Evershed flow increases with radial distance until the outer penumbra. Some authors find that the flow ends at the visible limit of the spot (Title et al. 1993; Wiehr & Degenhardt 1994) while others claim that it persits further (Rimmele 1995; Stanchfield et al. 1997). As can be seen in the left panel of Fig. 1.7, the Evershed flow displays a filamentary structure.

1.4.4 Relation of the Evershed flow with the penumbral brightness

As discussed in Sect. 1.4.2 the sunspot penumbra is composed by many bright and dark filaments radially oriented and the Evershed flow preferentially occurs along filamentary structures. The correlation between the intensity and flow patterns is, consequently, an obvious question. Unfortunately, the relation between the intensity and the Evershed flow is not well established. Different results are found in the literature:

- Evershed flow correlated with dark features (Schröter 1965; Beckers 1968; Wiehr & Degenhardt 1992; Rimmele 1995; Westendorp Plaza et al. 2001b; Tritschler et al. 2004).
- No significant correlation between the intensity a flow patterns (Wiehr & Stellmacher 1989; Lites et al. 1990; Hirzberger & Kneer 2001).
- Evershed flow present in bright and dark filaments. In some cases, Evershed channels link bright and dark features (Schlichenmaier et al. 2005).

Recent observations of DC penumbral filaments indicate that the Evershed flow is more conspicuous inside the DCs (Bellot Rubio et al. 2005; Rimmele & Marino 2006; Langhans et al. 2007). Although the flow is also correlated with brighter features than the DCs (Rimmele & Marino 2006). Since DC penumbral filaments begin at penumbral grains, these results would agree with the findings of Schlichenmaier et al. (2005). Anyway, further investigations are needed to clarify this question.

1.5 Spectropolarimetry at the visible and infrared

High resolution filtergrams allow us to study the size and distribution of the penumbral filaments (cf. Sects. 1.4.2) but they provide very little information

wave model was discarded as the origin of the Evershed effect.

on the magnetic field. A complete description of the thermal, dynamical, and magnetic configuration can only be done by means of inversions of full vector Stokes spectropolarimetric measurements. Inversion techniques allow to disentangle the different effects of the atmospheric parameters on the Stokes profiles. To reliably determine the conditions of the atmosphere, there are several aspects that should be taken into account as explained in the following subsections.

1.5.1 Selection of spectral lines

One should carefully select the spectral lines that are going to provide the information we are searching for. Some are more sensitive than others to the various physical quantities of the atmosphere. Therefore, some lines are better suited to circumvent the undesired effects of the always present noise. This outline the importance of the selection of lines with the highest *sensitivities to the different atmospheric quantities*. Such lines would allow us to better discriminate from their profiles subtle changes on the conditions of the atmosphere. It is well known that the sensitivities of the Stokes parameters to the variations of the atmospheric conditions are given by the so-called response functions (RFs; Ruiz Cobo & del Toro Iniesta 1992). However, if one wants to select the most sensitive spectral lines from a list of candidates, one should calculate the RFs for each line and parameter in order to compare their values in a fairly long process. An analytical formulation of the sensitivities of the Stokes parameters to the physical quantities does not exist except for specific situations where the physical conditions prevailing in the solar atmosphere can be described with a Milne-Eddintong model (Orozco Suárez & Del Toro Iniesta 2007). Therefore, the issue of line selection according to their ability to carry information on the different physical quantities deserves special attention. On the other hand, to accurately study the atmosphere in the vertical direction it is also often important to select spectral lines that are formed in a broad range of layers in the photosphere. In this thesis, this goal will be reached by the simultaneous observation of visible and infrared spectral lines.

1.5.2 Simultaneous inversion of visible and infrared spectral lines

It is evident that the use of spectral lines with different height coverage and sensitivities would allow to better constrain the range of acceptable solutions resulting from the inversions, i.e. the accuracy of the results. Due to their simple Zeeman patterns and large effective Landé factors, the most commonly

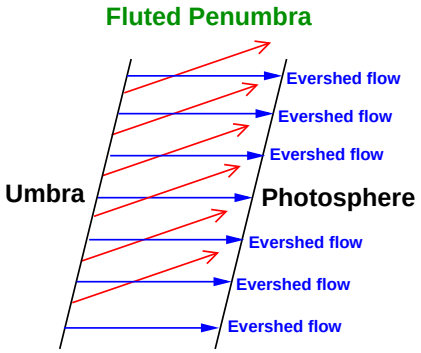

FIGURE 1.8:— Sketch of the fluted penumbra proposed by Title et al. (1993). Black lines indicate the inner and outer boundaries of the penumbra. Blue arrows represent horizontal field lines where the Evershed flow is mainly concentrated (i.e. intra-spines). Red arrows indicate more horizontal field lines representing spines where the Evershed flow is less conspicuous.

used spectral lines in solar spectropolarimetry in the visible and the infrared are the pair of Fe I lines at 630 nm and that at 1565 nm, respectively. These lines have their advantages and limitations. For example, Martínez González et al. (2006) demonstrated that atmospheres with different values of the field strength and temperature lead to the same emergent Stokes profiles of the 630 nm pair of Fe I lines, i.e. there is a cross-talk between temperature and field strength. Hence, it seems suitable to combine lines in the visible and the infrared wavelengths in order to improve the diagnostic capabilities of a single spectral range alone. This kind of observations are now possible and promise to improve the results derived from inversion techniques.

1.6 Penumbral structure from spectropolarimetric measurements

Over the years different degrees of sophistication have been used in the analysis of visible and infrared spectral lines emerging from sunspots. In the next sections we describe the *horizontal* (i.e. parallel to the local solar surface) and *vertical* (i.e. along the atmosphere) structure of the penumbra as inferred from these analyses. Spectropolarimetry has deeply improved our understanding of the fine structure of sunspot penumbrae.

1.6.1 Fluted penumbra and its relation with the Evershed flow

Using magnetograms and Dopplergrams, Title et al. (1993) introduced the concept of *fluted penumbra* (cf. Fig. 1.8): the Evershed flow is confined to radially oriented filaments displaying more horizontal magnetic fields than their surroundings. These filaments were called *intra-spines* by Lites et al. (1993) who analyzed Milne-Eddintong (ME) inversions of the Fe I pair at 630 nm. Basically, they found that the penumbral magnetic field is organized in filaments

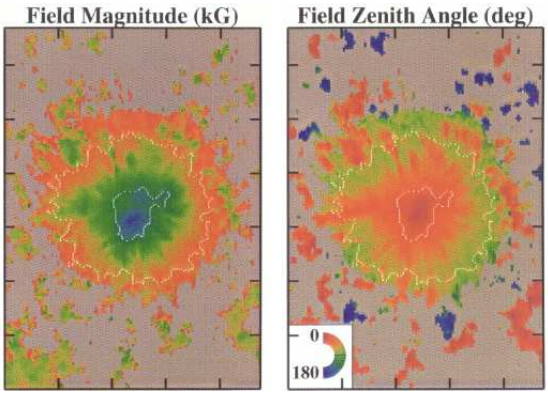

FIGURE 1.9:— Field strength and LRF inclination derived from a Milne-Eddintong inversion of the Fe I lines at 630 nm. The color scale ranges from 0 kG (red) to 3 kG (blue) for the field strength, and from 0° (red) to 180° (blue) for the field inclination. White lines indicate the inner and outer penumbral boundaries. Note the alternating structure of filaments displaying strong and vertical fields (spines) and weaker and more horizontal fields (intra-spines). [Adapted from Stanchfield et al. (1997)].

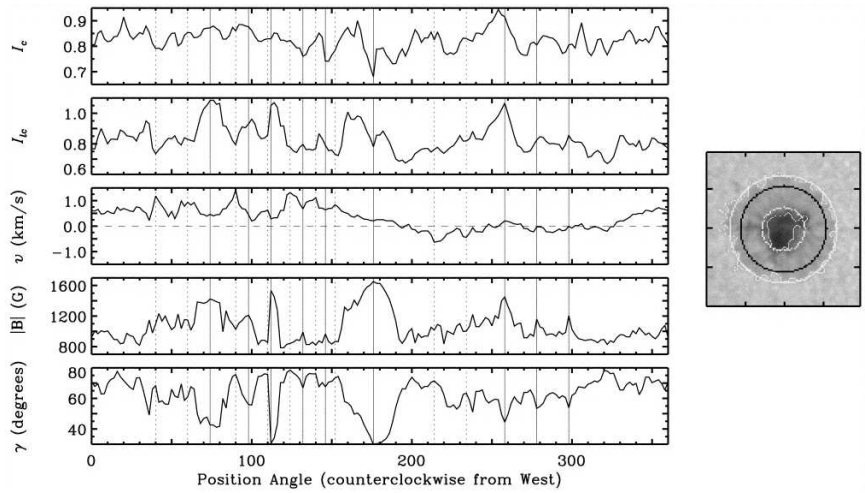

FIGURE 1.10:— From *top* to *bottom*: Variation of the continuum intensity, line core intensity, Doppler velocity, magnetic field strength, and LRF inclination around the azimuthal cut showed in the right panel ($\sim$ 0.8R). The solid and vertical dashed lines indicate the positions of the spines and intra-spines, respectively. [taken from Stanchfield et al. (1997)].

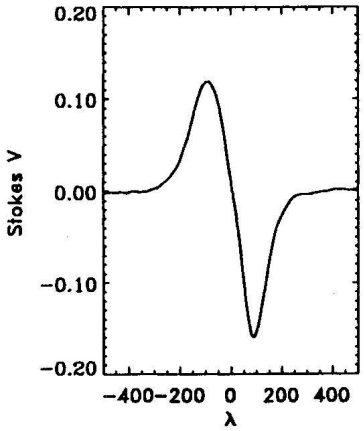

FIGURE 1.11:— Asymmetrical Stokes V profile observed at the center-side of a sunspot penumbra. [Taken from Sánchez Almeida & Lites (1992)].

called *intra-spines* and *spines* that azimuthally alternate (cf. Fig. 1.9). These filaments display different atmospheric properties. Intra-spines possess more horizontal and weaker fields than spines (cf. Fig. 1.10) and the Evershed flow is more conspicuous inside them (Rimmele 1995; Stanchfield et al. 1997; Westendorp Plaza et al. 2001a). In other words, the geometry of the penumbral magnetic field is compatible with two components displaying different inclinations which are horizontally interlaced (cf. Fig. 1.8). The Evershed flow is concentrated in the more horizontal component. Hence, the correlation between the Evershed flow and the filamentary structure of the magnetic field of the sunspot penumbrae is clearer than the displayed between the Evershed flow and the intensity (cf. Sect. 1.4.4).

1.6.2 Gradients of the physical properties with depth

Observations of the circular polarization profiles emerging from the sunspot penumbra indicate that they are rather asymmetric (Illing et al. 1974a,b, 1975; Kemp & Henson 1983; Makita 1986). This is because the red and blue lobes of the profiles do not display either the same area or the same peak amplitudes (cf. Fig. 1.11). Such asymmetries are quantified by the so-called Stokes V area asymmetry $\delta A = \int V(\lambda) d\lambda / \int |V(\lambda)| d\lambda$ and $\delta a = (|a_{\rm r}| - |a_{\rm b}|)/(|a_{\rm r}| + |a_{\rm b}|)$ where $a_{\rm r}$ and $a_{\rm b}$ are the peak amplitudes of the red and blue lobes. It is well known that asymmetries are produced by a combination of velocity and magnetic field gradients along the LOS (Auer & Heasley 1978; Landolfi & Deglinnocenti 1982; Landolfi & Landi degl'Innocenti 1996). Sánchez Almeida & Lites (1992) demonstrated that those asymmetries can be produced by large gradients of the velocity ($dv/d\tau \sim 1.5$ km s^{-1}) and inclination ($d\gamma/d\tau \sim 45°$). Hence, it is clear that variations of the physical quantities along the atmosphere may exist in sunspots.

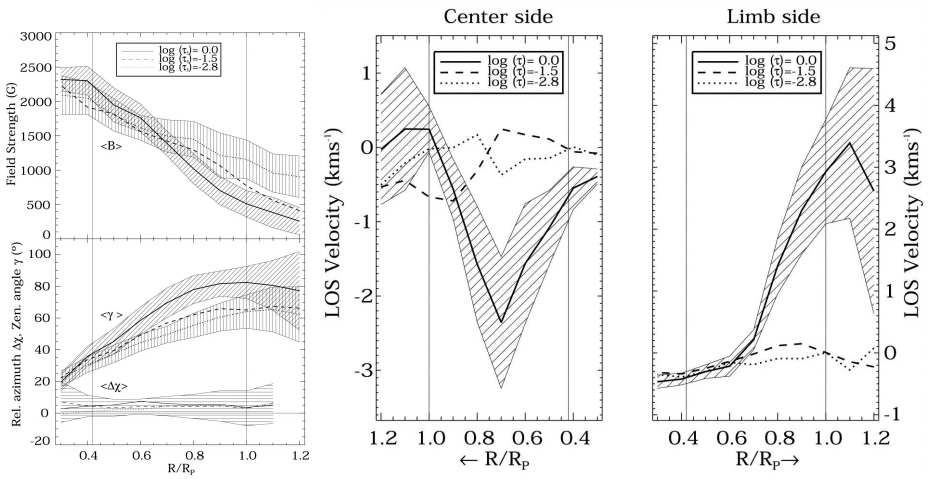

FIGURE 1.12:— Azimuthal averages of the field strength, inclination, relative azimuth (right panel) and LOS velocities (left panels) at $\log\tau = 0$ (solid lines), $\log\tau = -1.5$ (dashed lines), and $\log\tau = -2.8$ (dotted lines). Shaded areas indicated the rms variation of the parameters along the radial paths. [Taken from Westendorp Plaza et al. (2001b) and Westendorp Plaza et al. (2001a)]

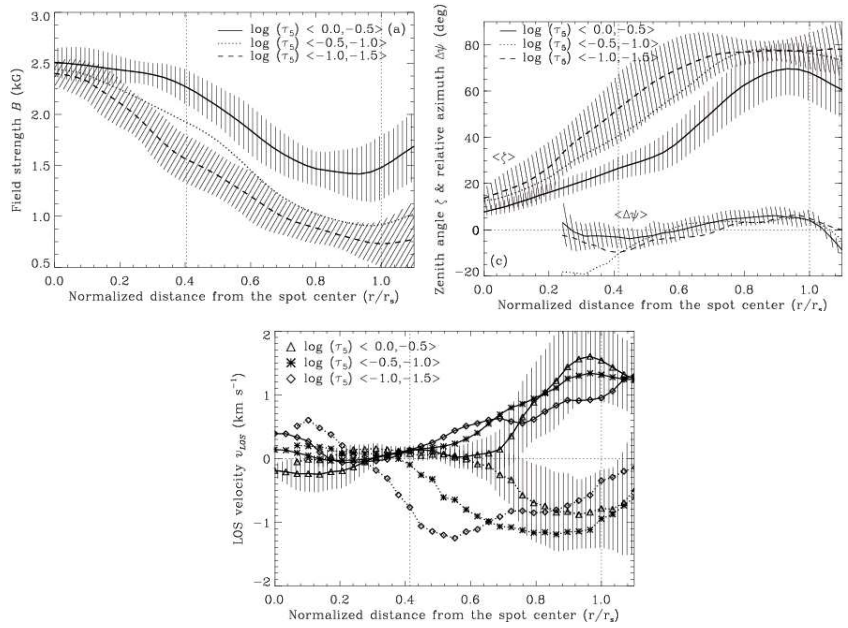

FIGURE 1.13:— Radial variations of the field strength, inclination, and LOS velocity at $\log\tau =< 0.0, -0.5 >$ (solid lines), $\log\tau =< -0.5, -1.0 >$ (dotted lines), and $\log\tau =< -1.0, -1.5 >$ (solid lines) (dashed lines). [Taken from Mathew et al. (2003)]

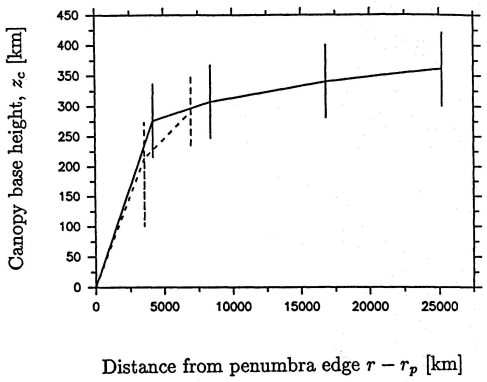

FIGURE 1.14:— Base height of the superpenumbral canopy, z_c, versus distance from the outer penumbral boundary $r - r_p$. Solid line indicates the results for the limb side of a sunspot and dashed line for the center side of another spot. [taken from Solanki et al. (1994)].

Inversions with gradients of the physical quantities along the LOS were performed for the first time by Westendorp Plaza et al. (1997, 2001b,a) for the pair of Fe I visible lines at 630 nm. They calculated the gradients of the physical quantities with optical depth. Fig. 1.12 displays the results of the average radial variation of the atmospheric quantities for the magnetic field strength, inclination, and LOS velocities in the limb and center side penumbra. As can be seen, the signs of the gradients of those quantities can be expressed in terms of the geometrical height as follows:

$$\frac{dB}{dz} > 0, \frac{d\gamma}{dz} < 0, \frac{dv}{dz} < 0 \tag{1.1}$$

A few years later, the same type of inversions were carried out by Mathew et al. (2003) for the infrared lines at 1565 nm. Fig. 1.13 shows the azimuthal averages derived from those inversions. Surprisingly, the signs of the gradients derived from the inversions of the infrared lines are the opposite than those inferred from the visible lines (cf. Eq. 1.1). A possible explanation of this contradictory behavior will be disscused in Sect. 1.6.4.

1.6.3 Continuity of the Evershed flow at the outer penumbral boundary

As discussed in Sect. 1.4.3, filtergrams observations do not clarify what happens with the Evershed flow at the outer penumbral boundary. Solanki et al. (1994) investigated this issue performing one component inversions of I and V Stokes profiles of the Fe I 1565 nm lines. They consider a canopy formed by horizontal field lines overlaying a non-magnetic atmosphere and they determine the height of the canopy base (cf. Fig. 1.14). They found that the Evershed flow continues into the canopy. Taking into account the smaller density of the material at the

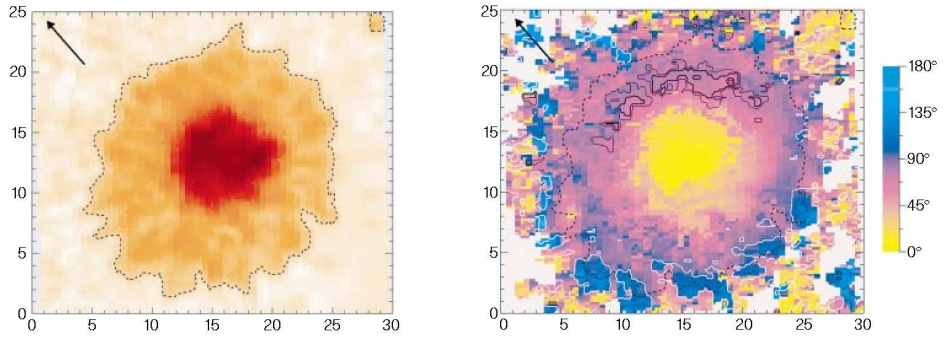

FIGURE 1.15:— Intensity continuum at 630 nm and field inclination at $log\tau = 0$ as measured from the normal to the solar surface. Dashed lines indicate the boundaries of the spot. White and black contours enclose pixels with redshifted and blueshifted Doppler velocities. Dashed lines indicate the boundaries of the spot. [from Westendorp Plaza et al. (1997)]

high layers of the canopy, they concluded that only a small fraction ($\sim 10\%$) of the flow can propagate to the canopy.

The definitive solution to the dilemma was given by Westendorp Plaza et al. (1997). They carried out inversions with gradients of the atmospheric parameters (cf. former section) and found correspondence between field lines bending back to the solar interior and redshifted Doppler velocities, i.e. velocity directed away from the observer, in deep atmospheric layers (cf. Fig. 1.15) at the outer penumbra. This explains why the Evershed flow abruptly ends at the outer boundary of the spot: it returns to the solar interior. Hence, it is now accepted that most of the Evershed flow partly dives down below the photosphere (Westendorp Plaza et al. 1997) while a small fraction continues into the canopy (Solanki et al. 1994; Rezaei et al. 2006) at the outer penumbra.

1.6.4 Uncombed penumbral model

As discussed in Sect. 1.6.2 asymmetries on the Stokes profiles indicate that physical properties vary along the LOS. Solanki & Montavon (1993) proposed a new scenario able to produce the area asymmetries of the spectral lines: a penumbra formed by two magnetic components with different velocities and inclinations, the so-called *uncombed penumbral model* (cf. Fig. 1.16). The component displaying more horizontal fields is assumed to be formed by flux tubes with finite vertical extension. These tubes are embedded in the more vertical component. For obvious reasons, the two components are called *tube* and *background*, respectively. In contrast with the fluted penumbra proposed by Title et al. (1993), the two components are not only interlaced in the horizontal direction but also in the vertical direction (cf. Fig. 1.17). The discontinuities of

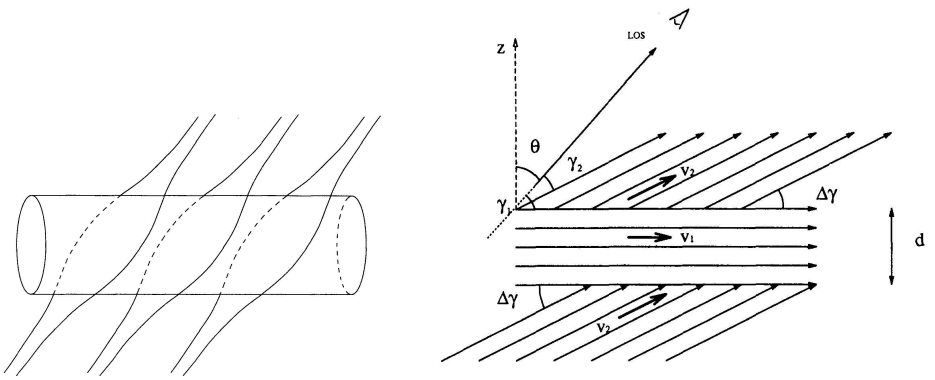

FIGURE 1.16:— *Left*: Illustration of the uncombed penumbral model. The penumbra is assumed to be composed by horizontal flux tubes driving the Evershed flow embedded in a more vertical surrounding. *Right*: Sketch of the magnetic field and velocity which represent a vertical cut along the axis of the tube. The direction of the observer (LOS), the heliocentric angle (θ), the velocities of the tube and background components (v_1 and v_2), and the diameter of the tube (d) are indicated. [Taken from Solanki & Montavon (1993)]

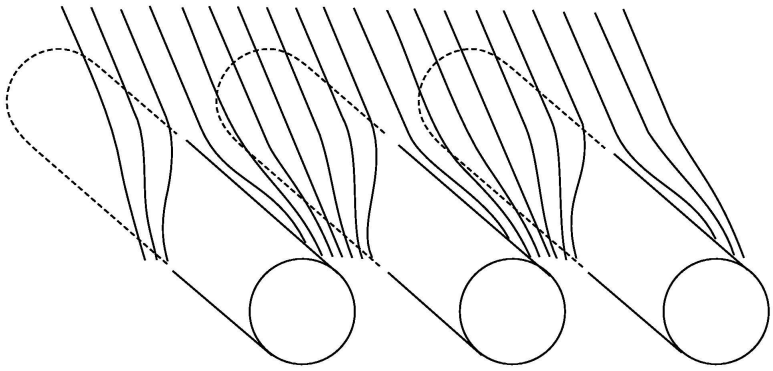

FIGURE 1.17:— Magnetic structure of the penumbra in the uncombed model. The flux-tube component is represented by cylinders while the field lines around the tube represent the background. [Taken from Solanki et al. (2006)]

the atmospheric properties between the boundaries of the flux tube give rise to asymmetric Stokes profiles.

Net circular polarization maps

Schlichenmaier et al. (2002) and Müller et al. (2002, 2006) demonstrated that using the uncombed penumbral model they were able to reproduce the asymmetries on the Stokes profiles in different spectral ranges. They calculated the Net Circular Polarization (NCP), defined as $\int V(\lambda)d\lambda$, of the sunspot penumbra as follows. They consider a penumbra composed by horizontal flux tubes carrying the Evershed flow embedded in a more horizontal background at rest (cf. Fig. 1.18) and compute the emerging synthetic profiles by integrating the radiative transfer equation. Then, they calculate the synthetic NCP maps from the profiles and compare with observations. As can be seen in the left panels of Fig. 1.18, their results nicely reproduce the shape of the NCP map of a sunspot for the Fe I lines at 1564.85 nm and 630.25 nm.

Gradients of the physical quantities explained by the uncombed model

As discussed in Sect. 1.6.2 the gradients of the physical quantities derived from the inversion of the visible and infrared lines have different signs. A possible explanation arise in terms of the uncombed penumbral. Martínez Pillet (2000) demonstrated that the gradients derived from the inversions of the visible lines are explained if the visible lines sample the upper boundary of a flux tube embedded in a more horizontal background with stronger fields. Taking into account that the infrared lines are formed deeper in the atmosphere than the visible ones, Mathew et al. (2003) and Borrero et al. (2004) probed that the gradients of the infrared lines are explained if the lines sample the lower boundary of the tube. The upper panels of Fig. 1.19 show the stratifications retrieved from the one-component inversions of synthetic profiles emerging from the uncombed model outlined by the dotted-dashed lines. As can be seen, the atmospheres derived from the inversion of the visible (dashed lines) and infrared (solid lines) profiles reproduce the opposite sign of the gradients.

1.6.5 Properties of the tube and background atmospheres

Inversions adopting two magnetic components interlaced horizontally but not vertically have been carried out by del Toro Iniesta et al. (2001), Bellot Rubio et al. (2003, 2004), and Borrero et al. (2004). As Bellot Rubio et al. (2003) demonstrated, if one assumes two magnetic components filling the resolution

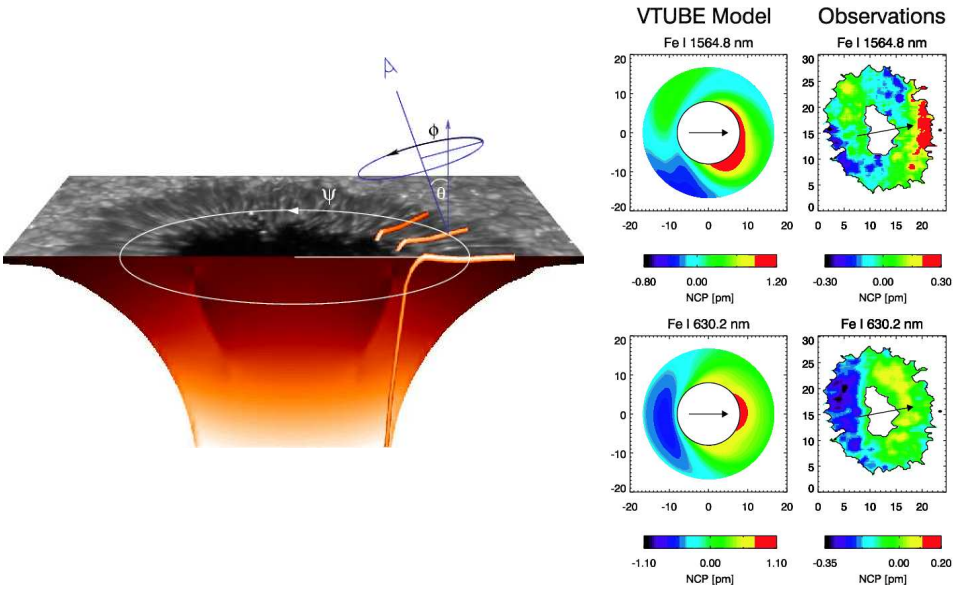

FIGURE 1.18:— *Left*: Illustration of the model employed by Müller et al. (2002). Horizontal magnetic flux tubes carrying the Evershed flow are radially oriented. *Right*: Comparison of the synthetic maps of net circular polarization of the Fe I lines at 1564.85 nm and 630.25 nm (left panels) with the corresponding observed maps (right panels) for a sunspot located at an heliocentric angle of $\theta = 30°$. [Taken from Müller et al. (2002, 2006)]

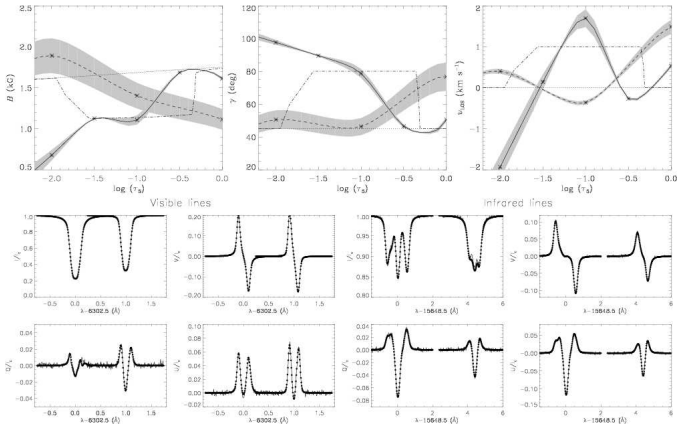

FIGURE 1.19:— *Top panels*: Magnetic field strength, field inclination, and line of sight velocity. Atmospheres used to synthesize the Stokes profiles are outlined by the dotted-dashed lines. The atmospheres derived from the one-component inversion of the visible lines and infrared lines are displayed by the dashed and solid lines, respectively. The shaded areas represent the standard deviations of the parameters for inversions starting at different initial values. *Bottom panels*: Synthetic (solid lines) and best fit profiles (dots). [Taken from Mathew et al. (2003)]

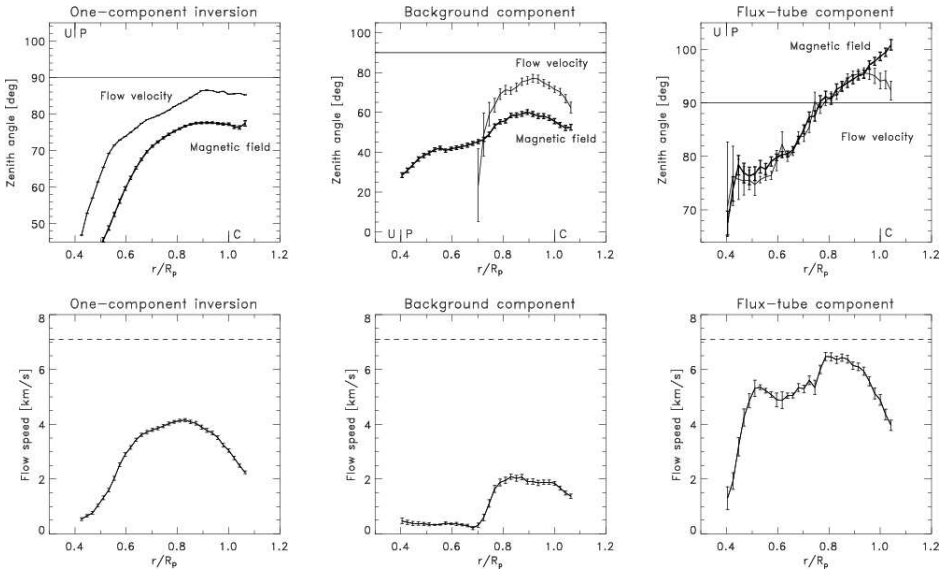

FIGURE 1.20:— *Top:* Evolution of the magnetic (thick lines) and velocity field (thin lines) inclinations derived from one-component (left panel) and two component inversions (center-right panels). *Bottom:* Radial variation of flow speed. The horizontal dashed lines outline the local sound speed. The results for the background and tube components are shown in the center and right panels, respectively. Error bars indicate the rms variation of the quantities. [Taken from Bellot Rubio et al. (2003)]

element there is a perfect alignment of the magnetic and velocity field vectors in the component describing the penumbral flux tubes (cf. top right panel of Fig. 1.20). In contrast, the one component inversions do not fulfill the frozen-in magnetic fields condition of the plasma (cf. top left panel of Fig. 1.20). The results of these inversions inversions (cf. Fig. 1.21) are consistent with the uncombed penumbral model, i.e. a penumbra formed by horizontal flux tubes embedded in a more vertical background magnetic field. The tube atmosphere carry most of the Evershed flow (cf. bottom panels of Fig. 1.20) and possess weaker fields than the background except in outer penumbra (cf. Fig. 1.22). Moreover, it is more inclined than the background at all radial distances. In the middle penumbra and beyond the magnetic field and the flow returns to the solar interior.

Accounting for two magnetic components interlaced not only horizontally but also vertically was the next logical step. This type of inversions has been carried out by Borrero et al. (2005) for the infrared lines at 1565 nm and by Borrero et al. (2006) for the visible lines at 630 nm. They calculate averages of the atmospheric parameter along radial cuts on the limbward side penumbra

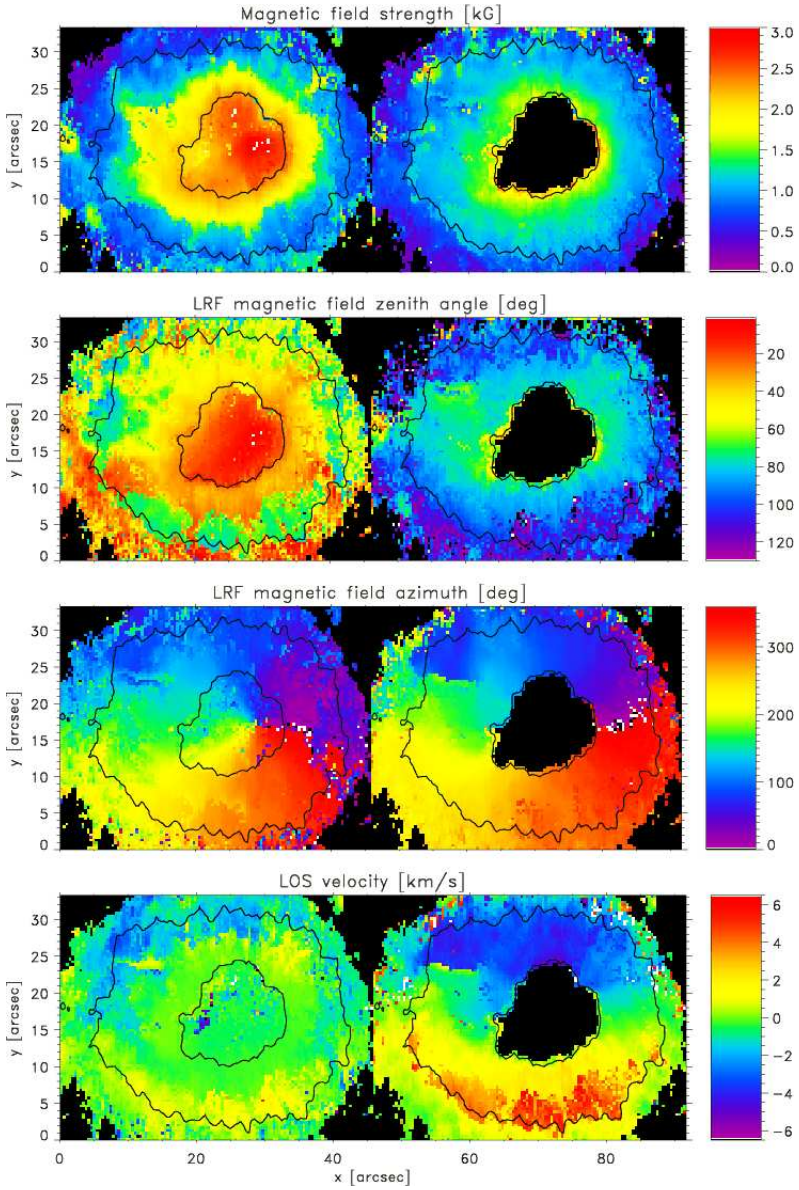

FIGURE 1.21:— Magnetic and kinematic configuration of a sunspot inferred from the two-component inversion of the Stokes profiles. From *top* to *bottom*: magnetic field strength, magnetic field inclination, magnetic field azimuth, and LOS velocity (positive values indicate redshifts) for the background (*left*) and tube (*right*) components. Inclination and azimuth are expressed in the local reference frame. [Taken from Bellot Rubio et al. (2004)]

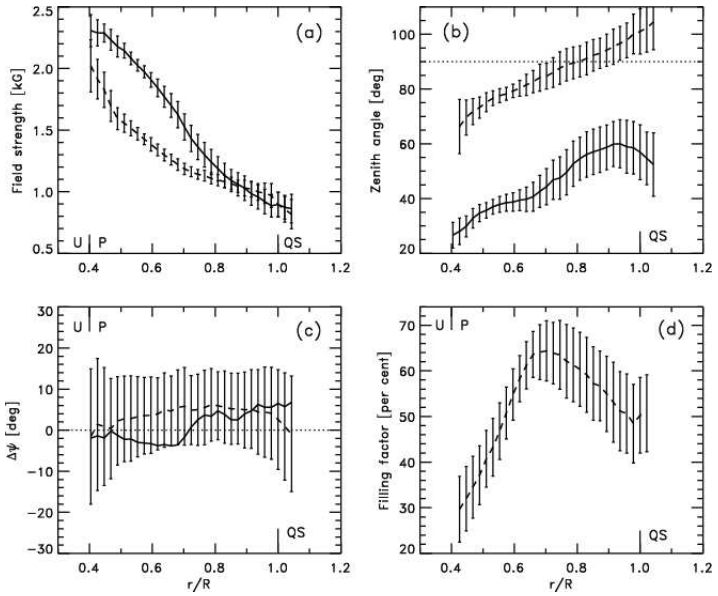

FIGURE 1.22:— Radial evolution of the field strength, field inclination, relative azimuth, and filling factor of the tube for the tube (dashed lines) and background components (solid lines). Error bars indicate the standard deviation of the parameters along the azimuthal paths. [Taken from Bellot Rubio et al. (2004)]

near the line of symmetry. Basically, their results are in agreement with the findings of Bellot Rubio et al. (2004) (cf. Fig. 1.23). Moreover, Borrero et al. (2005, 2006) found hot flux tubes in the inner penumbra that become cooler at larger radial distances (cf. top right panel of Fig. 1.23). At large radial distances, Borrero et al. (2005) measured flow speeds exceeding the critical speed of the medium and they found evidence for the formation of a shock front. Moreover, Borrero et al. (2006) retrieved flux tubes with the lower boundary bellow $\tau = 1$ and as thick as 100-300 km from the inversion (cf. Fig. 1.31).

1.6.6 Origin of spine/intra-spine structure of the penumbra

Bellot Rubio et al. (2004) realized that the azimuthal variations of the penumbral magnetic field found by Title et al. (1993) and Lites et al. (1993) in terms of one magnetic component disappears when one assumes two magnetic atmospheres filling the resolution element (cf. Fig. 1.21). However, Bellot Rubio et al. (2004) found that the quantity displaying azimuthal fluctuations is the filling factor. In fact, if one plots the inclinations and field strengths derived from one-component inversions along a radial path at the mid-penumbra against the corresponding filling factors inferred from the two-component inversions,

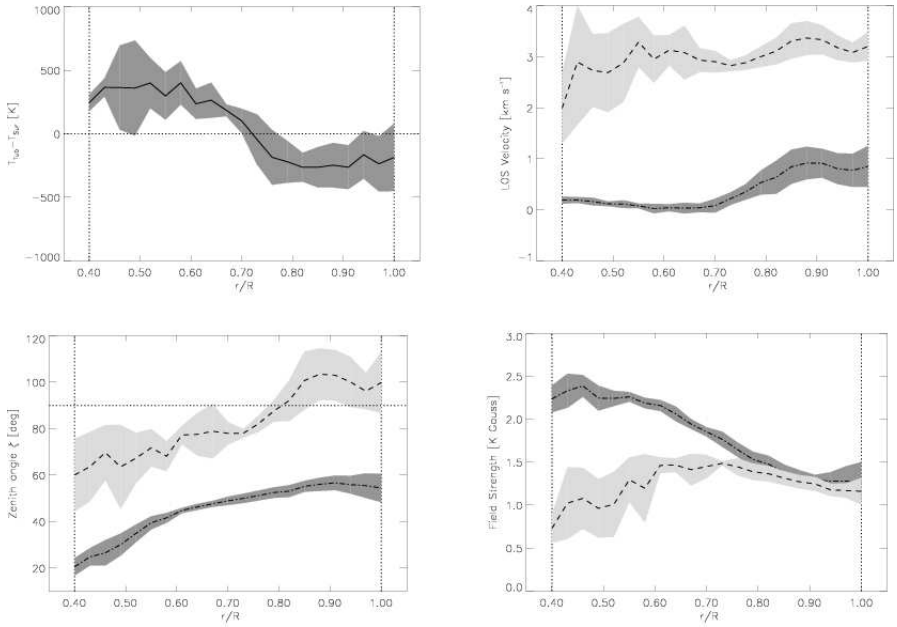

FIGURE 1.23:— Radial variation of the atmospheric properties of the background (dot-dashed lines) and and the penumbral flux tube (dashed lines) components. From left to right and top to bottom: temperature difference between the flux tube and background, LOS velocity, magnetic inclination, and magnetic field strength. The curves have been constructed taken the quantities at a geometrical depth that corresponds to the central position of the flux tube. [Taken from Borrero et al. (2006)]

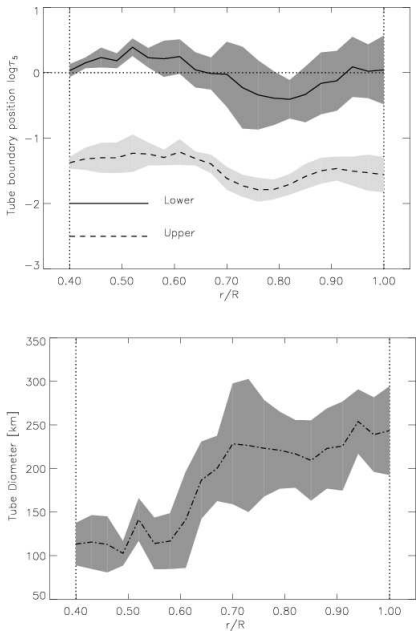

FIGURE 1.24:— *Top:* Lower (dashed line) and upper boundaries (solid line) of the flux tube given in units of the logarithm of the optical depth as a function of the radial distance. *Bottom:* Radial evolution of the tube diameter. [Taken from Borrero et al. (2006)]

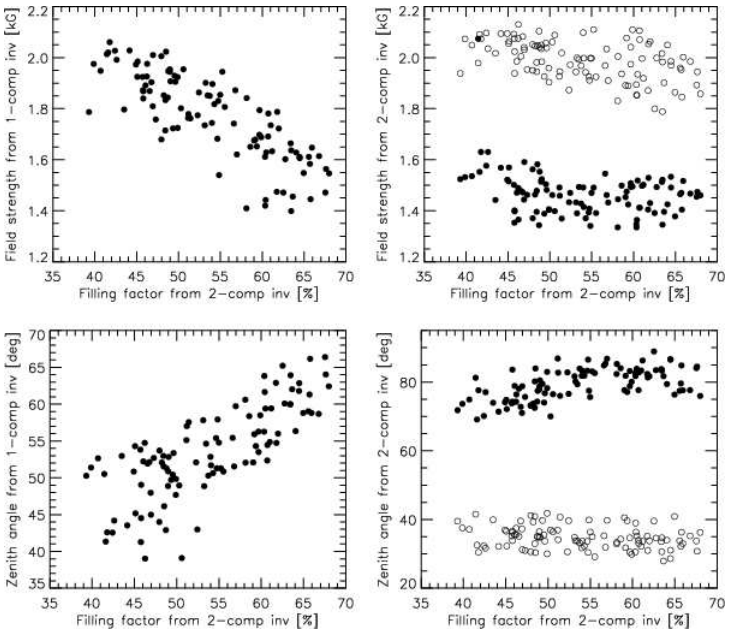

FIGURE 1.25:— *Left panels*: field strength (top) and field inclination (bottom) derived from one-component inversions of pixels along an azimuthal path at r/R = 0.6 against the filling factor of the tube deduced from the two-component inversion. *Right panels*: field strengths (top) and field inclinations (bottom) in the background (open circles) and tube (filled circles) component from the two-component inversion as a function of the filling factor for the same azimuthal path. [Taken from Bellot Rubio et al. (2004)]

they are strongly correlated (cf. left panels of Fig. 1.25). In contrast, the field strength and inclination of the tube and background components remain relatively constant along the same azimuthal path (cf. right panels of Fig. 1.25). In summary, the filling factor displays variations along azimuthal cuts, while the atmospheric properties of the tube and background do not seem to change so much along the same paths. This indicates that the penumbra is fluted in the sense that there are locations where the filling factor of the tube is increased.

1.7 Temporal evolution of the Evershed flow

Despite we are far from a complete understanding of the Evershed flow, its magnetic and dynamic configuration are relatively well known. However, what does we know about its temporal evolution?. To our knowledge, the first investigation of the time evolution of the Evershed flow was carried out by Shine et al. (1994). They study the evolution of several sunspots located at different heliocentric angles by means of filtergrams, Dopplergrams, and magnetograms

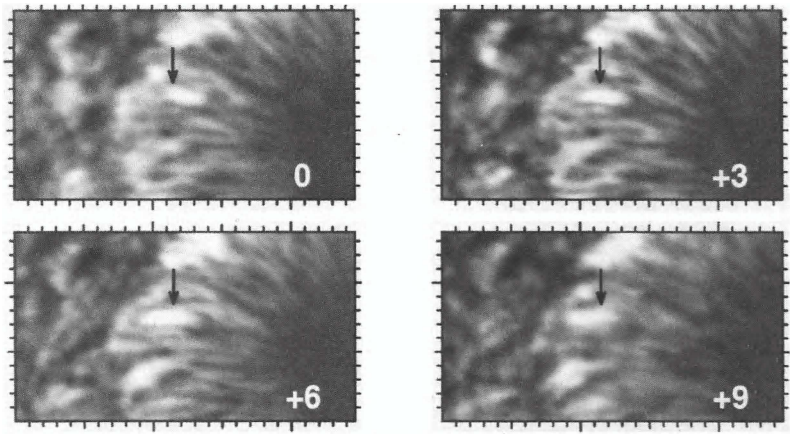

FIGURE 1.26:— Evershed cloud as seen in a Dopplergram calculated from Fe I 557.6 nm. The arrow indicate the position of the EC. Time is shown in minutes at each panel. White and black colours indicate velocities directed towards (i.e. blueshifts) and away (i.e. redshifts) the observer. Each tickmark represents $1''$. [Taken from Shine et al. (1994)]

taken with the 48 cm Swedish solar observatory[2]. When they analyzed the evolution of the penumbra, they realized about the existence of outwards motions of patterns which are seen with low contrast in the inner penumbra and become more visible in the outer penumbra in the Dopplergrams (cf. Fig. 1.26). These coherent structures appear cloud-like because of their diffusive boundaries and they called them *Evershed clouds* (ECs). ECs appear in the inner penumbra and propagate with roughly constant velocities around 3.5 km s^{-1} until the outer boundary of the spot where they seem to vanish. Shine et al. (1994) generally measure larger proper motions than the Doppler velocities when both are assumed horizontal.

Although these authors found the Evershed effect mainly concentrated in the darker penumbral regions, ECs are correlated with locally brighter continuum features than their surroundings. They also describe temporary extensions of the Doppler velocity beyond the usual spot boundary associated with locally darker continuum signals. In contrast, Rimmele (1994) do not find any correlation between the ECs and the continuum intensity.

Unfortunately, Shine et al. (1994) were not able to draw any conclusion from the magnetograms. They observed some cases where the ECs were correlated with a weaker magnetogram signal but this could be produced by variations of the field strength and/or inclination.

In order to study the evolution of the ECs with time, they selected fixed

[2]The telescope was updated to the actual 1 m configuration on 2002.

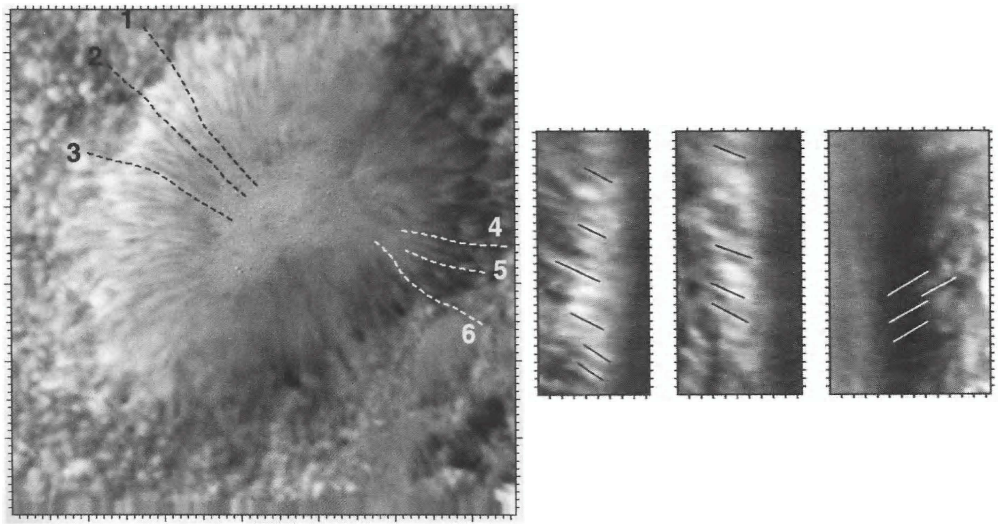

FIGURE 1.27:— *Left* panel: Dopplergram of a sunspot where some penumbral filaments are outlined by the dashed lines. Each tickmark represents one arcsecond. *Right* panels: Space/time slices in Dopplergrams along penumbral filaments filtered from the 5-minutes solar oscillation. The two first panels and the last are constructed from filaments in the diskward and limbward penumbra, respectively. The lines mark the propagation of different ECs along the filaments. The tickmarks on the x and y-axis represent $1''$and 5 min, respectively. White and black colours indicate blueshifted and redshifted Doppler velocities. [Taken from Shine et al. (1994)]

paths following the direction of flow filaments where the ECs were seen to propagate outwards (cf. left panel of Fig. 1.27). The right panels of Fig. 1.27 show the evolution of the Dopplergram signal with time along three penumbral filaments[3]. The x-axis represent the spatial direction along the filament while the time increases along the y-axis. As can be seen, the space/time slices show patterns (straight lines) with an irregular repetitive behavior. These patterns are produced by the propagation of the ECs along the filaments. The two-dimensional power spectrum of one of these space/time slices is shown in Fig. 1.28. As can be seen, there is an obvious but not very sharp peak on frequencies around 1.6 mHz ($\sim$ 10 min) for phase velocities of 3-4 km s^{-1} moving outwards from the spot (see white line on Fig. 1.28) that can be ascribed to the propagation of the ECs. Although with slightly different values this quasi-periodic behavior was later confirmed by Rimmele (1994) and Rouppe van der Voort (2003) while Georgakilas & Christopoulou (2003) found evidence of temporal variations with timescales around 25 min.

A summary of the main phenomenological properties of the ECs found by

[3]They removed the 5-minutes solar oscillation via three-dimensional Fourier filtering.

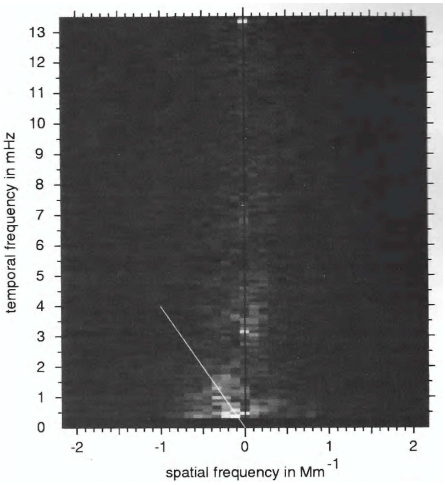

FIGURE 1.28:— Two-dimensional power spectrum of one of the Dopplergram space/time slices. White line indicates points of the spectrum with phase velocities of 4 km s^{-1} directed to the outer penumbral boundary. [Taken from Shine et al. (1994)]

TABLE 1.2:— Phenomenological properties of ECs

Size [km]	Radial spacing [km]	Periodicity [min]	$v_{\rm LOS}$ [km s^{-1}]	$v_{\rm prop}$ [km s^{-1}]
1000	2000-3000	10-24	3-5	3.5

the previous investigations (Shine et al. 1994; Rimmele 1994; Rouppe van der Voort 2003; Georgakilas & Christopoulou 2003) is given in Table 1.2. The physical properties of the ECs remain a mistery and we still even lack of a complete description of the observational properties of the ECs. Concerning the EC phenomenon, there are many unresolved questions: what is the physical nature of the penumbral filaments where the ECs are seen to propagate outwards?; are the ECs related with the uncombed structure of the penumbra?; what happens with the ECs when they disapear; are the ECs associated with a change of the magnetic field configuration?; what is the physical mechanism that produce the ECs?. It is obvious the need for a study of the temporal evolution of the Evershed flow by means of full vector spectropolarimetric measurements.

1.8 Moving magnetic features around sunspots

Sunspots are surrounded by small magnetic elements (1-2″) moving outwards (0.5-2 km s^{-1}) called moving magnetic features (MMFs). They were discovered by Sheeley (1969). Most of what we know about MMFs has been learned from magnetograms. This is the reason why they have been classified in terms of their polarity as measured by magnetograms in three different types by Shine et al. (2000):

- Type I MMFs: Bipolar structures. Usually the flux patch located far-

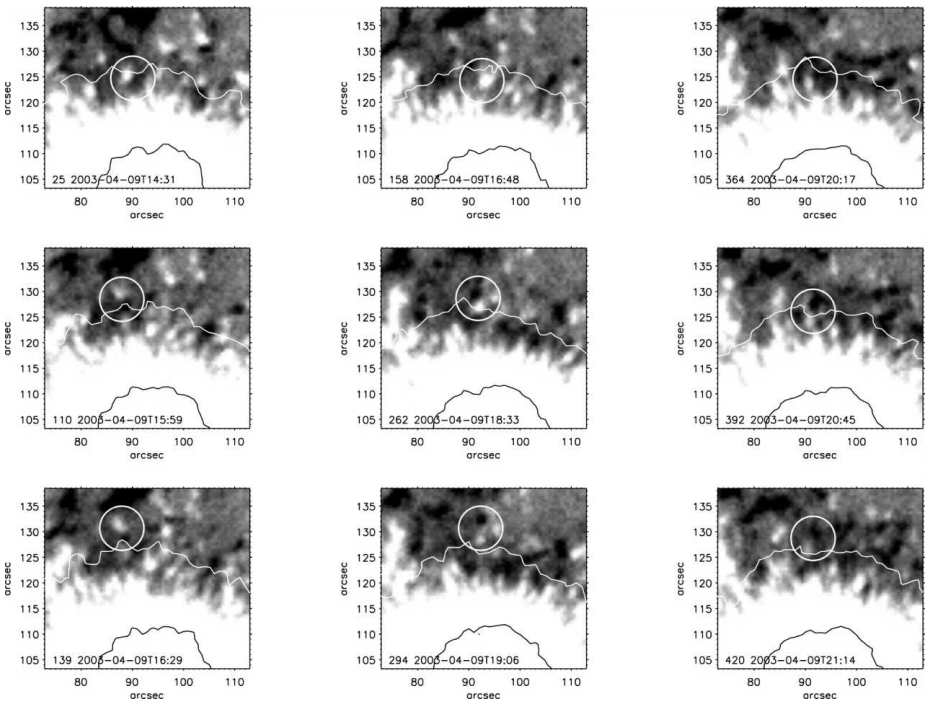

FIGURE 1.29:— Magnetograms showing three bipolar MMFs since they appear inside the spot (top panels) until they reach the moat (bottom panels). Each column corresponds to a different MMF while the time increases from top to bottom in the different panels. The circles outline the MMFs. [Taken from Sainz Dalda & Martínez Pillet (2005)]

ther from the sunspot have the same polarity as the spot (Lee 1992; Yurchyshyn et al. 2001; Zhang et al. 2003).

- Type II MMFs: Unipolar structures with the same polarity of the spot.
- Typre III MMFs: Unipolar structures with the opposite polarity of the spot.

MMFs are seen to appear in the surroundings of the spots and at least some of them originate inside the penumbra (Sainz Dalda & Martínez Pillet 2005; Ravindra 2006; Penn et al. 2006). Some investigators have been able to simultaneously detect MMFs in the photosphere, chromosphere, and corona (Leka et al. 1994; Lin et al. 2006). Hence, it is clear that the MMFs seen in the photosphere must be related with physical processes taking place into the higher layers of the Sun (Zhang & Wang 2002; Ryutova et al. 2007). The relation between the decay of the sunspots and MMFs has also been investigated. In

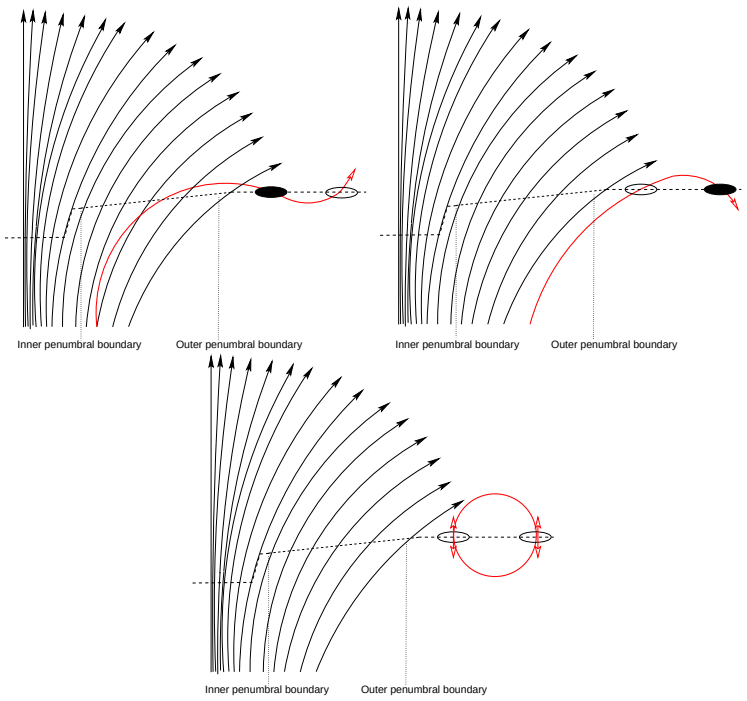

FIGURE 1.30:— Geometrical models of bipolar MMFs. The red line outline the flux tube performing the $\mho$, Ω, and O-loops that originate the bipolar MMFs. The dashed line indicates $\tau = 1$ in the photosphere. Black lines display the background field.

fact, some authors find evidence of the MMFs being probably part of the decay process of sunspots (Martínez Pillet 2002; Kubo et al. 2007).

The relation between the MMFs and the magnetic field of the sunspots was proposed a few years later of their discovery by Harvey & Harvey (1973). Basically, they suggested that the bipolar MMFs are produced by the intersection of the same flux tube with the solar surface. In this context three different geometries of the magnetic field have been proposed (cf. Fig. 1.30):

- $\mho$-loops (Zhang et al. 2003).
- Ω-loops (Harvey & Harvey 1973; Nye et al. 1984; Ryutova et al. 1998; Thomas et al. 2002).
- O-loops (Wilson 1986).

Unfortunately, the magnetic field configuration of bipolar MMFs is still unknown. For this reason, we cannot discriminate between the three different possibilities. More recently, some investigators pointed out the possible

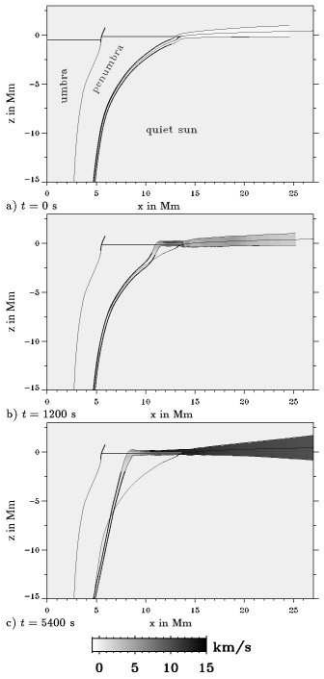

FIGURE 1.31:— Evolution of a thin flux tube in the MTM. Umbra and penumbra are separated by the peripatopause while the penumbra and quiet Sun by the magnetopause. At the beginning, the tube lies along the magnetopause (top). As a consequence of the heating induced by the field free material the tube becomes buoyant (center) and raises. When the tube reaches $\tau = 1$ the medium becomes subadiabatical and the inner footpoint migrates inwards (bottom). The horizontal line outline $\tau = 1$ in the photosphere. The gray scale outline the magnitude of the flow velocity. [Taken from Schlichenmaier et al. (1998a)]

link between MMFs and the penumbral component carrying the Evershed flow (Martínez Pillet 2002; Schlichenmaier 2002; Thomas et al. 2002). However, this relationship has not yet been proved.

Despite the phenomenological properties of the MMFs are well known, a number of fundamental questions concerning the nature and origin of the MMFs remain unanswered: what is the origin of the MMFs?; how are they originated?; what is their magnetic configuration?; are bipolar MMFs produced by the intersection of the same flux tube with the solar surface?; in that case, are they produced by O-loops, Ω-loops, or ℧-loops?; what is the relation between the MMFs and the Evershed flow?. A total or partial answer to the former questions would be more than welcome.

1.9 Theoretical models of the Evershed flow

1.9.1 Moving tube model

The moving tube model (MTM) has been developed by Schlichenmaier et al. (1998a,b) who investigated the time evolution of a thin flux tube[4] placed in

[4]The magnetic diffusivity is neglected and the physical variables do not change across the tube. The physical variables can only vary along the tube.

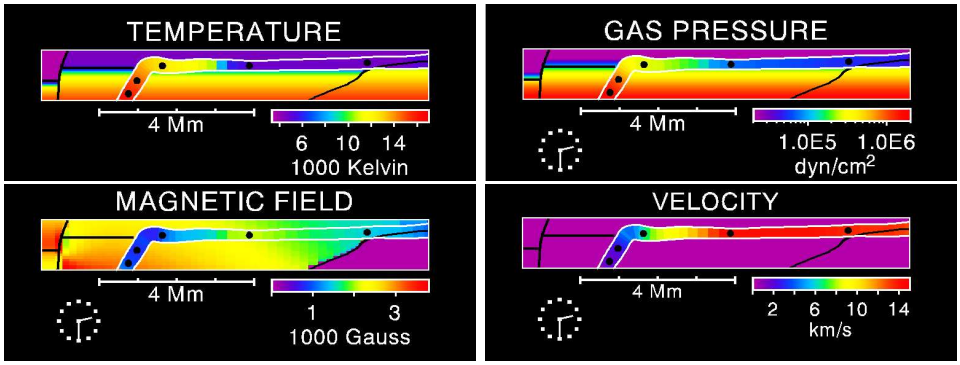

FIGURE 1.32:— Temperature, gas pressure, magnetic field strength, and flow velocity of the tube and the surrounding atmosphere. [Taken from http://www.kis.uni-freiburg.de/∼schliche/]

the sunspot model of Jahn & Schmidt (1994). Initially the flux tube lies along the magnetopause (cf. top panel of Fig. 1.32), i.e. a current sheet separating the sunspot of the adjacent quiet sun. Then, the tube is heated by the field free hotter plasma located below. This produces an expansion of the tube that makes it less dense and, consequently, buoyant (cf. center panel of Fig. 1.32). When the tube arrives at the photospheric layers, the medium becomes subadiatic and the tube ceases its vertical movement[5]. The tube cools because of the radiatives losses producing a gradient of pressure along it that accelerates a flow of material. At this stage, the tube lies almost horizontal to the solar surface and the inner footpoint (i.e. the intersection of the tube with $\tau = 1$) migrates inward (cf. bottom panel of Fig. 1.32).

Figure 1.32 shows temperature, gas pressure, field strength, and flow velocity of the tube and the surrounding atmosphere. As can be seen, the inner footpoint is hotter than their surroundings while the other parts of the tube are cooler. The pressure decreases along the tube originating an accelerated flow of material. Moreover the field strength is lower in the tube than in its surroundings in the inner penumbra becoming equal in the outer.

MTM provides a natural explanation of the Evershed flow and the motion of bright penumbral grains to the inner penumbra. Schlichenmaier (2002) improved the treatment of artificial viscosities obtaining tubes that develop kinks that travel outwards. Thereby the tube displays field lines pointing to the solar interior. Moreover, this provides a mechanism that could explain the formation of MMFs in/around sunspots. However, MTM does not reproduce the observed time variability of the Evershed flow. It is clear that further numerical

[5]This process is known as convective exchange of flux tubes.

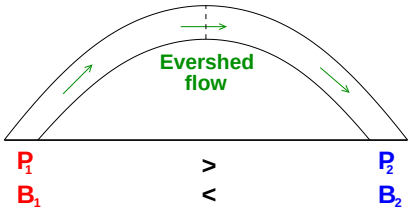

FIGURE 1.33:— Illustration of the siphon flow model . P_1 and P_2 indicates the gas pressure of the inner and outer footpoints. B_1 and B_2 are the corresponding quantities for the field strength. [Adapted from Meyer & Schmidt (1968)]

modelling has to be implemented in this promising model.

1.9.2 Siphon flow model

The siphon flow model (SFM) was initially proposed by Meyer & Schmidt (1968), although an increasing degree of sophistication has been included by different investigators (Degenhardt 1989; Thomas 1988; Thomas & Montesinos 1991; Montesinos & Thomas 1989, 1997). In this model the Evershed flow occurs between the two footpoints of an arched thin flux tube (cf. Fig. 1.33). If the footpoints are located at the same geometrical height, they must be in total pressure balance:

$$P_1 + \frac{B_1^2}{8\pi} = P_2 + \frac{B_2^2}{8\pi}, \tag{1.2}$$

where P and $\frac{B^2}{8\pi}$ are the gas and magnetic pressure, respectively. In order to originate the flow along the tube, the gas pressure of the outer footpoint must be lower than the one of the inner ($P_1 > P_2$). This implies that the magnetic field strength at the outer footpoint must be greater[6] ($B_1 < B_2$). In contrast, the observations indicate that the field strength decreases with radial distance in sunspots. Montesinos & Thomas (1997) claimed that such contradiction between the SFM and the observations could be produced by the different geometrical heights at which the field strength of the two footpoints are measured. In fact, it is known that the medium is more transparent in the inner penumbra and, consequently, the magnetic field inferred from the observations at smaller radial distances corresponds to deeper atmospheric layers.

The SFM, however, does not take into account the temporal evolution of the flow. Montesinos noted that siphon flows could be transient because of the changing conditions of the footpoints.

1.10 Overview of the thesis

Despite considerable efforts have been devoted to understand the physical nature of the Evershed flow since almost a century ago (Evershed 1909), we are

[6]Note that the MTM predict greater field strengths and lower gas pressure of the tube at larger radial distances (cf. Fig. 1.32).

still far from a complete understanding of the phenomenon. In this thesis we investigate, for the first time, the temporal evolution of the Evershed flow by analyzing simultaneous full vector spectropolarimetric observations in visible (630 nm) and near infrared (1565 nm) lines. This allow us not only to characterize the EC phenomenon from a phenomenological point of view but also to provide information to further constrain the physical nature of the Evershed flow. In addition, the relation between the Evershed flow and the origin and nature of moving magnetic features is investigated. We suggest qualitative geometrical models that are in agreement with the uncombed penumbral model and reproduce our observations of ECs and MMFs. The thesis is structured as follows:

- A brief summary of the fundamentals of spectropolarimetry and radiative transfer is given in Chapter 2. Nomenclature and definitions employed along the thesis are introduced here.

- In Chapter 3 we develop a simple phenomenological model capable of describing the sensitivities of the lines in terms of simple line parameters. The sensitivities of visible and infrared are examined in detail demonstrating that both visible and infrared lines have their advantages and limitations. This proves that it is desiderable to combine them in order to retrieve the physical properties of the solar atmosphere more reliably.

- In Chapter 4 we describe in detail the observations and data reduction, including the various corrections applied to the spectropolarimetric measurements and the alignment of the different data sets. A description of the telescope and its polarimeters is also given.

- Chapter 5 gives a brief overview of the different techniques employed in the analysis of the spectropolarimetric measurements in this thesis: since simple line parameters calculation to complex inversions of the Stokes profiles in terms of one-component and uncombed model atmospheres. The wavelength scale used for the VIS and IR data sets and its accuracy is discussed.

- In Chapter 6 we present the one-component inversions of the pair of visible Fe I lines at 630 nm and the pair of infrared Fe I lines at 1565 nm emerging from three sunspots located at different heliocentric angles. Although the inversions of the lines of two spectral ranges lead to essentially similar physical parameters, we find a cross-talk between temperature and stray light affecting visible lines. This problem is minimized by inverting the

lines of the two spectral ranges simultaneously. This demonstrates that simultaneous inversion of the visible and infrared spectral lines improve the diagnostic capabilities of a single spectral range alone and allows to characterize the physical properties of the atmosphere more reliably.

- Chapter 7 presents an in-depth observational characterization of temporal evolution of the Evershed flow, which is mainly due to the appearance of ECs. We determine the sizes, proper motions, location in the penumbra, and frequency of appearance of ECs, as well as the typical Doppler velocities, linear and circular polarization signals, Stokes V asymmetries and continuum intensities exhibited by ECs by analyzing the Stokes profiles of the spectral lines at 1565 nm and 630 nm. We find that ECs appear in the mid penumbra and propagate outwards following the intra-spines. The frequency of appearance of ECs varies between 14 and 40 min in different intra-spines. ECs exhibit the largest Doppler velocities and linear-to-circular polarization ratios of the whole penumbra. In addition, lines formed deeper in the atmosphere show larger Doppler velocities, much in the same way as the quiescent Evershed flow. We find two groups of ECs: type I ECs, which vanish in the outer penumbra, and type II ECs, which cross the boundary of the spot and reach the moat. Most of the observed ECs belong to type I.

- In Chapters 8 and 9 the physical properties of ECs are determined by inverting the Stokes parameters of four lines at 630 nm and three lines at 1565 nm. Two different semiempirical models are used to interpret the observed Stokes spectra: one-component model atmospheres, and uncombed models that take into account the fine structure of the penumbra. According to the results of one-component inversions, the EC phenomenon can be understood as a perturbation of the magnetic and dynamic configuration of the intra-spines along which the ECs migrate outwards. The uncombed inversions, on the other hand, suggest that ECs are the results of enhancements of the visibility of penumbral flux tubes, rather by changes in the magnetic field vector. The feasibility of this mechanism is examined with simple numerical experiments that use penumbral flux tubes in mechanical equilibrium with a background field. We find that the enhancements of the visibility of penumbral flux tubes can be produced by variations of the temperature and density that leads to a modification of the optical depth scale that allows to see a greater fraction of the tube. While the one-component inversions confirm many of the properties indicated by a simple line parameter analysis, we tend to

give more credit to the results of the uncombed inversions because they take into account, at least in an approximate manner, the fine structure of the penumbra. In fact, our results suggest that type I ECs could be variations of the thermodynamical properties propagating along flux tubes extending along the entire penumbra that return to the solar interior in the spot boundary.

- The temporal evolution of the type II ECs in the moat and its relation with the origin and nature of MMFs is investigated in Chapter 10. We find that type II ECs modify the spot boundary in their passage and once they enter the moat they adopt a roundish shape and propagate with smaller velocities until they vanish. Then, some of them are detected as MMFs in the magnetograms. We find two different types of MMFs originating inside the spot: i-MMFs, which precursors are the type II ECs, and s-MMFs which are originated inside the spines where the Evershed flow is less conspicuous. According to the results of the uncombed inversions, the precursors of i-MMFs and s-MMFs exhibit large and small values of the filling factor of the tube atmosphere, respectively. This implies that they are representatives of the conditions of the tube and background atmosphere. For this reason, we conjecture that s-MMFs are background field lines detached from the spot that contribute to the removal of flux that produces the decay of the spot while i-MMFs could be produced by the intersection of flux tubes channeling the Evershed flow with the solar atmosphere. Supporting this idea, we observe two MMFs migrating outwards along the same intra-spine that reach the moat one after other becoming a bipolar MMF. The geometry of the magnetic field vector inside the two MMFs is compatible with a $\mho$-loop. In this context we propose qualitative geometrical models that are in agreement with our observations of type II ECs and MMFs. Our results outline the need of full vector spectropolarimetric observations in order to derive the variations of the physical properties with time by means of inversions of the Stokes profiles. Due to the strong polarization signal of the spot and canopy, magnetograms are not suitable to study the formation process of MMFs in/around sunspots.

- Chapter 11 summarizes the main conclusions of the thesis and outline the future lines of research opened by our work.

2

The Radiative Transfer Equation for polarized light

2.1 Stokes parameters

The Stokes parameters I, Q, U, and V provide a convenient description of the polarization state of the light because each parameter corresponds to a sum or difference of measurable intensities. Following the operational definition given by Rees (1987):

- I represents the sum of the intensities transmitted through perfect linear polarizers whose transmission axes are orthogonal. For example, when the transmission axes of the polarizers, α, are oriented at $\alpha = 0°$ and $\alpha = 90°$ (see Fig. 2.1).

- Q is the difference between the intensities transmitted through linear polarizers oriented orthogonally, e.g., with $\alpha = 0°$ and $\alpha = 90°$.

- U is the difference between the intensities transmitted through linear polarizers when $\alpha = 45°$ and $\alpha = 135°$.

- V is the difference between the intensities transmitted by a quarter wave plate followed by linear polarizers oriented at $\alpha = 45°$ and $\alpha = 135°$. In other words, V is the difference between clockwise and counterclockwise circularly polarized light (see Fig. 2.1).

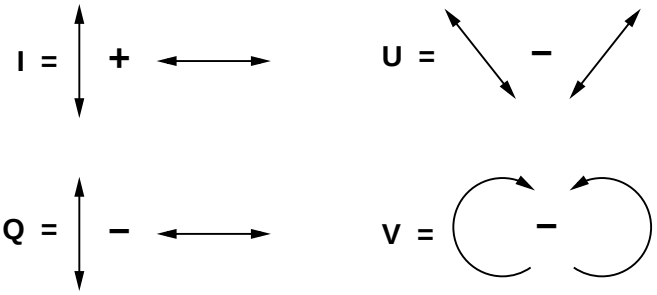

FIGURE 2.1:— Illustration of the operational definition of the Stokes parameters.

The Stokes parameters can also be described in terms of the amplitudes and phases of a monochromatic time-harmonic plane wave. The electric field vector, $\boldsymbol{E}$, of a monochromatic wave has the following components in the plane perpendicular to the direction of propagation:

$$\begin{aligned} E_x &= A_x(t)\ \mathrm{e}^{-i(2\pi\nu t-\delta_x(t))}, \\ E_y &= A_y(t)\ \mathrm{e}^{-i(2\pi\nu t-\delta_y(t))}, \end{aligned} \tag{2.1}$$

where $A_x(t)$, $A_y(t)$ are amplitudes, $\delta_x(t)$ and $\delta_y(t)$ are phases, and ν is the frequency of the wave. Taking into account the operational definition of the Stokes parameters and Eq. 2.1:

$$\begin{aligned} I &= \langle A_x^2\rangle + \langle A_y^2\rangle, \\ Q &= \langle A_x^2\rangle - \langle A_y^2\rangle, \\ U &= 2\langle A_x A_y \cos\delta\rangle, \\ V &= 2\langle A_x A_y \sin\delta\rangle, \end{aligned}$$

where $\delta = \delta_x(t) - \delta_y(t)$ is the phase difference between E_x and E_y and $\langle\ \rangle$ stands for the time average.

The polarization state of the light is usually characterized by the so-called Stokes vector[1] $\boldsymbol{I}(\lambda) = (I, Q, U, V)^\dagger$, where $\dagger$ denotes transposition. Their components satisfy

$$I^2 \geq Q^2 + U^2 + V^2, \tag{2.2}$$

which means that the fraction of polarized light cannot exceed the total amount of available photons. The equality is only reached for totally polarized light. A

[1] In this thesis we will also refer to them as Stokes profiles.

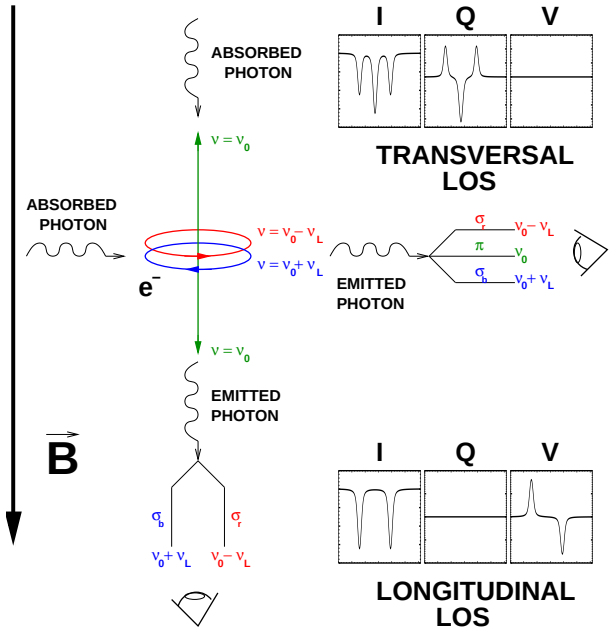

FIGURE 2.2:— Illustration of the normal Zeeman effect in terms of the classical Lorentz's theory of the atom.

general introduction to polarization and the Stokes parameters can be seen in del Toro Iniesta (2003b). There the polarization of quasi-monochromatic light is also discussed.

2.2 Zeeman effect

In 1896, Peter Zeeman found that when a source of light is placed in a magnetic field, spectral lines split into several components differing in frequency[2]. The first interpretation of this physical phenomenon was given by the Lorentz's theory of the atom in the frame of the classical theory. In this model the atoms emit light of frequency ν_0 because they contain electrons performing simple harmonic motion of the same frequency. As a result, only photons of that frequency are absorbed and re-emitted forming a spectral line.

The situation becomes different when a magnetic field is applied. According to the Larmor theorem, the oscillation of the electron can be decomposed in three different components (cf. Fig.2.2): a linear oscillator parallel to the vector magnetic field ($\boldsymbol{B}$) of unshifted frequency ν_0 (π-component), and two circular

[2]For a historical description on the discovery of the Zeeman effect, see del Toro Iniesta (1996)

components oscillating clockwise and counterclockwise on a plane perpendicular to $\boldsymbol{B}$ with frequencies shifted by $\pm\nu_{\rm L}$ from ν_0 (σ-components). $\nu_{\rm L}$ is the so-called Larmor frequency given by:

$$\nu_{\rm L} = \frac{eB}{4\pi m_{\rm e} c}, \tag{2.3}$$

where e and $m_{\rm e}$ are the mass and electric charge of the electron, c is the speed of light, and B is the magnetic field strength.

According to the Lorentz's description of the atom, the observed Zeeman pattern depends on the relative orientation of the vector magnetic field ($\boldsymbol{B}$) and the direction of observation. If one observes along the direction of $\boldsymbol{B}$ (cf. Fig.2.2), only the emissions associated with the σ-components can be detected[3]. Hence, one would observe the intensity profile split in two different components at $\nu_0 \pm \nu_{\rm L}$. Since the σ-components are circular, the atom only generates circularly polarized ligth (i.e. $\boldsymbol{I}(\lambda) = (I, 0, 0, V)^\dagger$). On the other hand, if the line of sight (LOS) is perpendicular to the magnetic field, the observed intensity profiles would display three different components at ν_0 and $\nu_0 \pm \nu_{\rm L}$. From this view, the three components representing the oscillation of the electron are seen as linear. Therefore one would only detect linearly polarized light, whose Stokes vector is $\boldsymbol{I}(\lambda) = (I, Q, 0, 0)^\dagger$ when Q is defined to be positive along the π-component axis. When the line of sight is inclined with respect to $\boldsymbol{B}$, the Zeeman pattern displays three components which are partially linearly and circularly polarized (i.e. elliptically polarized). This phenomenon is known as the *normal Zeeman effect*.

In general, spectral lines split into more than three components in the presence of a magnetic field. These patterns were called *anomalous* because they were not explained by the classical theory. The *anomalous Zeeman effect* can only be described in terms of the quantum theory. In quantum mechanics, spectral lines are the result of electronic transitions between different atomic levels. In LS-coupling[4], the levels are characterized by three different quantum numbers S, L, and J representing the total spin angular momentum, total orbital angular momentum, and the total angular momentum, respectively.

[3]The electric and magnetic components of the radiation oscillate in the plane perpendicular to the direction of propagation. The π-component oscillates perpendicularly to that direction, so it cannot be excited by light propagating parallel to $\boldsymbol{B}$.

[4]This coupling scheme, also known as Russel-Saunders coupling, is valid for light atoms that do not have their electrons in highly excited levels. The electron spins, $s_{\rm i}$ interact among themselves forming a total spin angular momentum, $S = \sum_i s_{\rm i}$. The same happens with the orbital angular momentum of the electrons, $l_{\rm i}$, resulting in a single orbital angular momentum $L = \sum_i l_{\rm i}$. The interaction between L and S forms a total angular momentum $J = L + S$.

TABLE 2.1:— Unnormalized strengths $S_{\alpha,i}$ of the Zeeman components

	$\Delta M = +1$ (σ_b)	$\Delta M = 0$ (π)	$\Delta M = -1$ (σ_r)
$\Delta J = +1$	$(J_u + M_u)(J_l + M_u)$	$2(J_u^2 - M_u^2)$	$(J_u - M_u)(J_l - M_u)$
$\Delta J = 0$	$(J_u + M_u)(J_u - M_u + 1)$	$2M_u^2$	$(J_u - M_u)(J_u + M_u + 1)$
$\Delta J = -1$	$(J_l - M_u)(J_u - M_u + 2)$	$2(J_l^2 - M_u^2)$	$(J_l + M_u)(J_u + M_u + 2)$

The presence of a magnetic field breaks the degeneracy of the (S, L, J) atomic levels splitting them into $2J + 1$ sublevels with quantum numbers $M = -J, ..., J$. For electric dipole transitions, the selection rules only allow transitions from a lower (l) to an upper (u) level with $\Delta J = J_u - J_l = 0, \pm 1$ and $\Delta M = M_u - M_l = 0, \pm 1$. Transitions having $\Delta M = 0$ are called π-components, while $\Delta M = \pm 1$ produce σ_r and σ_b components. If $N_\mathrm{p,b,r}$ denotes the number of transitions of each component:

- $N_\mathrm{p} = 2J_\mathrm{min} + 1$ π-transitions ($\Delta M = 0$).
- $N_\mathrm{b} = J_\mathrm{u} + J_\mathrm{l}$ σ_b-transitions ($\Delta M = +1$).
- $N_\mathrm{r} = J_\mathrm{u} + J_\mathrm{l}$ σ_r-transitions ($\Delta M = -1$).

Their shifts with respect to the original wavelength of the transition, λ_0, are given by:

$$\Delta\lambda = \frac{e\lambda_0^2 B}{4\pi m_\mathrm{e} c^2}\,(g_l M_l - g_\mathrm{u} M_u), \tag{2.4}$$

where g_l and g_u are the Landé factors of the lower and upper levels. In LS-coupling the Landé factor of a generic level i is calculated by means of its quantum numbers (S_i, L_i, J_i):

$$g_i = \begin{cases} \frac{3}{2} + \frac{S_i(S_i+1) - L_i(L_i+1)}{2J_i(J_i+1)} & \text{if } J_i \neq 0, \\ 0 & \text{otherwise.} \end{cases} \tag{2.5}$$

In general, a spectral line produced by $l \rightarrow u$ transitions splits into $N_\mathrm{p} + N_\mathrm{b} + N_\mathrm{r}$ components shifted from line center by an amount given by Eq. 2.4 when a magnetic field is applied. The strengths of the various components are normalized for each type of transition depending on their ΔM. The normalized strengths can be expressed as

$$s_{\alpha,i} \equiv \frac{S_{\alpha,i}}{\sum_i S_{\alpha,i}}, \quad \alpha = \Delta M = +1, 0, -1, \text{ or b, p, r,} \tag{2.6}$$

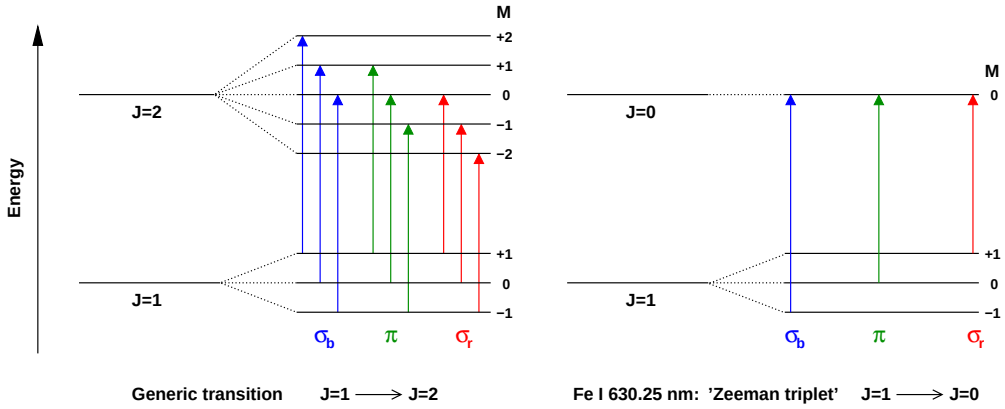

FIGURE 2.3:— Zeeman patterns of a generic transition with $J_l = 1 \rightarrow J_u = 2$ (left) and the Zeeman triplet of Fe I 630.25 nm (right). π-components ($\Delta M = 0$) are outlined with green arrows, while σ_r and σ_b are indicated with red and blue arrows.

where the unnormalized strengths $S_{\alpha,i}$ are given in Table. 2.1.

The left panel of Fig. 2.3 shows the Zeeman pattern for a generic transition $J_l = 1 \rightarrow J_u = 2$. The right panel of the same figure displays the allowed transitions for Fe I 630.25 nm ($J_l = 1 \rightarrow J_u = 0$). In this case there are only one π-component and two σ-components. This is the simplest Zeeman pattern and is called, for obvious reasons, *normal Zeeman triplet*. Those patterns are also produced when the Landé factors of both levels are equal.

In many cases the fine structure of the Zeeman pattern cannot be resolved as, for example, when one observes spectral lines emerging from the atmosphere of sunspots. The thermal motions broaden the absorption profiles of the different Zeeman components, removing the fine structure of the pattern and resulting in only three visible components. For this reason, it is sometimes useful to treat the Zeeman patterns as *effectives Zeeman triplets* (see del Toro Iniesta 2003b) substituting the various components by a single component located at their center of gravity. The center of gravity of the π-components is always zero, while the center of gravity of the σ components is shifted by

$$\Delta\lambda = \frac{e\lambda_0^2}{4\pi m_e c^2}\, g_{\rm eff}\, B, \tag{2.7}$$

where the effective Landé factor, $g_{\rm eff}$, is

$$g_{\rm eff} = \frac{1}{2}(g_l + g_u) + \frac{1}{4}(g_l - g_u)\,\left[J_l(J_l+1) - J_u(J_u+1)\right]. \tag{2.8}$$

This parameter gives an idea of the sensitivity of the spectral line to magnetic fields. As we will show in Sect. ?, the greater the $g_{\rm eff}$ the greater the response to B.

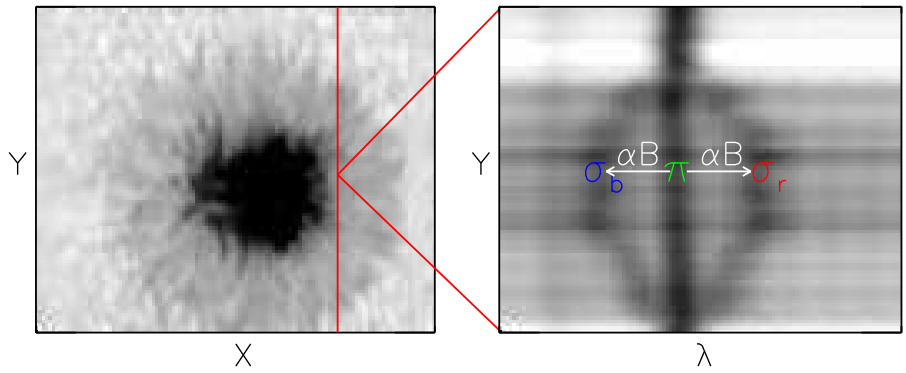

FIGURE 2.4:— *Left panel*: Map of the continuum intensity at 1565 nm for a sunspot. *Right panel*: Intensity profile of Fe I 1564.85 nm along the vertical red line displayed on the left panel.

Since the Zeeman splitting depends linearly on the magnetic field strength (Eq. 2.4), this phenomenon provides an unique tool for the diagnostic of sunspot magnetic fields. The first observations of magnetically split lines in sunspots were reported by Hale (1908). Since then, the use of lines having large sensitivity to B has allowed us to directly derive the magnetic field strength from the Zeeman splitting of the σ components when the field is strong enough (see Fig. 2.4).

2.3 The Radiative Transfer Equation (RTE)

The change of the polarization state of the light, i.e. the Stokes vector $\boldsymbol{I}$, produced by a magnetized atmosphere is governed by the radiative transfer equation (RTE):

$$\frac{d\boldsymbol{I}}{d\tau_{\rm c}} = \boldsymbol{K}(\boldsymbol{I} - \boldsymbol{S}), \tag{2.9}$$

where $\tau_{\rm c}$ is the continuum optical depth, $\boldsymbol{K}$ the propagation matrix, and $\boldsymbol{S}$ the source function vector. The continuum optical depth is given by:

$$\tau_c = \int_z^{z_0} \chi_{\rm cont}\, {\rm d}z, \tag{2.10}$$

where $\chi_{\rm cont}$ is the absorption coefficient of the continuum at a specified wavelength and z the geometrical height measured from the bottom (z) to the top

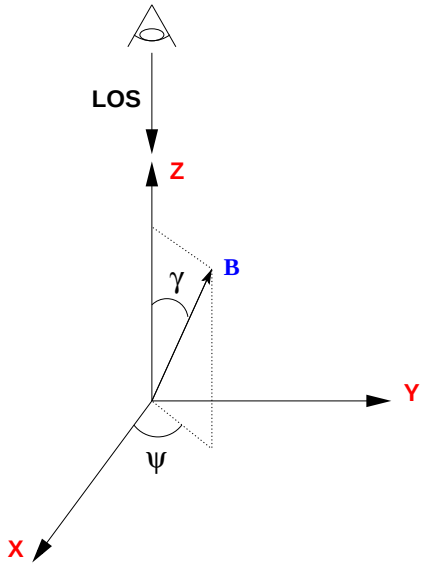

FIGURE 2.5:— Illustration of the angles defining the orientation of the vector magnetic field.

(z_0) of the atmosphere. The propagation matrix can be written in the form:

$$\boldsymbol{K} = \begin{pmatrix} \eta_I & \eta_Q & \eta_U & \eta_V \\ \eta_Q & \eta_I & \rho_V & -\rho_U \\ \eta_U & -\rho_V & \eta_I & \rho_Q \\ \eta_V & \rho_U & -\rho_Q & \eta_I \end{pmatrix}, \tag{2.11}$$

where η_I accounts for the absorption processes, the other η-terms represent the extinction of the Stokes parameters, and ρ-terms stand for the magneto-optical effects (i.e. anomalous dispersion) which produce a cross-talk between the different Stokes parameters. The source function vector $\boldsymbol{S}(\lambda) = (S_I, S_Q, S_U, S_V)^\dagger$ is defined as $\boldsymbol{S} = \boldsymbol{K}^{-1}\boldsymbol{j}$ where $\boldsymbol{j}$ is the emission vector. In general, both $\boldsymbol{K}$ and $\boldsymbol{S}$ depend on the medium and radiation field properties.

2.4 RTE in Local Thermodynamic Equilibrium

There is a particularly interesting case known as Local Thermodynamic Equilibrium (LTE) in which simple expressions for $\boldsymbol{K}$ and $\boldsymbol{S}$ are obtained. The LTE regime implies that the following conditions are meet:

- The plasma is dominated by collisions.
- The thermodynamic properties of the matter are in equilibrium locally: (a) the populations of the atomic levels are given by the Saha and Boltzmann equations; and (b) the distribution of thermal motions is Maxwellian.

- The radiation field is locally given by the Planck law.
- Scattering processes take place in complete redistribution. This means that there is no coherence between the frequencies and directions of the incoming and scattered photons.
- The effect of the magnetic field is fully described by the Zeeman pattern.

Under these conditions the source function is the Planck function at the temperature of the corresponding layer

$$\boldsymbol{S}(\lambda) = (B_\lambda(T), 0, 0, 0)^\dagger, \tag{2.12}$$

while the elements of $\boldsymbol{K}$ are:

$$\begin{aligned}
\eta_I &= 1 + \frac{k_0}{2}\left[\eta_\mathrm{p}\sin^2\gamma + \frac{\eta_\mathrm{b}+\eta_\mathrm{r}}{2}\left(1+\cos^2\gamma\right)\right], \\
\eta_Q &= \frac{1}{2}k_0\left(\eta_\mathrm{p} - \frac{\eta_\mathrm{b}+\eta_\mathrm{r}}{2}\right)\sin^2\gamma\cos 2\psi, \\
\eta_U &= \frac{1}{2}k_0\left(\eta_\mathrm{p} - \frac{\eta_\mathrm{b}+\eta_\mathrm{r}}{2}\right)\sin^2\gamma\sin 2\psi, \\
\eta_V &= \frac{1}{2}k_0\left(\eta_\mathrm{r} - \eta_\mathrm{b}\right)\cos\gamma, \\
\rho_Q &= \frac{1}{2}k_0\left(\rho_\mathrm{p} - \frac{\rho_\mathrm{b}+\rho_\mathrm{r}}{2}\right)\sin^2\gamma\cos 2\psi, \\
\rho_U &= \frac{1}{2}k_0\left(\rho_\mathrm{p} - \frac{\rho_\mathrm{b}+\rho_\mathrm{r}}{2}\right)\sin^2\gamma\sin 2\psi, \\
\rho_V &= \frac{1}{2}k_0\left(\rho_\mathrm{r} - \rho_\mathrm{b}\right)\cos\gamma.
\end{aligned} \tag{2.13}$$

where $k_0 = \chi_\mathrm{lin}/\chi_\mathrm{cont}$ is the line-to-continuum absorption coefficient ratio, and γ and ψ are the inclination and azimuth of the vector magnetic field as seen by the observer (Fig. 2.5). The absorption and anomalous dispersion profiles η_i and ρ_i $(i = p, b, r)$ are given by:

$$\eta_\alpha = \frac{1}{\sqrt{\pi}}\sum_i s_{\alpha,i}\,H(u + u_{B,\alpha,i} - u_\mathrm{LOS}, a) \tag{2.14}$$

and

$$\rho_\alpha = \frac{1}{\sqrt{\pi}}\sum_i s_{\alpha,i}\,F(u + u_{B,\alpha,i} - u_\mathrm{LOS}, a). \tag{2.15}$$

where i runs for the different Zeeman components having $\Delta m = \alpha$. η_α and ρ_α are expressed in terms of the Voigt (H) and Faraday-Voigt (F) functions:

$$H(u,a) = \frac{a}{\pi}\int_{-\infty}^{\infty}\frac{\mathrm{e}^{-y^2}}{(u-y)^2+a^2}\,\mathrm{d}y, \tag{2.16}$$

$$F(u,a) = \frac{1}{2\pi}\int_{-\infty}^{\infty}\frac{(u-y)\mathrm{e}^{-y^2}}{(u-y)^2+a^2}\,\mathrm{d}y. \tag{2.17}$$

These functions depend on the damping parameter, a:

$$a = \frac{\lambda_0^2}{(4\pi c\Delta\lambda_D)}(\Gamma_{\rm rad}+\Gamma_{\rm col}), \tag{2.18}$$

where $\Gamma_{\rm rad}$ and $\Gamma_{\rm col}$ are the line damping coefficients accounting for the radiative lifetime of the levels and the collisions with external perturbers, and the Doppler width is:

$$\Delta\lambda_D = \frac{\lambda_0}{c}\left(\frac{2kT}{M}+v_{\rm mic}^2\right)^{1/2}. \tag{2.19}$$

with k the Boltzmann constant, T the temperature, M the mass of the atom, and $v_{\rm mic}$ the microturbulent velocity. In H and F the distance from line center (u) is expressed in units of the Doppler width,

$$u = \frac{\lambda-\lambda_0}{\Delta\lambda_D}. \tag{2.20}$$

As can be seen in Eqs. 2.14 and 2.15, H and F are evaluated in different wavelengths ($u_{B,\alpha,i}-u_{\rm LOS}$). $u_{\rm LOS}$ accounts for shifts produced by macroscopic LOS velocities ($v_{\rm z}$), while the $u_{B,\alpha,i}$ mark the positions of the various Zeeman components. Those quantities are normalized as follows:

$$u_D = \frac{v_z\lambda_0}{c\Delta\lambda_D}, \tag{2.21}$$

$$u_{B,\alpha,i} = \frac{\Delta\lambda}{\Delta\lambda_D}, \tag{2.22}$$

with $\Delta\lambda$ the wavelength shifts given by Eq. 2.4.

Eqs. 2.12 and 2.13 show that under LTE conditions, $\boldsymbol{S}$ and $\boldsymbol{K}$ only depend on the medium properties and on the geometry of the magnetic field vector. The problem is that those dependences are non-linear, which complicates the

solution of the RTE. In fact, excepting a few particular cases[5], the RTE has no analytical solution. As we will discuss in Sect.5.4, this problem can be addressed with the aid of numerical techniques.

[5]In the case of Milne-Eddintong atmospheres $\boldsymbol{K}$ is constant and $\boldsymbol{S}$ vary linearly with height. Those conditions lead to an analytical solution of the RTE (Unno 1956; Landi degl'Innocenti & Landolfi 2004)

3

Sensitivity of infrared and visible spectral lines to physical parameters

3.1 Introduction

Astrophysicists obtain information about the thermal, magnetic, and dynamic structure of the solar atmosphere by measuring and interpreting the intensity and polarization profiles of spectral lines. In doing so they exploit the fact that the physical parameters of the atmosphere leave clear signatures in these profiles. For example, mass motions shift the spectral lines, whereas magnetic fields induce circular and linear polarization. Different levels of sophistication can be used to interpret the observations, from simple measurements of line bisectors or equivalent widths to complex inversions of the radiative transfer equation. In all cases, it is agreed that one should carefully select the spectral lines to be observed, so that they react mainly to one atmospheric parameter. By combining lines that are sensitive to different parameters, it is in principle possible to uniquely determine the physical properties of the medium where they are formed.

Unfortunately, such an ideal case is only seldom encountered in practice. Magnetically insensitive lines do exist, but all lines react to temperature and velocities to a larger or smaller extent. If, for example, one is interested in determining the velocity field in a sunspot by means of bisector analyses, it is clear that the appropriate line should be magnetically insensitive. The selected line should also exhibit little response to temperature, but it is hopeless to expect zero temperature sensitivities. The claim that certain lines do not react

to temperature has caused some confusion in the literature.

Once these general considerations are agreed upon, the question remains as to how to select the best lines for the particular problem under consideration. Over the years, lines suitable for measuring magnetic fields have been identified on the basis of their large Zeeman splittings (e.g., von Klüber 1948; Solanki et al. 1992; Rueedi et al. 1998) or some other special properties as, for example, the absence of linear polarization (which removes undesired instrumental crosstalk between the Stokes parameters; see Vela Villahoz et al. 1994) and their large Stokes V amplitudes (e.g., Solanki et al. 1987, 1990; Rueedi et al. 1995). Also, lines with zero Landé factors have been identified to allow meaningful Doppler shift measurements in sunspots (e.g., von Klüber 1948). It is important to bear in mind, however, that the sensitivity to magnetic fields is not determined by the amount of Zeeman splitting alone. In fact, lines with similar Zeeman splittings but different thermal widths are seen to exhibit different responses to magnetic fields.

The response of spectral lines to temperature and velocities, by contrast, is not so well characterized. Although simple considerations indicate how a given line reacts to temperature (e.g., Gray 1992), these estimates must be viewed with caution because of the many simplifying assumptions on which they are based[1]. To the best of our knowledge, no detailed analysis of the sensitivity of spectral lines to mass motions has ever been published. Thus, one is forced to rely on an intuition that lines in the red part of the spectrum are better suited to the determination of velocities because the Doppler shift is proportional to wavelength.

The importance of a proper selection of spectral lines has been emphasized by recent advances in solar instrumentation. We are now able to put spectrographs and polarimeters in space and to observe the near infrared part of the spectrum from the ground. Prominent examples of existing or future space-based/balloon-borne instruments include the Michelson Doppler Imager (MDI; Scherrer et al. 1995) onboard SOHO, the Solar-B spectropolarimeter (Lites et al. 2001), the vector magnetograph and visible spectropolarimeter of Sunrise (Solanki et al. 2003; Gandorfer et al. 2004), the Helioseismic and Magnetic Imager (HMI; Scherrer & SDO/HMI Team 2002) onboard the Solar Dynamics Observatory, and the Visible-light Imager and Magnetograph of Solar Orbiter (Marsch et al. 2002; see also the proceedings edited by Battrick & Sawaya-Lacoste 2001). The lines observed by these instruments are often picked up from a small list of candidates for which detailed radiative transfer calculations

[1]The most important is perhaps the neglect of variations in the source function when the temperature is changed.

are carried out. This limited search range is imposed, among other reasons, by the lack of a simple formulation capable of describing the sensitivity of the lines to the various atmospheric parameters.

In this Chapter we study the sensitivity of spectral lines to the physical conditions of the solar atmosphere, that is, to temperature, velocity, and magnetic fields. We follow two complementary approaches. First, we compute response functions for a set of lines widely used in solar physics. Both visible and near infrared lines are considered. We investigate the sensitivity of these lines in three different model atmospheres simulating the conditions of sunspot umbrae and penumbrae, as well as the quiet sun. Second, we develop an analytical model that is able to explain the sensitivities of the lines as inferred from the numerical calculations. This model provides relations that can be used to determine the sensitivity of any line by plugging in simple parameters, such as line widths and residual intensities.

To illustrate the diagnostic potential of visible and infrared lines, we selected the Fe I 630.25 nm and Fe I 1564.85 nm lines for closer scrutiny. These are the lines measured by a number of state-of-the-art spectropolarimeters, including the Advanced Stokes Polarimeter (ASP; Elmore et al. 1992), the Polarimetric Littrow Spectrograph (POLIS; Schmidt et al. 2003), the La Palma Stokes Polarimeter (LPSP; Martínez Pillet et al. 1999), and the Tenerife Infrared Polarimeter (TIP; Collados et al. 1999).

The Chapter is organized as follows. The meaning of response functions, details of the numerical calculations, and the description of our analytical model are given in Sect. 3.2. We investigate the sensitivity of the selected lines to velocities, magnetic fields, and temperatures in Sects. 3.3, 3.4, and 3.5, respectively. A discussion of the results is given in Sect. 3.6. Finally, Sect. 3.7 summarizes our conclusions.

3.2 Sensitivity of spectral lines

According to Ruiz Cobo & del Toro Iniesta (1994), the sensitivity of Stokes profiles to perturbations of the atmospheric parameters are given by the so-called response functions (RFs). They provide direct information on how changes in the physical conditions of the solar atmosphere cause modifications of the emergent spectrum. Response functions appear naturally after linearization of the radiative transfer equation, and were first called weight functions by Mein (1971); RFs were extended to polarized radiative transfer by Landi Deglinnocenti & Landi Deglinnocenti (1977)

Let us summarize here the definition and main properties of RFs. Following del Toro Iniesta (2003b), we shall call $x_i(\tau_c)$ a generic atmospheric parameter

(index i will denote temperature, magnetic field strength, inclination or azimuth, line-of-sight velocity, etc) as a function of the continuum optical depth at 500 nm, $\tau_{\rm c}$. Modification of the observed Stokes spectrum[2], $\delta\boldsymbol{I}(\tau_{\rm c}=0;\lambda)$, after small perturbations $\delta x_i(\tau_{\rm c})$ is given by

$$\delta\boldsymbol{I}(0)=\sum_{i=1}^{m}\int_0^\infty \boldsymbol{R}_i(\tau_{\rm c})\,\delta x_i(\tau_{\rm c})\,{\rm d}\tau_{\rm c}, \tag{3.1}$$

where m stands for the number of physical quantities relevant to line formation, and the response functions can be written as

$$\boldsymbol{R}_i(\tau_{\rm c})\equiv\boldsymbol{O}(0,\tau_{\rm c})\,\left[\boldsymbol{K}(\tau_{\rm c})\frac{\partial\boldsymbol{S}}{\partial x_i}-\frac{\partial\boldsymbol{K}}{\partial x_i}[\boldsymbol{I}(\tau_{\rm c})-\boldsymbol{S}(\tau_{\rm c})]\right], \tag{3.2}$$

with $\boldsymbol{O}(0,\tau_{\rm c})$ the evolution operator from $\tau_{\rm c}$ to the surface, $\boldsymbol{K}$ the propagation (or absorption) matrix normalized to the continuum absorption coefficient at 500 nm, and $\boldsymbol{S}$ the source function vector. Equation (3.2) reflects the fact that perturbations δx_i induce modifications in both $\boldsymbol{K}$ and $\boldsymbol{S}$. These modifications evolve through the atmosphere, as governed by the evolution operator, until they reach the observer. Equation (3.1) draws a complicated scenario, in which the sometimes subtle differences between the Stokes profiles of a single line as formed in various solar atmospheres are made up of a sum of contributions, one for each of the many atmospheric quantities. The sensitivity of the Stokes vector to perturbations of each quantity is given by the corresponding response function vector: $\boldsymbol{R_i}$ tells us how much δx_i "contributes" to $\delta\boldsymbol{I}(0;\lambda)$.

3.2.1 Sensitivity to constant perturbations

RFs have proven useful in practical applications. For example, they are incorporated in a number of inversion codes including SIR (Stokes Inversion based on Response functions; Ruiz Cobo & del Toro Iniesta (1992) and SPINOR (Frutiger 2000). Unfortunately, the quantitative interpretation of the RFs is not straightforward. There is, however, a particularly interesting case in which the meaning of RFs can easily be understood. Assume that we are just dealing with constant perturbations, i.e.,

$$\delta x_i(\tau_{\rm c})=\delta x_i={\rm constant}\forall i=1,2,...,m. \tag{3.3}$$

[2]As usual, by Stokes spectrum we understand the four Stokes parameters as functions of wavelength, λ. We will formally represent it as a vector $\boldsymbol{I}(0;\lambda)\equiv(I,Q,U,V)$. The wavelength dependence is dropped in Eq. (3.1) for simplicity.

In such a case, Eq. (3.1) reduces to

$$\delta \boldsymbol{I}(0) = \sum_{i=1}^{m} \boldsymbol{R}_i' \, \delta x_i, \tag{3.4}$$

where

$$\boldsymbol{R}_i' \equiv \int_0^\infty \boldsymbol{R}_i(\tau_c) \, \mathrm{d}\tau_c = \frac{\partial \boldsymbol{I}(0)}{\partial x_i}. \tag{3.5}$$

Therefore, the integrated response functions $\boldsymbol{R}_i'$ play the role of partial derivatives of the emergent Stokes spectrum with respect to a given atmospheric parameter. Since the concept of partial derivative is familiar to the reader, the usefulness of RFs is quickly understood.

3.2.2 Calculation of response functions

In the following sections, the sensitivity of visible and infrared lines to various atmospheric parameters is characterized by their RFs as evaluated in three solar model atmospheres: the Harvard-Smithsonian Reference Atmosphere of the quiet sun (HSRA; Gingerich et al. 1971), the penumbral model of del Toro Iniesta et al. (1994), and the hot umbral model of Collados et al. (1994). The lines selected for analysis are listed in Table 4.1 together with their atomic parameters. All of them are widely used in solar physics. Our list contains some magnetically insensitive transitions (with zero effective Landé factor, g_{eff}) and lines that are often quoted to be insensitive to temperature, such as Fe I 557.61 nm.

The RFs as a function of wavelength and optical depth (Eq. 3.2) are computed numerically using the SIR code. In order to illustrate the differences between visible and infrared lines, the RFs will be discussed in detail for Fe I 630.25 nm and Fe I 1564.85 nm. Both of them are normal Zeeman triplets with large Landé factors (2.5 and 3.0, respectively), and can be considered as prototypes of visible and infrared lines. The range of optical depths where Fe I 630.25 nm and Fe I 1564.85 nm are formed is determined by the wavelength of the transition, the excitation potential of the lower atomic level, and the oscillator strength. In general, the Fe I line at 1564.85 nm is able to probe deeper photospheric layers because of the reduced continuum opacity of H^- in the infrared (the minimum opacity occurs at 1642 nm). Fe I 1564.85 nm is not formed in high photospheric layers due to its large excitation potential: such layers are cool and the number of atoms capable of absorbing goes to zero very quickly. By contrast, the visible Fe I line at 630.25 nm does not reach layers much lower than $\tau_c = 1$ (due to the increased H^- opacity), but its smaller excitation potential means that it can be formed in the upper photosphere. These

TABLE 3.1:— Set of visible and infrared lines considered in this work. λ_0 represents the central wavelength, χ the excitation potential of the lower level, $\log gf$ the logarithm of the oscillator strength times the multiplicity of the lower level, and $g_{\rm eff}$ the effective Landé factor.

Species	λ_0 [nm]	χ [eV]	$\log gf$	$g_{\rm eff}$
Ni I	491.20	3.75	−0.87	0.00
Fe I	524.71	0.09	−4.95	2.00
Fe I	525.02	0.12	−4.94	3.00
Fe I	537.96	3.69	−1.65	1.00
Ti II	538.10	1.57	−2.05	0.90
Fe I	557.61	3.43	−0.91	0.00
Fe I	569.15	4.30	−1.36	0.00
Fe II	614.93	3.89	−2.70	1.33
Fe I	617.33	2.22	−2.98	2.50
Fe I	630.25	3.69	−1.24	2.50
Fe I	630.35	4.32	−2.55	1.50
Ti I	630.38	1.45	−1.44	0.92
Ni I	676.78	1.83	−1.89	1.50
Fe I	709.04	4.23	−1.21	0.00
Fe II	722.45	3.89	−3.39	0.00
Si I	1062.76	5.86	−0.29	1.75
Fe I	1089.63	3.07	−2.85	1.50
Fe I	1142.23	2.20	−2.89	1.98
Fe I	1221.33	4.64	−1.93	2.50
Fe I	1558.83	6.37	+0.25	1.50
Fe I	1564.85	5.43	−0.67	3.00

considerations will help us understand some of the differences between the RFs of visible and infrared lines.

For the other lines in Table 4.1, our sensitivity analysis is based on *integrated* RFs as defined by Eq. (3.5). For each line, we integrate over optical depth the RFs provided by SIR, and select the maximum value across the line profile. That is, the sensitivity of a given line will be characterized by a single number to allow easy intercomparisons.

It is important to mention that the Stokes profiles and RFs computed by SIR are normalized to the continuum intensity of the quiet sun (represented by the HSRA model) at the central wavelength of the line. This implies that the Stokes profiles are non-dimensional, and that the units of the RFs are the inverse of those of the corresponding atmospheric parameter. Throughout the Chapter, the RFs at $\tau_{\rm c}$ are multiplied by the optical thickness $\Delta\tau_{\rm c}$ of the corresponding atmospheric layer (the stepsize of the spatial grid used in the

calculations is $\Delta \log \tau_c = 0.1$).

3.2.3 Weak line model

To understand the sensitivity of the lines as inferred from the RFs, we use a simple phenomenological model for the shape of weak spectral lines[3]. More specifically, we assume that the emergent Stokes I profile can be described (in the absence of strong magnetic fields) by a Gaussian of the form

$$I(\lambda) = A_2 - A_0 \exp\left[\frac{-(\lambda - \lambda_0)^2}{2A_1^2}\right]. \tag{3.6}$$

Here, λ_0 stands for the wavelength of the transition, A_0 and A_1 are the depth and width of the line, respectively, and A_2 measures the local continuum intensity.

In the strong field regime, the σ components of the Stokes V profile will be represented as

$$V(\lambda) = \pm A_0^V \exp\left[\frac{-(\lambda - \lambda_0 \pm \lambda_B)^2}{2(A_1^V)^2}\right], \tag{3.7}$$

where A_0^V and A_1^V are the amplitude and width of the Stokes V lobes, and the Zeeman splitting is $\lambda_B = C\, g_{\rm eff}\, B\, \lambda_0^2$, with $C \equiv 4.67 \times 10^{-13}$ Å^{-1} G^{-1} and B the field strength (assumed to be constant with height).

For sufficiently small fields, we use the weak field approximation (Landi degl'Innocenti 1992) to represent the Stokes V profile:

$$V(\lambda) = -\lambda_B \cos\gamma \frac{\partial I_0}{\partial \lambda}. \tag{3.8}$$

Here, I_0 is the intensity profile that would emerge from the same atmosphere without magnetic fields and γ the (height-independent) inclination of the magnetic field vector. In practice, one observes emergent profiles from the solar atmosphere and they are affected by the magnetic field. For this reason, instead of I_0 we consider the intensity profile formed in the magnetic atmosphere. If the field is weak enough, this profile has approximately the same shape as I_0 and can be described by Eq. (3.6). So inserting Eq. (3.6) into Eq. (3.8) leads to

$$V(\lambda) \simeq -\lambda_B \cos\gamma\, A_0^* \frac{(\lambda - \lambda_0)}{(A_1^*)^2} \exp\left[\frac{-(\lambda - \lambda_0)^2}{2(A_1^*)^2}\right], \tag{3.9}$$

[3]The majority of photospheric lines in the solar spectrum are weak.

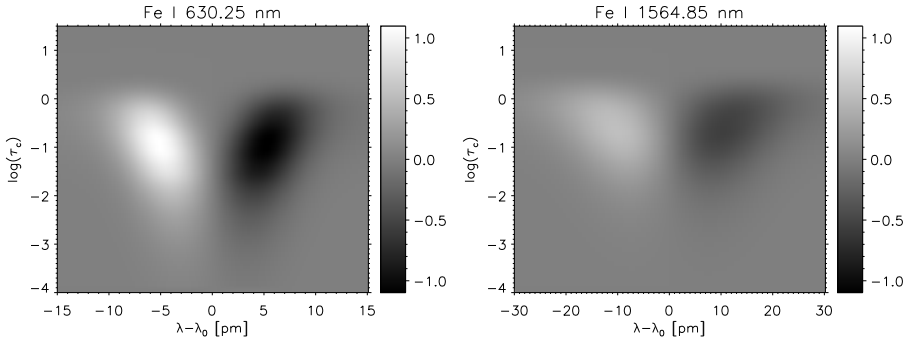

FIGURE 3.1:— RF of Stokes I to $v_{\rm LOS}$ multiplied by $\Delta\tau_{\rm c}$ [10^{-2} (km/s)$^{-1}$] for Fe I 630.25 nm (left) and Fe I 1564.85 nm (right) in the HSRA quiet Sun model. The gray scale is the same in the two panels to facilitate comparisons.

where A_0^* and A_1^* stand for the depth and width of the intensity profile formed in the atmosphere with magnetic field.

At this point, we emphasize that our description of the Stokes profile shapes does not pretend to be accurate. It just provides simple analytical expressions that can easily be differentiated with respect to the atmospheric parameters.

3.3 Sensitivity to line-of-sight velocity

Figure 3.1 shows the RFs of Stokes I to velocity as a function of λ and $\tau_{\rm c}$ for Fe I 630.25 nm and Fe I 1564.85 nm. The HSRA quiet sun model has been used for the computations. No matter the optical depth we are looking at, in the absence of magnetic fields the RFs to LOS velocity perturbations have always two lobes. Since the lines are in absorption, a positive (redshifted) velocity increases the intensities in the blue wing and decreases them in the red wing. For this reason, the RFs show positive blue lobes and negative red lobes. Figure 3.1 also demonstrates that the visible and infrared lines are sensitive to LOS velocity perturbations in a broad range of layers. That is, the lines are not "formed" at a single depth. Other important properties of the RFs displayed in Fig. 3.1 are: (a) Fe I 1564.85 nm is not sensitive to velocities in layers below $\log\tau_{\rm c}\sim 0$ and above $\log\tau_{\rm c}\sim -2$; and (b) the visible line shows a greater sensitivity than the infrared line.

Some of these properties are easy to understand. The fact that Fe I 1564.85 nm does not probe high photospheric layers is due to its large excitation potential, as explained in Section 3.2.2. The other two properties are counter-intuition. Due to the small H^- opacity in the infrared, Fe I 1564.85 nm should react to

velocity perturbations in layers deeper than $\log \tau_c \sim 0$, but this is not what we see in Figure 3.1. Also, one would expect larger sensitivities for the infrared line because the Doppler shift is proportional to wavelength. As shown below, the behavior exhibited by the RFs of Fig. 3.1 can be explained by the phenomenological model introduced in Sect. 3.2.3.

If the line is formed in an atmosphere in which matter moves at a constant velocity with component along the line of sight $v_{\rm LOS}$, then the intensity profile of Eq. (3.6) is shifted by

$$\lambda_{\rm LOS} = \lambda_0 \frac{v_{\rm LOS}}{\rm c}, \tag{3.10}$$

and becomes

$$I(\lambda) = A_2 - A_0 \exp\left[\frac{-(\lambda - \lambda_0 - \lambda_{\rm LOS})^2}{2A_1^2}\right]. \tag{3.11}$$

According to the results of Sec. 3.2.1, the RF of Stokes I to constant perturbations in $v_{\rm LOS}$ is given by

$$\begin{aligned} R'_{v_{\rm LOS},1}(\lambda) \equiv \frac{\partial I}{\partial v_{\rm LOS}} &= -\frac{A_0 \lambda_0}{A_1^2 {\rm c}} (\lambda - \lambda_0 - \lambda_{\rm LOS}) \times \\ &\quad \times \exp\left[\frac{-(\lambda - \lambda_0 - \lambda_{\rm LOS})^2}{2A_1^2}\right], \end{aligned} \tag{3.12}$$

which has extrema at

$$\lambda_{\rm ext} = \lambda_0 + \lambda_{\rm LOS} \pm A_1. \tag{3.13}$$

Thus, the maximum sensitivity of the line to velocity shifts is reached in the line wings. Taking the negative sign in Eq. (3.13), the maximum of the RF is

$$R'_{v_{\rm LOS},1}(\lambda_{\rm max}) = {\rm e}^{-1/2} \frac{A_0}{A_1} \frac{\lambda_0}{\rm c}. \tag{3.14}$$

Therefore, as one would expect from the Doppler shift relationship in Eq. (3.10), the larger the wavelength the greater the sensitivity of the line to LOS velocities. But this is only so, however, provided the *shape ratio* A_0/A_1 remains constant. A_0/A_1 is in fact the ratio between the depth and the width of the line, and can be regarded as a measure of the slope of the intensity profile in the line wings. As mentioned before, Fe I 630.25 nm shows larger LOS velocity sensitivities than Fe I 1564.85 nm all across the line profile. A larger shape ratio is the reason for its greater sensitivity. Thus, the *shape ratio* turns out to be dominant for the line behavior: the stronger and narrower the line, the greater the sensitivity to velocities. Our analytical model also explains why the infrared line is not sensitive to velocities below $\log \tau_c \sim 0$: near the continuum,

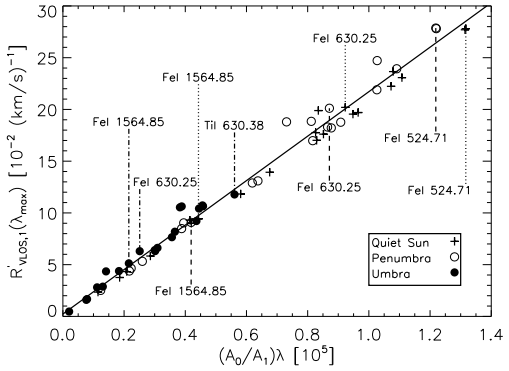

FIGURE 3.2:— Maximum value of the integrated RF to $v_{\rm LOS}$ for the lines of Table 4.1, as a function of the shape ratio multiplied by the central wavelength of the transition. Quiet Sun (crosses), penumbral (circles) and hot umbral (filled circles) atmospheres have been used. The most sensitive lines, Fe I 630.25 nm, and Fe I 1564.85 nm are marked with labels in the quiet Sun (dotted lines), penumbral (dashed lines), and umbral (dotted-dashed lines) models.

the spectral line is so broad that the shape ratio (i.e., the slope of the intensity profile at that position) is almost zero, resulting in very small RFs to $v_{\rm LOS}$.

Figure 3.2 shows the maximum of the *integrated* RF to velocity perturbations for the various lines of Table 4.1 in the quiet sun, umbral, and penumbral atmospheres. For simplicity, the magnetic field has been set to zero in the umbral and penumbral models[4]. Motivated by Eq. (3.14), the sensitivity of the lines is plotted as a function of the shape ratio times the central wavelength. Our simple analytical calculations provide an excellent description of the sensitivity of visible and infrared lines in the three atmospheres. This has important practical consequences. The relationship shown in Fig. 3.2 is universal for weak lines: if one is interested in knowing how much a given line reacts to velocity changes, a simple estimate of the coefficients A_0 and A_1 (as defined by Eq. 3.6) will make it possible to compare its sensitivity with those of other lines. To facilitate such a comparison, Tables A.1, A.2 and A.3 list the coefficients required to compute the x-position of the various lines displayed in Fig. 3.2.

As can be seen in Fig. 3.2, the sensitivity of the lines to velocities is generally reduced in the umbral model (filled circles). The reason is the lower temperatures of the umbra as compared with the penumbra and the quiet sun. Such low temperatures produce smaller A_0 and larger A_1 (i.e., smaller shape ratios) for the majority of neutral lines in the sample.

In Fig. 3.2, the most sensitive lines, Fe I 630.25 nm, and Fe I 1564.85 nm are marked with labels for the quiet Sun (dotted lines), the penumbral (dashed lines), and umbral (dash-dotted lines) models. The most sensitive line in the umbra is Ti I 630.38 nm. In the penumbra and the quiet Sun, one should prefer

[4]In the presence of magnetic fields, the response of magnetically-sensitive lines to velocity perturbations would be smaller due to the reduced shape ratios that would result.

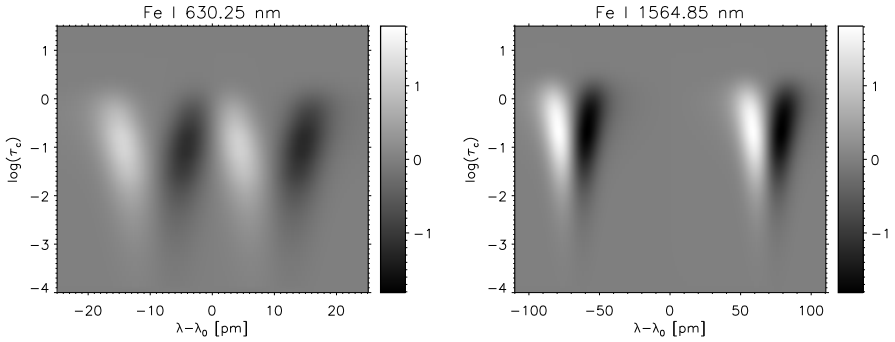

FIGURE 3.3:— Normalized RF of Stokes V to B multiplied by $\Delta\tau_c$ [10^{-5} G^{-1}] for Fe I 630.25 nm (left) and Fe I 1564.85 nm (right) in the HSRA model with a longitudinal magnetic field of $B = 2000$ G. The same gray scale is used in the two panels.

Fe I 524.71 nm due to its large sensitivity to $v_{\rm LOS}$. Consistent with our previous findings, the Fe I line at 630.25 nm is observed to be more sensitive to velocity perturbations than Fe I 1564.85 nm in all three models.

3.4 Sensitivity to magnetic field strength

In this section, the sensitivity of spectral lines to changes in the magnetic field strength is examined using the RFs for Stokes V. We concentrate on the behavior of Stokes V because the determination of magnetic fields in the solar atmosphere relies very often on the interpretation of circular polarization profiles. Stokes V reacts differently to magnetic fields in the strong and weak field regimes, so we need to consider the two cases separately.

3.4.1 Strong field regime

In Fig. 3.3, the RFs of Stokes V to magnetic field strengths are plotted as functions of λ and τ_c for the Fe I lines at 630.25 nm and 1564.85 nm. We have used the HSRA quiet sun model with a constant longitudinal ($\gamma = 0$) magnetic field of $B = 2000$ G. The field is sufficiently large so as to consider that the strong field regime applies. The RFs to B-perturbations exhibit four lobes, two for each σ component. The signs of the RFs reflect how the Stokes V signal varies when the field is increased: in the strong field regime, the amplitudes of the Stokes V lobes do not change, only their wavelength separation does. The main properties of the RFs displayed in Fig. 3.3 are:

1. The two lines react to B in a broad range of optical depths, from $\log\tau_c \sim 0.2$ to ~ -3 in the case of the visible line and from ~ 0.5 to ~ -2.5 in the

case of the infrared line. Thus, Fe I 1564.85 nm is able to probe slightly deeper layers than Fe I 630.25 nm.

2. The infrared line is more sensitive to B. This is what one would expect from the fact that the Zeeman splitting is proportional to $g_{\rm eff}\,\lambda_0^2$.

We now use the phenomenological model of Sect. 3.2.3 to gain a better understanding of the line parameters that determine the sensitivity to B. In the strong field regime, the lobes of Stokes V can be represented[5] by Eq. (3.7). Differentiating this expression with respect to B one obtains that the RF of Stokes V to constant perturbations in B is

$$R'_{B,4}(\lambda) = -\frac{A_0^V\, C g_{\rm eff}\lambda_0^2}{(A_1^V)^2}\,(\lambda-\lambda_0+\lambda_{\rm B})\exp\left[\frac{-(\lambda-\lambda_0+\lambda_{\rm B})^2}{2(A_1^V)^2}\right]. \qquad (3.15)$$

The RF has extrema at

$$\lambda_{\rm ext} = \lambda_0 - \lambda_{\rm B} \pm A_1^V, \qquad (3.16)$$

so the maximum sensitivity is reached in the wings of the σ components. Taking the negative sign for A_1^V in Eq. (3.16) one finally has

$$R'_{\rm B,4}(\lambda_{\rm max}) = {\rm e}^{-1/2}\, C\,\frac{A_0^V}{A_1^V}\, g_{\rm eff}\lambda_0^2. \qquad (3.17)$$

Equation (3.17) tells us that the sensitivity of Stokes V to B is proportional to the shape ratio A_0^V/A_1^V, the Landé factor $g_{\rm eff}$, and λ_0^2. Now the wavelength of the transition plays a crucial role, as it can effectively compensate for small shape ratios. Indeed, this explains why the infrared Fe I line at 1564.8 nm is more sensitive to B than Fe I 630.25 nm.

Figure 3.4 shows the maximum value of the integrated RF to magnetic field perturbations for the lines of Table 4.1 with $g_{\rm eff} \neq 0$. Different symbols represent the quiet sun, penumbral, and umbral atmospheres. The following magnetic field strengths and inclinations have been assumed for the three models: (2000 G, 0°), (1500 G, 70°), and (2000 G, 10°), respectively. Very roughly, these values represent the conditions of plage regions and sunspot penumbrae and umbrae. We plot the maximum of the integrated RFs as a function of the parameter $(A_0^V/A_1^V)\, g_{\rm eff}\lambda_0^2$. Also in this case, the phenomenological model explains the sensitivity of the lines to B remarkably well. We stress that any other combination of B and γ values in the atmospheric model would have led to the same linear relationship in Fig. 3.4 (with different values of the RFs and

[5]Only the blue lobe of Stokes V, positive sign in Eq. (3.7), is considered here. Results for the red lobe are analogous.

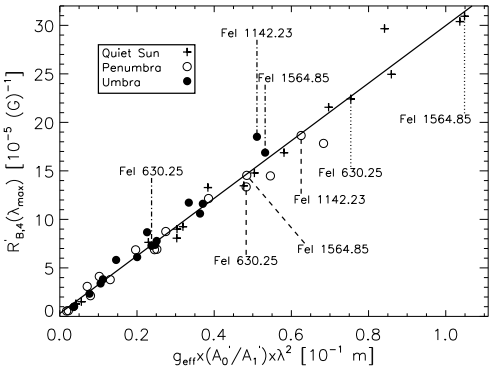

FIGURE 3.4:— Maximum values of the integrated RF to B for the set of lines in Table 4.1 with $g_{\rm eff} \neq 0$ vs $(A_0^V/A_1^V)\, g_{\rm eff} \lambda_0^2$ (strong field regime). The sensitivities have been evaluated in the quiet sun (crosses), penumbral (circles), and umbral (filled circles) models. Dotted, dashed, and dash-dotted lines mark the most sensitive lines, Fe I 630.25 nm, and Fe I 1564.85 nm in the quiet sun, penumbral, and umbral atmospheres, respectively.

the shape ratio, of course). Thus, the figure can be used to gauge the sensitivity of any weak line to magnetic field perturbations in any atmosphere. To do that, it suffices to estimate the parameter A_0^V/A_1^V of the Stokes V profile of the line as it emerges from the atmosphere under consideration.

As can be seen in Fig. 3.4, the sensitivity to B is larger in the quiet sun model. This can be traced to the higher temperatures (which lead to larger shape ratios) and the more vertical orientation of the magnetic field vector[6] (which maximizes A_0^V). Lines in the umbra and the penumbra exhibit similar sensitivities. Although the penumbral model has higher temperatures (which would result in larger sensitivities), the more horizontal orientation of the field actually reduces the sensitivity.

In Fig. 3.4, we have marked specific lines emerging from the penumbral and umbral models with dashed and dash-dotted lines, respectively. The most sensitive line in the umbra and penumbra is Fe I 1142.32 nm. Note also that the Fe I line at 1564.85 nm is observed to be more sensitive than Fe I 630.25 nm in all three models.

3.4.2 Weak field regime

Figure 3.5 shows the RFs of Stokes V to B for Fe I 630.25 nm and Fe I 1564.85 nm as emerging from the HSRA model with a constant longitudinal field of 200 G. Such a small field ensures that the lines are formed in the weak field regime. The atmospheric model adopted would be representative of quiet Sun internetwork fields (e.g., Khomenko et al. 2003). Contrary to the previous case, the RFs of Stokes V to B exhibit only two lobes in the weak field regime.

[6]Although not explicitly written in Eq. (3.7), the Stokes V amplitude depends on γ. This dependence shows up clearly when comparing the results for differently inclined magnetic fields, as in our example.

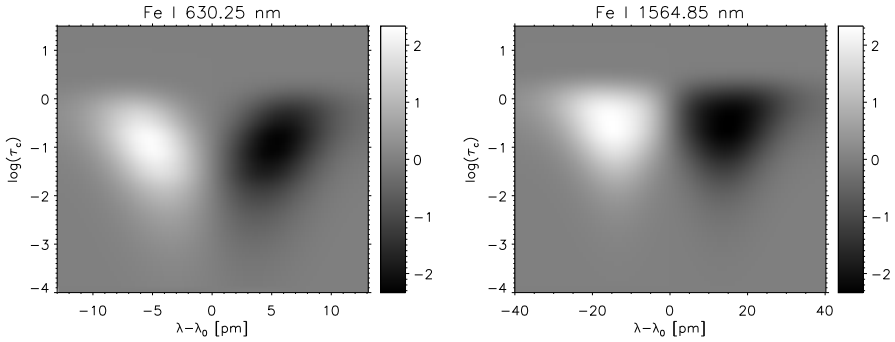

FIGURE 3.5:— Normalized RF of Stokes V to B multiplied by $\Delta\tau_c$ [10^{-5} G^{-1}] for Fe I 630.25 nm (left) and Fe I 1564.85 nm (right) in the HSRA model with a longitudinal magnetic field of $B = 200$ G. This corresponds to the weak field regime.

The reason is that enhancements of the field strength increase the amplitude of the Stokes V lobes, but do not shift them. Thus, RFs have positive blue lobes and negative red lobes.

The two lines probe similar layers as in the strong field regime, but now their sensitivities to B are more or less the same. This finding, already reported by del Toro Iniesta & Ruiz Cobo (1997), is somewhat surprising because the amplitude of Stokes V in the weak field regime is proportional to $g_{\rm eff}\lambda_0^2$. Thus, one would expect the infrared line to be much more sensitive to B than the visible line.

Again we use the phenomenological model of Sect. 3.2.3 to explain these features. Differentiating Eq. (3.9) with respect to B, the RF of Stokes V to constant perturbations of the field strength can be written as

$$R'_{B,4}(\lambda) = -C\, g_{\rm eff}\, \lambda_0^2\, \cos\gamma\, A_0^*\, \frac{(\lambda-\lambda_0)}{(A_1^*)^2} \exp\left[\frac{-(\lambda-\lambda_0)^2}{2(A_1^*)^2}\right], \tag{3.18}$$

and so the maximum value of the RF is

$$R'_{\rm B,4}(\lambda_{\rm max}) = {\rm e}^{-1/2}\, C\, \cos\gamma\, \frac{A_0^*}{A_1^*}\, g_{\rm eff}\lambda_0^2. \tag{3.19}$$

Formally, the response of Stokes V to B in the weak field regime is very similar to that in the strong field regime (compare Eq. 3.19 with Eq. 3.17), except for the explicit $\cos\gamma$ dependence. Now, however, the shape ratio A_0^*/A_1^* refers to the Stokes I profile, *not* to the Stokes V profile. That is, the sensitivity to B is determined by the sharpness of the intensity profile, together with the cosine of the field inclination γ, the Landé factor $g_{\rm eff}$, and λ_0^2. Fe I 630.25 nm has a

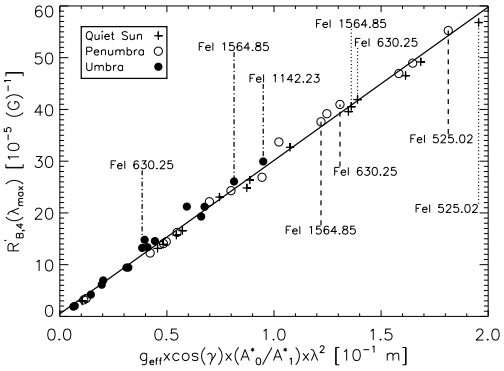

FIGURE 3.6:— Maximum values of the integrated RF to B for the lines of Table 4.1 with $g_{\rm eff} \neq 0$ vs the parameter $(A_0^*/A_1^*)\cos\gamma g_{\rm eff}\lambda_0^2$ (weak field regime). The sensitivities have been evaluated in the quiet sun (crosses), penumbral (circles), and hot umbral (filled circles) models with a longitudinal magnetic field of 200 G. Dotted, dashed, and dash-dotted lines mark specific transitions in the quiet sun, penumbral, and umbral models, respectively.

greater shape ratio than Fe I 1564.85 nm. This compensates for the smaller $g_{\rm eff}\lambda_0^2$ of the visible line, explaining why both lines exhibit more or less the same sensitivity in the quiet sun atmosphere.

In Figure 3.6 we plot the maximum value of the integrated RF to field strength perturbations for the lines of Table 4.1 with $g_{\rm eff} \neq 0$. For the three models considered we use a longitudinal magnetic field of 200 G. The most sensitive lines in the umbra and penumbra turn out to be Fe I 1142.32 nm and Fe I 525.02 nm, respectively. The Fe I line at 1564.85 nm is more sensitive than Fe I 630.25 nm only in the umbral model. In hotter atmospheres, like the penumbral and quiet Sun models, a smaller shape ratio makes the infrared line slightly less sensitive to B than the visible Fe I line at 630.25 nm.

Comparing Figs. 3.4 and 3.6 it is clear that the sensitivities of Stokes V to magnetic field perturbations in the weak field regime are larger than in the strong field regime. This result may look strange at first, but can be understood by noting that the shape ratio of Stokes I (A_0^*/A_1^*) is about twice as large as that of Stokes V (A_0^V/A_1^V) in the strong field case. According to Tables A.1 and A.3, $A_1^* \sim A_1^V$, while $A_0^* \sim 2A_0^V$ for most of the lines. Physically, the larger sensitivity in the weak field regime results from the fact that changes in B modify the amplitude of the Stokes V profile, whereas in the strong field regime only the lobe separation varies. Due to the larger slope of Stokes I in the line wing as compared with the slope of the V profile (the parameters determining the sensitivity to B in the two cases), changes in amplitude are much clearly seen than profile shifts. In practice, however, the inference of field strengths is less reliable in the weak field regime, because the amplitude of Stokes V also depends on other parameters such as temperature and magnetic filling factor. Discriminating between these parameters and the magnetic field strength is often a difficult task.

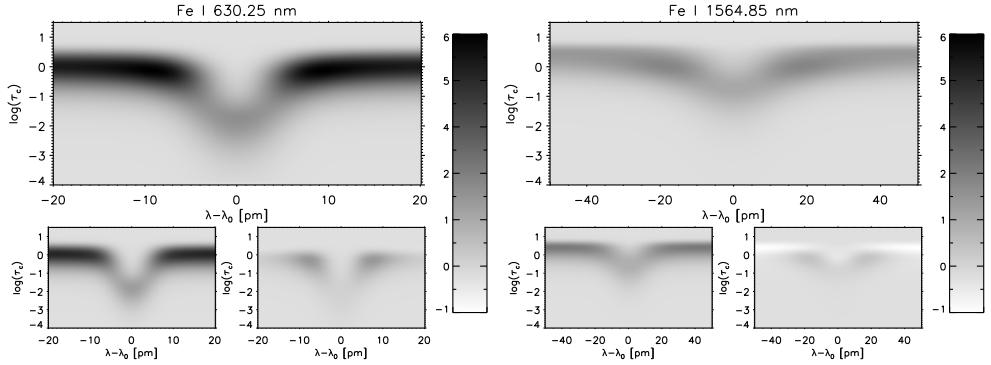

FIGURE 3.7:— **Top:** Normalized RF of Stokes I to T multiplied by $\Delta\tau_{\rm c}$ [10^{-5} K^{-1}] for Fe I 630.25 nm (left) and Fe I 1564.85 nm (right) in the HSRA quiet sun model. **Bottom:** The two subpanels below each line display the first (left) and second (right) signed terms on the rhs of Eq. (3.2) contributing to the RF. That is, the first and third subpanels show how Stokes I varies due to changes in the source function, while the second and fourth subpanels display how Stokes I reacts to the opacity variations induced by temperature changes. Note that the gray scale is inverted in this figure, with black representing positive values and white negative values.

3.5 Sensitivity to temperature

In this section we investigate how the intensity profiles and equivalent width of spectral lines react to temperature perturbations. The response of Stokes V to T is similar to that of Stokes I, because the circular polarization profile is the difference between the *intensity* profiles corresponding to right-handed and left-handed circularly polarized photons. As described by Eq. (3.2), changes in temperature induce modifications of both the propagation matrix and the source function. Below we demonstrate that the sensitivity of Stokes I to temperature perturbations is mainly determined by variations of the source function ($\partial \boldsymbol{S}/\partial T$), whereas that of the equivalent width is mostly due to changes in absorption ($\partial \boldsymbol{K}/\partial T$).

3.5.1 Response of Stokes I to temperature

The upper panels of Fig. 3.7 show the RFs of Stokes I to temperature for the Fe I lines at 630.25 nm and 1564.85 nm as emerging from the HSRA quiet sun model. In the lower panels we plot the two (signed) terms on the rhs of Eq. (3.2) contributing to each RF: variations in the source function (left) and in the opacity (right). Inspection of these panels reveals that:

1. Variations in the source function result in a larger contribution to the RFs

than opacity changes. Thus, the sensitivity of Stokes I to temperature is dominated by changes in the source function, with opacity variations playing a less important role.

2. The variation of $\boldsymbol{S}$ with T is always positive: temperature enhancements increase the emissivity and therefore the emergent intensity, both in the continuum and in the line.

3. The term associated with variations of $\boldsymbol{K}$ with T is predominantly positive except in the deepest photospheric layers. In the line, this reflects the well known fact that an increase of temperature leads to reduced absorption due to the larger ionization of iron. As a result of the smaller absorption, the emergent intensity increases. At continuum wavelengths, we find negative values deep in the atmosphere, indicating an increase of the continuum absorption after temperature enhancements. This phenomenon is better seen in the Fe I line at 1564.85 nm (fourth bottom panel).

Having discussed the various contributions to the sensitivity of Fe I 630.25 nm and Fe I 1564.85 nm to temperature, we summarize below the main features of the RFs displayed in the upper panels of Fig. 3.7:

1. The RFs are positive everywhere for the two lines. That is, enhancements of the temperature always increase the emergent intensity (in either the line, the continuum, or both), regardless of the atmospheric layer where the enhancement occurs. This is due to the fact that the main contribution to the RF is that associated with changes in the source function, which is always positive.

2. The visible line is sensitive to T perturbations from $\log\tau_{\rm c} \sim 0.5$ up to ~ -3.0 and the infrared line from $\log\tau_{\rm c} \sim 0.8$ to ~ -1.5. Therefore, Fe I 1564.85 nm is able to probe slightly deeper layers than Fe I 630.25 nm, but it does not react to temperature changes in the mid-photosphere. The reason was explained in Sect. 2.2.

3. The two lines are sensitive to T over a broader range of optical depths than to any other atmospheric parameter (compare Figs. 3.1, 3.3, and 3.5 with Fig. 3.7). The reason was explained by del Toro Iniesta & Ruiz Cobo (1996): in LTE the source function depends only on temperature, and so the first term on the rhs of Eq. (3.2) is non-zero only for $x_{\rm i} = T$. As a result, the RFs to temperature have the slowest trend to zero with

depth. This property makes it possible to obtain information on temperatures in layers where no information on other atmospheric parameters is reachable.

4. The infrared line is less sensitive to T than the visible line.

To understand the difference in sensitivity between visible and infrared lines (item 4 of the list above) we apply again the phenomenological model of Sect. 2.3. Differenciating Eq. (3.6) with respect to T, the RF of Stokes I to constant perturbations of T can be written as

$$\begin{aligned} R'_{T,1}(\lambda) &= \frac{\partial A_2}{\partial T} - \left[\frac{\partial A_0}{\partial T} + \frac{\partial A_1}{\partial T}\frac{A_0}{A_1^3}(\lambda-\lambda_0)^2\right] \times \\ &\quad \times \exp\left[\frac{-(\lambda-\lambda_0)^2}{2A_1^2}\right], \end{aligned} \tag{3.20}$$

with extrema at

$$\lambda^{\rm a}_{\rm ext} = \lambda_0 \pm A_1\sqrt{2 - \frac{A_1}{A_0}\frac{\partial A_0/\partial T}{\partial A_1/\partial T}}, \tag{3.21}$$

$$\lambda^{\rm b}_{\rm ext} = \lambda_0, \tag{3.22}$$

$$\lambda^{\rm c}_{\rm ext} = \lambda_{\rm c}. \tag{3.23}$$

Here, $\lambda_{\rm c}$ stands for continuum wavelengths. At these locations, the RF has relative maxima or minima:

$$\begin{aligned} R'_{T,1}(\lambda^{\rm a}_{\rm ext}) &= \frac{\partial A_2}{\partial T} - 2\frac{A_0}{A_1}\frac{\partial A_1}{\partial T} \times \\ &\quad \times \exp\left[-1 + \frac{1}{2}\frac{A_1}{A_0}\frac{\partial A_0/\partial T}{\partial A_1/\partial T}\right], \end{aligned} \tag{3.24}$$

$$R'_{T,1}(\lambda^{\rm b}_{\rm ext}) = \frac{\partial A_2}{\partial T} - \frac{\partial A_0}{\partial T}, \tag{3.25}$$

$$R'_{T,1}(\lambda^{\rm c}_{\rm ext}) = \frac{\partial A_2}{\partial T}. \tag{3.26}$$

Most neutral lines show the maximum value of the RF in the line wing ($\lambda^{\rm a}_{\rm ext}$). Very weak lines with optically thin cores have the maximum at the central wavelength ($\lambda^{\rm b}_{\rm ext}$). Finally, singly-ionized lines show a minimum at the central wavelength whilst $\lambda^{\rm a}_{\rm ext}$ is complex (since the discriminant of Eq. 3.21 is negative). The latter have, of course, their maxima on the interval boundaries, that is, at continuum wavelengths ($\lambda^{\rm c}_{\rm ext}$). In summary, if we call $P_{\rm T}$ the maximum value of the RF for a given line, this can be one of the three possibilities: $R'_{T,1}(\lambda^{\rm a}_{\rm ext})$, $R'_{T,1}(\lambda^{\rm b}_{\rm ext})$, or $R'_{T,1}(\lambda^{\rm c}_{\rm ext})$.

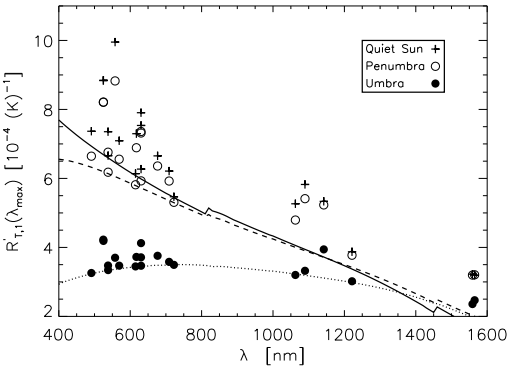

FIGURE 3.8:— Maximum value of the integrated RF of Stokes I to T for the lines of Table 4.1 vs the wavelength of each transition. The sensitivities have been evaluated in the quiet Sun (crosses), penumbral (circles), and umbral (filled circles) models. Solid, dashed, and dotted curves represent the partial derivatives of the continuum intensity with respect to temperature ($\partial A_2/\partial T$) in the quiet Sun, penumbral, and umbral models.

In all three cases the maximum value of the RF to T is determined mostly by the variation of the continuum intensity with temperature, i.e., by $\partial A_2/\partial T$. This can be demonstrated as follows. Using the Eddington-Barbier approximation, we may write

$$\frac{\partial A_2}{\partial T} \propto \frac{\partial B_\lambda[T(\tau_\lambda = 1)]}{\partial T}, \tag{3.27}$$

with B_λ the Planck function evaluated at the temperature of the layer where $\tau_\lambda = 1$. The three curves displayed in Fig. 3.8 represent the variation of $\partial A_2/\partial T$ with wavelength in the quiet sun, umbral and penumbral atmospheres. We also plot in this figure the maximum value of the integrated RF to T for the lines of Table 4.1 in the same models. As can be seen, the term $\partial A_2/\partial T$ accounts for most of the sensitivity of the lines to temperature, independently of the atmospheric model or wavelength. Of course, a perfect match between the curves and the data points is not to be expected, because the curves display only one of the terms (the dominant one) contributing to the RF. It is apparent from the figure that the sensitivity of the lines tend to be smaller at longer wavelengths. This is because the derivative of the Planck function with T decreases with λ for typical solar temperatures, which explains why Fe I 630.25 nm is more sensitive to T than the infrared Fe I line at 1564.85 nm.

In Fig. 3.9 we consider all the terms contributing to the response of Stokes I to T. Here we plot the maximum value of the integrated RF to temperature perturbations for the lines of Table 4.1 as a function of the parameter $P_{\rm T}$ (given by Eqs. 3.24, 3.25 or 3.26 as appropriate). Clearly, the phenomenological model does an excellent job in explaining the sensitivities of the various lines to temperature.

In general, the response of Stokes I to T is reduced in the umbral model. The low temperatures of this model cause smaller values of $\partial A_2/\partial T$ (see Fig. 3.8) and consequently smaller sensitivities. Consistent with our previous findings

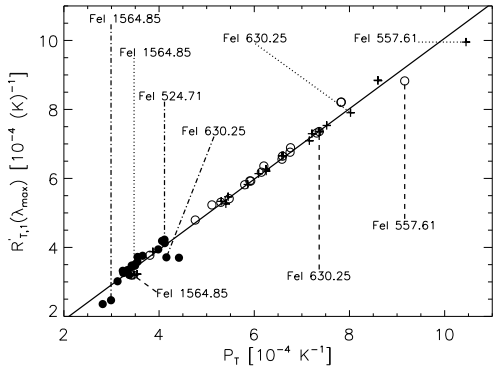

FIGURE 3.9:— Maximum value of the integrated RF of Stokes I to T for the lines of Table 4.1 vs the parameter $P_{\rm T}$ (see text for details). Quiet Sun (crosses), penumbral (circles), and umbral (filled circles) atmospheres have been used. The most sensitive lines, Fe I 630.25 nm, and Fe I 1564.85 nm in these models are marked with dotted, dashed, and dot-dashed lines, respectively

(cf. Fig. 3.7), Fe I 630.25 nm exhibits larger sensitivities than Fe I 1564.85 nm in all the models. Note, however, that the sensitivity of the infrared line is different from zero. Hence, there is a measurable change in the profile that can be used to retrieve the thermal structure of the photosphere. Figure 3.9 also shows that Fe I 557.61 nm is the most sensitive line of our set, disproving the general belief that Fe I 557.61 nm does not react to temperature changes.

3.5.2 Response of equivalent width to temperature

The equivalent width W of a spectral line is defined as

$$W = \Delta \sum_{i=1}^{q-1} [1 - I(\lambda_i)/I_{\rm c}], \tag{3.28}$$

where Δ is the wavelength sampling interval, $I(\lambda_i)$ the intensity at each wavelength, and $I_{\rm c}$ the continuum intensity. Some authors (e.g., Moore et al. 1966; Gray 1992) use the change of W with temperature as a diagnostic of the sensitivity of the lines to temperature perturbations.

Figure 3.10 shows the RFs of W to T as a function of $\log \tau_{\rm c}$ for Fe I 630.25 (solid line) and Fe I 1564.85 nm (dotted line) in the quiet Sun model. Both curves are double lobed. As explained by Ruiz Cobo & del Toro Iniesta (1994), the shape of these RFs results from the competition between $\boldsymbol{K}$ and $\boldsymbol{S}$ in the final modification of W (cf. Eq. 3.2). A positive lobe coming from the derivative of $\boldsymbol{S}$ with respect to T dominates the behavior of the RFs in the deep layers, indicating that temperature enhancements in those layers increase the equivalent width due to the availability of more photons to be absorbed. The negative lobe in higher layers corresponds to the derivative of $\boldsymbol{K}$ with T, and implies a decrease of W after an increase in temperature, i.e., a line weakening. Higher temperatures result in less Fe I atoms and, consequently, the

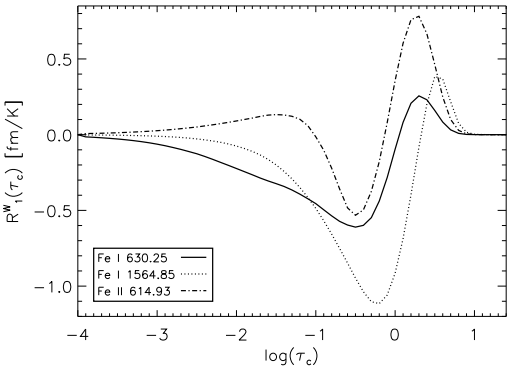

FIGURE 3.10:— Response function of the equivalent width to temperature perturbations for Fe I 630.25 (solid line), Fe I 1564.85 nm (dotted line), and Fe II 614.93 nm (dash-dotted line) in the quiet Sun model.

equivalent width is reduced. Of course, since the same increase of temperature enhances the number of Fe II absorbers, lines like Fe II 614.93 nm (dash-dotted line in Fig. 3.10) exhibit a positive lobe in mid and high photospheric layers.

A comparison of the RFs of Fe I 630.25 nm and Fe I 1564.85 nm depicted in Fig. 3.10 reveals two additional features: (a) the variation of W with T is larger for the infrared line than for the visible line[7]; and (b) the equivalent width of the infrared line is sensitive to temperature perturbations in deeper layers than the visible line.

According to our phenomenological model, the equivalent width of weak spectral lines can be written as

$$W = \int \left(1 - \frac{I}{A_2}\right) \mathrm{d}\lambda = \sqrt{2\pi}\, \frac{A_0\, A_1}{A_2}, \tag{3.29}$$

and so the derivative of W with respect to T is

$$\frac{\partial W}{\partial T} \equiv P_{\mathrm{W}} = W \left(\frac{1}{A_0} \frac{\partial A_0}{\partial T} + \frac{1}{A_1} \frac{\partial A_1}{\partial T} - \frac{1}{A_2} \frac{\partial A_2}{\partial T} \right). \tag{3.30}$$

Therefore, as expected, variations of the equivalent width can be produced by changes in the line depth, the line width, and/or the continuum intensity. In Fig. 3.11 we plot the integrated RF of W to T for the lines of Table 4.1 in the quiet sun, umbral and penumbral atmospheres, against the parameter P_{W} defined above. Clearly, the phenomenological model succeeds in providing a good description of how the equivalent width reacts to temperature changes.

In the quiet sun and penumbral models, the variation of W with T is negative for all the Fe I lines and positive for the Fe II lines. This indicates that

[7] $R_T^{\prime W}$, i.e., the integral of the RF of W to T with depth, is around -0.09 for Fe I 630.25 nm and -0.12 for Fe I 1564.85 nm in the quiet Sun model.

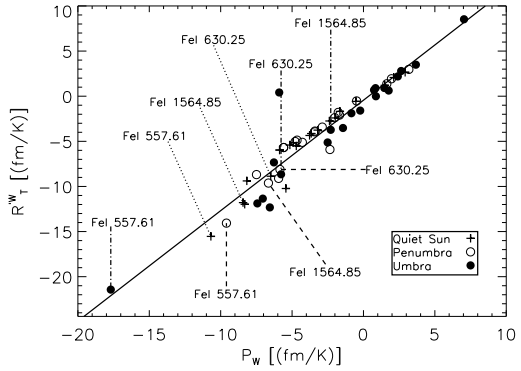

FIGURE 3.11:— Integrated RF of equivalent width to temperature perturbations vs $P_{\rm W}$ for HSRA (crosses), penumbral (circles) and umbral (filled circles) model atmospheres.

absorption processes dominate the behavior of W: temperature enhancements decrease the number of neutrals and increase that of singly-ionized absorbers, i.e., the neutral lines are weakened and the singly-ionized lines get strengthened. In the umbra, a few Fe I lines exhibit *positive* variations of W with T; these lines have large excitation potentials, so it is difficult to populate their lower atomic levels in the cool umbral atmosphere. As a result, $\partial \boldsymbol{S}/\partial T$ dominates over $\partial \boldsymbol{K}/\partial T$, which explains why these lines become stronger after temperature enhancements.

Remarkably enough, Fe I 557.6 nm is the line showing the largest change of W with T in the three atmospheric models under consideration. This gives additional support to our claim that Fe I 557.6 nm can be used to infer the thermal stratification of the solar atmosphere. Figure 3.11 also demonstrates that the infrared Fe I line at 1564.85 nm exhibits larger changes of W than Fe I 630.25 nm in all models except in the umbra, where the lower atomic level of the infrared line is not well populated.

3.6 Discussion

There are many ways to derive the physical properties of stellar atmospheres from spectral line profiles, but the question still remains which lines are best suited to retrieve a given atmospheric parameter. We have addressed this question by analyzing the response functions of a number of weak lines commonly used in solar physics. Our analysis provides a better understanding of the diagnostic capabilities of these lines.

Describing the shapes of Stokes I and V in terms of simple parameters (such as line widths and depths), we have been able to explain why different lines exhibit different sensitivities to the same atmospheric parameter (e.g., LOS velocities, magnetic field strengths or temperatures). By sensitivity we

mean the change of the intensity and circular polarization signal at a given wavelength caused by a height-independent perturbation of an atmospheric parameter. If the sensitivity is small, the changes in the emergent spectrum may not be detectable depending on the noise of the observations. Thus, it is always advisable to select lines having large sensitivities to a given parameter, in order to ensure that the subtle variations it produces in the spectrum are not buried by the noise.

3.6.1 Visible vs. infrared lines

The formation height of spectral lines depends primarily on the excitation potential and oscillator strength of the atomic transition, together with the temperature of the atmosphere, rather than on the central wavelength of the transition. Therefore, it is not possible to draw general conclusions about differences between visible and infrared lines; each line has to be investigated separately. However, we have identified some trends that explain the peculiarities of many lines in the two spectral regions:

1. The thermal width of the lines (represented roughly by A_1) increases linearly with wavelength. Therefore, the intensity and circular polarization profiles of infrared lines are broader, leading to a general reduction of the sensitivity to LOS velocities and magnetic fields (in the weak field limit).

2. The ratio of Zeeman splitting to thermal width increases linearly with wavelength. Thus, changes in the magnetic field strength are much easier to detect in the infrared when the field is sufficiently large.

3. In general, the excitation potential of infrared lines is rather large, implying that high temperatures are necessary to populate their lower atomic levels. As a consequence, many infrared lines are not formed in the mid and upper photospheric layers, where the temperatures are low. Fe I 1142.23 nm is an exception to this rule. With an excitation potential of 2.2 eV, this line is able to sample higher atmospheric layers than Fe I 630.25 nm.

4. Intensity contrasts induced by temperature fluctuations are smaller in the infrared because the Planck function changes less with T at longer wavelengths. This is the reason for the lower sensitivity of infrared lines to temperature as compared with visible lines. However, the variation of W with T is generally larger for infrared lines, due to their broader intensity profiles.

Since the continuum opacity reaches a minimum in the solar photosphere at about 1.6 μm, one could expect to obtain extra information on deep layers by studying infrared lines close to this wavelength. The detailed comparison between Fe I 630.25 nm and Fe I 1564.85 nm presented here shows that such an extra information is not that significant except perhaps for temperature: the deepest layer to which the infrared line is sensitive is at most 70 km deeper than the corresponding one for the visible line. The main advantage of the infrared, then, is not in going deeper but in having a combination of large sensitivity to magnetic fields and reasonable sensitivity to velocities in a narrow range of layers. This allows for a good discrimination of the different structures that may coexist in the resolution element as, for example, in the case of sunspot penumbrae.

Both visible and infrared lines have their strengths and limitations. Simultaneous observations of the Sun in the visible and infrared would certainly improve the diagnostic capabilities of a single spectral range alone. This kind of observations are now possible with the new generation of solar polarimeters, such as TIP and POLIS, operated simultaneously at the Vacuum Tower Telescope of Teide Observatory, and the Spectro-Polarimeter for Infrared and Optical Ranges (SPINOR), to be installed at the Dunn Solar Telescope of NSO/Sacramento Peak Observatory (Socas-Navarro et al. 2006).

3.6.2 Temperature insensitive lines

One of the main results of this work is that lines considered to be temperature insensitive do indeed show a significant temperature dependence. Fe I 557.6 nm belongs to this group of lines. In Rowland's tables (cf. Moore et al. 1966), the equivalent width of Fe I 557.6 nm is mentioned not to change much from the quiet sun to sunspot umbrae (two atmospheres with rather different temperatures). This is probably the reason why Fe I 557.6 nm is regarded as the prototype of temperature insensitive lines by most solar physicists. Recent observations, however, demonstrate that the equivalent width of this line is at least 30% larger in the umbra than in the quiet sun (see Fig. 5 of Tritschler et al. 2004). The high spatial and spectral resolution observations of Tritschler et al. are in agreement with the results of this work, where we see that Fe I 557.6 nm undergoes the largest change of equivalent width with T among the various lines in the sample. Of course, there are other lines not considered here that show larger temperature sensitivities. Molecular lines are a good example: many of them show up only in the cool umbrae, disappearing completely in hotter atmospheres due to the dissociation of the parent molecules.

Another line which is often quoted to be a poor diagnostics of temperature

is Fe I 1564.85 nm. Our analysis shows that, due to the smaller change of the Planck function with T at longer wavelengths, the intensity profiles of infrared lines are less influenced by temperature variations than visible lines. In this sense, Fe I 1564.85 nm is indeed not as appropriate as, e.g., Fe I 630.25 nm for retrieving the thermal stratification of the solar photosphere. However, Fe I 1564.85 nm does react to temperature perturbations, as demonstrated by Figs. 9 and 11. In particular, the change of the equivalent width of Fe I 1564.85 nm with T is larger than that of Fe I 630.25 nm in the quiet sun and penumbral models.

3.6.3 Applicability

The calculations have been carried out in three model atmospheres representing the conditions of sunspot umbrae and penumbrae, as well as those of the quiet sun. For simplicity, we have assumed constant (height-independent) magnetic fields and LOS velocities in these models. Such an assumption has allowed us to characterize the sensitivity of spectral lines to a given atmospheric parameter by means of a single number (the maximum value of the integrated response function across the line profile). That is, our approach neglects possible variations of the atmospheric parameters with height. Since we know that vertical gradients exist in the solar atmosphere (e.g., in sunspot penumbrae), it is important to discuss whether the results of this Chapter would be applicable to atmospheres featuring gradients of the physical quantities.

The strength of our phenomenological model lies in that it identifies the physical mechanism(s) responsible for the sensitivity of spectral lines. The response to LOS velocities, for instance, is determined by the sharpness of the intensity profile, and this is true in any atmospheric model. Gradients of LOS velocity do modify the shape of Stokes I but, unless they are very strong, the intensity profile can always be described reasonably well by a gaussian (with different parameters, of course). Thus, a preliminary selection of lines can be done by means of the recipes obtained in this work. In the real sun, the sensitivities of the lines will be different from those predicted by our model, but they will differ by the same factor for all the lines. Hence, Fe I 524.71 nm will always be the most sensitive line of our set to LOS velocities, even if the atmosphere features variations of this quantity with height. The same applies to the response of the lines to other atmospheric parameters.

At this point it is important to recall that the sensitivity of spectral lines to LOS velocities and magnetic fields is determined by the shape ratios of Stokes I and Stokes V. The shape ratio measures the slope of the corresponding Stokes profile. This quantity can be significantly modified by the instrument used

to take the observations. In fact, spectrographs or spectropolarimeters with poor spectral resolutions may degrade the diagnostic potential of the lines by broadening their intensity and circular polarization profiles. In other words: the same lines may show different sensitivities when observed with different instruments or telescopes. This fact is often disregarded.

3.6.4 The most sensitive lines of the set

The sensitivity of spectral lines depends on the values of the physical parameters of the atmosphere where they are formed. Hence, lines which are universally the most sensitive to a given parameter regardless of the model atmosphere do not exist. Anyway, one can identify for each atmospheric quantity some spectral lines in Table 4.1 which have a high response:

- If one is interested in retrieving temperatures from line profiles, Fe I 557.61 nm, Fe I 525.02 nm, and Fe I 524.71 nm display quite large changes after subtle modifications of the temperature.

- As explained in Sect. 3.6.1, infrared lines usually exhibit lower sensitivity to LOS velocity as compared with the visible lines. Therefore, the lines with better response to $v_{\rm LOS}$ are usually in the visible part of the solar spectrum. In fact, the most sensitive lines of our set are Fe I 524.71 nm, Fe I 525.02 nm, and Ni I 676.70 nm. On the other hand, LOS velocities are often estimated from measurements of line bisectors. Magnetically insensitive lines ($g_{\rm eff} = 0$) with a low response to temperature perturbations are then advisable. In this case, one should prefer Ni I 491.21 nm, Fe I 709.04 nm, or Fe I 569.15 nm.

- Stokes V from Fe I 1142.23 nm, Fe I 525.02 nm, and Fe I 1564.85 nm show the largest reaction to field strength modifications in the strong field regime. In the weak field regime, Fe I 1142.23 nm and Fe I 525.02 nm are also the most sensitive lines of the set.

3.7 Summary

We have characterized the response of weak spectral lines to LOS velocities, magnetic fields, and temperatures by means of their response functions evaluated in three model that represent the conditions of the quiet sun, sunspot umbrae, and penumbrae. In addition, we have developed a simple phenomenological model that is able to predict the response of any weak line to these

atmospheric parameters. Thus, for the first time, we have at our disposal simple rules to select the most appropriate line for the problem we are interested in.

Not surprisingly, the response of Stokes I to LOS velocities increases with both the sharpness of the profile and the wavelength. In general, visible lines show higher sensitivities than infrared lines because their intensity profiles are sharper.

The response of Stokes V to magnetic field strength is formally the same in the strong and weak field limits, because it depends on the sharpness of the Stokes V or Stokes I profiles, as well as on the amount of Zeeman splitting. The strong variation of the Zeeman splitting with wavelength usually compensates for the broader profiles of infrared lines, making them the lines of choice for determining magnetic field strengths.

We have shown that the main contribution to the sensitivity of Stokes I to temperature is the variation in the source function with T, and that opacity changes play a less important role. Since variation of the Planck function with T is smaller at longer wavelengths, infrared lines are less affected by temperature perturbations than visible lines. However, they show a large modification of the equivalent width with T.

Our set of lines includes some lines that are often quoted to be temperature insensitive, such as Fe I 557.61 nm. We have demonstrated that this line in particular exhibits the highest temperature sensitivity among the various lines considered in this work. In fact, one cannot speak of temperature insensitive lines: even if the absorption does not change much after temperature variations, the source function will always change, leading to detectable effects in the emergent spectrum.

Ideally, one would like to use a spectral line that shows very high sensitivity to all atmospheric parameters at the same time, but this line does not exist. Visible and infrared lines have both advantages and limitations. It is desirable, then, to combine different lines in order to characterize the physical properties of the solar atmosphere more reliably.

4

Observations and data reduction

4.1 Introduction

A complete understanding of the Evershed flow requires a good knowledge of the magnetic fields of sunspot penumbrae. Different observational techniques have been used in the determination of the magnetic field, but only the inversion of all four polarization profiles of spectral lines allow to derive both the geometry and the strength of the vector magnetic field. As demonstrated in the previous chapter, IR and VIS lines carry information from different layers of the photosphere and display different sensitivities to the atmospheric parameters. This is the reason why the simultaneous use of IR and VIS lines is advantageous to better constrain the properties of the medium where the lines were formed.

In the last years, advances in instrumentation have allowed to carry out imaging and spectroscopic observations of the penumbra at very high spatial resolution ($\sim 0\farcs1$–$0\farcs2$) (Scharmer et al. 2002; Rouppe van der Voort et al. 2004; Bellot Rubio et al. 2005). Even at such a spatial resolution there is evidence of unresolved structures. The problem with these observations is that they provide very little information about the magnetic field.

These arguments motivated us to plan observations at the Vacuum Tower Telescope (VTT) of Observatorio del Teide (Tenerife, Spain). Simultaneous spectropolarimetric measurements of visible and near-infrared spectral lines can be performed at the VTT and, recently, an adaptative optic system has been installed. This kind of observations are those needed to investigate the temporal evolution of the Evershed flow, determining the variation of the vector

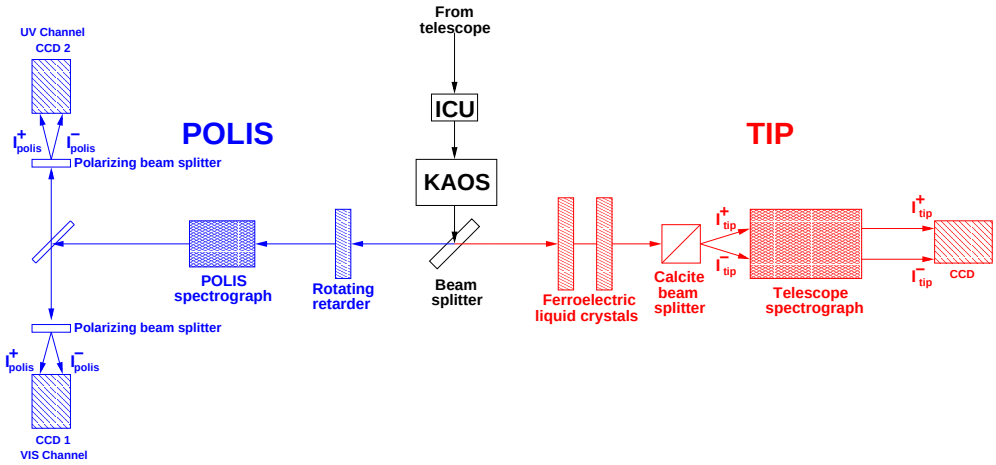

FIGURE 4.1:— Main optical elements of POLIS (blue) and TIP (red). ICU means Instrument Calibration Unit. KAOS is the Kiepenheuer Adaptative Optic System.

magnetic field at the highest spatial resolution ever reached[1]. Moreover, high resolution filtergrams taken at the Dutch Open Telescope (DOT) are used in order to compare them with the spectropolarimetric data.

The chapter is organized as follows. We first describe the VTT and DOT instruments in Sects. 4.2 and 4.3. Sections 4.4 and 4.5 give details about the observations at the VTT. Finally, Section 4.6 explains the reduction of the polarimetric data.

4.2 Vector spectropolarimetry at the Vacuum Tower Telescope

This section summarizes the main characteristics of the adaptative optics (AO) system and polarimeters operating at the VTT. We describe the way AO corrects for the atmospheric turbulence and how the polarimeters measure the four Stokes profiles.

4.2.1 The Kiepenheuer Adaptative Optic System: KAOS

The AO system operating at the VTT, KAOS (Soltau et al. 2002), has been developed to compensate the perturbations[2] of the wavefront that can be ex-

[1] At present, the best spectropolarimetric observations have spatial resolutions of the order of $1''$.

[2] The perturbations are caused by small scale density variations of the atmosphere which produce changes in the refraction index leading to perturbations of the originally plane waves

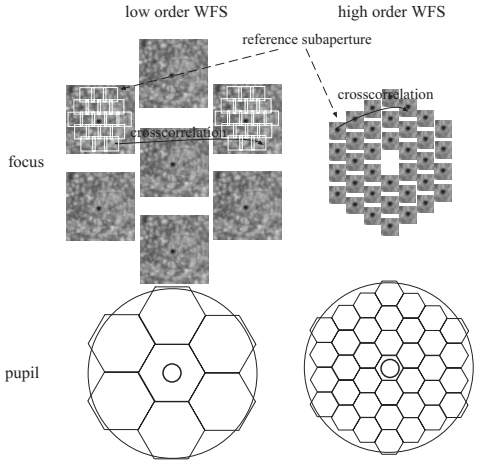

FIGURE 4.2:— KAOS wave wavefront sensors (*bottom row*). The sensors have 7 and 36 elements and correct for low (*left*) and high (*right*) order aberrations, respectively. The corresponding field patterns on the detector are shown at the top row. *Courtesy of D. Soltau* (KIS).

pressed in terms of the six lowest radial degrees of Zernike functions. KAOS consists of a deformable mirror with 35 actuators and two wavefront sensors (see Fig.4.2). The sensors calculate the wavefront perturbation produced by the atmosphere on a reference image, and modifies the shape of the deformable mirror. The correction is restricted to a field of view of about $10''$ in diameter from the target selected as reference image. As shown in Fig. 4.1, KAOS is located before the telescope focus, so it corrects for atmospheric turbulence before the light is analyzed by the polarimeters.

4.2.2 The Polarimetric Littrow Spectrograph: POLIS

POLIS (Schmidt et al. 2003; Beck et al. 2005b) has been designed for simultaneous observations of the Stokes profiles of VIS and ultraviolet (UV) spectral lines formed in the photosphere and chromosphere, respectively. The Stokes profiles of the Fe I lines at 630.15 nm and 630.25 nm are measured by a CCD camera, hereafter referred to as the VIS channel. Another CCD is used to observe the line core and the blue wing of the Ca II H line at 396.85 nm (hereafter UV channel).

An illustration of the optical layout of POLIS is displayed in the left part of Fig. 4.1 (blue ray path). VIS light coming from the telescope is deviated by a chromatic[3] beam splitter[4] into the POLIS optical bench without loss of light.

coming from the Sun.

[3]Light is splitted depending on wavelength: VIS light is directed to POLIS while IR goes to TIP.

[4]In 2003, the beam splitter was achromatic to deviate half of the light to POLIS and the other half to TIP. It was upgraded to a chromatic beam splitter in 2004.

A rotating retarder is used for modulating the incoming light beam. Then, the light is dispersed by the Littrow spectrograph and the beam is reimaged in the focal plane of CCD 1 (VIS channel) and CCD 2 (UV channel). In front of each camera, polarizing beam-splitters divide the modulated light into two orthogonally polarized beams[5]:

$$\begin{aligned} I^{\pm}_{\rm polis}(\alpha(t),\delta) &= \frac{r^{\pm}}{2}[I \pm Q(\cos^2 2\alpha(t) + \sin^2 2\alpha(t)\cos\delta) \\ &\pm \sin 2\alpha(t)\cos 2\alpha(t)(1-\cos\delta) \mp V \sin 2\alpha(t)\sin\delta], \end{aligned} \quad (4.1)$$

where α and δ are the angular position and the fixed retardance of the modulator, and $r^{\pm}$ are the transmission of the beams given by the polarizing beam splitters. We note that Eq. 4.1 is only valid for an ideal polarimeter; in practice, the effect of the optical elements on the polarization state of the light has to be calculated. In order to derive the Stokes profiles, POLIS takes eight intensity images changing the modulator orientation continuously. These intensity images are linear combinations of the Stokes profiles (Eq. 4.1). The adopted modulation scheme (Lites et al. 1993) provides a linear system of eight equations and four unknown quantities (I, Q, U, and V):

$$\boldsymbol{I}_{\rm mes} = \boldsymbol{O}\boldsymbol{I}_{\rm in}, \quad (4.2)$$

where $\boldsymbol{I}_{\rm mes}$ is the measured intensity, $\boldsymbol{I}_{\rm in}$ is the Stokes vector of the incident light, and $\boldsymbol{O}$ is the 8×4 modulation matrix.

Inverting the former equation, one obtains the values of the Stokes profiles in terms of the demodulation matrix, $\boldsymbol{D}$:

$$\boldsymbol{I}_{\rm in} = \boldsymbol{D}\boldsymbol{I}_{\rm mes}. \quad (4.3)$$

4.2.3 The Tenerife Infrared Polarimeter: TIP

IR light (red ray path in Fig. 4.1) deviated by the chromatic beam splitter is directed to TIP (Martínez Pillet et al. 1999; Collados et al. 1999). This polarimeter is able to work in a broad range of wavelengths ($1 - 2.3$ μm). The instrument modulates the incoming light by means of ferroelectric liquid crystals (FLCs), electro-optical devices with a fixed retardance and an optical axis that can change its orientation in a few milliseconds. In practice, the two FLCs act as a half ($\lambda/2$) and a quarter ($\lambda/4$) wave plates that modify the orientation of their optical axis by $\Delta\theta \sim 45^{\circ}$ when the voltage changes from +15 V to −15 V. After the incoming beam is modulated by the FLCs, a

[5]The use of orthogonal beams reduces the amount of seeing induced cross-talk (Lites 1987).

calcite beam splitter (i.e., a Savart plate) splits the beam into two orthogonally polarized beams ($I^{\pm}_{\rm TIP}$) and the light is dispersed by the telescope spectrograph. The light detected by the camera is a combination of the Stokes profiles:

$$I^{\pm}_{\rm tip} = M^{\pm}_{1,1} I + M^{\pm}_{1,2} Q + M^{\pm}_{1,3} U + M^{\pm}_{1,4} V, \tag{4.4}$$

where

$$\begin{aligned} M^{\pm}_{1,1} &= M_{\pm} M(\lambda/2) M(\lambda/4), \\ M^{\pm}_{1,2} &= M_{\pm} M(\lambda/2 + \Delta\theta) M(\lambda/4), \\ M^{\pm}_{1,3} &= M_{\pm} M(\lambda/2) M(\lambda/4 + \Delta\theta), \\ M^{\pm}_{1,4} &= M_{\pm} M(\lambda/2 + \Delta\theta) M(\lambda/4 + \Delta\theta). \end{aligned} \tag{4.5}$$

$M_{\pm}$ and M are the Mueller matrices of the beam splitter and the FLCs. The orientations of the optical axis of the FLCs are changed in the four possible combinations to perform four intensity measurements (Eq. 4.4), resulting in a linear system of four equations and four unknowns from which I, Q, U, and V are determined.

4.3 Filtergrams from the Dutch Open Telescope (DOT)

Speckle-reconstructed G-band filtergrams at 430.5 ± 0.5 nm taken at the DOT were downloaded from the public data archive available at *http://dotdb.phys.uu.nl/DOT*. The data cadence and sampling were 30 s and $0\farcs071$ per pixel, respectively. The speckle technique is used to improve the spatial resolution. Each reconstruction needs a burst of 100 individual frames with exposure times of 1 ms. This procedure freezes the effect of the random atmospheric turbulence on the images and allows to reach the diffraction limit of the telescope ($\sim 0\farcs2$ at 430.5 nm). Details on the data processing are described by Sütterlin et al. (2004).

4.4 Observations of the temporal evolution of the penumbra

NOAA Active Region 10781 was observed on 2005 June 30 from 8:47 to 11:23 UT and on 2005 July 1 from 9:31 to 10:51 UT at the VTT. TIP and POLIS were operated simultaneously to record the full Stokes profiles of the spectral lines around 1565 nm and 630 nm (see Table 4.1). The same spot was observed on 2005 June 30 with the DOT from 8:45 to 9:38 UT. Table 4.2 gives details of the observations at the VTT. The observed active region was located at

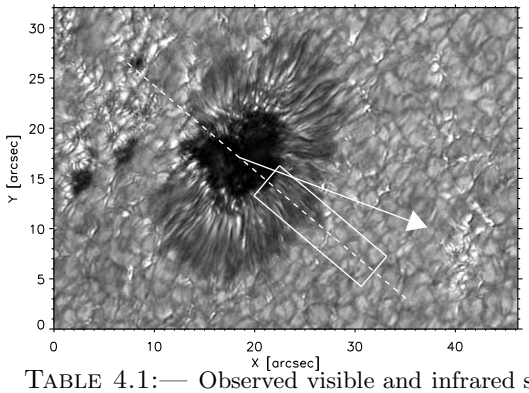

FIGURE 4.3:— Speckle-reconstructed G-band filtergram of AR 10781 taken at the Dutch Open Telescope (DOT) on 2005 June 30, 9:34 UT. The box shows the fraction of the center-side penumbra and adjacent moat scanned by TIP and POLIS. The arrow marks the direction to disk center.

TABLE 4.1:— Observed visible and infrared spectral lines. λ_0 represents the central wavelength, χ the excitation potential of the lower level, $\log gf$ the logarithm of the oscillator strength times the multiplicity of the lower level, and $g_{\rm eff}$ the effective Landé factor. *a*, *b*, and *c* taken from Nave et al. (1994), Borrero et al. (2003), and Pierce & Breckenridge (1974), respectively. Note that O_2 are telluric absorption lines.

Polarimeter	Species	λ_0 [nm]	χ [eV]	$\log gf$	transition	$g_{\rm eff}$
POLIS	Fe I	630.1501^a	3.65^a	-0.72	${}^5P_2$–${}^5D_2$	1.67
POLIS	Fe I	630.2494^a	3.69^a	-1.24	${}^5P_1$–${}^5D_0$	2.50
POLIS	Fe I	630.3460	4.32	-2.55	${}^5G_6$–${}^5G_5$	
POLIS	Ti I	630.3753	1.45	-1.44	${}^3F_3$–${}^3G_3$	
POLIS	O_2	630.2001^c				
POLIS	O_2	630.2761^c				
TIP	Fe I	1564.7410^a	6.33^a	-0.95	${}^7D_1$–${}^5P_2$	1.25
TIP	Fe I	1564.8515^a	5.43^a	-0.68^b	${}^7D_1$–${}^7D_1$	3.00
TIP	Fe I	1565.2874^a	6.25^a	-0.05^b	${}^7D_5$–${}^6D_{4.5}4f[3.5]^0_4$	1.45

heliocentric angles of 43° and 35° on June 30 and July 1, respectively. The slit width was 0.″36 for TIP and 0.″18 for POLIS. During the observations, KAOS was used to reduce image motion and blurring. In order to observe the same field of view (FOV) the TIP and POLIS slits were aligned by rotating the main spectrograph of the VTT and moving the TIP camera. The pixel size was $0.''175 \times 0.''175$ and $0.''145 \times 0.''145$ for TIP and POLIS, respectively.

On 30 June, we performed rapid scans of a small portion of the center-side penumbra of the spot including the adjacent moat region (see Fig. 4.3). The scan step was 0.″2 for a total of 20 steps (4″). The integration time was 10.5 s per slit position, resulting in a cadence of 3.9 min. We performed 40 repetitions of the scan. The excellent seeing conditions, together with KAOS, allowed us to reach a spatial resolution of about 0.″6 at 1565 nm and 0.″7 at 630 nm[6].

[6]The distorting effect of atmospheric turbulence is greater at shorter wavelengths (Vernin & Muñoz-Tuñón 1992).

TABLE 4.2:— Log of the 2005 observations. The third column gives the heliocentric angle of the spot. The fourth and fifth columns show the scanning step and the integration time per slit position. The duration of the sequences and the seeing conditions are indicated in the last two columns.

Date	AR	θ [deg]	step size [arcsec]	t_i [s]	duration [min]	seeing [arcsec]
06/30/2005	10781	43	0.2	10.5	156	$\sim$ 0.6–0.7
07/01/2005	10781	35	0.2	5.5	80	$\sim$ 0.8–0.9

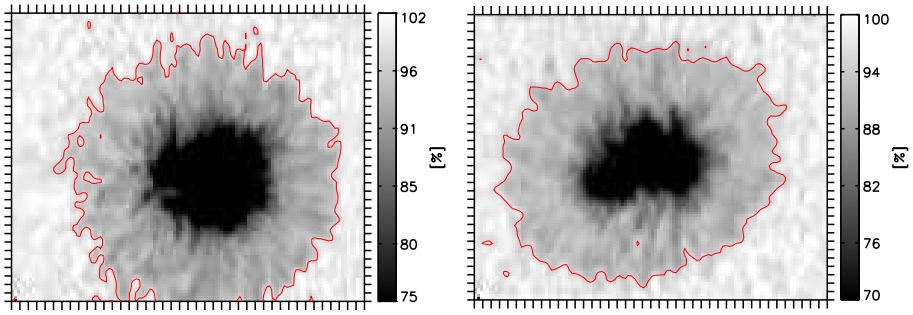

FIGURE 4.4:— Continuum intensity maps at 1565 nm for sunspots C (*left*) and A (*right*). The red contours outline the boundaries of the spots. Each tickmark represents 1″. Intensities are normalized to the continuum intensity of the the average quiet sun profile.

On 1 July, we observed a smaller portion of the center-side penumbra of the same active region: the scan step was 0.″2 for a total of 10 steps, producing maps of 2″. The integration time was 5.5 s per slit position, resulting in a cadence of 2 min. The seeing conditions were good and the spatial resolution was around 0.″8 in the IR and 0.″9 in the VIS.

4.5 Observations of sunspots at different heliocentric angles

On August 2003, three spots were observed with the VTT at different heliocentric angles (see Fig. 4.4 and Table 4.3). Hereafter, we will refer to these sunspots as A, B, and C. During the observations, a correlation tracker (Schmidt & Kentischer 1995; Ballesteros et al. 1996) was used to stabilize the solar image, allowing us to reach a spatial resolution of about 1″. The spectral lines around 630 nm were observed with POLIS while the Stokes profiles of the Fe I lines at 1565 nm were recorded with TIP (Table 4.1). The two polarimeters were operated simultaneously. The slits were aligned in order to observe the same FOV and their widths were 0.″36 for TIP and 0.″48 for POLIS. The pixel size

TABLE 4.3:— Log of the 2003 observations. The second and third column indicate the date of observation and NOAA number. The fourth column displays the heliocentric angle. The fifth and sixth columns are the scanning step and the integration time per slit position. The seeing is specified in the last column.

Sunspot	Date	AR	θ [deg]	step size [arcsec]	$t_{\rm i}$ [min]	seeing [arcsec]
A	08/03/03	10425	50	0.40	5.0	$\sim$ 1.0–1.1
B	08/07/03	10430	8	0.35	3.3	$\sim$ 1.0–1.1
C	08/09/03	10430	27	0.35	3.3	$\sim$ 1.0–1.1

was $0\farcs175 \times 0\farcs175$ and $0\farcs35 \times 0\farcs35$ for TIP[7] and POLIS, respectively.

4.6 Data reduction

4.6.1 Calibration of the polarimetric data

In order to remove the different response of the CCD pixels to homogeneous illumination, gain tables calculated using flat fields and dark current images have been applied. Then, the intensity signals measured by the polarimeters have been converted to Stokes profiles. With that aim, an instrumental calibration unit (ICU) was used. The ICU consists of a linear polarizer followed by a retarder. These elements can be rotated to produce known polarization states, $\boldsymbol{I}_{\rm cal}$. Evaluating the difference between the measured Stokes profiles ($\boldsymbol{I'}_{\rm cal}$) and $\boldsymbol{I}_{\rm cal}$, one determines the Mueller matrix of all the optical elements from the ICU downstream (including the polarimeter), $\boldsymbol{X_{\rm pol}}$:

$$\boldsymbol{I'}_{\rm cal} = \boldsymbol{X_{\rm pol}} \boldsymbol{I}_{\rm cal} \tag{4.6}$$

The optical elements of the telescope (primary and secondary mirrors, plus the coelostat) produce instrumental polarization, i.e. cross-talk between the Stokes profiles. The theoretical Mueller matrix of the telescope, $\boldsymbol{X_{\rm tel}}$, is known (Beck et al. 2005a). The true Stokes profiles emerging from the Sun, $\boldsymbol{I}_{\rm sun}$, can then be calculated from the measured by the polarimeters, $\boldsymbol{I'}_{\rm sun}$, as

$$\boldsymbol{I}_{\rm sun} = \boldsymbol{X_{\rm pol}^{-1}} \boldsymbol{X_{\rm tel}^{-1}} \boldsymbol{I'}_{\rm sun}. \tag{4.7}$$

The accuracy on the determination of the polarimetric profiles has been estimated to be of the order of 10^{-3} in units of the continuum intensity (Beck et al. 2005a).

[7]The TIP camera was upgraded in 2005.

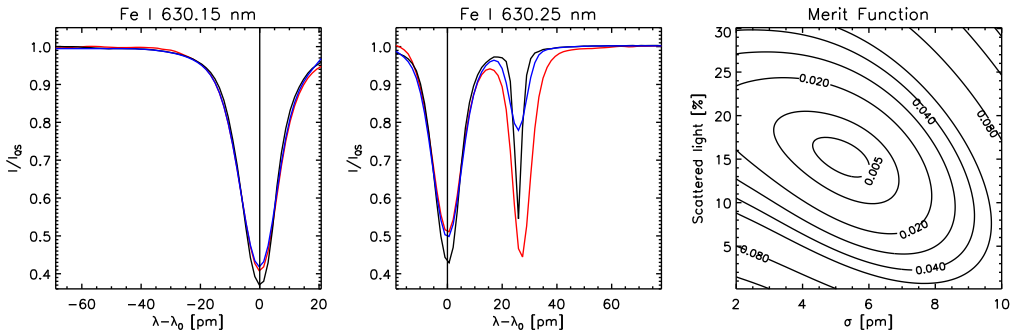

FIGURE 4.5:— Comparison of the spectra at disk center of Fe I 630.15 nm (*left panel*) and Fe I 630.25 nm (*center panel*) as observed with FTS (black) and POLIS (red) for the 1 July dataset. The blue profiles are the best fits obtained by combining the FTS profiles with the fraction of scattered light and the resolving power of POLIS as explained in the text. The merit function of the fit is showed in the *right panel*. Note that the O_2 telluric line is not considered in the fit.

4.6.2 Scattered light correction

The presence of residual O_2 telluric lines in the polarization profiles of POLIS (cf. Fig.4.6) confirmed the existence of spectrally undispersed scattered light. If a constant fraction of the incident light enters the camera without going through the grating, the intensity measurements are contaminated by a certain amount of light artificially produced by the instrument. This scattered light might be due to incomplete shielding of the light path inside the compact POLIS shelter.

We correct the spectra for scattered light following Allende Prieto et al. (2004). The amount of scattered light and the resolving power of the polarimeters are calculated by comparing our average quiet-sun intensity profiles with those in the Fourier Transform Spectrometer (FTS) atlas. The FTS profiles are not affected by scattered light and the point spread function (PSF) of the FTS can be considered as a Dirac delta function for our purposes. Hence, if we add a certain fraction of scattered light to the FTS profiles and convolve them with the PSF of our instruments, we should be able to reproduce the profiles of the spectral lines recorded by the polarimeters, i.e.,

$$I = \left(\frac{I_{\rm FTS} + K}{1 + K} \right) * G(\sigma), \tag{4.8}$$

where I are our disk-center profiles, $I_{\rm FTS}$ are the profiles of the FTS atlas, K is the fraction of scattered light, G the instrumental profile[8] of the polarimeter,

[8]We assume a normalized gaussian profile for the PSF.

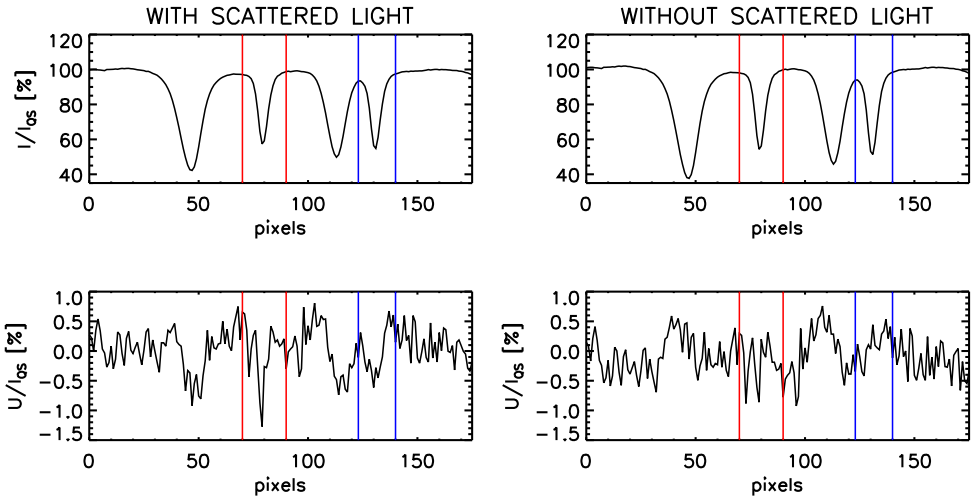

FIGURE 4.6:— Stokes I (*top*) and Stokes U (*bottom*) profiles of the VIS lines at 630 nm uncorrected (*left*) and corrected (*right*) for scattered light. The vertical color lines indicate the positions of the O_2 telluric lines.

σ the width of the instrumental profile, and $*$ represents convolution.

In Fig. 4.5 we show an example of the fits that we obtain by using Eq. 4.8 for the disk center profiles of Fe I 630.15 nm and Fe I 630.25 nm recorded on 1 July 2005. As can be seen, the two visible lines are well reproduced. The merit function of the fit shows a minimum for $K \simeq 15\%$ and $\sigma \simeq 6$ pm. The same results are obtained for the profiles measured on 30 June 2005, while for the 2003 data set the fraction of scattered light is around 13% and the PSF remains in the same value. We note that the theoretical resolving power of POLIS is limited by the slit and it is always smaller than that inferred from the fits. In fact, it is around 2 pm in 2005 and 5 pm in 2003. In Fig. 4.6 we display an example of the effect of the correction on the polarization profiles. As can be seen, Stokes U display clear signatures of the telluric lines which disappear after the correction.

The same calculation applied to the TIP data does not allow us to find a minimum of the merit function. For this reason, we fix the resolving power of TIP using the theoretical value (~ 3 pm in 2005). In this way we are able to estimate the fraction of scattered light, which turns out to be around 14% in the 2005 dataset.

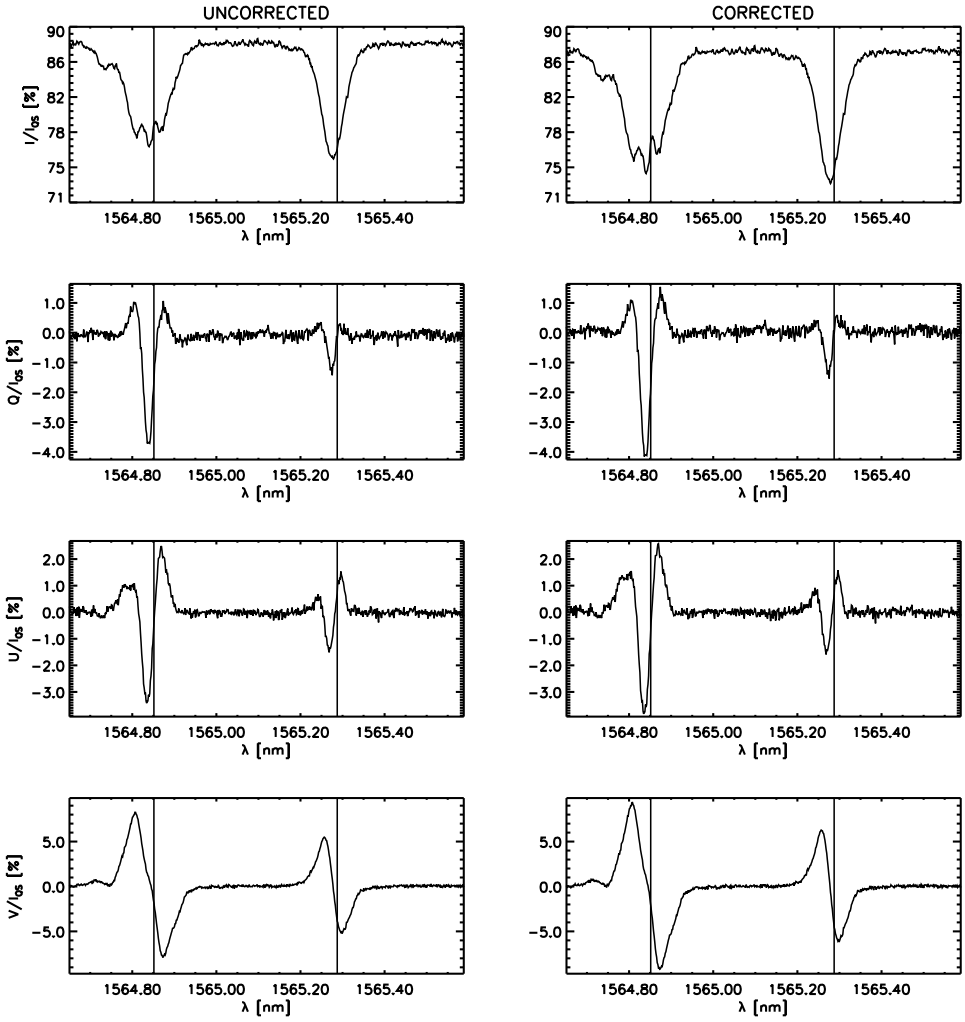

FIGURE 4.7:— Stokes profiles uncorrected (left) and corrected (right) for scattered light and residual cross-talk. The amount of scattered light is 14%, while the residual cross-talks $V \to Q$, $V \to U$, $Q \to V$, $U \to V$ are estimated to be 2%, -3%, -10%, and 14%.

4.6.3 Residual cross-talk correction

After removing the instrumental polarization produced by the telescope, a certain amount of residual cross-talk is present in the Stokes profiles. This is because the telescope model uses theoretical values of the refractive indexes of the mirrors which differ from the real ones.

Basically, the true Stokes parameters are contaminated by a fraction of the other Stokes profiles:

$$I_i^{\rm true} = I_i + \sum_{j=1}^{4} C_{ij} I_j, \tag{4.9}$$

where i runs from 1 to 4 (standing for I, Q, U, and V), $I_i^{\rm true}$ and I_i are the true and measured Stokes profiles, and C_{ij} (the cross-talk coefficient) is the fraction of I_j contaminating I_i.

In order to correct for residual cross-talk, we follow the statistical method described by Schlichenmaier & Collados (2002). The residual cross-talk from I to Q, U, and V is calculated by forcing the continuum of the polarization profiles to zero. The cross-talks $V \rightarrow Q$ and $V \rightarrow U$ are estimated with the following procedure. We first select the profiles for which the maximum of the absolute value of V is, at least, 6.5 times larger than the maximum absolute values of Q and U. For these pixels, most of the Q and U signals are produced by cross-talk from V:

$$Q(\lambda) = -C_{42} V(\lambda), \tag{4.10}$$

$$U(\lambda) = -C_{43} V(\lambda). \tag{4.11}$$

The cross-talk coefficients C_{42} and C_{43} are computed from a linear fit of the Stokes profiles (Eqs. 4.10 and 4.11) for the selected pixels. The least-squares fit equations give:

$$C_{42} = \frac{\sum_k Q(\lambda) V(\lambda)}{\sum_k V(\lambda)^2}, \tag{4.12}$$

$$C_{43} = \frac{\sum_k Q(\lambda) U(\lambda)}{\sum_k V(\lambda)^2}, \tag{4.13}$$

where k runs for the pixels. The same method is employed for calculating C_{24} and C_{34}. We emphasize that this procedure can only be carried out for the IR lines of the set. The small Zeeman splitting of the VIS lines does not allow to properly disentangle the residual cross-talk in the various Stokes profiles.

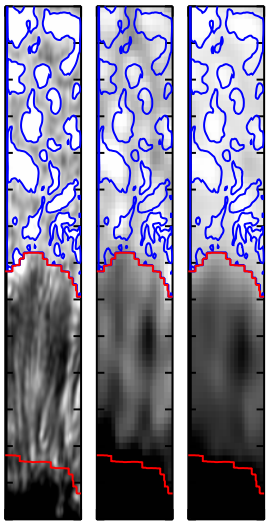

FIGURE 4.8:— From left to right: Maps of speckle-reconstructed G-band intensity, continuum intensity at 1565 nm, and continuum intensity at 630 nm observed on 2005 30 June, 9:26 UT. Red lines mark the inner and outer boundaries of the penumbra. Blue contours outline pixels with G-band intensities greater than $0.5 \times I_{\rm qs}$. Each tickmark on the y-axis represents $1''$.

Figure 4.7 shows the Stokes profiles emerging from a pixel before and after applying the scattered light and residual cross-talk corrections for TIP. The corrected Stokes profiles display larger amplitudes. This is because they are normalized to the continuum intensity of the quiet sun. The subtraction of the scattered light produce smaller normalization factors and, consequently, stronger polarization signals. The residual cross-talk correction only produces little modifications in the asymmetries of the profiles.

4.6.4 Alignment of TIP, POLIS, and DOT data

Alignment of TIP and POLIS

Since the refractive index of the air depends on wavelength, the images of the Sun at different wavelengths are shifted with respect to each other. This well-known phenomenon is called differential refraction and produces displacements between the TIP and POLIS data sets. In order to remove these shifts, we follow the method described by **?**). It basically consists in performing a cross-correlation of the intensity maps using the largest pixel size (the TIP pixel) as a reference. To that aim, the POLIS data are binned to the TIP pixel size. After that, one calculates the shifts between both data sets by correlating the continuum intensity maps of POLIS and TIP. Figure 4.8 displays, as an example, the continuum intensity maps at 1565 nm (center panel) and 630 nm (right panel) after removing the shifts. As can be seen, the correspondence between the intensity structures is quite precise. In fact, the accuracy of the

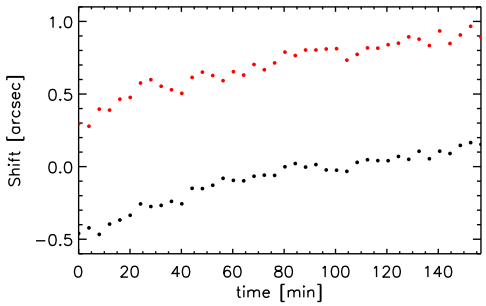

FIGURE 4.9:— Shifts between the infrared and visible continuum intensity maps along (black) and perpendicular (red) to the slit for the time sequence observed on 30 June 2005.

alignment between TIP and POLIS is around 0.″1 (**?**).

The position of the Sun on the sky changes during the day. Hence, the differential refraction produces time-dependent shifts between the VIS and IR spectropolarimetric data. When the time sequences are long, one should take into account the temporal dependence of the displacements. This is why we calculate the displacements between IR and VIS spectra for each repetition of the maps observed in 2005. Figure 4.9 displays the calculated shifts between the continuum intensity maps of the sunspot at 1565 nm and 630 nm as a function of time for the sequence observed on 30 June 2005. The total displacements accumulated during the 156 min of observation are around 1″ and 0.″6 in the directions perpendicular and parallel to the slit, respectively. This means that co-spatial Stokes profiles in the visible and the near-infrared are not strictly simultaneous, but the time difference is always smaller than $\sim$ 55 s. For the sunspot maps observed on 2003 we calculate a unique shift per map.

Alignment of VTT and DOT data

The way filtergrams and spectropolarimetric data are obtained is different. The DOT filtergrams are 2D images taken at once, while the spectropolarimetric maps recorded at the VTT are constructed by scanning the slit across the solar surface, which takes time. If one wants to compare both kind of observations, the positions observed by the polarimeters have to be located on the DOT filtergrams taken at the same time they were observed at the VTT. Following **?**), we align the POLIS slit-jaw images with the DOT G-band images. This is done by degrading the G-band data to the same pixel size than the slit-jaw images. After the rotation between the images of the two telescopes is removed, shifts between the slit-jaw and the G-band images are determined by cross-correlation. At this point, one knows where the positions of the POLIS/TIP slits are in the G-band images. Finally, one constructs *artificial* G-band maps

by selecting the co-spatial G-band strip which is closer in time to the polarimetric data. We note that the DOT and VTT observations are not strictly co-temporal, but the differences are small enough ($\leq$ 30 s) to work with both data sets as if they had been taken simultaneously.

5

Data analysis

5.1 Introduction

By interpreting the Stokes profiles, one can estimate the atmospheric conditions of the medium where the spectral lines are formed. In this work, we retrieve the physical information contained in the polarization profiles by means of two different approximations: (a) the calculation of line parameters; and (b) the simultaneous inversions of all four Stokes parameters. In this chapter we describe both kind of techniques and the wavelength scale used for the IR and VIS data sets.

5.2 Line parameters

The simplest way to analyze the observations is by computing parameters extracted from the polarization profiles. Those parameters reflect the atmospheric conditions of the solar photosphere, providing a first estimate of their values. We have derived the following observables from the Stokes profiles of the IR and VIS spectral lines:

- Continuum intensities, I. The Eddintong-Barbier approximation is valid for the continuum intensities (del Toro Iniesta et al. 1994; Bellot Rubio et al. 2006). This implies that I depends on the temperature of the layers where the continuum is formed [$\sim \log(\tau) = 0$].
- Stokes V zero-crossing velocity. The LOS velocity is estimated from the Doppler shift of the Stokes-V zero-crossing wavelength, λ_{ZC} (Fig. 5.1).

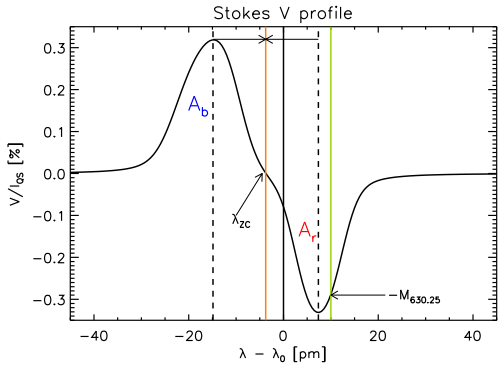

FIGURE 5.1:— Line parameters calculated from Stokes V. Dashed lines show the position of the maxima of the Stokes V lobes. λ_{ZC} indicates the zero-crossing wavelength (orange line). λ_0 is the rest wavelength (black line). A_b and A_r are the areas of the blue and red lobes of Stokes V. $M_{630.25}$ is the magnetogram signal of Fe I 630.25 nm (green line).

λ_{ZC} is calculated as the mid-point between the maxima of the Stokes V lobes (dashed lines in Fig. 5.1). This velocity is representative of the magnetic atmosphere inside the resolution element and can only be computed for pixels exhibiting normal two-lobed Stokes V profiles.

- Total polarization signals. For fully split lines, if the magnetic field orientation remains constant along the LOS (Solanki 1993):

  - The total linear polarization, L= $\sum_i \sqrt{Q(\lambda_i)^2 + U(\lambda_i)^2}$, is proportional to $\sin^2 \gamma_{\rm LOS}$ (cf. Fig. 2.5). Hence, the larger the value of L the greater the magnetic field inclination to the LOS ($\gamma_{\rm LOS}$).
  - The total circular polarization, V= $\sum_i |V(\lambda_i)^2|$, is proportional to $\cos \gamma_{\rm LOS}$. Therefore it is smaller when the field inclination is larger.
  - The linear-to-circular polarization ratio, L/V, is greater when the inclination increases (L/V$\sim \sin^2 \gamma_{\rm LOS}/\cos \gamma_{\rm LOS}$).

  In any case, we would like to stress that the polarization signals only provide rough estimations of $\gamma_{\rm LOS}$. The magnetic field is known to vary with heigth in the solar photosphere and the spectral lines are not always in the strong field regime.

- The Stokes V area asymmetry is given by

$$\delta A = \frac{|A_r| - |A_b|}{|A_r| + |A_b|}, \tag{5.1}$$

where A_r and A_b are the areas of the red and blue lobes of Stokes V (see Fig. 5.1). δA arises as a consequence of velocity gradients along the LOS (Auer & Heasley 1978; Sánchez Almeida & Lites 1992). The combination

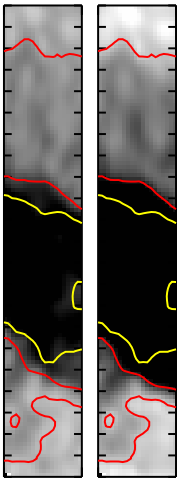

FIGURE 5.2:— Maps of continuum intensity at 1565 nm (left) and 630 nm (right) observed on 30 June 2005, 10:25 UT. Red lines mark the inner and outer borders of the penumbra, while yellow contours outline pixels with $I/I_{\rm qs} < 0.4$ in the 630 nm map. Each tickmark in the y-axis represents $1''$.

of such gradients with magnetic field or temperature gradients leads to an amplification of the asymmetries.

- We construct magnetograms , M, as (minus) the Stokes V signal of Fe I 630.25 nm at $\Delta\lambda = +10$ pm from line center (see Fig. 5.1). M provides a rough estimation of the longitudinal magnetic flux (Landi degl'Innocenti 1992).

5.3 Wavelength scale

The velocity scale for the IR and the VIS lines has been set assuming that the umbra is at rest (Beckers 1977; Koch 1984). Basically, the wavelength scale is defined by the rest wavelength and the spectral dispersion. We estimate the rest wavelengths by calculating the mean position of the Stokes V zero-crossings of the pixels located in the darkest regions of the umbra[1]. Hereafter we refer to this calibration as *umbral calibration*. For the time sequence observed on 30 June we select pixels with continuum intensities $I/I_{\rm qs} < 0.4$ at 630 nm. In Fig. 5.2 we indicate those pixels with yellow contours for the map recorded at 10:25 UT. The dispersion is computed by determining the number of pixels between the line core positions of Fe I 1564.85 nm and Fe I 1565.52 nm for

[1]For the POLIS data, the small focal length of the spectrograph produce a curvature of the spectrum along the slit. In order to remove that effect, we use the O_2 telluric line at 630.20 nm to align all the spectra individually. This correction has been applied before the determination of the wavelength scale.

TABLE 5.1:— Mean dispersions of the Doppler shifts (in m s^{-1}) of the selected umbral pixels for the different spectral lines. The errors are the standar deviations of the averages.

Date	$\sigma_{630.15}$ [m s^{-1}]	$\sigma_{630.25}$ [m s^{-1}]	$\sigma_{630.35}$ [m s^{-1}]	$\sigma_{1564.85}$ [m s^{-1}]	$\sigma_{1565.29}$ [m s^{-1}]
06/30	83 ± 16	80 ± 17	100 ± 20	86 ± 16	120 ± 16
07/01	64 ± 30	63 ± 31	74 ± 34	64 ± 28	60 ± 28

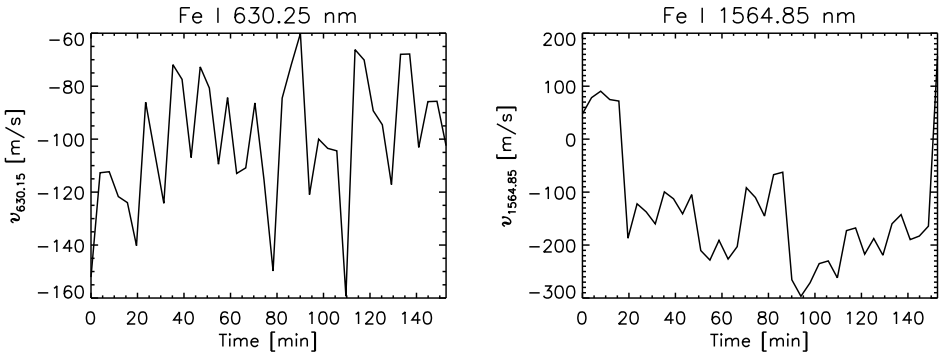

FIGURE 5.3:— Mean velocity of the umbra observed on 30 June 2005 for Fe I 630.25 nm (left) and Fe I 1564.85 nm (right). An absolute calibration is performed for the VIS line, while for the IR line the calibration is computed by means of an average quiet sun profile corrected for convective blueshift.

TIP and the O_2 telluric lines for POLIS. In order to estimate a lower limit[2] for the calibration error, we calculate the dispersion of the Doppler shitfs of the selected umbral pixels with respect to their mean value for each map. In Table 5.1 we show the average of those quantities for each spectral line in the two sequences. The errors represent the standar deviations of those averages. As can be seen, the mean dispersions are always smaller than 120 m s^{-1} with low scatter (rms $<$ 34 m s^{-1}) between the different maps. Such small values could be produced by small velocity fields of the umbral dots (Socas-Navarro et al. 2004) and/or the presence of oscillatory phenomena in the selected areas.

Besides using the Stokes V zero-crossings of the umbra, we tried different calibrations for the VIS and IR lines. For the VIS lines an absolute calibration is possible using the O_2 telluric lines (Martínez Pillet et al. 1997). For the infrared lines the wavelength scale was fixed by the line core positions, corrected for convective blueshift (Borrero & Bellot Rubio 2002), of the average

[2]The accuracy of the laboratory wavelengths is ±30 pm and ±50 pm for the IR and VIS lines. This leads to uncertainties of ±60 pm and ±100 pm in the determination of the wavelength scale dispersion.

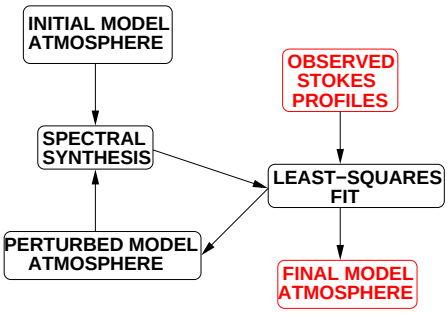

FIGURE 5.4:— Basic diagram of an iterative inversion scheme.

quiet Sun profile for each repetition. Figure 5.2 displays the mean velocities of the umbra observed on 30 June, calculated by averaging the velocities of the same pixels than those selected in the umbral calibration, as inferred from the calibrations of Fe I 630.25 nm (left panel) and Fe I 1564.85 nm (right panel) as a function of time. As can be seen, the umbral velocities derived from the VIS line are around ~ 100 m s^{-1}. Those small velocities could be due to both systematic errors in the wavelength calibration and the presence of umbral dots. This indicates that the umbra is basically at rest as we assumed in the umbral calibration. In contrast, the umbral velocities inferred from the IR line display larger values of ~ 200 m s^{-1}. As pointed out by Beck et al. (2007), this could be due to a wavelength offset of the average quiet sun profiles produced by the moat flow and/or by a reduction of the convective blueshifts produced by the magnetic field, or due to the fact that we observe at off center positions. Another possibility is that the umbral dots show large blueshifts in the deep layer where the IR lines form. Offsets between the velocity scale of the two spectral ranges can lead to systematical errors in the determination of the atmospheric parameters. For this reason, we decide to use the *umbral calibration* for the two spectral ranges.

5.4 Inversions of the radiative transfer equation

The line parameters described in the previous section depend on several atmospheric quantities. For example, the total polarization signals do not only depend on the magnetic field inclination but also on temperature and magnetic field strength. This is the reason why they just provide rough estimates of the physical parameters under some restrictive assumptions. The only way to properly disentangle the various effects of the atmospheric parameters on the shapes of the polarization profiles is by means of Stokes inversion (see reviews by del Toro Iniesta & Ruiz Cobo 1996; del Toro Iniesta 2003a; Socas-Navarro 2001; Bellot Rubio 2006).

As discussed in Sect. 2.4, the evolution of the Stokes profiles along the atmosphere is governed by the RTE and has no analytical solution. Only the use of numerical methods allows us to address the problem of line formation in the presence of magnetic fields. There are different strategies to face the numerical problem. Basically, there are two kind of methods classified as iterative and non-iterative. Iterative algorithms spend more computing time than the non-iterative ones. However, they are more accurate and provide a greater amount of physical information (del Toro Iniesta & Ruiz Cobo 1996; del Toro Iniesta 2003a). The basic scheme of an iterative algorithm is illustrated in Fig. 5.4. Codes based on these algorithms work as follows. An initial guess atmosphere is assumed in order to calculate the corresponding synthetic profiles. Initially, the synthetic profiles deviate from the observed ones. For this reason, a perturbed model atmosphere is computed by a least square algorithm which minimizes the differences between them. Then, synthetic profiles emerging from that new atmosphere are calculated and the cycle starts again until the synthetic profiles match the observed ones.

There are a few numerical codes which use the general scheme of Fig. 5.4. In the next section we describe the singularities of the code employed in this thesis.

5.4.1 Stokes Inversion based on Response functions (SIR)

The SIR code was developed by Ruiz Cobo & del Toro Iniesta (1992). It assumes LTE conditions (see Sect. 2.4) for a plane-parallel atmosphere in hydrostatic equilibrium. The LTE approximation is suitable for spectral lines formed under the conditions of the solar photosphere (Shchukina et al. 1997).

Numerically, SIR computes the elements of $\boldsymbol{S}$ and $\boldsymbol{K}$ from the guess model atmosphere. This atmosphere is characterized by the values of the physical quantities (T, B, $v_{\rm LOS}$, etc) at a given optical depth:

$$\boldsymbol{x}(\tau_{\rm c}) = [x_1(\tau_{\rm c}), x_2(\tau_{\rm c}), \ldots, x_{m-1}(\tau_{\rm c}), x_m(\tau_{\rm c})], \tag{5.2}$$

where m runs for the atmospheric parameters and $\tau_{\rm c}$ is the continuum optical depth at 500 nm. The synthetic profiles, $\boldsymbol{I}^{\rm syn}$, are calculated by solving the RTE by means of an Hermitian method (Bellot Rubio et al. 1998). The differences between the observed, $\boldsymbol{I}^{\rm obs}$, and synthetic profiles are estimated by the merit function:

$$\chi^2(\boldsymbol{x}) \equiv \frac{1}{\nu} \sum_{s=1}^{4} \sum_{i=1}^{q} \left[I_s^{\rm obs}(\lambda_i) - I_s^{\rm syn}(\lambda_i; \boldsymbol{x}) \right]^2 w_{s,i}^2, \tag{5.3}$$

where s stands for the Stokes parameters, i for the wavelength, ν is the number of free parameters, and $w_{s,i}^2$ give the relative weights assigned to the Stokes parameters. The minimization of χ^2 is performed iteratively by modifying the guess model atmosphere ($\boldsymbol{x}$). This process is complicated because $\boldsymbol{I}^{\rm syn}$ depends non-linearly on the atmospheric parameters. A Marquardt algorithm is implemented in order to find the minimum of χ^2. The algorithm makes use of the derivatives of χ^2, which can be written in terms of the Response Functions (RFs; Ruiz Cobo & del Toro Iniesta 1992; del Toro Iniesta et al. 1994). The use of RFs allows to reduce considerably the computing time because they are evaluated at the same time as the RTE is solved.

In order to reduce the number of free parameters, the perturbations are calculated in selected positions, called nodes, of the grid in which the model atmospheres is discretized. The perturbations in the remaining points are linear or cubic-spline interpolations of the perturbations at the nodes. If one assumes one node for a given physical quantity, then a constant perturbation is applied to the entire atmosphere. With two nodes, the perturbations are calculated at the lower and upper extremes of the model atmosphere. A different number of nodes can be specified for each atmospheric parameter. Moreover, they can be changed in each cycle[3]. Usually, SIR needs two or three cycles to match the observed profiles (i.e. to arrive at the final solution). The interested reader is referred to del Toro Iniesta (2003b) for details and the basics of inversion techniques.

Singularities of the simultaneous inversion of VIS and IR profiles

The simultaneous inversion of the VIS and IR Stokes profiles required some modifications of SIR. For example, the stray light contamination is known to be wavelength dependent. Moreover, the PSFs of TIP and POLIS are different (cf. Sect. 4.6.2). For this reason, the inversion code was modified to account for the two different stray light contributions of the spectral ranges and the different PSFs of the polarimeters.

5.4.2 Conversion from Observer to Local Reference Frame

The vector magnetic fields derived from the inversions are inferred in the line-of-sight (LOS) reference frame. In order to know the real geometry of the field, it is necessary to transform it to the Local Reference Frame (LRF). In this section we describe the two reference frames and the method employed in the conversion of the vector magnetic field from the LOS to the LRF.

[3]A cycle is the set of iterations with the same number of nodes.

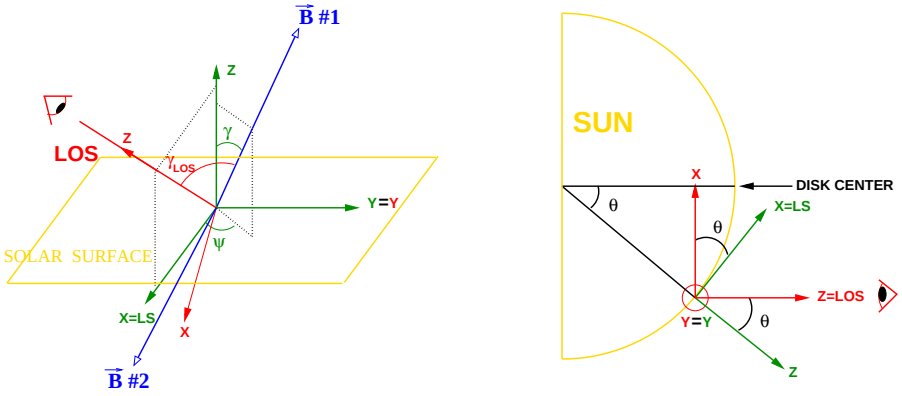

FIGURE 5.5:— *Left*: Illustration of the local reference frame (green lines) and the LOS reference frame (red line). The magnetic field vectors #1 and #2 (blue lines) lead to the same emergent Stokes profiles. Only the angles of solution #1 are plotted. *Right*: Side view of the orientation of the LRF with respect to the LOS frame. Note that the y-axes of both reference frames are identical.

Figure 5.5 displays two different views of the LRF (green lines) and the LOS reference frame (red lines). The LRF is defined as the orthonormal coordinate system whose z-axis is perpendicular to solar surface and the x-axis points to disk center along the line of symmetry (LS). In the LOS reference frame, the z-axis points to the observer and the x-axis is defined by the projection of the LS in the plane perpendicular to the z-axis. As can be seen in the panels of Fig. 5.5, the y-axes of the two reference systems coincide. Hence, if one rotates the LOS frame around the y-axis by the heliocentric angle θ, both systems become identical (right panel of Fig. 5.5).

The choice of an appropriate reference frame simplifies the transformation of the vector magnetic field to the LRF. This is done calculating the cartesian projections of the vector in the LOS system:

$$\boldsymbol{B}_{\rm LOS} = |\boldsymbol{B}| \begin{pmatrix} \cos\psi_{\rm LOS} \sin\gamma_{\rm LOS} \\ \sin\psi_{\rm LOS} \sin\gamma_{\rm LOS} \\ \sin\gamma_{\rm LOS} \end{pmatrix}, \tag{5.4}$$

where $\psi_{\rm LOS}$ and $\gamma_{\rm LOS}$ are the azimuths and inclinations in the LOS reference frame. Both $\psi_{\rm LOS}$ and $\gamma_{\rm LOS}$ increase counter-clockwise from the LS and the LOS, respectively.

Then, the projections of those quantities in the LRF are obtained applying a simple rotation of angle θ along the y-axis:

$$\boldsymbol{B}_{\rm LRF} = \begin{pmatrix} \cos\theta & 0 & \sin\theta \\ 0 & 1 & 0 \\ -\sin\theta & 0 & \cos\theta \end{pmatrix} \boldsymbol{B}_{\rm LOS}. \tag{5.5}$$

In this way, we can calculate the orientation of the magnetic field vector in the LRF which is given by the inclination, γ, and the azimuth, ψ:

$$\boldsymbol{B}_{\rm LRF} = |\boldsymbol{B}| \begin{pmatrix} \cos\psi\sin\gamma \\ \sin\psi\sin\gamma \\ \sin\gamma \end{pmatrix}, \tag{5.6}$$

The inclinations and azimuths are measured counter-clockwise from the local z-axis and the LS respectively (see left panel of Fig. 5.5). When $\psi = 0^\circ$ and $\gamma = 90^\circ$ the magnetic field points to the disk center along the LS, while $\gamma = 0^\circ$ means that the field is vertically oriented away from the solar surface.

5.4.3 Resolution of the azimuth ambiguity

It is well-known that a rotation of 180° of the vector magnetic field in the plane perpendicular to the line of sight does not modify the emergent Stokes profiles (Unno 1956). The left panel of Fig. 5.5 illustrates two vector magnetic fields whose azimuths differ 180° in the LOS reference frame. Hereafter, we call them solutions #1 and #2. Both configurations produce the same projection of the magnetic field along the LOS and, consequently, the same emergent Stokes profiles. This is the so-called 180°ambiguity of the LOS azimuths. Because of this ambiguity, one does not know if the vector magnetic field given by the inversion is the real one or must be rotated 180°. In order to decide among the two possibilities, we translate both solutions from the LOS reference frame to the LFR.

In Fig. 5.6 we show the inclinations of the magnetic field in the LRF, γ, resulting from the two possible solutions of the LOS azimuth ambiguity for a map displaying the penumbra of a sunspot. The orientation of the magnetic field is indicated with arrows. As can be seen, the variation of the magnetic field orientation is smooth in both solutions. Since the sunspots fields are known to be radial (Westendorp Plaza et al. 2001b; Bellot Rubio et al. 2004), the orientation of the arrows and the vertical fields observed in the outer penumbra reveal that solution #2 is not realistic and the correct one is solution #1. We resolve the problem of the azimuth ambiguity taking the solution #1 for pixels inside the spot and demanding a smooth variation of the magnetic field orientation at larger radial distances in the moat. This is the method employed for the different types of inversion presented in this thesis.

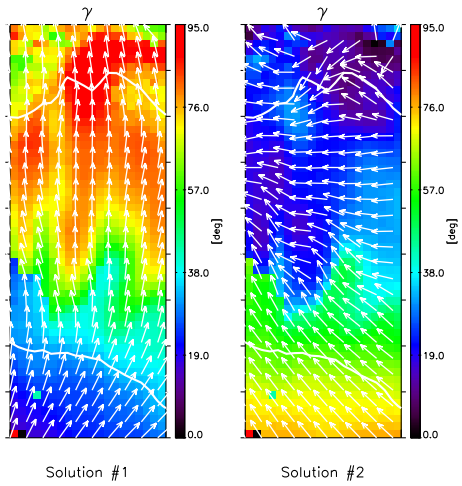

FIGURE 5.6:— Maps of magnetic field inclination of a sunspot penumbra in the LRF for solutions #1 and #2. The arrows indicate the direction of the magnetic field in the LRF. White lines represent the inner and outer penumbral boundaries.

5.4.4 Semi-empirical models

According to current views, the penumbral magnetic field is *uncombed* (Solanki & Montavon 1993; Martínez Pillet 2000; Bellot Rubio et al. 2004; Borrero et al. 2004, 2005, 2006). In this scenario, the penumbra is formed for two magnetic components of different inclinations. There is evidence that the more horizontal component must be formed by flux tubes carrying the Evershed flow while the other component is basically at rest. The width of the tubes is still a matter of debate, but in all cases it is supposed to be below the spatial resolution of the best spectropolarimetric observations (100-300 km).

In order to account for the magnetic field structure of the sunspot penumbra, different degrees of sophistication are used in this thesis. The simplest approximation assumes that the penumbra is composed by *one magnetic component* (cf. Chapter 8). The results derived from this simple inversion would be an average of the atmospheric quantities of the two components. The next logical step is to account for the unresolved structure of the penumbra in the simplest scenario: *two magnetic components* which are interlaced horizontally but not vertically. Finally, the effect of the tubes in the vertical direction is modeled by gaussians placed along the atmosphere of arbitrary extension. The results of the inversions accounting for the uncombed structure of the penumbra are shown in Chapter 9

Pixels outside the spot, i.e. in the moat, are also inverted. In this case, two components are assumed to fill the resolution element: one is magnetic and the other non-magnetic. This is because, in general, the Stokes profiles of these pixels can be reproduced with a single magnetic component.

6

Inversion of visible and infrared sunspot Stokes profiles

6.1 Introduction

Inversion techniques allow us to extract detailed information from Stokes profiles. Over the years, different degrees of sophistication have been used in the analysis of visible (VIS) and near-infrared (IR) spectral lines emerging from sunspots (cf Chapter 1). Until now, all the analyses have used either visible or infrared lines. Recent advances in instrumentation have opened the door to simultaneous measurements in both spectral ranges. As discussed in Chapter 3, it is expected that the use of the two spectral ranges would allow us to derive the physical properties of the solar atmosphere more reliably. In order to investigate this topic, we take advantage of the new observing capabilities to examine the structure of sunspots observed at different heliocentric angles (cf. Sec. 4.5) as derived from the inversion of visible and infrared lines. Due to their simple Zeeman pattern and the high sensitivity to magnetic field (cf. Chapter 3), we decided to observe the VIS Fe I lines at 630 nm and the IR Fe I lines at 1565 nm. A comparison of the atmospheric parameters derived from the one-component inversions of IR and VIS Stokes profiles is performed in Sect. 6.2. As we will show, the differences in the magnetic structure of the sunspots derived from the two spectral ranges are small. In contrast, the differences in the thermal structure are significant in the umbra of spots. The origin of such differences is investigated in Sect. 6.3. The improvement in the determination of the atmospheric parameters produced by the simultaneous inversions

of the two spectral ranges is shown in Sec. 6.4, while the main conclusions are discussed in Sect. 6.5.

6.2 Comparison of VIS and IR one component inversions

In this section, we analyze the magnetic and thermal configuration of Sunspot B (cf. Sect. 4.5) as inferred from the inversion of the IR and VIS Stokes profiles. The results for spots A and C are similar and are shown in Appendix B. One-component model atmospheres without gradients are used in the analysis, i.e., we assume that the resolution element is filled with a magnetic atmosphere whose physical quantities (except for the temperature) do not vary with height.

6.2.1 Magnetic configuration

The two first rows of Fig. 6.1 show the field strengths (B), LOS inclinations (γ), and LOS azimuths (ψ) derived from the inversion of the IR and VIS Stokes profiles of sunspot B[1]. The differences between those quantities are shown in the panels of the third row. As can be seen, the magnetic configuration derived from IR and VIS data sets is essentially the same. This is more obvious in the histograms of the bottom panels. In fact, in the umbra the mean and standard deviation of the differences are 150 G and 55 G for B, respectively, and $-2°$ and $3°$ for γ (cf. Table 6.1). As expected, we always retrieve stronger magnetic fields from the IR lines. This is a clear signature of their deeper height of formation (see Chapter 3) and of the sunspot magnetic structure. For the differences in magnetic field azimuth, the mean value of the distribution in the umbra is $-2°$, with a standard deviation of $5°$.

In the penumbra the situation becomes more complicated. The existence of at least two magnetic components in this region is well established (del Toro Iniesta et al. 2001; Bellot Rubio et al. 2004; Borrero et al. 2004, 2005, 2006) . In our inversions the penumbra is described in terms of one single component, which would represent some kind of average of the various magnetic atmospheres present in the resolution element. The problem is that the exact way the averaging is done is not known a priori, and may be different for VIS and IR lines. Thus, one-component inversions can only provide a rough description of the penumbra. For meaningful comparisons between both spectral ranges, one should take into account the unresolved structure of the penumbra, i.e., multi-component inversions are required. In spite of these problems, the differences between the two ranges are also small in the penumbra, with mean

[1]The results for sunspots A and C are shown in Figs. B.1 and B.2, respectively.

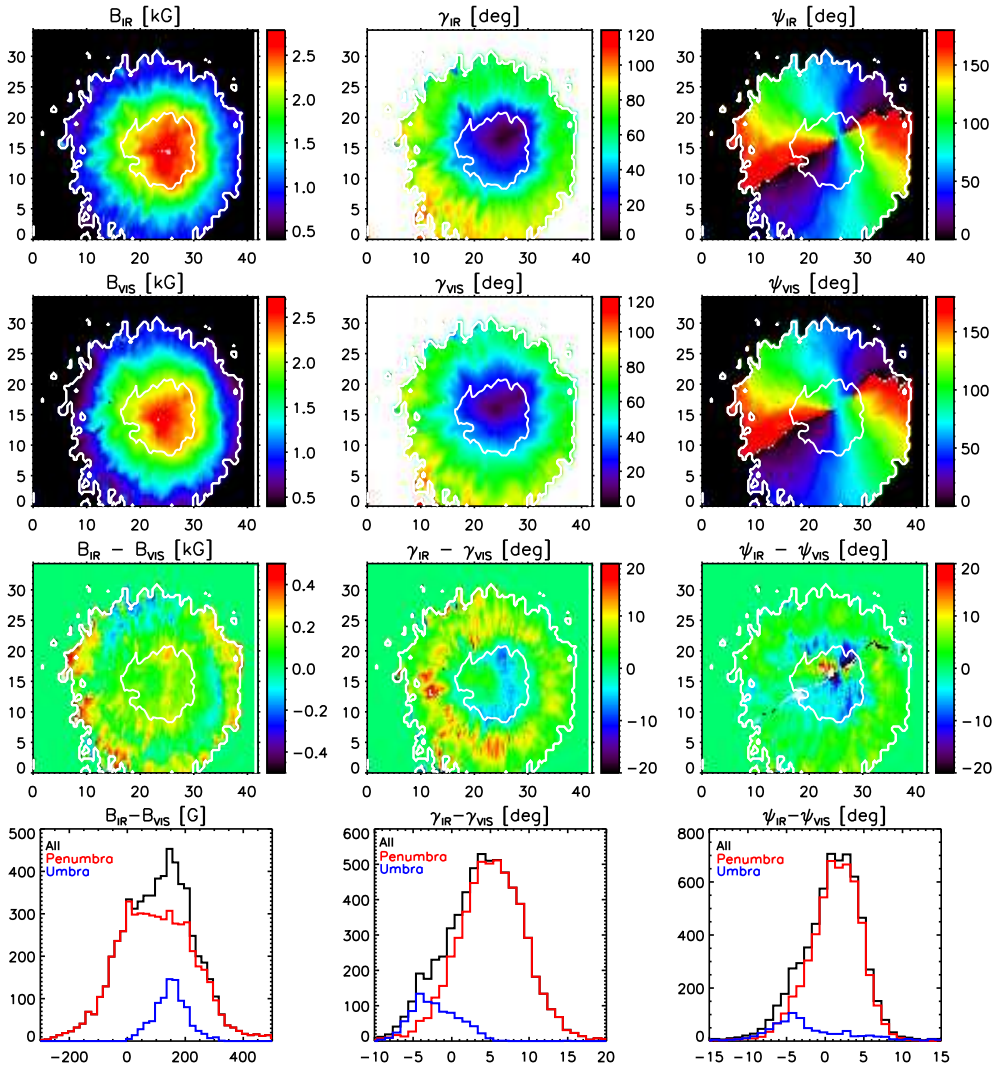

FIGURE 6.1:— From *top* to *bottom*: Maps of B, γ, and ψ derived from the inversions of IR and VIS Stokes profiles of sunspot B, differences between them, and histograms of the differences between the atmospheric quantities for the penumbra (red), umbra (blue), and all the inverted points (black). Numbers on the x- and y-axis for the first three rows are given in arc seconds on the maps.

TABLE 6.1:— Mean values and standard deviations (errors) of the histograms in Figs. 6.1 and 6.3.

	$B_{\rm IR} - B_{\rm VIS}$ [G]	$\gamma_{\rm IR} - \gamma_{\rm VIS}$ [deg]	$\psi_{\rm IR} - \psi_{\rm VIS}$ [deg]	$T_{\rm IR} - T_{\rm VIS}$ [K]
Umbra	150 ± 55	-2 ± 3	-2 ± 5	8 ± 143
Penumbra	98 ± 131	5 ± 5	1 ± 3	22 ± 122

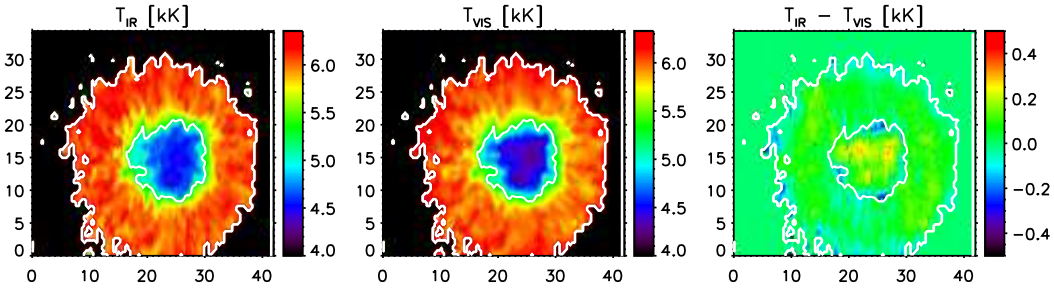

FIGURE 6.2:— From *left* to *right*: Temperatures at $\log\tau = 0$ derived from IR and VIS inversions and the differences between them.

values and standard deviations of 98 ± 131 G for B, $5° \pm 5°$ for γ, and $1° \pm 3°$ for ψ.

Both in the umbra and in the penumbra, the inversion of VIS and IR lines lead to very similar magnetic parameters. The differences may be understood taking into account the different formation heights, the limitations of the lines, and the simplicity of the assumed model atmosphere. We believe these results demonstrate the reliability of Stokes inversions.

6.2.2 Thermal configuration

Figure 6.2 shows the temperatures at $\log\tau = 0$ (T) derived from IR and (*left*) VIS (*center*) data sets and their differences (*right*). The histograms of the differences in temperatures of the umbra are displayed in Fig. 6.3. As can be seen, there are differences as large as 300 K. Since our models are suitable

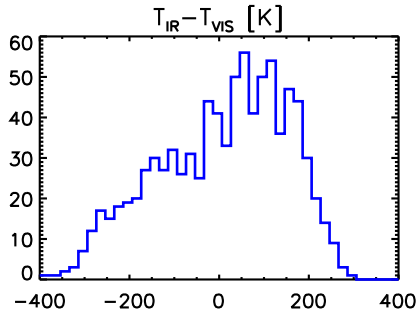

FIGURE 6.3:— Histogram of the differences in temperature at $\log\tau = 0$ for the umbra of sunspot B.

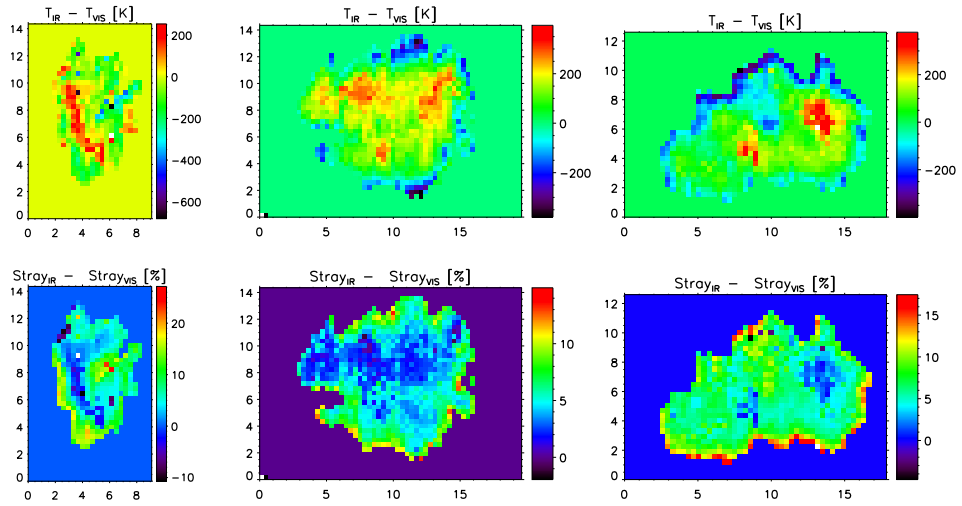

FIGURE 6.4:— Differences between the stray light (*bottom*) and temperatures (*top*) derived from IR and VIS inversions for the umbras of sunspots A (*left*), B (*center*), and C (*right*).

for the umbra[2], the temperatures at $\log \tau = 0$ should coincide. The origin of such differences is illustrated in Fig. 6.4 where the discrepancy between the temperatures (top panels) and the corresponding differences in the stray light derived from IR and VIS (bottom panels) are shown for the umbras of sunspots A, B, and C. Note the strong correlation between the top and bottom panels. Such a correlation leads us to conclude that the differences in temperature are mainly produced by the different stray lights determined from the inversion.

6.3 Cross-talk between temperature and stray light for VIS lines

SIR is able to retrieve a certain amount of stray light for each inverted point. As Martínez Pillet (1992) demonstrated, most of the stray light inside the sunspot comes from the quiet sun. This implies that the amount of stray light should increase with radial distance from the sunspot center. As can be seen in Fig. 6.5, it only happens for the IR lines. We suspect that the code is not able to discriminate between enhancements of temperature and stray light when VIS lines are inverted. In other words, there is a cross-talk between temperature and stray light for the VIS lines. The reason is the smaller Zeeman splitting of VIS lines as compared with that of IR lines, which makes it more difficult

[2]Stokes profiles of the umbra are well reproduced with one magnetic component.

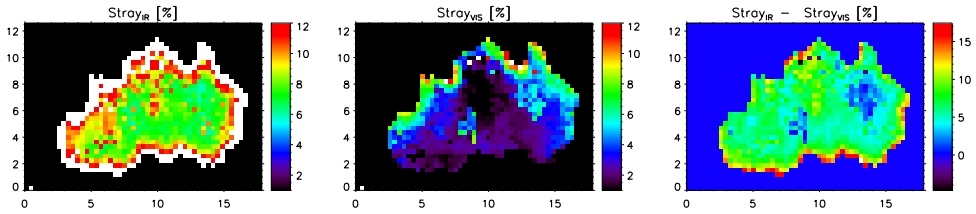

FIGURE 6.5:— Maps of stray light derived from IR (*left*), VIS (*center*), and the differences between them (*right*) for the umbra of sunspot C.

to separate the different effects of stray light and temperature on the Stokes profiles. This problem is critical in the penumbra, because the Fe I lines at 630 nm are typically in the weak field regime for magnetic fields below 1400 G (Lites & Skumanich 1990). Our results are in agreement with the work of Martínez González et al. (2006), who used two different atmospheric components to study the distribution of magnetic fields in internetwork regions of the quiet Sun.

6.4 Improvement with simultaneous inversion

A wrong determination of the stray light contamination leads to systematic errors not only in the temperature, but also in the strength and orientation of the magnetic field. Basically, a larger stray light results in stronger and more inclined fields to adjust to the new (cooler) temperatures. As shown in the maps of the left panels of Fig. 6.1, the differences in B increase in the outer penumbra, coinciding with the regions where the differences in stray light are larger (see right panel of Fig. 6.6). The cross-talk between stray light and the other atmospheric parameters can be minimized by performing simultaneous (SIM) inversions of VIS and IR lines. In this kind of inversions, we recover a unique temperature stratification and two different stray light factors, one for each spectral range (cf. Sect. 5.4.1). Comparing the top and bottom panels of Fig. 6.6, one can see that the differences in stray light are reduced in the outer penumbra when both spectral ranges are inverted simultaneously. The influence of the stray light on the atmospheric parameters determined from the VIS lines can be assessed by repeating the inversion with the stray light fixed to the values retrieved from the SIM inversions. Figure 6.7 shows that the differences between field strengths derived from the VIS and the IR lines are reduced when the stray light contamination of the VIS lines is fixed. Table 6.2 displays the standard deviations of the differences between the atmospheric parameters retrieved from the VIS inversion when the stray light is a free parameter and when is fixed. As shown, the differences between T, B, and γ

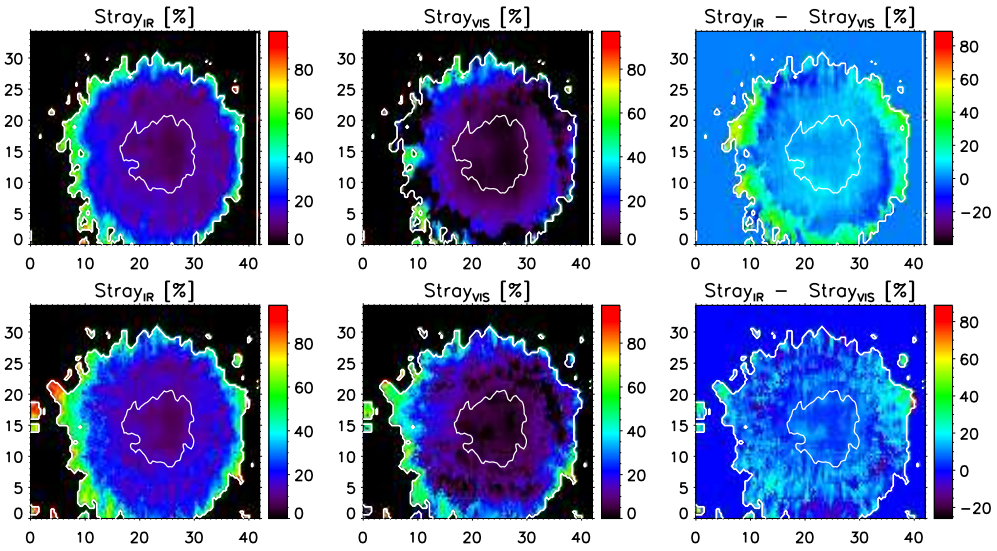

FIGURE 6.6:— *Top*: Stray light inferred from IR (*left*) and VIS (*center*) inversions and the differences between them (*right*) for sunspot B. *Bottom*: IR (*left*) and VIS (*center*) Stray light inferred from the simultaneous inversions of the VIS and IR Stokes profiles and the differences between them (*right*) for the same sunspot.

derived from the two spectral ranges are reduced when the stray light of the VIS lines is fixed to the values inferred from the SIM inversions.

Simultaneous observations of VIS and IR lines can also be used to improve the determination of vertical gradients of atmospheric parameters in sunspots. We have calculated the average vertical gradients of field strength and inclination from SIM inversions using one-component atmospheres, but only for the umbra, since meaningful analyses of penumbral profiles require uncombed model atmospheres. Assuming hydrostatic equilibrium, we obtain $<dB/dz> = -2.3 \pm 0.6$ G km^{-1} and $<d\gamma/dz> = -0.019 \pm 0.015$ deg km^{-1}, i.e.,

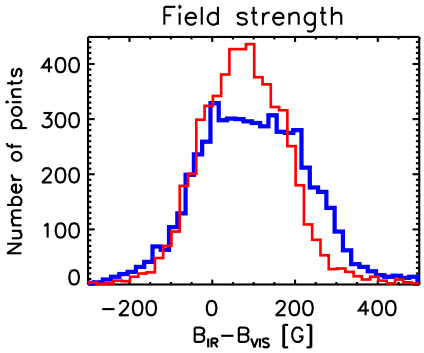

FIGURE 6.7:— Histogram of the differences in field strength for the penumbra of sunspot B when the stray light of the VIS lines is kept as a free parameter (red) or fixed to the values resulting from the simultaneous inversion (blue).

TABLE 6.2:— Variation of the standard deviations of the differences between temperatures, field strengths, inclinations, and azimuths derived from IR and VIS inversions for the penumbra when the VIS stray light is a free parameter and when it is fixed by the values recovered by the simultaneous inversions.

	$\sigma_{\Delta T}$ [K]	$\sigma_{\Delta B}$ [G]	$\sigma_{\Delta\gamma}$ [deg]	$\sigma_{\Delta\psi}$ [deg]
VIS Stray light free	122	131	5	3
VIS Stray light fixed	111	105	3	3
$\Delta\sigma$ [%]	**-9.3**	**-20**	**-36**	**0**

stronger and more inclined fields occur deep in the atmosphere.

6.5 Summary and outlook

We have shown that one-component inversions of visible and infrared lines without gradients lead to similar physical parameters for a sunspot, with small differences produced by the different formation heights, the limitation of the lines, the simple model atmosphere used in the inversion, and the cross-talk between temperature and stray light affecting the visible lines. This demonstrates that inversion techniques provide unique results.

The T-stray light cross-talk leads to systematic errors in the temperatures and magnetic fields determined from visible lines. The SIR code considers only unpolarized stray light coming from the quiet Sun. But there is also polarized stray light from the surroundings into the resolution element (Sánchez Cuberes et al. 2005). For this reason, a more realistic treatment of the stray light contamination seems necessary. In fact, the current approach is valid only as a first approximation (Martínez Pillet 1992). Anyway, we stress that the cross-talk is not only a problem related to simplistic treatments of the stray light, but also a problem of the visible lines themselves. Due to the smaller Zeeman splitting of these lines, the code is not able to discriminate between enhancements of temperature and larger stray light contaminations (see Figs. 6.4 and 6.5). The cross-talk can be minimized by using both spectral ranges simultaneously. In this case, a better estimate of the stray light contamination in the visible is found. Simultaneous inversions reduce the errors in the determination of the other physical quantities.

Visible and infrared lines have advantages and limitations (cf. Chapter 3). Hence, it is desirable to combine both spectral ranges in order to characterize the physical properties of the solar atmosphere more reliably. In this Chapter it has been demonstrated that this combination improves the determination of the atmospheric parameters, allowing us to discriminate between different

scenarios.

7

Temporal evolution of the Evershed flow: observational characterization

7.1 Introduction

The Evershed flow has been studied intensively over the last decades (Solanki 2003). Most of what we know today about this dynamical phenomenon, however, has been learned from observations that do not reflect its temporal evolution. The study of the time evolution of the flow requires stable observing conditions during long periods of time. This is the reason why there are only a few investigations published about the topic (Shine et al. 1994; Rimmele 1994; Rouppe van der Voort 2003; Georgakilas & Christopoulou 2003). The main result of them all is that the Evershed flow displays variations on time scales ranging from 8 min to 25 min. This quasi-periodic behavior is produced by the so-called Evershed clouds (ECs) which propagate from the mid penumbra to the outer penumbral boundary, where they seem to vanish.

A good knowledge of ECs is crucial for a complete understanding of the nature and origin of the Evershed flow. Unfortunately, their observational properties are not well characterized yet. Previous investigations were based on high resolution filtergrams and Dopplergrams, but the polarization signals of ECs have never been observed. For these reasons, a detailed description of the observational properties of ECs (including their polarization signatures) is warranted.

In this chapter we present the first study on the temporal evolution of the Evershed flow that makes use of high-cadence, high-precision, full vector spec-

tropolarimetric observations in visible (630 nm) and near infrared (1565 nm) lines. The spatial resolution of our observations is one of the highest achieved in solar spectropolarimetry. It is around 0.″6 at 1565 nm (reaching the diffraction limit of the telescope) and 0.″7 at 630 nm.

The chapter is organized as follows. We first identify and determine the lifetimes, proper motions, and sizes of the ECs (Sect. 7.2). We then describe the properties of the penumbral filaments along which they are observed to move outward (Sect. 7.3) and the periodicity of the EC phenomenon (Sect. 7.4). Section 7.5 is devoted to characterize the main observational properties of the ECs by means of line parameters such as Doppler velocities and polarization signals. In Sect. 7.6 we compare these properties with those of the rest of penumbral points. Next, the dependence of the Doppler velocities on height is investigated (Sect. 7.7). In Sect. 7.8 we study the correlation between the proper motions along the LOS and the Doppler velocities of ECs. The evolution of the observational parameters of the ECs as they propagate outwards is the subject of Sect. 7.9 while their disappearance at the outer penumbral boundary is described in Sec. 7.10. Finally, Sect. 7.11 summarizes our results.

7.2 Identification, morphology, and proper motions of ECs

In Figs. 7.1–7.3 we show the temporal evolution of the center-side penumbra and the moat region of AR 10781 for the 156 min of the time sequence observed on 2005 June 30. The first panel displays the continuum intensity at 1565 nm. The next two panels display the LOS velocities calculated[1] from the Stokes V zero-crossing shifts of Fe I 1565.28 nm and Fe I 630.25 nm. The last two panels show the logarithm of the total linear polarization of Fe I 1564.85 nm and Fe I 630.25 nm. Figures C.1 and C.2 (Appendix **??**) give the same information for the July 1 dataset.

We identify ECs as structures of enhanced velocity signal which propagate outwards across the penumbra. During the 236 minutes of our observations, fifteen ECs appear in the mid-penumbra and then migrate to the outer penumbral boundary. They are observed in the two spectral ranges simultaneously. We have outlined them with contours of different colors and letters in Figs. 7.1–7.3 and Figs. C.1–C.2. The boundaries of the ECs have been defined as isocontours of specific values of the Doppler velocity, hence they should be considered as approximate.

In order to quantify the radial distances where the ECs appear, we must

[1]The velocity is computed only for pixels exhibiting normal two-lobed V profiles with amplitudes greater than 0.2% for Fe I 630.25 nm and 0.5% for Fe I 1564.85 nm.

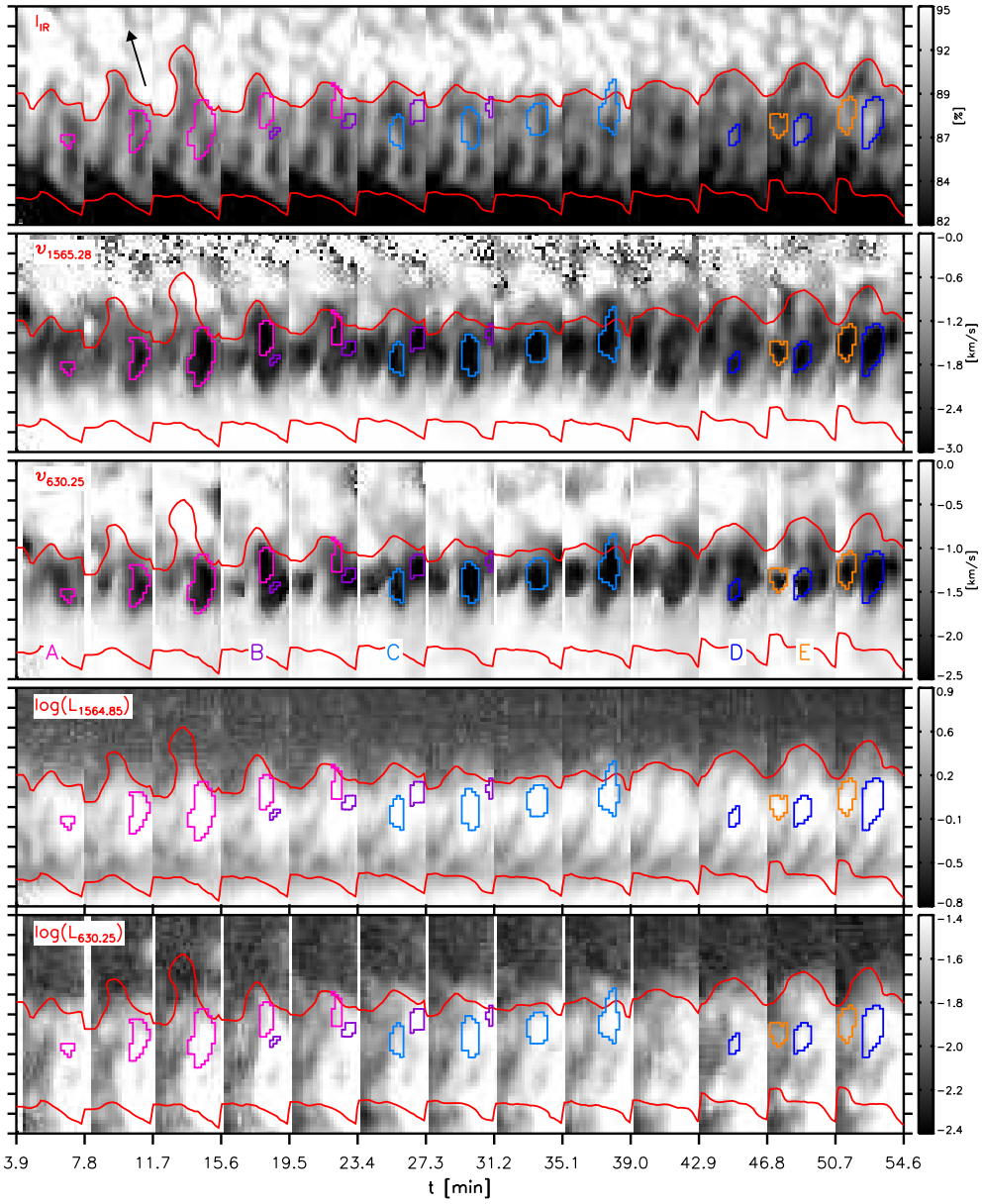

FIGURE 7.1:— Time evolution of line parameters in the center-side penumbra of AR 10781. From *top* to *bottom*: Continuum intensity at 1565 nm, Stokes V zero-crossing velocity of Fe I 1565.28 nm and Fe I 630.25 nm, logarithm of the total linear polarization of Fe I 1564.85 nm and Fe I 630.25 nm. Color contours outline the ECs. The letters at the bottom of the third panel label each EC. Red lines indicate the inner and outer penumbral boundaries. Each tickmark in the y-axis represent $1''$. The arrow marks the direction to disk center. $t = 0$ min corresponds to June 30, 8:47 UT.

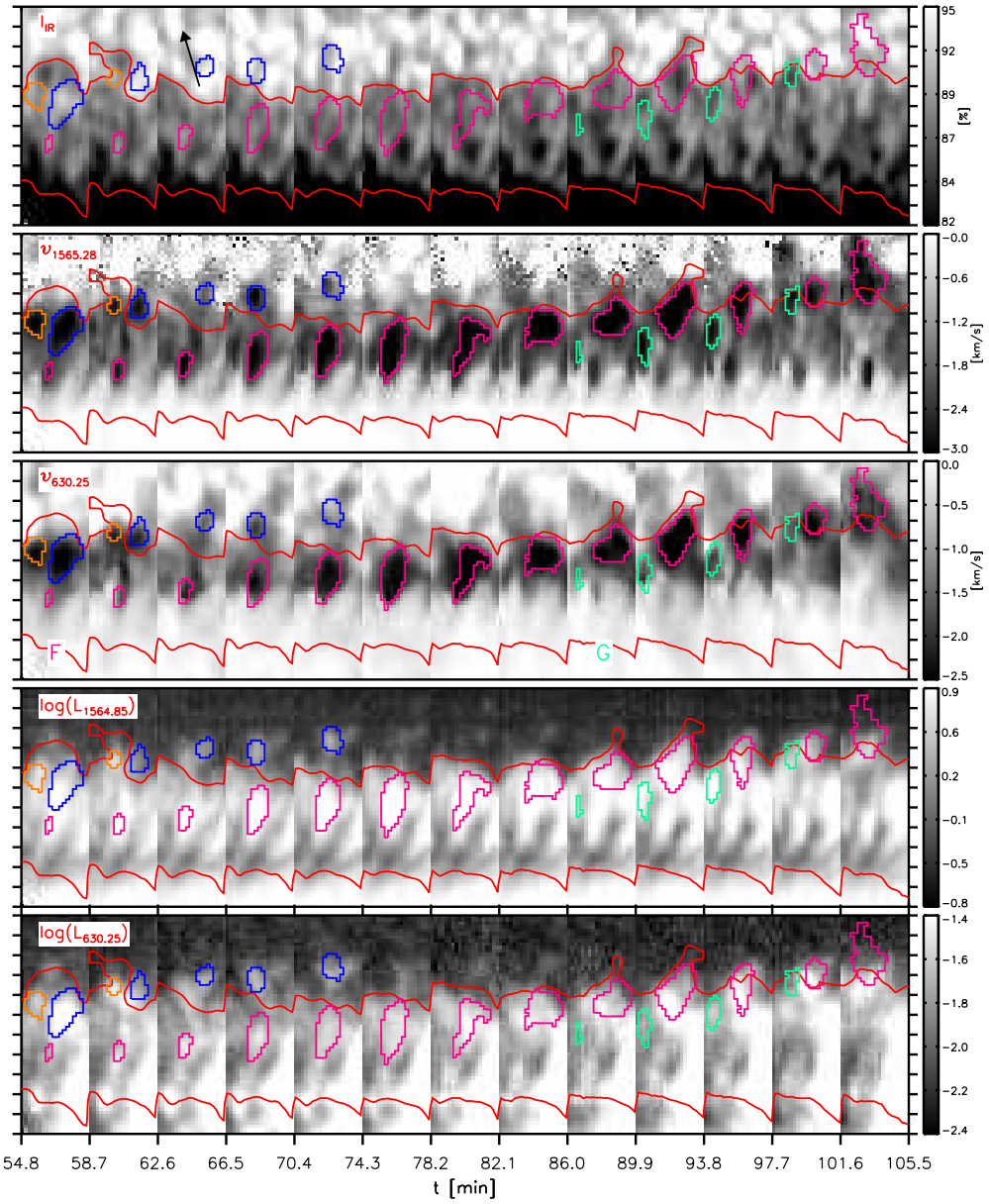

FIGURE 7.2:— Same as Fig. 7.1, from $t = 54.8$ to $t = 105.5$ min.

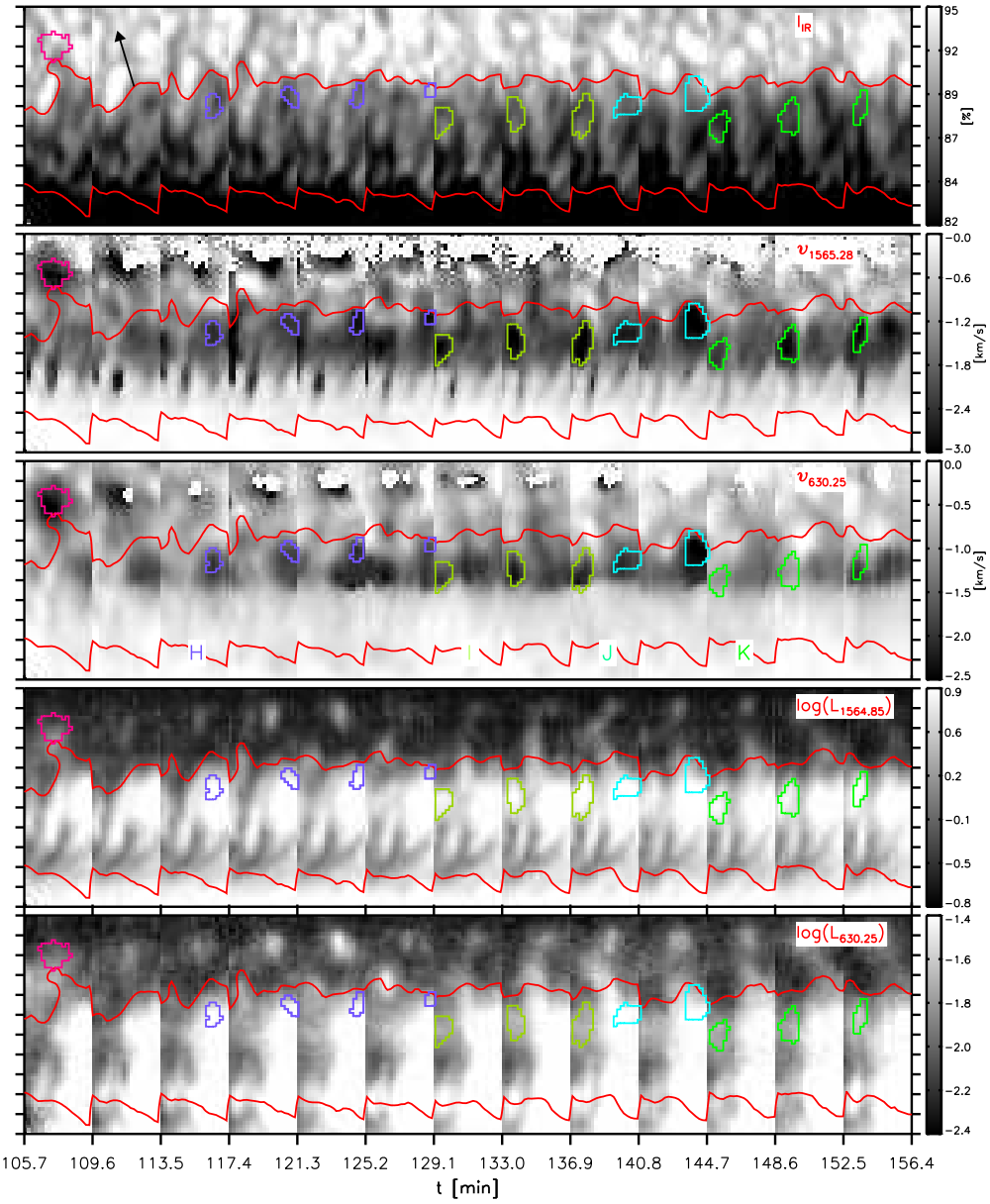

FIGURE 7.3:— Same as Fig. 7.1, from $t = 105.7$ to $t = 156.4$ min.

TABLE 7.1:— Phenomenological properties of the observed ECs. Each letter in the first column refers to an EC. ECs reaching the quiet photosphere are marked in bold face. Parentheses indicate ECs that go out or appear outside of the FOV. The date and time of appearance of each EC are specified in the second and third columns. The fourth column displays the radial distance at which the EC is seen for the first time. Only the values for the ECs that appear inside the FOV are given. The fifth column displays the time each EC stays inside the penumbra. The seventh column shows the propagation velocity, corrected for the viewing angle. The errors are the standard deviations in the determination of the proper motions. The last two columns display the maximum lengths and widths attained by each EC, corrected for projections effects. The last row gives the mean values of the quantities.

EC	Date	$t_{\rm app}$ [min]	$r_{\rm app}$	τ [min]	Filament	$v_{\rm prop}$ [km s^{-1}]	$\mathcal{L}$ [km]	$\mathcal{W}$ [km]
A	06/30	3.9	0.4	15.6	2	2.7 ± 0.5	2700	1000
(B)	06/30	15.6	0.5		2	2.9 ± 0.0	500	400
C	06/30	23.4	0.4	11.7	2	2.2 ± 0.7	2600	800
D	06/30	42.9	0.5	11.9	2	3.3 ± 0.3	2300	900
E	06/30	46.8	0.5	11.9	1	3.1 ± 0.4	1700	800
F	06/30	54.8	0.4	39.0	2	1.7 ± 0.1	3000	1200
G	06/30	86.0	0.6	11.7	1	3.7 ± 0.8	1700	500
(H)	06/30	113.5	0.7		3	1.7 ± 0.0	1000	500
(I)	06/30	129.1			1	1.5 ± 0.4	2000	800
J	06/30	136.9	0.7	3.9	3	3.5 ± 0.0	1500	800
K	06/30	144.7	0.5	7.8	1	2.1 ± 0.6	1700	800
(L)	07/01	5.9	0.7			2.2 ± 0.8	1200	600
M	07/01	9.9	0.7	7.9		4.2 ± 0.6	1800	800
(**N**)	07/01	23.8				2.0 ± 0.2	1200	500
(O)	07/01	61.6	0.8			1.4 ± 0.5	1100	600
Mean			**0.6**	**13.5**		**2.6**	**1700**	**700**

define a radial scale. The borders of the penumbra vary with time, so we have chosen to calculate their temporal average. This allow us to define the mean penumbral radial distance, hereafter r, as the normalized distance from the inner ($r = 0$) to the outer ($r = 1$) average edges of the penumbra.

Table 7.1 summarizes some phenomenological properties of the observed ECs. The radial distances where they appear, $r_{\rm app}$, vary from 0.4 to 0.7 with an average of 0.6. Their lifetimes, τ, inside the penumbra range from 3.9 min to 39 min with an average of 13.5 min[2]. It is important to note that ECs can be classified in two different groups: (a) ECs that suddenly disappear at the outer penumbra, hereafter type I; and (b) ECs which are seen to reach the quiet

[2] τ is only calculated for the ECs that do not go out of the FOV

photosphere and enter the moat (D, F, M, and N), type II in the following. Most of the ECs belong to the first group. The evolution of type II ECs outside the spot will be studied in detail in Chapters 10 and 11.

The propagation velocities of the ECs inside the penumbra, corrected for the viewing angle, range from 1.4 km s^{-1} to 4.2 km s^{-1} with an average of 2.6 km s^{-1} (seventh column of Table 7.1). These velocities are in rough agreement with the range of values found by previous investigators (Shine et al. 1994; Rimmele 1994; Georgakilas & Christopoulou 2003). To compute the propagation velocity of each EC we have fitted straight lines to the positions of its upper edge (the farthest one from the umbra) as a function of time (see the left and central panels of Fig. 7.4). The slopes of these lines give the apparent propagation velocities of the ECs along the line of symmetry[3] (LS) and its perpendicular direction. Due to projection effects the distances are contracted along the LS in our maps. Hence, if one wants to calculate the real proper motions, the velocity along the LS must be corrected for LOS effects. In order to apply this correction, we assume that the proper motions of ECs are horizontal to the solar surface[4]. In this case, the real velocity along the LS is the apparent velocity divided by the cosine of the heliocentric angle. Thus, the modulus of the proper motion is given by the velocities along the LS, corrected for projection effects, and along the perpendicular direction. We note that if the ECs have non-purely horizontal motions their vertical components must be small. Otherwise they would go out of the line forming region in a few minutes[5].

In our observations, most ECs appear as elongated structures along the radial direction, and their sizes usually increase as they migrate outwards (see, e.g., Figs. 7.1-7.3). To quantify the typical sizes of the ECs we define a major and a minor axis for each one. The major axis is the segment connecting the edges of the EC along its longer direction. The minor axis is perpendicular to the major axis and passes through its midpoint. An example is shown in the right panel of Fig 7.4. We compute the length, $\mathcal{L}$, and width, $\mathcal{W}$, of the ECs along these two axes, and correct them for projection effects. The maximum length of the ECs ranges from 500 km to 3000 km with an average of 1700 km, while the maximum width ranges from 400 km to 1200 km with an average of

[3]The line of symmetry is the projection of the LOS onto the solar surface. In the case of sunspots, it coincides with the line connecting the sunspot center and the disk center.

[4]In our images we only see the apparent motions of the ECs. The real direction of these motions is unknown. If one wants to correct them for LOS effects, a given geometry must be assumed.

[5]The thickness of the photosphere is considered to be around 500 km. If the vertical motions were greater than 600 m/s, the ECs would cross the entire photosphere departing from the bottom in less than their mean lifetime ($\sim$ 13.5 min).

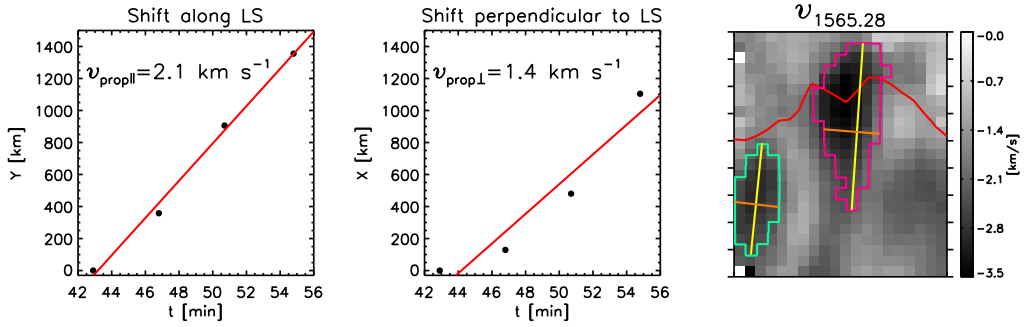

FIGURE 7.4:— Position of EC D along (left panel) and perpendicular (center panel) to the LS. The slopes of the red lines give the propagation velocities along the two axes. The green and pink contours in the right panel outline ECs F and G, respectively. The yellow and orange lines represent the lengths and widths of the two ECs.

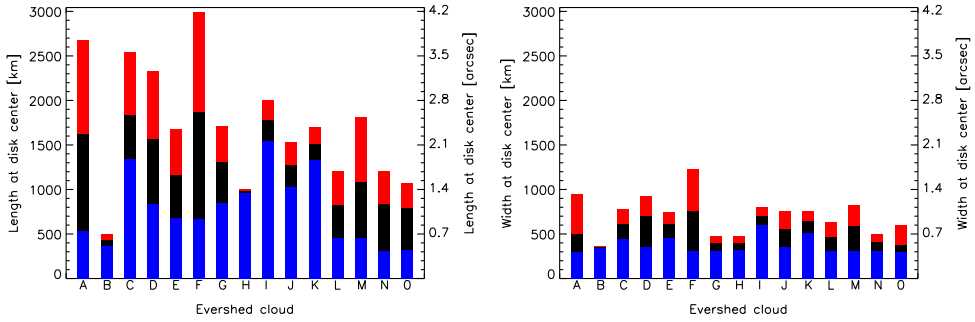

FIGURE 7.5:— Maximum (red), averaged (black), and minimum (blue) lengths (*left*) and widths (*right*) of the ECs, corrected for projection effects.

700 km (cf. the two last columns of Table 7.1). Note that for these computations we only use the ECs which are not partially outside the FOV. In Fig. 7.5 we show histograms of the the maximum (red), minimum (blue), and averaged (black) sizes along the major and minor axes for each EC. This figure also demonstrates that the lengths are usually greater than the widths.

Shine et al. (1994) described the ECs as cloud-like structures with size roughly 1000 km in length and a radial spacing of about 2000 km between subsequent ECs. Our lengths are slightly larger than those of Shine et al. (1994)[6], while the typical separation between two consecutive ECs is around 500 km in our observations (cf. second panels of Fig. 7.1 at $t = 15.6$ min and Fig. 7.2 at $t = 54.8$ min).

[6]These authors do not specify if they report maximum, mean, or minimum EC lengths

7.3 Relation with penumbral filaments

The second, third, and fourth panels of Figs. 7.1–7.3 demonstrate that ECs move outward following penumbral filaments with larger values of the LOS velocity and total linear polarization than their surroundings. At least three different penumbral filaments can be distinguished in the June 30 data set[7]. One of them is visible in the middle of the maps during the whole time sequence. The other two are partially outside of the FOV. We label the left-side, center, and right-side filaments as #1, #2, and #3, respectively. Hereafter we will call these structures *flow filaments*[8]. The sixth column of Table 7.1 identifies the filament along which each EC is seen to propagate outwards.

Figure 7.6 blows up the velocity and polarization maps of the penumbra at $t = 93.8$ min. The flow filaments have been outlined with contours of different colors which enclose areas of increased LOS velocity and linear polarization. The various panels display Doppler velocities (v), total linear polarizations (L), and total circular polarizations (V), along with their ratio L/V. As can be seen, the filaments show up as structures with enhanced v, L, and L/V, and their contrast is much higher in the quantities inferred from the infrared lines. They exhibit larger circular polarization signals than their surroundings in Fe I 1564.85 nm, but smaller signals in Fe I 630.25 nm.

In Fig. 7.7 the total linear polarization of Fe I 1564.85 nm and Doppler velocities of Fe I 1565.28 nm are shown as a function of time for the maps where EC A is seen to propagate inside the penumbra. Pink and yellow contours outline EC A and filament #2 respectively. While the shape of the filament changes with time, it always remains visible from the inner to the outer penumbral boundary. We note that the pixels with larger values of the linear polarization (marked with orange contours) coincide with the positions of EC A. Even if the cloud does not show up in the velocity maps ($t = 0$ min), there is an enhancement of L associated with the pixels where one would locate it. The illustrated behavior is also observed in the rest of the ECs. Hence, in addition to higher LOS velocities, ECs display larger linear polarization signals than the filaments where they are seen to migrate outwards.

The polarization signals provide a rough estimate of the magnetic field inclination under some restrictive assumptions: if the lines are fully split and the

[7] For the July 1 dataset, the small size of the maps ($2''$) and poorer seeing conditions do not allow us to clearly identify the structure of the penumbral filaments.

[8] Observations of sunspot penumbrae at very high spatial resolution (Scharmer et al. 2002) find filamentary structures narrower than 100 km ($\sim 0\farcs1$). Hence, it is appropriate to consider that the penumbral filaments seen in our observations (at a resolution of $\sim 0\farcs6$) are a collection of unresolved individual Evershed channels. For this reason we call them flow filaments.

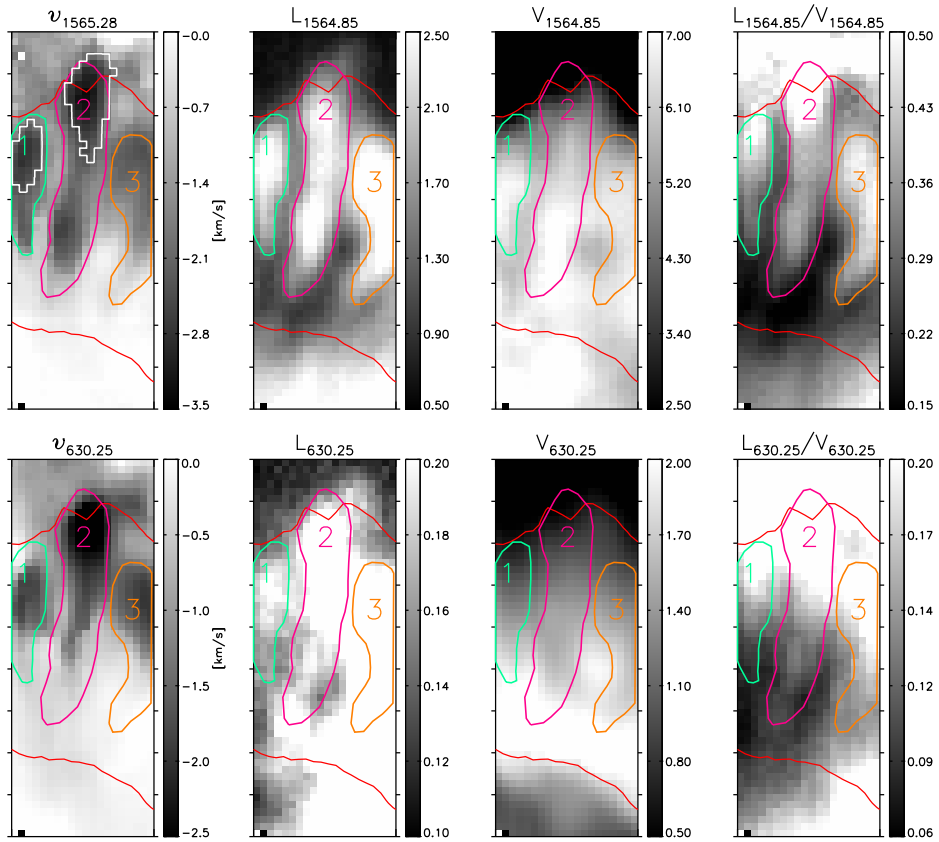

FIGURE 7.6:— From *left* to *right*: Maps of Stokes V zero-crossing velocity for Fe I 1565.28 nm (top) and Fe I 630.25 nm (bottom), total linear polarization, total circular polarization, and L/V ratio for Fe I 1564.85 nm (top) and Fe I 630.25 nm (bottom) at $t = 93.8$ min. Color contours mark, and numbers label, the three different flow filaments. White contours outline ECs F and G.

orientation of the magnetic field remains constant along the LOS, then a higher inclination to the LOS implies larger L and smaller V signals, i.e., larger L/V ratios. Thus, Fig. 7.6 suggest that the flow filaments have more inclined magnetic fields than their surroundings, while Fig. 7.7 could indicate that the ECs are the most inclined structures inside them. However, the different behavior of the observables (in particular Stokes V) emphasizes the need of inversions for a proper interpretation of the measurements. Stokes inversions will allow us to decide whether flow filaments and ECs are indeed structures harboring more inclined fields than their environs (Chapters 8 and 9).

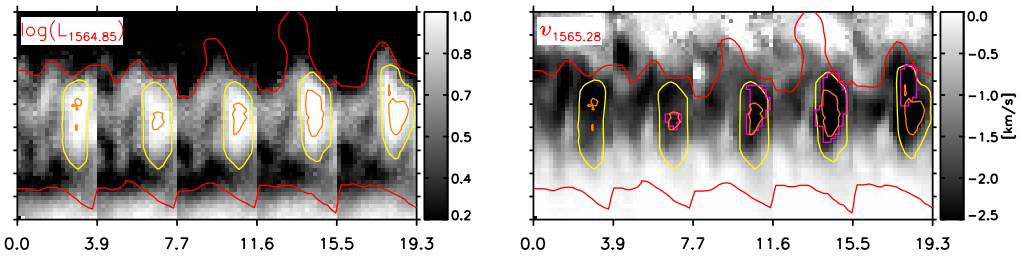

FIGURE 7.7:— Maps of the logarithm of the total linear polarization of Fe I 1564.85 nm (*left*) and Stokes V zero-crossing velocity of Fe I 1565.28 nm (*right*) as a function of time. Each tick in the y-axis represents $1''$. Yellow and pink contours mark filament #2 and EC A respectively. Orange contours outline pixels with $\log(L_{1564.85}) > 1$.

7.4 Periodicity

As mentioned in Sect. 7.1, the Evershed flow displays variations on time scales of 8–25 min. The quasi-periodic behavior is produced by ECs moving radially outwards along flow filaments. The periodic times scales of 15 min are associated with the appearance (Shine et al. 1994) or appearance/disappearance (Rimmele 1994) of ECs in isolated filaments. A precise estimation of the frequency of this repetitive behavior requires a Fourier analysis of the data sets. This implies the selection of spatial paths which accurately follow the direction of the filaments in each map. Looking at Figs. 7.1–7.3, it is obvious that the orientation of the filaments changes with time. Hence, one should carefully select different paths for each map, otherwise the power spectrum will be contaminated with information from spatial points outside the filament and will show artificial peaks. We consider it very difficult to properly select paths tracing a single filament during the whole sequence, so we do not attempt this kind of analysis. However, a visual inspection of the observations already provides valuable information about the periodic appearance of ECs.

In Figs. 7.1 and 7.2 one can observe a repetitive behavior associated with the appearance of ECs along filament #2. Its time scale is about 15 min. A cycle begins with EC A at $t = 3.9$ min. This EC arrives at the penumbral border around 15 minutes later. At that moment, another EC appears in the mid-penumbra (EC B) and a new cycle begins. After EC B reaches the outer penumbral edge, EC C appears and another cycle starts. New cycles take place in the filament with ECs D and F. This behavior is irregular and does not happen during the whole time sequence. For filament #1 the periodic time scale seems to be of the order of 40 min. This is the time gap between the appearances of ECs E, G, and I (third column of Table 7.1). Filament #3

TABLE 7.2:— Maximum Doppler shifts, linear-to-circular polarization ratios, and Stokes V asymmetries attained by each EC. The second and third columns are the unsigned blueshifts of Fe I 1564.85 nm and Fe I 630.25 nm. The fourth and fifth columns display the ratios of total linear and circular polarization of Fe I 1564.85 nm and Fe I 630.25 nm. The last two columns are the area asymmetries of Fe I 1564.85 nm and Fe I 630.25 nm. The errors represent the standard deviation of the individual parameters within each EC. The mean values of the observational parameters for the June 30 and July 1 data sets are marked in bold face.

EC	$\lvert v_{1564.85}\rvert$ [km s^{-1}]	$\lvert v_{630.25}\rvert$ [km s^{-1}]	$(L/V)_{1564.85}$	$(L/V)_{630.25}$	$\delta A_{1564.85}$ [%]	$\delta A_{630.25}$ [%]
A	3.3 ± 0.3	2.4 ± 0.2	0.44 ± 0.02	0.19 ± 0.03	5.9 ± 2.0	2.4 ± 2.3
B	3.4 ± 0.3	2.5 ± 0.3	0.50 ± 0.05	0.27 ± 0.02	7.3 ± 3.2	7.7 ± 1.8
C	3.2 ± 0.3	2.6 ± 0.3	0.45 ± 0.03	0.20 ± 0.03	6.9 ± 1.7	4.2 ± 3.3
D	3.2 ± 0.5	2.4 ± 0.5	0.44 ± 0.07	0.22 ± 0.04	5.8 ± 2.4	5.1 ± 2.8
E	3.1 ± 0.3	2.1 ± 0.4	0.44 ± 0.06	0.27 ± 0.02	5.3 ± 1.9	7.0 ± 3.7
F	3.4 ± 0.5	2.5 ± 0.4	0.56 ± 0.14	0.29 ± 0.05	6.5 ± 2.4	9.6 ± 6.5
G	3.0 ± 0.3	1.5 ± 0.1	0.55 ± 0.05	0.27 ± 0.03	9.1 ± 3.7	10.1 ± 1.6
H	3.1 ± 0.2	1.9 ± 0.3	0.49 ± 0.02	0.24 ± 0.01	6.1 ± 1.7	5.8 ± 2.5
I	3.1 ± 0.2	1.9 ± 0.2	0.36 ± 0.04	0.14 ± 0.02	3.6 ± 1.3	-2.4 ± 1.3
J	3.2 ± 0.3	2.3 ± 0.3	0.49 ± 0.02	0.24 ± 0.01	5.5 ± 2.6	1.7 ± 2.5
K	3.1 ± 0.2	1.5 ± 0.4	0.41 ± 0.05	0.16 ± 0.02	3.2 ± 1.5	-3.2 ± 2.3
Mean	**3.2**	**2.2**	**0.47**	**0.22**	**5.9**	**4.4**
L	2.1 ± 0.1	1.4 ± 0.1	0.87 ± 0.07	0.37 ± 0.03	4.7 ± 1.0	-2.1 ± 1.1
M	2.2 ± 0.1	1.5 ± 0.1	0.83 ± 0.06	0.41 ± 0.04	5.5 ± 1.4	4.7 ± 3.4
N	2.1 ± 0.2	1.2 ± 0.2	0.83 ± 0.08	0.38 ± 0.03	5.9 ± 2.5	6.9 ± 4.7
O	1.9 ± 0.3	1.0 ± 0.1	0.69 ± 0.02	0.31 ± 0.02	5.4 ± 2.7	3.3 ± 1.8
Mean	**2.1**	**1.3**	**0.81**	**0.37**	**5.4**	**3.2**

is visible during the second half of the sequence. Only two ECs are seen to follow this filament, and the time between their appearances is around 23 min. Our observations suggest the existence of different time scales associated with different filaments. Longer time series mapping larger regions of the penumbra are required to confirm or discard this possibility.

7.5 Observational properties of ECs

In this Section we determine the typical Doppler velocities, L/V ratios, and Stokes V asymmetries associated with ECs. To simplify the analysis, a single value of the parameters is calculated for each EC as follows. We first compute mean values of the line parameters within the EC in the different maps where

it is observed, and then take the maximum.

Table 7.2 shows the results for the spectral lines with higher sensitivity to magnetic fields (Fe I 1564.85 nm and Fe I 630.25 nm). The maximum unsigned blueshifts are about 3.2 km s^{-1} and 2.2 km s^{-1} for Fe I 1564.85 nm and Fe I 630.25 nm in the June 30 time sequence, and 2.1 km s^{-1} and 1.3 km s^{-1} in the 1 July data set. These velocities are lower than the values reported by Shine et al. (1994) and Rimmele (1994). The reason is that we calculate an average over a group of pixels, while they use velocities from individual pixels.

The mean ratios of total linear and circular polarization are of the order of 0.47 and 0.22 in Fe I 1564.85 nm and Fe I 630.25 nm for the June 30 observations, and around 0.81 and 0.37 for the July 1 data set. That is, ECs show much larger linear polarization signals in the infrared, as compared with their circular polarization signals. Thus, it is advantageous to use infrared lines to detect ECs with vector magnetographs.

The Stokes V area asymmetry of Fe I 1564.85 nm, $\delta A_{1564.85}$, amounts to 5.9% on June 30 and 5.4% on July 1, while $\delta A_{630.25}$ is around 4.4% and 3.2% on June 30 and July 1, respectively. For some ECs, the Fe I 630.25 nm area asymmetry is of the order of its standard deviation, suggesting that $\delta A_{630.25}$ has a strong dependence on radial distance.

The large variations of the Doppler shifts and L/V ratios of the ECs as observed on two consecutive days are consistent with the idea that the flow and magnetic field are almost horizontal to the solar surface. The sunspot was nearer to disk center on July 1. If the velocity and magnetic field vectors are horizontal to the solar surface, their projections to the LOS cause smaller blueshifts, larger linear polarization signals, and smaller circular polarization signals (i.e., larger L/V ratios) as the spot approaches the disk center. This explains why the velocities are higher on June 30 while the L/V ratios are larger on July 1.

7.6 Comparison of observables inside of ECs and flow filaments

In a sunspot penumbra, the physical properties are known to vary radially from the umbra to the outer penumbral boundary. For this reason, we compare the observational properties of the pixels inside the ECs with the rest of penumbral points inside the flow filaments as follows. We calculate the mean line parameters at each penumbral radial distance for the pixels inside the ECs and divide them by the mean parameters of the rest of points inside the flow filaments which are at the same radial distance. This calculation is done for each map

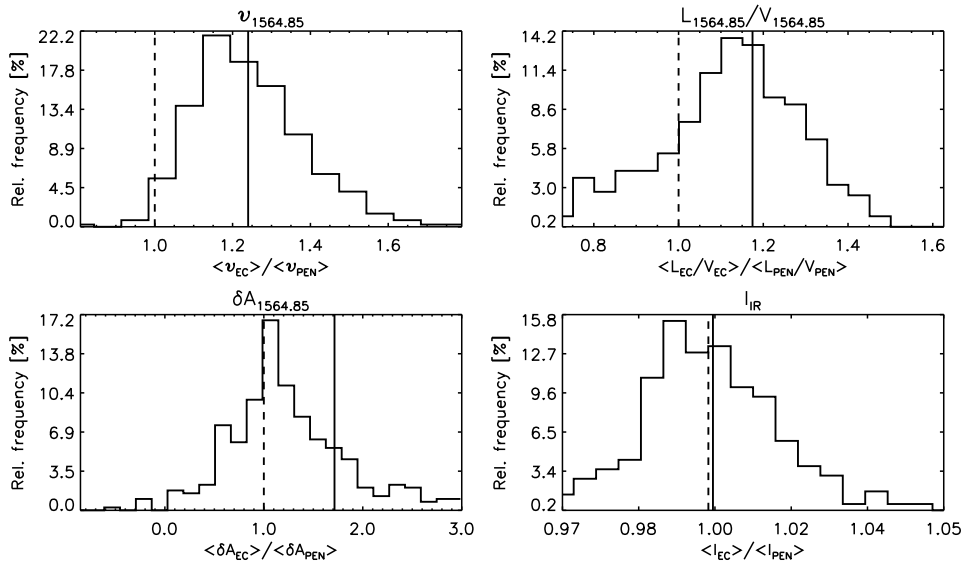

FIGURE 7.8:— Normalized distributions of the ratio of Doppler velocities (v), linear-to-circular polarization signals (L/V), Stokes V asymmetries (δA), and continuum intensities (I) of the ECs and the rest of penumbral points of the flow filaments located at the same radial distance. The line parameters are derived from Fe I 1564.85 nm. The vertical solid lines represent the mean of the distributions. The histograms display the results for the June 30 data set.

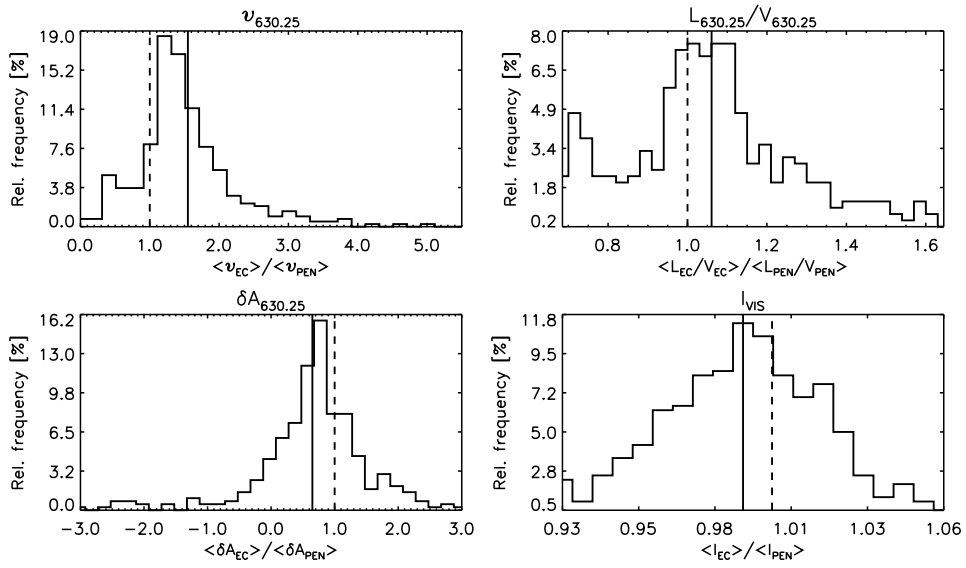

FIGURE 7.9:— Same as Fig. 7.8 for Fe I 630.25 nm.

separately. Figures 7.8 and 7.9 show histograms with the results of this analysis for the Fe I 1564.8 nm and Fe I 630.25 nm lines observed on June 30. The results for the July 1 data set are equivalent (not shown).

Interestingly, ECs exhibit larger LOS velocities and L/V ratios than the penumbral filaments in both Fe I 630.25 nm and Fe I 1564.85 nm. For fully split lines, the greater the L/V ratio, the higher the field inclination to the LOS. Hence, our observations suggest that ECs possess the most inclined magnetic fields of the penumbra. But only with inversions of all four Stokes profiles can one obtain precise estimates of the magnetic field inclination in the local reference frame. In Chapters **??** we will study the magnetic configuration resulting from the inversion of the observed lines.

ECs also show larger Fe I 1564.85 nm area asymmetries than the flow filaments. This might be the result of larger gradients of the physical quantities along the LOS and/or enhanced visibility of some magnetic components of the penumbra in the ECs as compared with the rest of penumbral points. By contrast, $\delta A_{630.25}$ is smaller than the filaments average inside the ECs. This opposite behavior is surprising and could be due to the different heights of formation of the two spectral lines.

The relation between ECs and continuum intensity is not well established in the literature. Shine et al. (1994) and Rouppe van der Voort (2003) report that ECs are mainly correlated with locally bright continuum features, while Rimmele (1994) and Georgakilas & Christopoulou (2003) do not find any correlation. Just by visual inspection of the observations it is difficult to discriminate if ECs are bright or dark continuum features. In the intensity histogram of Fig. 7.9, the ECs seem to show a preference for locally dark continuum intensities at 630 nm. A similar trend is observed in the continuum at 1565 nm (Fig. 7.8), but less pronounced. The reason is the stronger dependence of the continuum intensity on temperature in the visible (Cabrera Solana et al. 2005), which leads to higher continuum contrasts compared with the IR. These results have to be taken with caution because of the existence of unresolved structures at the angular resolution of our observations ($\sim 0.6'' - 0.7''$). In Fig. 7.10 we display cospatial maps of speckle-reconstructed DOT G-band intensity, continuum intensity at 630 nm, and continuum intensity at 1565 nm. The DOT and VTT observations are not strictly cotemporal, but the differences are small enough ($\sim$ 30 s) to work with both data sets simultaneously. The figure demonstrates that what we detect as dark/bright features in the spectropolarimetric data are indeed a mixture of both in the G-band filtergrams. As the ECs migrate outwards, the dark/bright features inside them change, but in general the G-band intensities are locally darker at the position of the ECs. This emphasizes the need of spectropolarimetric observations at

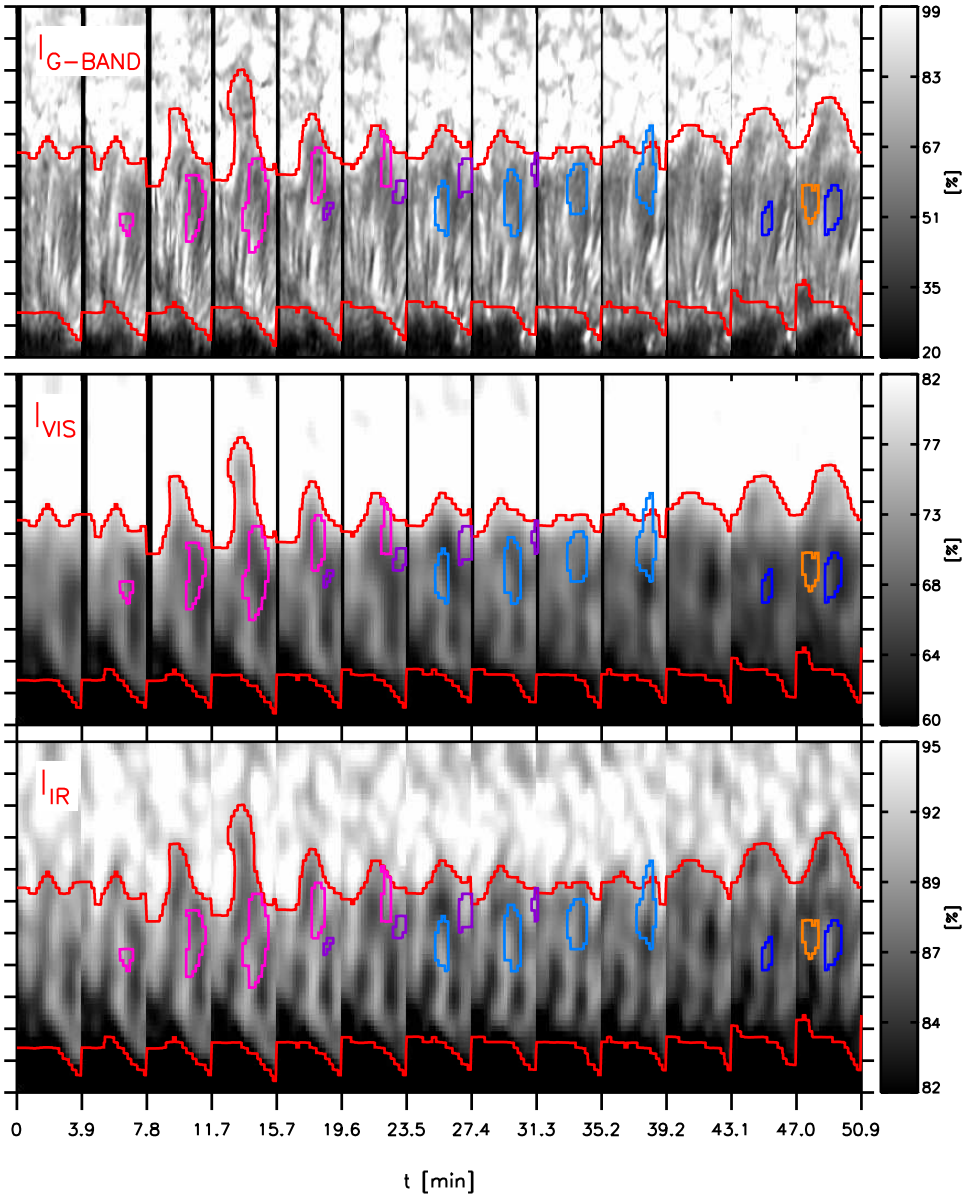

FIGURE 7.10:— From *top* to *bottom*: Cospatial speckle-reconstructed G-band filtergrams, continuum intensity maps at 630 nm, and continuum intensity maps at 1565 nm. Color contours outline the ECs.

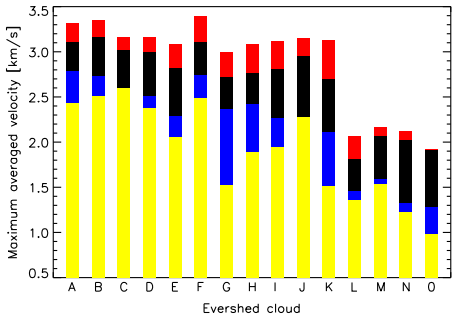

FIGURE 7.11:— Maximum Doppler velocities of the observed ECs as derived from the Stokes V zero-crossing wavelengths. *Red* represent maximum blueshifts for Fe I 1564.85 nm, *black* for Fe I 1565.28 nm, *blue* for Ti I 630.38 nm, and *yellow* for Fe I 630.25 nm. Note that the blueshifts are unsigned.

even higher spatial resolution.

Finally, we note that the histograms of Figs. 7.8 and 7.9 provide information about the average line parameters of the ECs independently of their position in the penumbra. These properties can change with radial distance. For example, Schlichenmaier et al. (2005) have suggested that flow filaments link bright and dark continuum features at different radial distances. As described in Sect. 7.3, ECs move along flow filaments. Hence, we may expect that ECs are associated with locally bright features in the inner penumbra and locally dark structures in the outer penumbra. This conjecture will be examined in detail in Sect. 7.9.

7.7 Dependence of LOS velocities on height

The magnitude of the Doppler velocity depends on the spectral line chosen to calculate it (cf. the first two columns of Table 7.2). Figure 7.11 shows the maximum unsigned Doppler velocities[9] of the ECs inferred from each spectral line. There we see that the velocities indicated by the infrared lines are the largest ones. The IR lines of the set are formed deeper than the others. This implies that the Evershed flow is more conspicuous in deep atmospheric layers, in agreement with previous findings (Westendorp Plaza et al. 2001a; Mathew et al. 2003; Bellot Rubio et al. 2006). The different velocities inferred from the different spectral lines may be the result of (a) a change of the modulus of the velocity vector with height; (b) a change of the inclination of the velocity vector with height; or (c) a combination of both effects. In any case, the lower the height of formation, the higher the Doppler velocities derived from the spectral line. Thus, infrared lines are advantageous for observational studies of Evershed clouds.

[9]The maximum velocities are calculated in the same way as in Sect. 7.5.

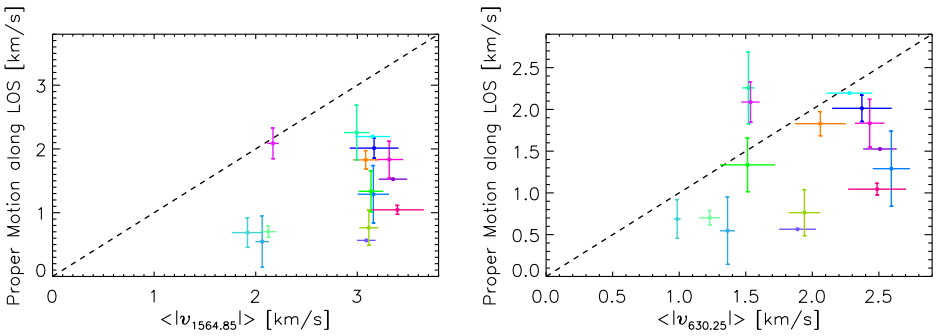

FIGURE 7.12:— Proper motions along the LOS vs maximum LOS velocities from Fe I 1565.28 nm (*left*) and Fe I 630.25 nm (*right*) for the different ECs. Circles represent the maximum average LOS velocities. The horizontal bars represent its standard deviations. The vertical bars are the errors in the determination of proper motions.

7.8 Proper motions vs Doppler velocities

In this Section we compare the projections of the proper motions of the ECs along the LOS[10], calculated as the proper motions along the LS multiplied by the sine of the heliocentric angle, with their maximum Doppler velocities. If the blueshifts associated with ECs in the center-side penumbra were produced by proper motions, then both quantities should be similar in magnitude.

Figure 7.12 plots the LOS projection of the propagation velocities of the ECs vs the maximum LOS velocities inferred from Fe I 1564.85 nm and Fe I 630.25 nm. The horizontal bars indicate the standard deviation of the Doppler velocities within each contour, and the vertical bars the errors in the determination of propagation velocities. The observed LOS velocities are systematically higher than the LOS component of the proper motion. Although this result could indicate that the Evershed flow cannot only be the manifestation of the radial propagation of ECs across the penumbra, we note that these differences could be explained in terms of the unresolved magnetic structure of the penumbra and the presence of small vertical motions.

7.9 Evolution of line parameters with radial distance

In Sect. 7.5 we compared the values of the line parameters inside the ECs with the rest of penumbral points inside the flow channels. This comparison allowed us to characterize the main observational properties of the ECs. Here we study

[10] As discussed in Sect. 7.2, the proper motions of the ECs are assumed to be horizontal to the solar surface.

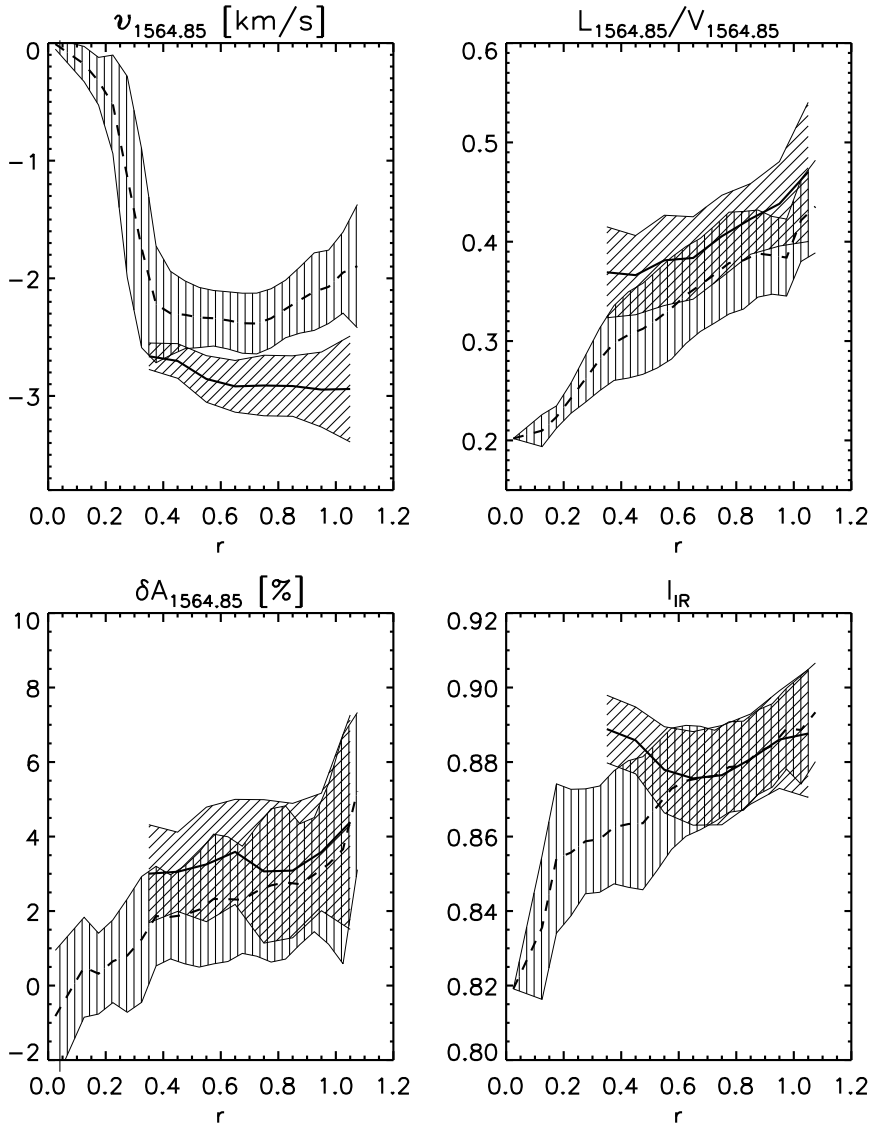

FIGURE 7.13:— Averaged Stokes V zero-crossing velocity, ratio of the total linear and circular polarization, area asymmetry, and continuum intensity of Fe I 1564.85 nm (*top*) for the pixels inside the ECs (solid line) and the rest of penumbral points (dashed line) as a function of its radial distance for the time sequence observed on 30 June 2005. Shaded areas indicate the standard deviations around the mean value.

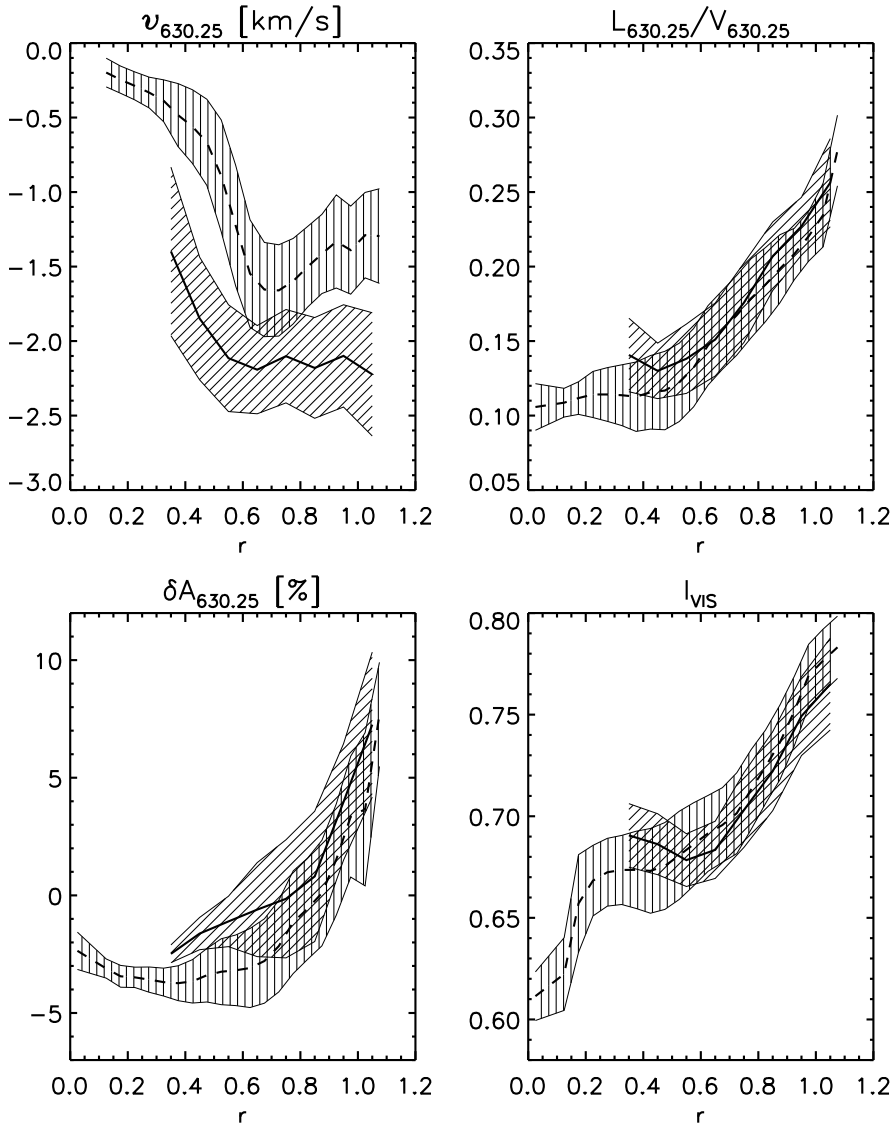

FIGURE 7.14:— Same as Fig. 7.13 for the quantities inferred from Fe I 630.25 nm.

the evolution of these parameters with radial distance. To that aim, we average the line parameters of the pixels inside the ECs which are at the same radial distance, and construct a curve of their variation with r. We note that those curves represent the average evolution of the ECs inside the penumbra. In order to compare the EC behavior with the flow filaments, we do the same calculation for the pixels inside the filaments excepting those of the ECs.

Figures 7.13 and 7.14 show the results for the pixels inside the ECs (solid lines) and the filaments (dashed lines) for Fe I 1564.85 nm and Fe I 630.25 nm, respectively. As can be seen, the Doppler velocities are greater inside the ECs at all radial distances. Also interesting is the different shape of the velocity curves. The velocity always increases within the ECs as they migrate outward, from $v_{630.25} = -1.8$ km s^{-1} and $v_{1564.85} = -2.8$ km s^{-1} at $r = 0.5$ to $v_{630.25} = -2.2$ km s^{-1} and $v_{1564.85} = -3.0$ km s^{-1} at $r = 1$. In the filaments, however, the velocity slightly decreases from $r \sim 0.6$ outward.

The ratio of linear-to-circular polarization is also larger inside the ECs at all radial distances which is more obvious for the IR line. Moreover, both the ECs and the flow channels display larger L/V values at larger radial distances. For the ECs, the L/V ratio increases from $(L/V)_{630.25} = 0.14$ at $r = 0.5$ and $(L/V)_{1564.85} = 0.38$ up to $(L/V)_{630.25} = 0.24$ and $(L/V)_{1564.85} = 0.47$ at $r = 1$.

The area asymmetry δA of the two lines also increases monotonically with radial distance, showing larger values within the ECs than in filaments. The area asymmetries change from $\delta A_{630.25} = -1.5\%$ and $\delta A_{1564.85} = 4.5\%$ at $r = 0.5$ to $\delta A_{630.25} = 6.2\%$ and $\delta A_{1564.85} = 7.2\%$ at $r = 1$.

The continuum intensity curves display an interesting evolution with radial distance. Both $I_{\rm IR}$ and $I_{\rm VIS}$ are greater than the filaments average inside the ECs at the radial distances where they appear ($r \sim 0.4$). From the middle to the outer penumbra, $I_{\rm IR}$ does not exhibit significantly different values than the flow filaments while $I_{\rm VIS}$ is smaller inside the ECs. In the outer penumbra, the continuum intensities at 630 nm are smaller inside the ECs[11]. That is, ECs are associated with locally brighter continuum features in the inner penumbra and locally darker features from the middle to the outer penumbra. Taking into account that ECs propagate along flow filaments, our observations confirm the results of Schlichenmaier et al. (2005), who described cases of flow filaments linking bright and dark features located at increasing radial distances.

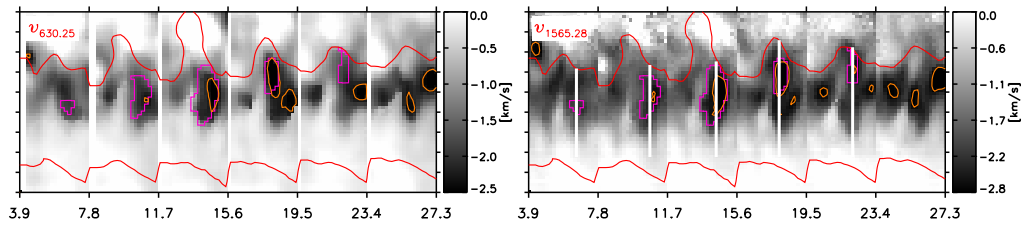

FIGURE 7.15:— Maps of Stokes V zero-crossing velocity of Fe I 630.25 nm (*left*) and Fe I 1565.28 nm (*right*) as a function of time. Pink contours mark EC A. Orange contours enclose pixels with $v_{630.25}$ and $v_{1565.28}$ lower than -2.3 km s^{-1} and -2.7 km s^{-1} , respectively. The vertical lines mark a radial cut passing through the EC. Each tick in the y-axis represents 1″.

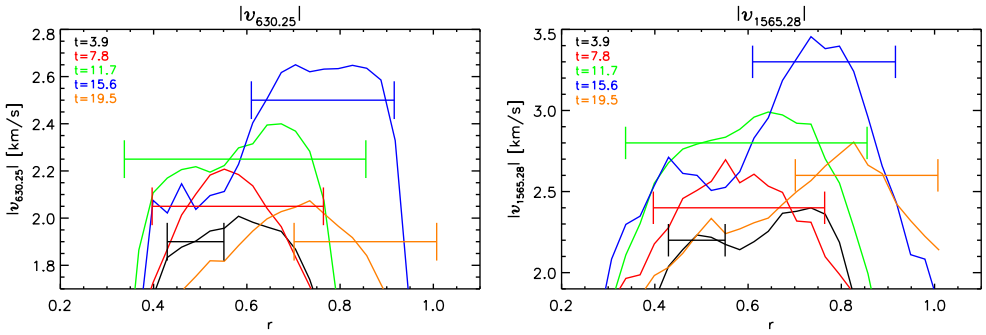

FIGURE 7.16:— Variation of $|v_{630.25}|$ and $|v_{1565.28}|$ along the radial cuts shown in Fig. 7.15. The colors indicate different times and the horizontal lines mark the upper and lower edges of EC A.

7.10 Disappearance of ECs at the outer penumbral boundary

Most of the Type I ECs suddenly disappear in the sequence observed on 30 June[12]. This indicates that the time employed by the ECs to disappear is usually shorter than the temporal resolution of the observations[13] (> 7.8 min). There is, however, an interesting case in which a type I EC is seen to vanish.

Figure 7.15 shows the evolution of the unsigned LOS velocities of EC A derived from Fe I 630.25 nm (*left*) and Fe I 1565.28 nm (*left*) until it disappears. As can be seen, since $t = 23.4$ min there is no sign of the EC in the positions

[11]The differences are smaller than the standard deviations of the distributions but the behavior persists all over the penumbra.

[12]The small size of the maps of the data set observed on 1 July does not allow us to observe how the type I ECs disappear.

[13]For this reason the process of disappearance of the ECs is not reflected in Figs. 7.13 and 7.14.

where one would expect to find it. In order to quantify the evolution of the velocities inside the EC, we choose radial cuts going from the inner to the outer penumbral boundary passing through the middle of the EC in each map. These cuts are indicated by the vertical solid lines in the right panel of Fig. 7.15. The variation of the LOS velocities along these cuts is shown in Fig. 7.16. Colors indicate different times and the horizontal lines mark the upper and lower edges of the EC. In agreement with the behavior displayed by Figs. 7.13 and Figs. 7.14, the EC velocities increase with radial distance until $t = 15.6$ min. Then, there is a strong drop in the velocities at $t = 19.5$ min after which the EC is no longer seen. This behavior is also observed for EC C and must be general for type I ECs.

7.11 Summary and conclusions

We have presented, for first time, a detailed description of the temporal evolution of the Evershed flow including its polarization signatures. The main findings of the observational description given in this chapter can be summarized as follows:

1. We identify fifteen ECs that appear in the mid penumbra. They propagate with speeds $v_{\rm prop} \sim 2.6$ km s^{-1} along penumbral filaments (i.e. flow channels) characterized by larger values of the linear polarization, linear-to-circular polarization ratios, and LOS velocities than their surroundings.

2. ECs can be classified in two types: (a) ECs that disappear in the outer penumbra (type I); and (b) ECs that cross the visible border of the spot and enter into the moat (type II). Most of the observed ECs belong to the type I.

3. EC motions are mainly radial to the sunspot.

4. ECs have greater lengths ($\sim$ 1700 km) than widths ($\sim$ 700 km) inside the penumbra, and their sizes increase as they migrate outward.

5. Our observations suggest the existence of different time scales associated with the appearance of the ECs in the filaments. We find periodic behaviors of the order of 15 min and 40 min in two different filaments.

6. ECs display larger Doppler velocities and L/V ratios in the infrared lines of the set. This implies that: (a) ECs are more conspicuous in deeper atmospheric layers; and (b) the use of infrared lines would be advantageous to detect ECs in vector magnetograms.

7. ECs possess greater Doppler velocities, L/V ratios, and area asymmetries than the filaments where they are seen to migrate outwards. This might imply that the magnetic and dynamic configuration of the penumbral filaments are modified by the ECs as they propagate along them. Assuming that the velocity and magnetic field vectors are aligned (Bellot Rubio et al. 2003), the enhancement of LOS velocity displayed by the ECs can only be produced by an increment in the modulus of the velocity vector.

8. The LOS velocities of the ECs are larger when the sunspot is farther from disk center, while their L/V ratios are smaller. These results are consistent with the idea that the flow and the magnetic field are almost horizontal to the solar surface.

9. ECs are locally brighter in the inner penumbra and locally darker from the middle through the outer penumbra. Taking into account that the ECs propagate along flow filaments, our findings confirm the results of Schlichenmaier et al. (2005) who described flow filaments linking locally bright and dark features (**teniendo en cuenta que ahora comparamos los pixeles de las ECs con los de los filamentos esto se me hace un poco confuso**).

10. The Doppler velocities of the ECs are systematically greater than the LOS projection of their proper motions, assumed horizontal to the solar surface.

11. The blueshifts, linear-to-circular polarization ratios, and area asymmetries of the ECs increase with the radial distance. In the rest of the penumbra L/V and δA display the same behavior, while the velocity decreases from the middle to the outer penumbra.

12. The disappearance time scales of type I ECs are usually faster than the temporal resolution of the observations (< 7.8 min).

The line parameters derived from the polarization profiles give us valuable information about the phenomenological properties of the ECs. In fact, some unexpected properties have been revealed. The problem with these observational parameters is that their interpretation in terms of physical quantities is not straightforward. For example, a greater value of the linear-to-circular polarization ratio can be associated with a more inclined magnetic field to the LOS, but one does not know the exact value of the inclination.

A proper interpretation of the observations requires the knowledge of the atmospheric parameters. These parameters can only be retrieved by means of

simultaneous inversions of all the four Stokes parameters. We will describe in detail the results of these inversions in the next chapters.

8

One-component view of the EC phenomenon

8.1 Introduction

The physical conditions of the solar atmosphere leave clear signatures on the shapes of the Stokes profiles. In the previous chapter we used simple observational parameters derived from the spectral lines in order estimate the physical conditions of ECs. The implications of those findings can only be fully understood in terms of their atmospheric parameters. The most accurate way to retrieve the physical quantities is by means of inversions of the observed Stokes spectra (see reviews by del Toro Iniesta & Ruiz Cobo 1996; del Toro Iniesta 2003a; Socas-Navarro 2001; Bellot Rubio 2006)

In this chapter we present the first investigation, to our knowledge, of the time evolution of the physical properties of the Evershed flow. As demonstrated in Chapter 6, the simultaneous inversion of visible and infrared spectral lines improves the determination of the atmospheric parameters. For this reason, to derive the thermal, magnetic, and dynamic configuration we perform simultaneous inversions of full vector spectropolarimetric observations of four visible and three infrared lines. This allows us to derive the conditions of the solar atmosphere where the spectral lines are formed. In this way, we shed some light on the possible nature of ECs and verify the indications suggested by the observational parameters.

The semiempirical models employed in the inversion process are briefly described in Sect. 8.2. The quality of the fits is discussed in Sect. 8.3. Sections 8.4

and 8.6 are devoted to characterize the physical properties of the ECs and their variation with radial distance. Next, we describe the uncombed structure of the penumbral filaments where the ECs are seen (Sect. 8.5). Section 8.7 investigates the variation of the magnetic and dynamical configuration of these penumbral filaments as the ECs propagate along them. A comparison of the flow velocity and tube speed inferred from the inversion is performed in Sect. 8.8. Section 8.9 is devoted to compare the physical quantities retrieved from the inversions with the line parameters derived in the previous chapter. Finally, our main results are summarized in Sect. 8.10.

8.2 One magnetic component model

We derive the thermal, magnetic, and dynamical configuration of the various structures in the FOV by means of simultaneous inversions of the visible and IR lines showed in Table 4.1. The Stokes profiles have been inverted using the SIR code (see Sect. 5.4).

The model atmosphere adopted as initial guess depends on the pixel inverted. To simplify the interpretation of the results, one-component atmospheres are used in the analysis of the penumbra (see Table. 8.1). According to current views, sunspot penumbrae are formed by at least two magnetic components with different field inclinations (Bellot Rubio et al. 2004; Borrero et al. 2005). Hence, the physical quantities retrieved from our inversions would represent some kind of average of the various magnetic atmospheres coexisting in the resolution element, i.e., they provide information about the global structure of the penumbra.

In order to modify the temperature gradient of the initial guess atmosphere we allow the temperature to vary with height (Table 8.1). As mentioned in Chapter 7, visible and IR lines display different Doppler velocities. Hence, if one wants to fit simultaneously the profiles of the IR and VIS lines a gradient of LOS velocity has to be assumed. In contrast, the vector magnetic field is supposed to be constant along the atmosphere. This implies that the inversion provides a mean value of the magnetic configuration for each resolution element (Ruiz Cobo & del Toro Iniesta 1994). The inversion also returns macro and microturbulence velocities, modelling the presence of unresolved motions. The effects of both the spectrograph PSFs (as given in Sect. 4.6.2) and the macroturbulence are taken into account by the inversions. As the amount of instrumental and atmospheric stray light contamination is expected to depend on wavelength, the inversion code determines these contributions separately for each spectral range. In this way, the Stokes profiles emerging from the pixel

TABLE 8.1:— Number of nodes employed for perturbating the atmospheres used in the inversion. The nodes of the physical quantities for the magnetic and non-magnetic atmospheres are given in the second and third columns, respectively. −1 indicates that both atmospheres share the same value of the physical quantity.

Parameter	Magnetic [Nodes]	Non-magnetic [Nodes]
temperature	3	1
velocity	2	1
field strength	1	0
inclination	1	0
azimuth	1	0
microturbulence	1	1
macroturbulence	1	−1
stray light	2	−1
filling factor	1	−1

are:

$$\boldsymbol{I} = (1-\alpha)\boldsymbol{I}_{\rm m} + \alpha\boldsymbol{I}_{\rm stray}, \tag{8.1}$$

where α is the amount of stray light, $\boldsymbol{I}_{\rm stray}$ is the average quiet Sun intensity profile representing the stray light contribution, and $\boldsymbol{I}_{\rm m}$ is the Stokes vector emerging from the magnetized atmosphere.

The adjacent moat is assumed to be filled with two atmospheric components, one of them magnetic and the other non-magnetic. The free parameters for the magnetic atmosphere are the same as before, while for the non-magnetic component only the temperature and velocity are allowed to vary (Table 8.1). In this case the emergent Stokes profiles arise as the combination of three different contributions:

$$\boldsymbol{I} = (1-\alpha)[f\boldsymbol{I}_{\rm m} + (1-f)\boldsymbol{I}_{\rm nm}] + \alpha\boldsymbol{I}_{\rm stray}, \tag{8.2}$$

where f is the filling factor of the magnetic component (i.e. the fraction of the pixel filled by the magnetic atmosphere) and $\boldsymbol{I}_{\rm nm}$ is the profile emerging from the non-magnetic component. We note that in this case $\boldsymbol{I}_{\rm stray}$ may represent a second non-magnetic component inside the resolution element with fixed atmospheric conditions.

We only invert pixels with normal two-lobed Stokes V profiles with amplitudes greater than 0.2% and 0.5% for visible and IR lines, respectively, resulting in 64160 and 30288 pixels on 30 June and 1 July. We refrain from analyzing irregular Stokes V profiles because they can only be modeled with more than one

magnetic component or/and atmospheres harboring strong vertical gradients of the physical quantities.

8.3 Quality of the fits

In Figs. 8.1 and 8.2 we display examples of the fits for a pixel of EC G inside (t = 93.8 min; $r \sim 0.8$) and outside (t = 101.6 min; $r \sim 1.7$) the penumbra, respectively. Taking into account the simple model assumed, the match between observed and synthetic profiles is reasonably good in both spectral ranges. The success of the fit is remarkable because seven spectral lines, from very different wavelengths and observed with different instruments have been inverted simultaneously in a consistent way. Thus, the scenario adopted for the inversion seems appropriate to determine 'average' properties in the penumbra and the sunspot moat. This is in agreement with the results of Chapter 6 where we demonstrated that one-component inversions of IR and VIS lines provide similar values of the physical quantities.

8.4 Physical properties of ECs

The solution adopted for the vector magnetic field in the LRF and the atmospheric parameters inferred from the inversion of the Stokes profiles are shown in Figs. 8.3–8.5 for the time sequence observed on 30 June and in Figs C.3 and C.4 for the time sequence observed on 1 July. The first panel displays the magnetic field strength. The next two panels display the magnetic field inclination in the LRF and the temperature at $\log\tau = 0$, T. T is representative of the temperature in the deep layers of the photosphere where the continuum of the spectral lines is formed. The last two panels display the LOS velocity at $\log\tau = -0.5$, $v_{\rm LOS}$, and the difference between the unsigned velocity in two different layers, $\Delta v_{\rm LOS} = |v_{\rm LOS}(\log\tau = -0.5)| - |v_{\rm LOS}(\log\tau = 0)|$. This quantity is proportional to the gradient of velocity with height.

The vector magnetic field displays the typical behavior observed in sunspots: it is weaker and more horizontal as the radial distance increases. It does not drop to zero outside the visible borders of the spot, which is the signature of the sunspot magnetic canopy (Solanki et al. 1994; Westendorp Plaza et al. 2001b; Rezaei et al. 2006). The ECs are visible as coherent structures with increased LOS velocity and field inclination. The presence of many MMFs in the surroundings of the spot is obvious in the first panel (see the arrows plotted in Fig. 8.5). Their origin and nature will be discussed in Chapter 10.

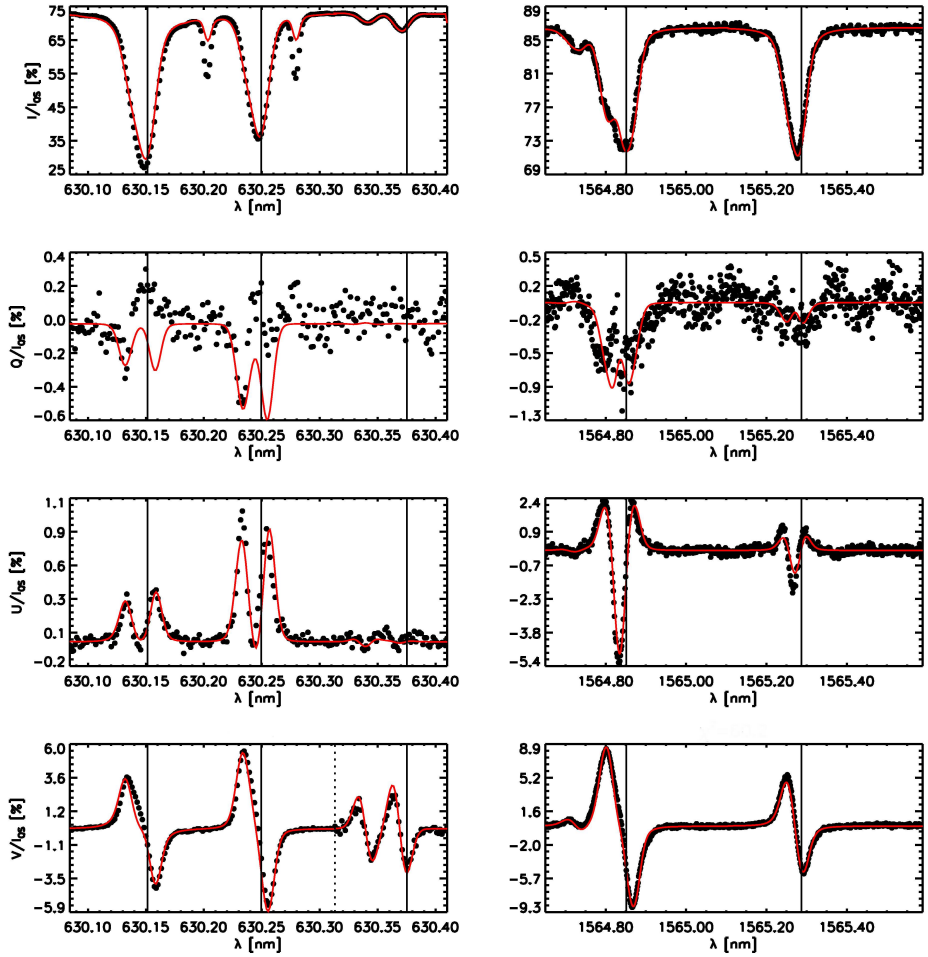

FIGURE 8.1:— Example of observed (dots) and best-fit (red lines) Stokes profiles for a pixel of EC G inside the penumbra ($r \sim 0.8$). Note that the O_2 telluric blends present in the visible spectra are not included in the inversion process. The vertical solid lines indicate the rest wavelengths of the lines. The Stokes V signal around Ti I 630.38 nm has been multiplied by six for better visibility (the vertical dotted line indicates where the spectral range around the titanium line starts). The merit function of the fit is $\chi^2 = 80.2$.

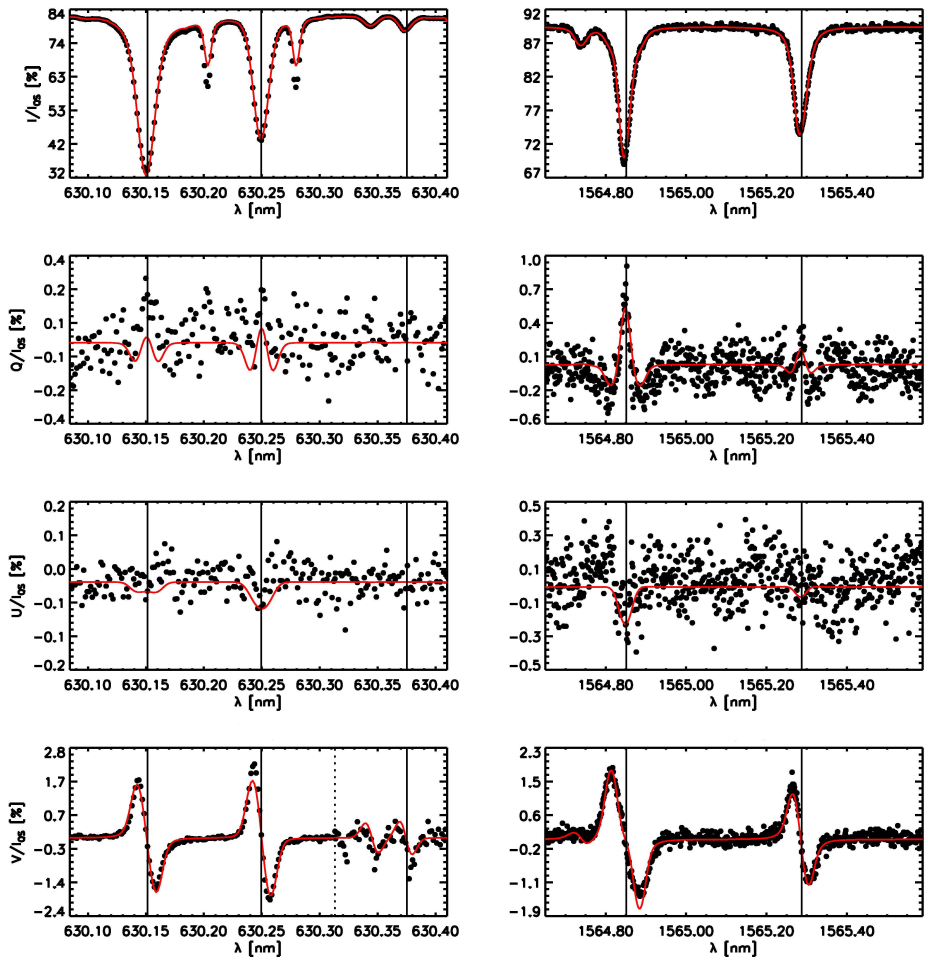

FIGURE 8.2:— Same as Fig. 8.1 for a pixel of EC G outside the penumbra ($r \sim 1.7$). The value of the merit function for this fit is $\chi^2 = 64.1$.

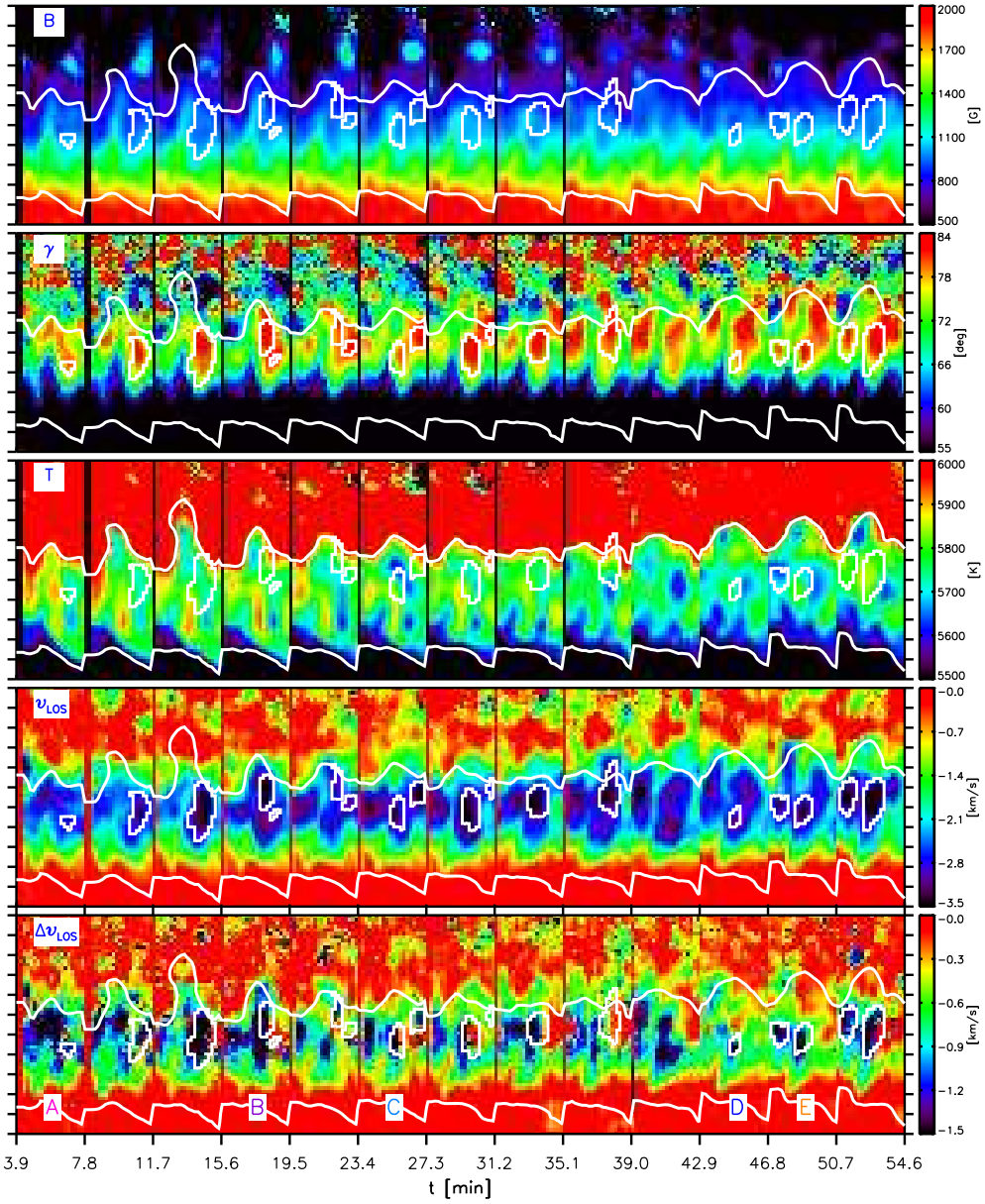

FIGURE 8.3:— From *top* to *bottom*: Magnetic field strength, magnetic field inclination, temperature at $\log\tau = 0$, LOS velocity at $\log\tau = -0.5$, and differences between the unsigned LOS velocities at $\log\tau = 0$ and $\log\tau = -0.5$. White contours outline the ECs and the inner and outer penumbral boundaries. The letters at the bottom of the last panel label each EC. Each tickmark in the y-axis represent $1''$. $t = 0$ min corresponds to June 30, 8:47 UT.

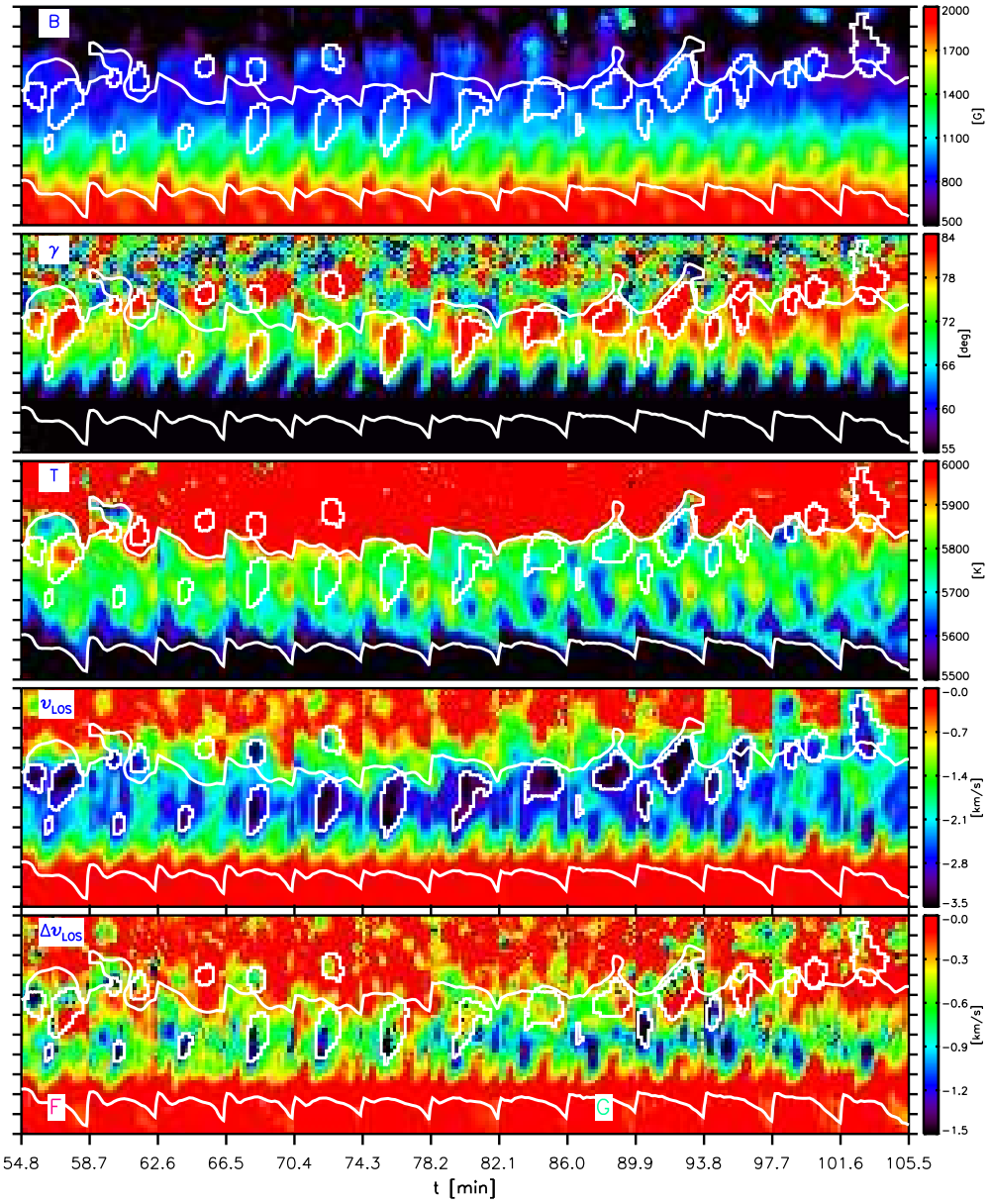

FIGURE 8.4:— Same as Fig. 8.3 from t=54.8 to t=105.5 min.

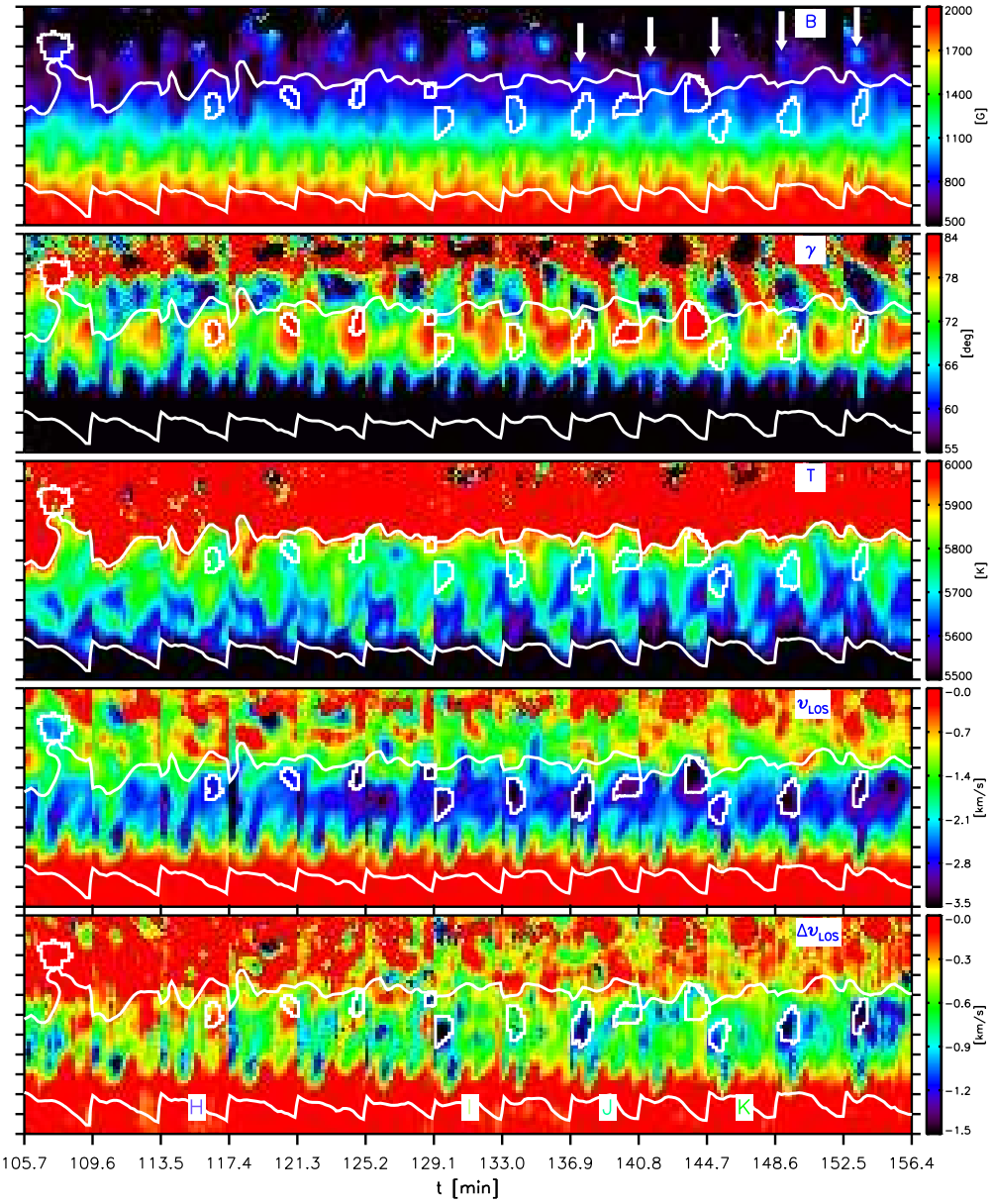

FIGURE 8.5:— Same as Fig. 8.4 from t=105.7 to t=156.4 min.

TABLE 8.2:— Physical properties of the observed ECs: magnetic field strength, magnetic field inclination in the LRF, modulus of the velocity vector at $\log\tau = -0.5$, and the difference between the modulus of velocity at $\log\tau = -0.5$ and $\log\tau = 0$. The errors represent the standard deviations of the physical parameters within each EC. The mean values of the physical quantities for 30 June and 1 July data sets are marked with bold face.

EC	B [G]	γ [deg]	$\lvert v\rvert$ [km/s]	$\Delta\lvert v\rvert$ [km/s]
A	1020 ± 20	81 ± 3	4.5 ± 0.4	-1.0 ± 0.6
B	1010 ± 20	83 ± 2	5.0 ± 0.5	-0.6 ± 0.4
C	1050 ± 60	80 ± 3	4.5 ± 0.3	-0.8 ± 0.6
D	1015 ± 50	82 ± 5	4.5 ± 0.8	-0.6 ± 0.6
E	976 ± 30	81 ± 3	4.2 ± 0.5	-1.1 ± 0.8
F	1068 ± 60	88 ± 5	4.8 ± 0.8	-0.4 ± 0.4
G	1013 ± 50	84 ± 2	4.2 ± 0.4	-0.6 ± 0.2
H	945 ± 40	83 ± 1	4.7 ± 0.3	-0.3 ± 0.2
I	998 ± 50	78 ± 4	4.1 ± 0.3	-1.0 ± 0.3
J	931 ± 40	83 ± 1	4.7 ± 0.3	-0.9 ± 0.3
K	1033 ± 40	79 ± 2	4.3 ± 0.3	-1.3 ± 0.1
Mean	**1005**	**82**	**4.5**	**-0.8**
L	1470 ± 20	60 ± 3	1.4 ± 0.5	-0.2 ± 0.1
M	1440 ± 70	73 ± 3	2.5 ± 0.5	-0.2 ± 0.1
N	1430 ± 110	77 ± 2	3.1 ± 0.4	-0.3 ± 0.1
O	1290 ± 30	75 ± 4	3.2 ± 0.2	-0.2 ± 0.1
Mean	**1408**	**71**	**2.6**	**-0.2**

Following the procedure described in Sect. 7.5, we calculate the maximum field strengths, field inclinations in the LRF, and LOS velocities at $\log\tau = -0.5$ attained by the ECs. Assuming that the velocity and magnetic field vectors are aligned, the modulus of the velocity at $\log(\tau) = -0.5$ is simply[1] $|v| = v_{\rm LOS}/\cos(\gamma_{\rm LOS})$. We also calculate the maximum value of the difference between the modulus of the velocity vector at $\log\tau = -0.5$ and $\log\tau = 0$ ($\Delta|v|$). The results are shown in Table 8.2.

The maximum field strength attained by the ECs ranges from 931 G to 1068 G with an average of 1005 G for the ECs observed on 30 June and from 1297 G to 1503 G with and average of 1412 G for the observed on 1 July.

In Sect. 7.5 we discussed the compatibility of the linear-to-circular polar-

[1]We note that the inclination is assumed constant along the atmosphere, while the LOS velocity is allowed to vary with height in the inversion process. For this reason, we use the LOS velocities at $\log\tau = -0.5$, obtaining the modulus of the velocity in that layer.

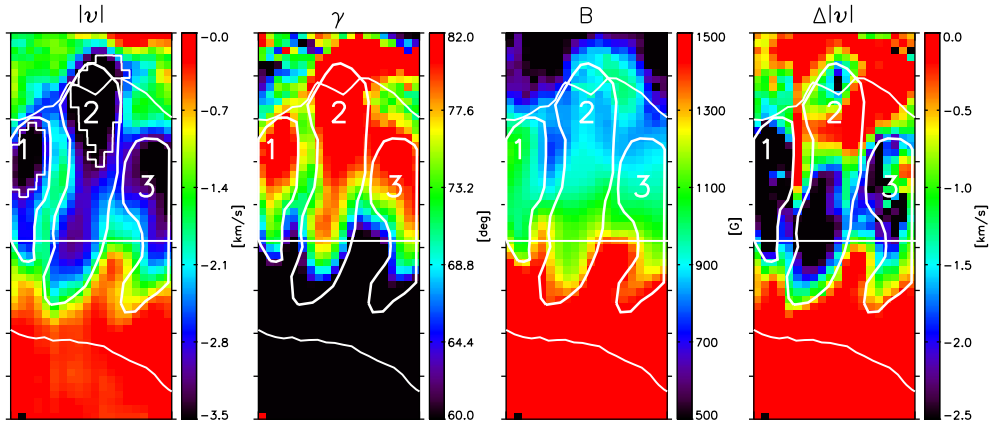

FIGURE 8.6:— From *left* to *right*: Maps of the modulus of the velocity vector at $log(\tau) = -0.5$, magnetic field inclination in the LRF, magnetic field strength, and $\Delta|v|$ at t = 93.8 min. The thin contours outline the ECs F and G and the penumbral borders. The thick contours delineate the three different penumbral filaments numbered accordingly. Horizontal white line outline a radial cut at $r = 0.5$.

ization ratios and LOS velocities with the scenario where the magnetic and velocity fields are nearly horizontal to the solar surface. Table 8.2 confirms the existence of very inclined magnetic fields inside the ECs. In fact, the field inclination is deduced to be of the order of 82° for the 30 June observations and 71° for the 1 July sequence.

Both $|v|$ and $\Delta|v|$ display higher values on 30 June (i.e. when the spot is farther from disk center). The values of $|v|$ are around 4.5 km s^{-1} and 2.6 km s^{-1} on 30 June and 1 July, while $\Delta|v|$ is about -0.8 km s^{-1}and -0.3 km s^{-1}on 30 June and 1 July, respectively. The changes in $|v|$ and $\Delta|v|$ cannot be explained by LOS effects. Thus, the properties of the spot seem to have varied between the two observations.

8.5 Relation between penumbral filaments and intra-spines

As discussed in the previous chapter, ECs move along filaments which possess larger values of the linear polarization, linear-to-circular polarization ratios, and LOS velocities than their surroundings (see Fig. 7.6). These filaments show up as inclined structures with large values of the LOS velocities in the second and fourth panels of Figs. 8.3–8.5. In Fig. 8.6 we plot the filaments at $t = 93.8$ min as seen in the modulus of the velocity, inclination, magnetic field strength, and $\Delta|v|$. Their properties are similar to those of the *intra-spines* reported by Lites et al. (1993). In these structures, the Evershed flow is more

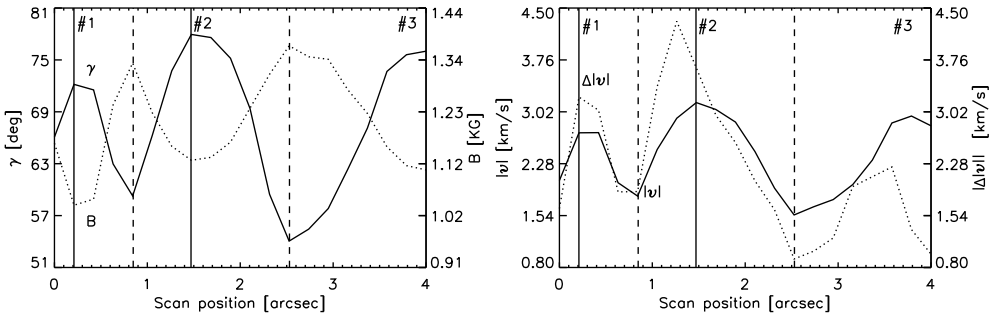

FIGURE 8.7:— *Left*: Variation of the field inclination in the LRF (solid line) and magnetic field strength (dotted line) as a function of the scan position for the radial cut showed in Fig. 8.6. *Right*: Variation of $|v|$ (solid line) and $\Delta|v|$ (dotted line) as a function of the scan position for the same horizontal cut. Vertical solid lines represent the positions of the penumbral filaments (i.e intra-spines) and vertical dashed lines indicate local minima of the inclination (i.e spines). Numbers label the three different flow filaments.

conspicuous (Stanchfield et al. 1997; Westendorp Plaza et al. 2001b) and the magnetic field is more inclined than in the *spines*. The radial evolution of the field strengths of the intra-spines leads to weaker fields than those displayed by the intra-spines in the inner penumbra and the opposite in the outer (cf. top left panel of Fig. 8.8). Remarkably, $\Delta|v|$ also displays greater values inside the intra-spines all the way from the inner to the outer penumbra. Both the spines and intra-spines alternate at a fixed radial distance along azimuthal paths. This organization of the velocity and magnetic fields is also called fluted (Title et al. 1993) or uncombed (Solanki & Montavon 1993) in the literature.

In Fig. 8.7 we plot the values of the atmospheric parameters along the radial cut marked by the horizontal white line in Fig. 8.6, at a normalized radial distance $r \sim 0.5$. As can be seen in the left panel, the positions where the magnetic field is more horizontal (intra-spines) coincide quite precisely with positions where the magnetic field is weaker. In contrast, both $|v|$ and $\Delta|v|$ reach their greatest values in the intra-spines.

8.6 Radial dependence of physical properties

The evolution with radial distance of the atmospheric parameters derived from the inversion is studied in this section. We calculate the curves of Figs. 8.8 and 8.9 in the same way as described in Sect. 7.9. The comparison of the of the physical properties of the ECs and the intra-spines gives the following results:

- The magnetic field strength of the ECs is weaker than the intra-spines

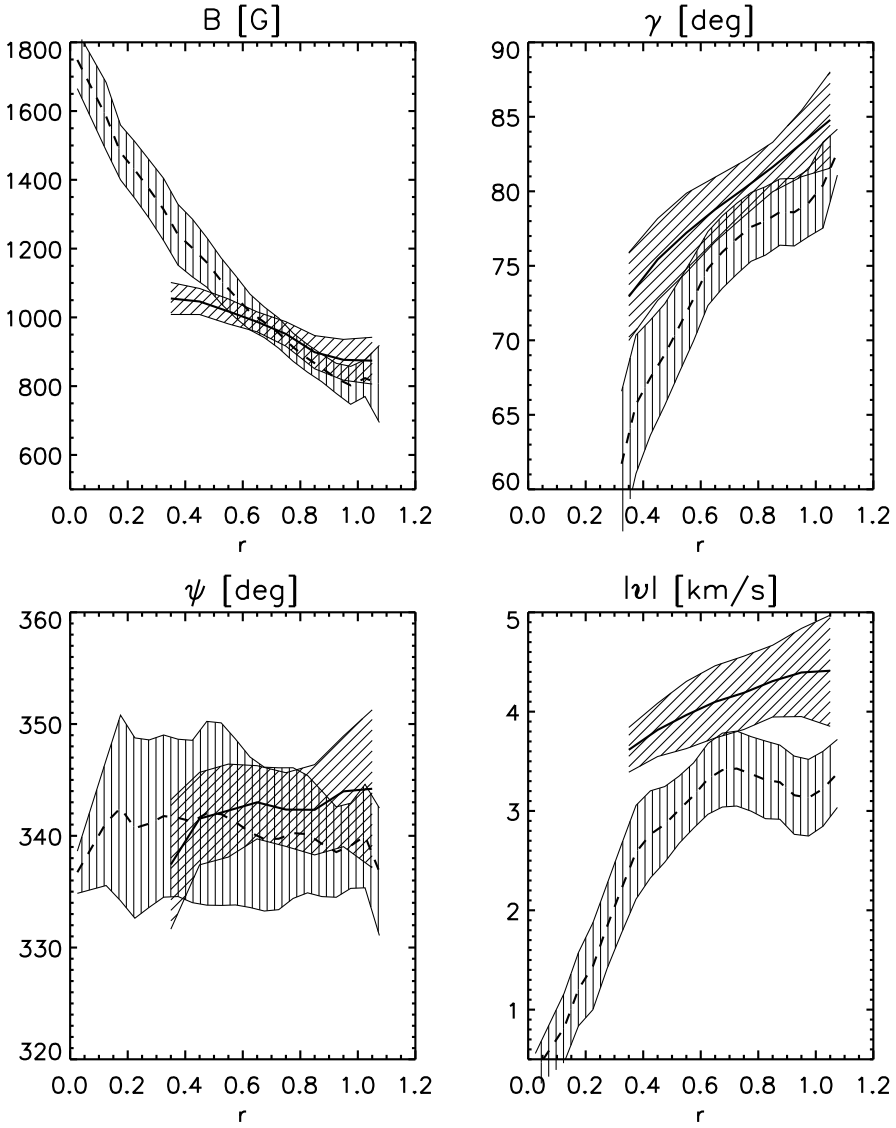

FIGURE 8.8:— Radial evolution of the magnetic field strength, inclination in the LRF, azimuth, and modulus of velocity for the ECs (solid line) and the rest of the penumbra (dashed line). The x-axis is the radial distance. Shaded areas outline the standard deviations.

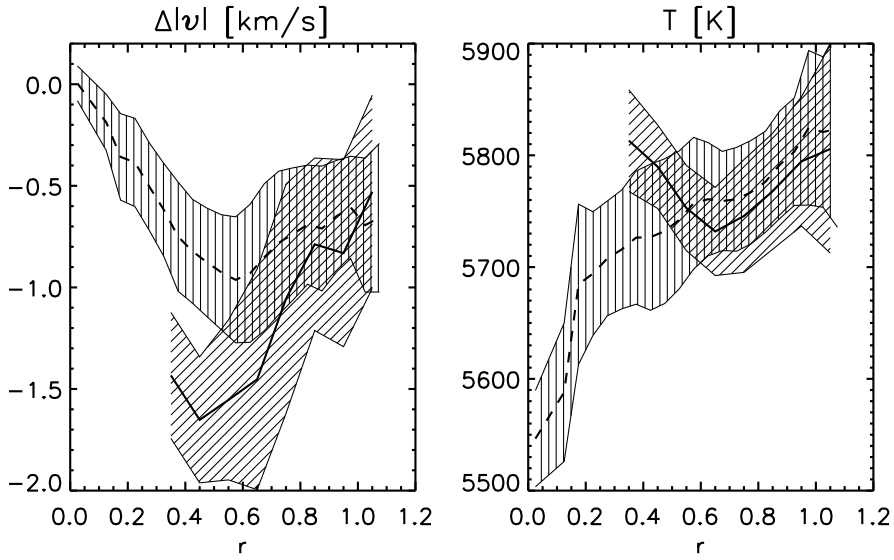

FIGURE 8.9:— Same as Fig. 8.15 for the variation of $\Delta|v|$ and T.

average from the inner to the mid penumbra, and stronger in the outer penumbra (upper left panel of Fig. 8.8).

- ECs harbor more inclined fields than the intra-spines at all radial distances (upper right panel of Fig. 8.8).
- The magnetic field azimuth of the ECs is oriented in the same direction than the azimuth of the intra-spines at all radial distances except in the outer penumbra (bottom left panel of Fig. 8.8).
- The modulus of the plasma velocity inside the ECs is greater than in the intra-spines at all radial distances (bottom right panel of Fig. 8.8).
- ECs display stronger gradients of velocity modulus than the intra-spines.
- ECs are hotter than the intra-spines in the inner penumbra and cooler from the mid to the outer penumbra.

In summary, we have demonstrated that the magnetic, dynamic, and thermal configuration of the ECs display rather different properties than those of the intra-spines.

8.7 ECs as perturbations propagating along intra-spines

In Section 7.3 we found that ECs exhibit greater linear polarization signals than the filaments where they propagate[2]. This suggests that they possess more inclined magnetic fields than the penumbral filaments in the LOS reference frame. If one assumes that the magnetic field and the velocity are parallel, an increment of the LOS inclinations would lead to a decrease in the corresponding LOS velocities. Hence, this observation seems to imply that the increase in LOS velocities associated with the ECs is produced by an increase in the modulus of the velocity vector, i.e., by a stronger Evershed flow. In this section we investigate the origin of the strong LOS velocities and linear polarizations of the ECs.

Figure 8.10 shows the LOS magnetic field inclinations and LOS velocities at $\log\tau = -0.5$ for the maps where EC A is seen to propagate outwards (top panels). EC A shows up as a coherent structure of enhanced $\gamma_{\rm LOS}$, implying that: (a) the strong linear polarization signal displayed by the EC in Fig. 7.7 can be ascribed to an increase of the field inclination to the LOS; and (b) the enhanced LOS velocities displayed by the EC can only result from an increase of the modulus of the velocity vector. To illustrate the origin of the increased LOS inclinations inside the ECs, in Fig. 8.11 we plot the observed and best-fit linear (i.e. $L(\lambda) = \sqrt{Q^2(\lambda) + U^2(\lambda)}$) and circular polarization profiles of Fe I 1564.85 nm emerging from a pixel before (#1) and during the passage (#2) of EC A (cf. the numbers in the top right panel of Fig. 8.10). As can be seen, the linear polarization profiles of #2 are greater than those displayed by #1. In contrast, their Stokes V profiles are comparable. This leads to greater linear-to-circular polarization ratios for #2 $[(L/V)_{1564.85} = 0.5]$ compared with #1 $[(L/V)_{1564.85} = 0.4]$ and, consequently, to more inclined fields in the LOS reference frame.

The bottom panels of Fig. 8.10 display γ and $|v|$. This figure explains the origin of the large values of $v_{\rm LOS}$ and $\gamma_{\rm LOS}$ inside the EC: *they are produced by an increase of the modulus of the velocity vector and more inclined magnetic fields*. Figure 8.12 quantify the variation of the atmospheric parameters along the radial cuts[3] showed in the right panels of Fig. 8.10 demonstrating that EC A possess the largest values of $\gamma_{\rm LOS}$, $v_{\rm LOS}$, γ, and $|v|$ of the entire filament. As the EC migrates outwards, these maxima increase their values and shift to larger radial distances until $t = 15.6$ min. At $t = 19.5$ min, i.e. the last map where the EC is seen, the values of the maxima are reduced. We note that the

[2] As an example, we illustrated this general behavior for EC A.

[3] These azimuthal cuts are coincident with those of Fig. 7.15

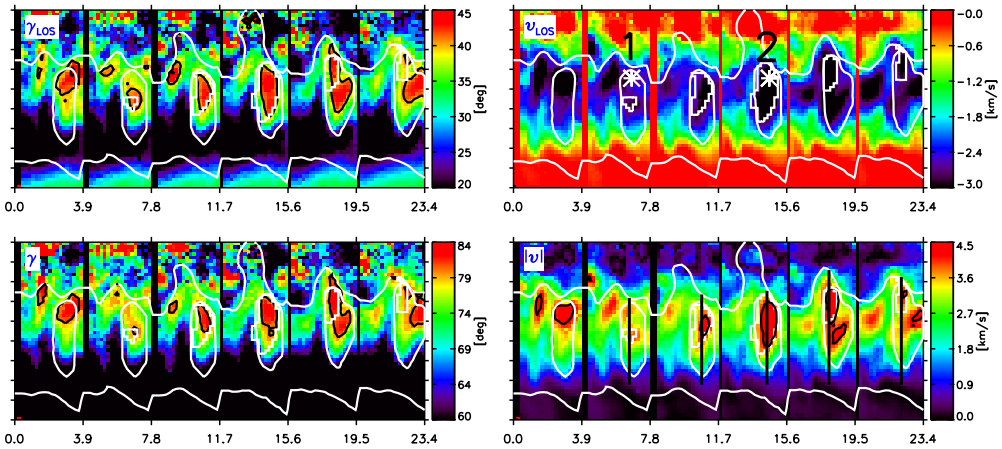

FIGURE 8.10:— *Left:* Maps of magnetic field inclination in the LOS reference frame (*top*) and LRF (*bottom*). *Right:* Maps of LOS velocities at $\log\tau = -0.5$ (*top*) and modulus of the velocity vector at $\log\tau = -0.5$. White contours mark EC A, the penumbral filament, and the boundaries of the penumbra. Black contours enclose pixels with γ, $\gamma_{\rm LOS}$, and $|v|$ greater than 80°, 40°, and 4.2 km s^{-1}respectively. The vertical black lines in the bottom right panel mark a cut passing through the EC and the filament. Asterisk mark and numbers label the same pixel in two different times: before (#1) and during (#2) the EC passage. Each tick in the y-axis represent 1″.

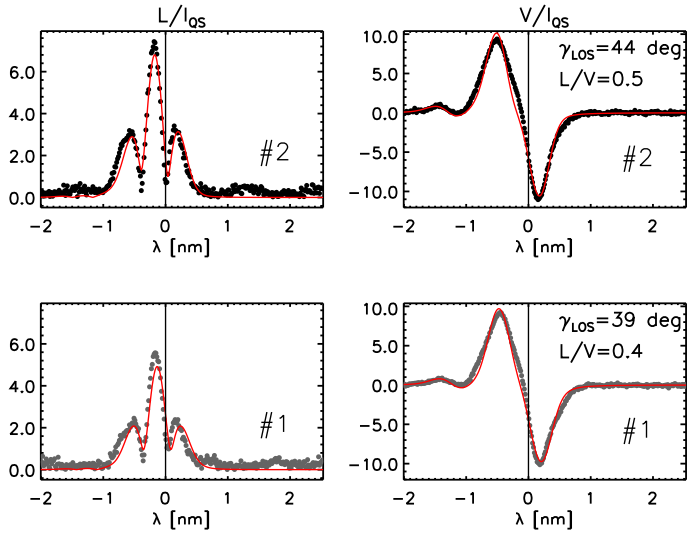

FIGURE 8.11:— Observed (dots) and best-fits (red lines) linear (right) and circular (left) polarization profiles of Fe I 1564.85 nm emerging from a pixel before (#1) and during the passage of EC A (#2). The pixel is located in the top right panel of Fig. 8.10.

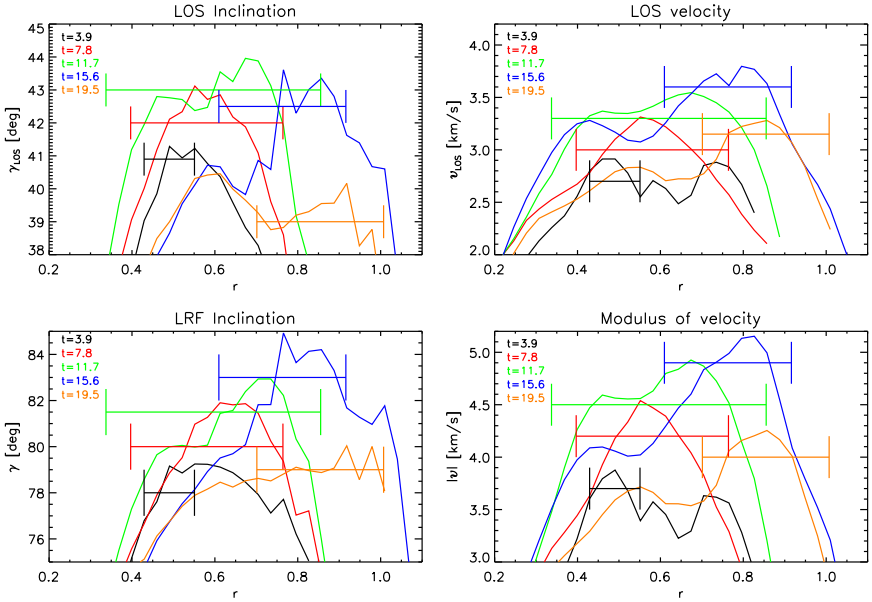

FIGURE 8.12:— *Left:* Variation of γ (*top*) and $\gamma_{\rm LOS}$ (*bottom*) along the radial cuts shown in Fig. 8.10. *Right:* Variation of $v_{\rm LOS}$ (*top*) and $|v|$ (*bottom*) along the same cuts. The colors indicate different times. The horizontal lines mark the upper and lower edges of EC A.

modification of the modulus of the velocity vector is greater than the variation of the field inclination produced by the ECs.

In order to visualize the variation of the filament inclination produced by the passage of EC A, we plot the orientation of the magnetic field with arrows in Fig. 8.13. As can be seen, the arrows become more inclined as EC A reaches larger radial distances. In other words, the passage of the EC modifies the magnetic field inside the filament, making it more horizontal. In the final stages ($t = 19.5$ min), the inclinations of the EC decrease.

In view of these results, one could define the ECs as quasi-periodic perturbations of the magnetic and velocity fields of the penumbral filaments. These perturbations cause the following observational properties: (a) they produce an enhancement of γ and $|v|$; (b) the amplitude of the perturbation increases as it propagates to larger radial distances; (c) when the EC starts to vanish the amplitude of the perturbation is reduced; and (d) the modification of γ is perpendicular to the direction of propagation of the perturbation[4].

Except for (c), the behavior described in this section for EC A is also

[4]As discussed in Sect. 7.2 the vertical component of the proper motions of the ECs is small compared with the radial component.

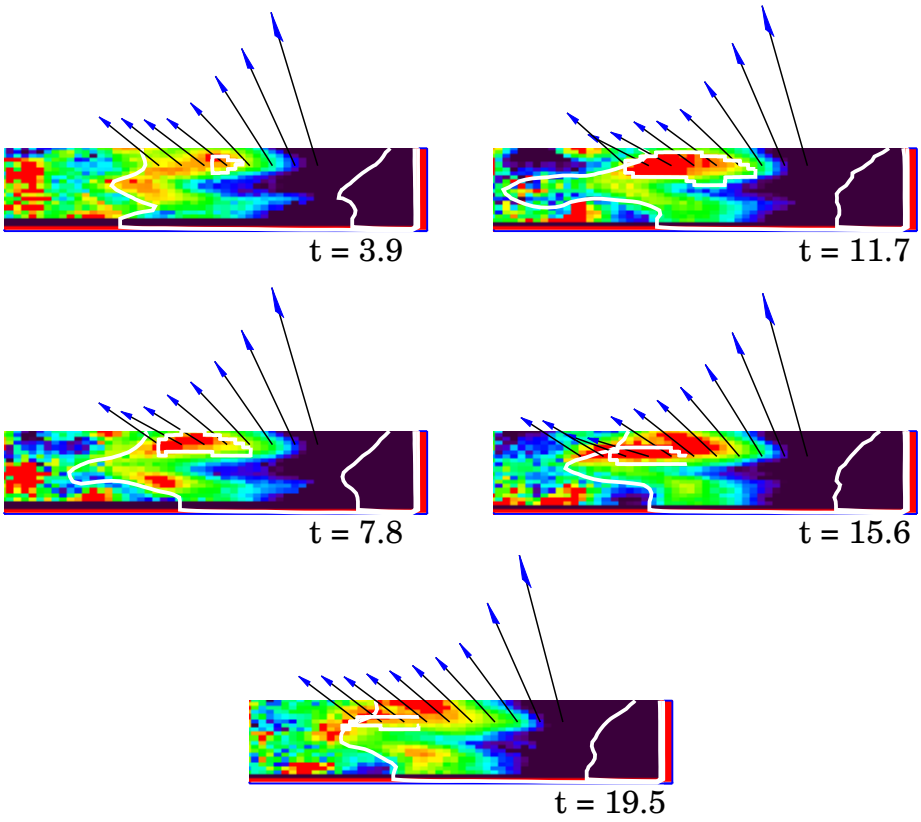

FIGURE 8.13:— Variation of γ along the cuts shown in Fig. 8.10 as EC A propagates from the inner ($t = 3.9$ min) to the outer ($t = 19.5$ min) penumbra. The color scale ranges from 55°(black) to 85°(red). Each arrow has the same length and indicates the orientation of the magnetic field vector retrieved from the inversion. White contours outline EC A and the penumbral boundaries.

observed in the other ECs of type I. Hence, it can be considered as a general property of the ECs.

8.8 Supercritical flows in the deep atmospheric layers

Acoustic waves are easily generated on a medium in the absence of magnetic fields. They propagate with the sound speed, c_s. If the material moves faster than c_s, a shock front develops and the flow becomes supersonic. In the case of thin magnetic flux tubes the same physical phenomenon occurs. Flux tubes support magneto-acoustic waves (Ferriz-Mas 1988) and among them a longitudinal mode which propagates at the so-called tube speed, $c_t = (c_A \times c_s)/(c_A^2 +$

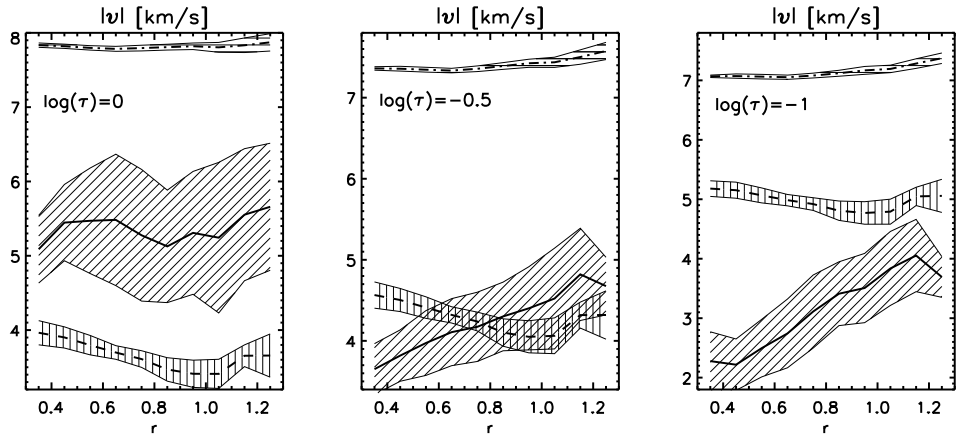

FIGURE 8.14:— Modulus of flow velocity (solid line), tube velocity (dashed line), and sound velocity (dotted-dashed line) for the pixels inside the ECs as a function of their radial distance. The panels display the velocities at $\log(\tau) = 0$ (*left panel*), $\log(\tau) = -0.5$ (*center panel*), and $\log(\tau) = -1$ (*right panel*). Shaded areas indicate the standard deviations.

$c_s^2)^{1/2}$, with c_A being the Alfvén speed. If the flow velocity is larger than c_t, a shock wave develops inside the tube (Ferriz-Mas & Moreno-Insertis 1987) and the flow is called supercritical. Borrero et al. (2005) found observational evidence for the formation of shock fronts in the outer penumbra of a sunspot using two component inversions.

In this section, we compare the flow speed (i.e. $|v| = v_{\rm LOS}/\cos\gamma_{\rm LOS}$) with the sound and tube speeds calculated from the temperature, field strengths, and densities retrieved from the inversion in three different layers ($\log\tau = 0, -0.5, -1$). This is done for the pixels inside ECs as a function of their radial distance. The results are summarized in Fig. 8.14. The flow velocities are always subsonic, but supercritical for all radial distances at $\log\tau = 0$, and from $r \sim 0.8$ to $r \sim 1.2$ at $\log\tau = -0.5$. Our results are in disagreement with the supersonic velocities predicted by the moving tube simulations of Schlichenmaier (2002). Anyway, we note that the flow velocities inferred from these inversions represent an average of the various magnetic components that are known to fill the resolution element in sunspot penumbrae: del Toro Iniesta et al. (2001) and Bellot Rubio et al. (2004) found supersonic flows using two magnetic components. We will come back to this point in Chapter 9.

8.9 Comparison of physical quantities with line parameters

In the previous chapter we found that the EC line parameters display char-

TABLE 8.3:— Comparison of the physical quantities inferred from the inversion with the line parameters as observed on 30 June and 1 July. The date of observation is shown in the first column. The unsigned LOS velocities inferred from the inversion at $\log(\tau) = -0.5$ ($|v_{\rm LOS}|$), and from the Stokes V zero-crossing of Fe I 1564.85 nm, and Fe I 630.25 nm are shown in second and third rows. The inclination to the LOS ($\gamma_{\rm LOS}$) and the linear-to-circular polarization ratios derived from Fe I 1564.85 nm and Fe I 630.25 nm are displayed in the fifth and sixth rows. The two last rows are the difference between the unsigned velocities at $\log(\tau) = -0.5$ and $\log(\tau) = 0$ ($|\Delta v_{\rm LOS}|$) and the area asymmetries of Fe I 1564.85 nm and Fe I 630.25 nm.

Date	$\lvert v_{\rm LOS}\rvert$ [km s^{-1}]	$\lvert v_{1564.85}\rvert$ [km s^{-1}]	$\lvert v_{630.25}\rvert$ [km s^{-1}]
06/30	3.0	3.2	2.2
07/01	1.0	2.1	1.3
	$\gamma_{\rm LOS}$ [deg]	$(L/V)_{1564.85}$	$(L/V)_{630.25}$
06/30	43	0.47	0.22
07/01	46	0.81	0.37
	$\lvert\Delta v_{\rm LOS}\rvert$ [km s^{-1}]	$\delta A_{1564.85}$ [%]	$\delta A_{630.25}$ [%]
06/30	−0.6	5.9	4.4
07/01	−0.3	5.4	3.2

acteristic values and behaviors[5]. These parameters somehow reflect the physical conditions of the solar atmosphere. We here verify the relation between the line parameters and the atmospheric quantities that produce them.

To that aim, we calculate the maximum values of $|v_{\rm LOS}|$, $\gamma_{\rm LOS}$, and $\Delta v_{\rm LOS}$ within each EC in the same way as in Sect. 7.5. Then, we compute the mean values on 30 June and 1 July. Table 8.3 compares these values with the mean Stokes V zero-crossing velocities, linear-to-circular polarization ratios, and area asymmetries for Fe I 1564.85 nm and Fe I 630.25 nm reported in Chapter. 7.

As expected, the values of the atmospheric parameters observed in two different days display similar trends as the line parameters:

- The LOS velocities inferred from the inversion at $\log\tau = -0.5$ are greater on 30 June (~ 3.0 km s^{-1}) than on 1 July (~ 1.0 km s^{-1}). $v_{\rm LOS}$ is obtained using the information provided by all the spectral lines and the Stokes V zero-crossing velocities of the IR and VIS lines display greater values on 30 June than on 1 July (cf. third and fourth columns of Table 8.3).

[5]For example, ECs display the greatest values of the linear-to-circular polarization ratios.

- ECs exhibit larger inclinations to the LOS on 30 June (43°) than on 1 July (46°). This is consistent with the greater linear-to-circular polarization ratios displayed by the ECs on 30 June as compared with 1 July (cf. sixth and seventh columns of Table 8.3).

- $\Delta v_{\rm LOS}$ is larger on 30 June (~ -0.6 km s^{-1}) than on 1 July (~ -0.3 km s^{-1}), which is consistent with the stronger area asymmetries displayed by the ECs on 30 June[6] (see two last columns of Table 8.3). We note that $\Delta v_{\rm LOS}$ takes on negative values only. This again agrees with the fact that ECs display larger values of the LOS velocities for the IR lines compared with the VIS lines, and that the IR lines are formed in deeper layers.

Finally, we study the similitudes between the radial evolution of the physical and line parameters of the ECs and the rest of penumbral points. In Fig. 8.15 we display the results for $v_{\rm LOS}$, $\gamma_{\rm LOS}$, and $\Delta v_{\rm LOS}$ and T. We construct the curves following the same method employed in Sect. 7.9. As expected, the curves of $v_{\rm LOS}$, $\gamma_{\rm LOS}$, and T mimic the curves of LOS velocities, linear-to-circular polarization, and continuum intensities shown in Figs. 7.13 and 7.14 for Fe I 1564.85 nm and Fe I 630.25 nm. In contrast, the area asymmetries of the spectral lines and $\Delta v_{\rm LOS}$ display different trends: δA monotonically increases with radial distance within the ECs, while the unsigned values of $\Delta v_{\rm LOS}$ display the opposite behavior.

In summary, these results demonstrate that the line parameters calculated in the previous chapter can be considered as good indicators of the average physical quantities which are present in the solar atmosphere. In other words, the values of linear-to-circular polarization ratios, LOS velocities, and continuum intensities have their origin in the values of $v_{\rm LOS}$, $\gamma_{\rm LOS}$, and T.

8.10 Summary and Conclusions

The magnetic, thermal, and dynamic properties of ECs have been derived for the first time in terms of one-component magnetic atmospheres. The main results of the chapter can be summarized as follows:

1. ECs move along the intra-spines described by Lites et al. (1993).

2. ECs seem to be perturbations of the magnetic and dynamic structure of the intra-spines. The perturbations produce an enhancement of γ and $|v|$

[6]The LOS velocity is the only physical quantity allowed to vary with height and, consequently, the source of area asymmetry in our inversions.

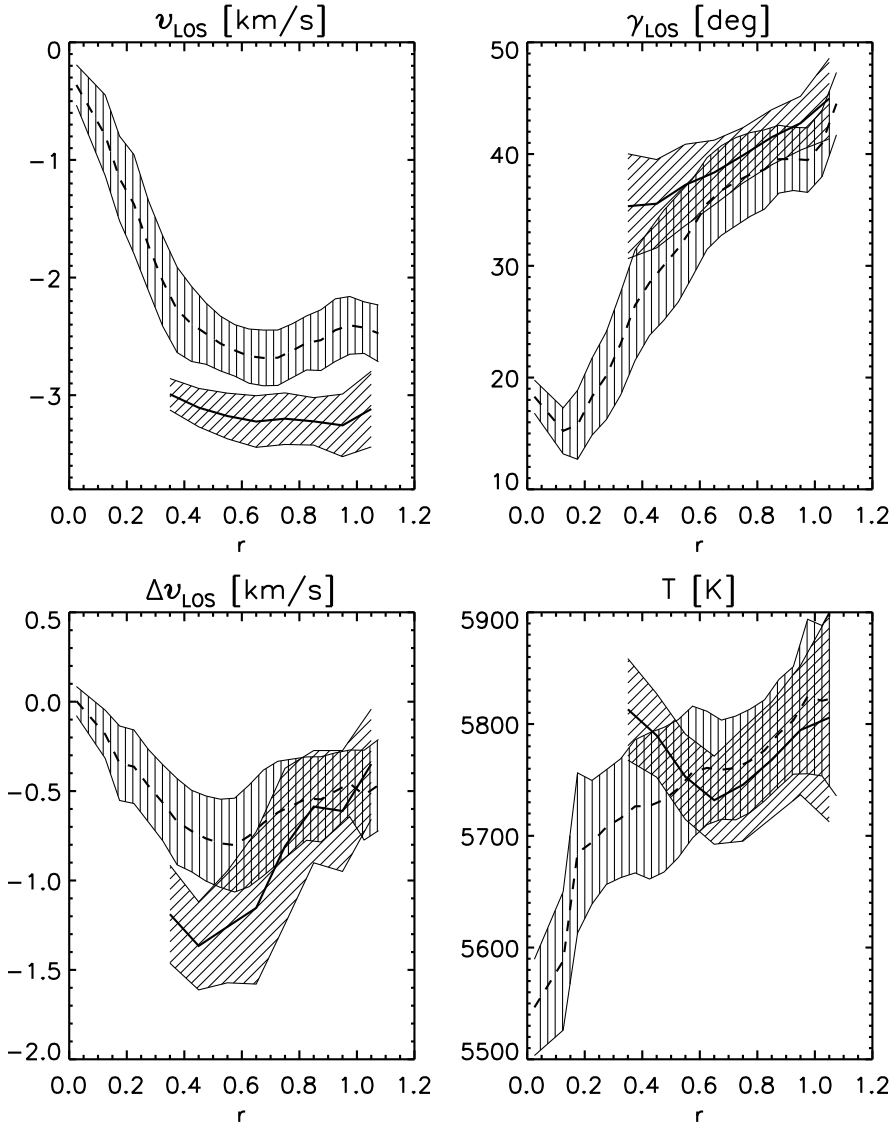

FIGURE 8.15:— Averaged LOS velocities at $\log(\tau) = -0.5$, inclinations to LOS, $\Delta v_{\rm LOS}$, and temperatures at $\log(\tau) = 0$ for the ECs (solid line) and the rest of the penumbra (dashed line). The x-axis is the radial distance. Shaded areas outline the standard deviations.

whose amplitudes increase with radial distance. **Moreover, the modification of γ is perpendicular to the direction of propagation of the ECs**.

3. When type I ECs start to vanish the amplitude of the perturbations decreases.

4. The vector magnetic field of the ECs has the following properties: (a) its strength is weaker than the displayed by the intra-spines in the inner penumbra and stronger in the outer penumbra; (b) its inclination is larger than that of the intra-spines at all radial distances, and become nearly horizontal as the outer penumbral edge is reached; and (c) it is oriented in the same direction than the field of the intra-spines except for the outer penumbra.

5. ECs harbor the strongest flows of the penumbra. The flow is supercritical in deep layers ($\log\tau = 0$).

6. The gradients of velocity are greater inside the ECs than in the rest of penumbral points.

7. ECs are hotter than their surroundings in the inner penumbra and cooler in the outer penumbra.

8. The linear-to-circular polarization ratios, LOS velocities, and continuum intensities are good indicators of $v_{\rm LOS}$, $\gamma_{\rm LOS}$, and T.

The physical mechanism that produce the EC phenomenon and, consequently, the perturbation of the magnetic configuration of the intra-spines, remains a mistery. It could be a wave superimposed on a steady or quasi-steady flow as suggested by Georgakilas & Christopoulou (2003). In fact, there are theoretical calculations (Spruit 1982) which predict waves guided by the field lines. These kind of waves are known as magnetoacoustic waves (MAGs). The problem is that MAGs cannot produce the kind of perturbations we have observed associated with the ECs. These waves produce perturbations which would cause both an increase and a decrease of the inclination inside the ECs, and the second is not observed.

Rouppe van der Voort (2003) suggested the propagation of moving kinks (Ryutova et al. 1998) along field lines as an explanation for the EC phenomenon, but neither Ω nor $\mho$-kinks are compatible with the geometry of the magnetic field we infer for the ECs. In both cases one should observe fields directed

toward the solar surface already in the inner penumbra, but these fields are not detected inside the ECs.

The one-component inversions allow us to infer the mean physical conditions of the ECs, but are not suitable to identify the physical mechanism that produces the ECs. It is well known that the Stokes profiles of the sunspot penumbrae are better reproduced taking into account its fine structure (Bellot Rubio et al. 2004; Borrero et al. 2004). For this reason, in the next chapter we investigate the nature of the ECs using two magnetic components.

9

Uncombed view of the EC phenomenon

9.1 Introduction

The typical size of the filamentary structure of the penumbra turns out to be around 150-250 km ($\sim 0\farcs2$) or even smaller. At the spatial resolution of our observations ($\sim 0\farcs6$ in the IR), atmospheres with very different properties could be mixed in the same resolution element. In fact, these atmospheres must be interlaced not only in the horizontal but also in the vertical direction, as the non-zero area asymmetries suggest. Fortunately, inversion techniques allow us to account for the unresolved structure of the penumbra. Previous investigations by del Toro Iniesta et al. (2001), Bellot Rubio et al. (2004), and Borrero et al. (2004, 2005, 2006) showed that the abnormal shapes of the polarization profiles observed in sunspot penumbrae can be reproduced in terms of two magnetic components. Their results are consistent with a penumbra formed by horizontal flux tubes carrying the flow which are embedded in a more horizontal background essentially at rest, in agreement with the uncombed model proposed by Solanki & Montavon (1993).

In this chapter we study the origin of the global physical properties of the ECs obtained in the previous chapter in terms of two magnetic components under two different geometrical approximations:(a) atmospheres horizontally interlaced; and (b) atmospheres interlaced in the horizontal and vertical directions. It will allow us to provide a natural explanation for the EC phenomenon. In Sect. 9.2 we describe the semi-empirical models employed in the inversion

process, while in Sect. 9.3 the quality of the fits is discussed. The position and radius of the tubes derived from the inversion are discussed in Section 9.4. Section 9.5 is devoted to compare the two magnetic components and their radial evolution inside the ECs. The main properties of the ECs in terms of two magnetic components are studied in Sect. 9.6. The origin of the EC phenomenon is discussed in Sec. 9.7, while the geometry of the tubes inside the penumbra is studied in Sect. 9.8. A summary of our conclusions is given in Sect. 9.10.

9.2 Uncombed models

9.2.1 Two components

As a first approximation, we adopt a simple semi-empirical model to describe the fine structure of the penumbra: two magnetic components (2C) with height independent atmospheric parameters[1] (see Table. 9.1). The results obtained by del Toro Iniesta et al. (2001), Bellot Rubio et al. (2004), and Borrero et al. (2004) demonstrate that one of the magnetic components display neglecting velocities compared with the other. For this reason, we assume one component at rest while the velocity can be fixed by the code for the other one. By analogy with the uncombed model, we refer to them as *background* and *tube* components, respectively. The assumption of constant atmospheric parameters makes the analysis of the results easy. Moreover, most of the information contained in the Stokes profiles can be extracted. Due to the absence of velocity gradients, however, the area asymmetries of the Stokes profiles cannot be reproduced.

If one models the penumbral structure with two independent magnetic components coexisting in the resolution element (cf. left panel of Fig. 9.1), the emergent Stokes profiles are a combination of the background, $\boldsymbol{I}_{\rm b}$, and tube, $\boldsymbol{I}_{\rm t}$, profiles:

$$\boldsymbol{I} = (1-\alpha)[f\boldsymbol{I}_{\rm t} + (1-f)\boldsymbol{I}_{\rm b}] + \alpha\boldsymbol{I}_{\rm stray}, \tag{9.1}$$

where f is the fractional area of the pixel filled by the tube component (the filling factor), α the amount of stray light[2], and $\boldsymbol{I}_{\rm stray}$ the average quiet Sun profile representing the contribution of the stray light contamination.

9.2.2 Gaussian

One of the main drawbacks of 2C models is that the atmospheric parameters of the components are unrelated in the vertical direction. For a more realistic treatment of the uncombed structure of the sunspot penumbrae, the horizontal

[1] Only temperature is allowed to vary along the atmosphere.

[2] As in the case of 1C inversions, each spectral range has a different straylight contribution.

TABLE 9.1:— Number of nodes employed for perturbating the magnetic atmospheres of the 2C and gaussian models. The nodes of the atmospheric quantities for the tube and background components are given in the second and third columns for the 2C models and in the fourth and fifth for the gaussian models. −1 indicates that the two atmospheres have the same value of the atmospheric parameter.

Parameter	Tube (2C) [Nodes]	Background (2C) [Nodes]	Tube (G) [Nodes]	Background (G) [Nodes]
temperature	2	2	3	2
velocity	1	0	1	0
field strength	1	1	1	1
inclination	1	1	1	1
azimuth	1	1	1	1
microturbulence	1	1	1	1
macroturbulence	1	−1	1	−1
stray light	2	−1	1	−1
filling factor	1	−1	1	−1
gaussian position	0	0	1	0
gaussian width	0	0	1	0

and vertical extension of the flux tubes is modeled as follows. A fraction of the resolution element is assumed to be filled by the background component while the rest is occupied by the background and tube atmospheres interlaced in the vertical direction (cf. right panel of Fig. 9.1). Hence, the emergent Stokes profiles are given by the contributions of the two atmospheres (see Eq. 9.1) which are horizontally and vertically interlaced. The tube atmosphere is modeled adding gaussian perturbations to the atmospheric quantities derived from the background component (see Fig. 9.2). The width (R_t) and position (C_t) of the gaussian are free parameters derived from the inversion that are the same for all the atmospheric parameters. In contrast, the amplitude of the gaussian depends on the parameter. For obvious reasons, we estimate R_t and C_t as the radius and central position of the tubes. As in the previous section, except for the temperature, the atmospheric quantities of the background are assumed to be constant with optical depth. The code does not allow to account for different stray-light contributions depending on the spectral range, but the effect of systematic errors in the determination of the stray-light produce little variations on the the magnetic atmospheric parameters (see Chapter 6). The number of free parameters is 19 (cf. Table 9.1) while in the case of 2C inversions is 17.

Gaussian inversions are strongly dependent on the initial model. Fortunately, the results of the 2C inversions provide an excellent initial guess. The initial models of the gaussian inversions are constructed for each inverted pixel

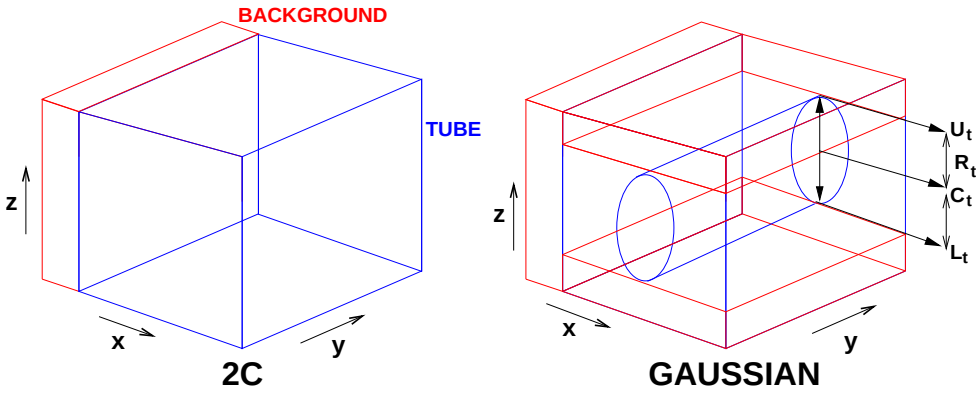

FIGURE 9.1:— Geometrical illustration of the atmospheres filling the resolution element in the 2C (*left*) and gaussian (*right*) models. Areas enclosed by red and blue lines represent the background and tube atmospheres. In the gaussian model the tube is characterized by its center position (C_t) and radius (R_t). U_t and L_t are the upper and lower boundaries of the tube. x and y-axis represent orthogonal directions on the solar surface while z-axis is the vertical direction of the resolution element.

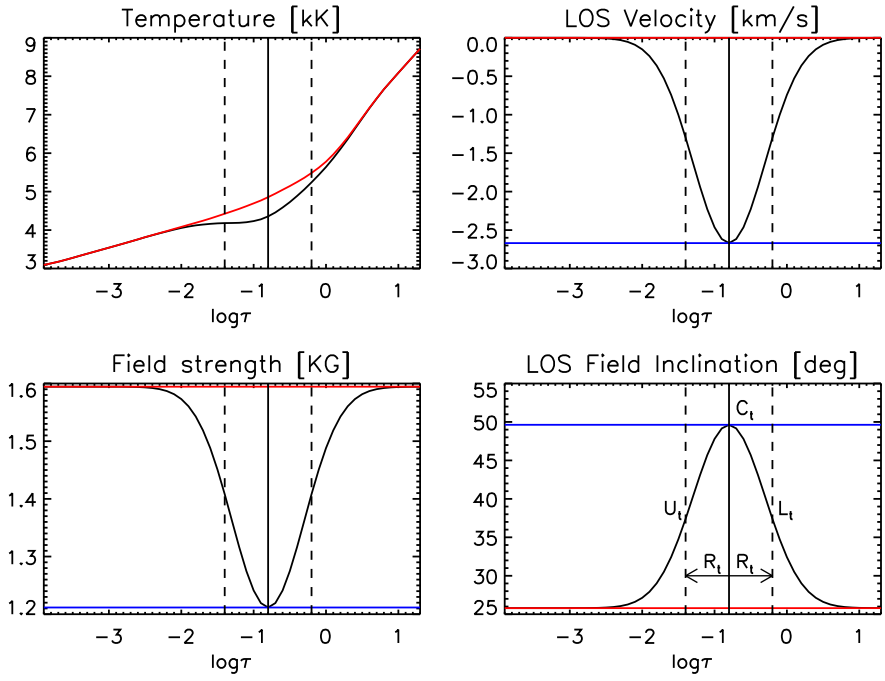

FIGURE 9.2:— Example of an initial gaussian model (black) constructed by means of the background (red) and tube (blue) atmospheres derived from the 2C inversions. The gaussian is initially placed at $\log\tau = -0.8$ with a width of $\log\tau = 0.5$.

as follows: the background atmosphere is the same than the one derived from the 2C inversion while the amplitude of the gaussian of the tube atmosphere is estimated as the difference between the atmospheric parameters of the background and the tube components (cf. Fig. 9.2). The width of the gaussian is set to an initial value of $\log\tau = -0.5$ and is placed at $\log\tau = -0.8$.

Outside the spot, the Stokes profiles can be reproduced with a single magnetic component. Hence, only pixels inside the penumbra have been inverted with 2C and gaussian models, resulting in 39105 and 13928 individual inversions on 30 June and 1 July, respectively.

9.3 Quality of the fits

In Fig. 9.3 an example of the observed (dots) and fitted (red lines) Stokes profiles derived from the 2C inversion inside the penumbra ($r \sim 0.3$) is shown. As can be seen, the polarization profiles are rather asymmetric. Although 2C models neglect velocity gradients, the fits are reasonably good. This is because the values of the area asymmetries of the IR and VIS lines (see Figs. 7.13 and 7.14) are small ($< 10\%$) inside the penumbra. Hence, 2C model atmospheres are a good first approximation of the fine structure of the penumbra. In Fig. 9.4 the fit derived from the gaussian inversion is shown for the same pixel. In this case, the code is able to fit the area asymmetries and the profiles are better reproduced.

9.4 Position and radius of the tubes

Figure 9.5 shows the centers (C_t), radius (R_t), and boundaries of the tubes within the ECs and the intra-spines along which they propagate as derived from the gaussian inversions. For the most part, the centers of the tubes are located above $\log\tau \sim 0$, with similar values for the ECs and the intra-spines. At least in the inner penumbra, the widths of the tubes are somewhat smaller inside the ECs, leading to upper (lower) boundaries located slightly deeper (higher) for the ECs. Since the tube lower boundary is below $\log\tau \sim 0$, the tubes derived from the inversion necessarily are optically thick and/or low-lying tubes. In any case, the spectral lines only sample the upper part of the tubes, while the lower boundary remains below the line forming region (cf. Chapter 3). A similar result has been obtained by Borrero et al. (2006) and Beck & Bellot Rubio (2007) from their uncombed inversions.

The differences in the optical depth of the upper boundary of the tube are sufficienlty small (and the scatter large enough) as to consider them negligible. In other words, we do not detect clear differences in the optical depth of the

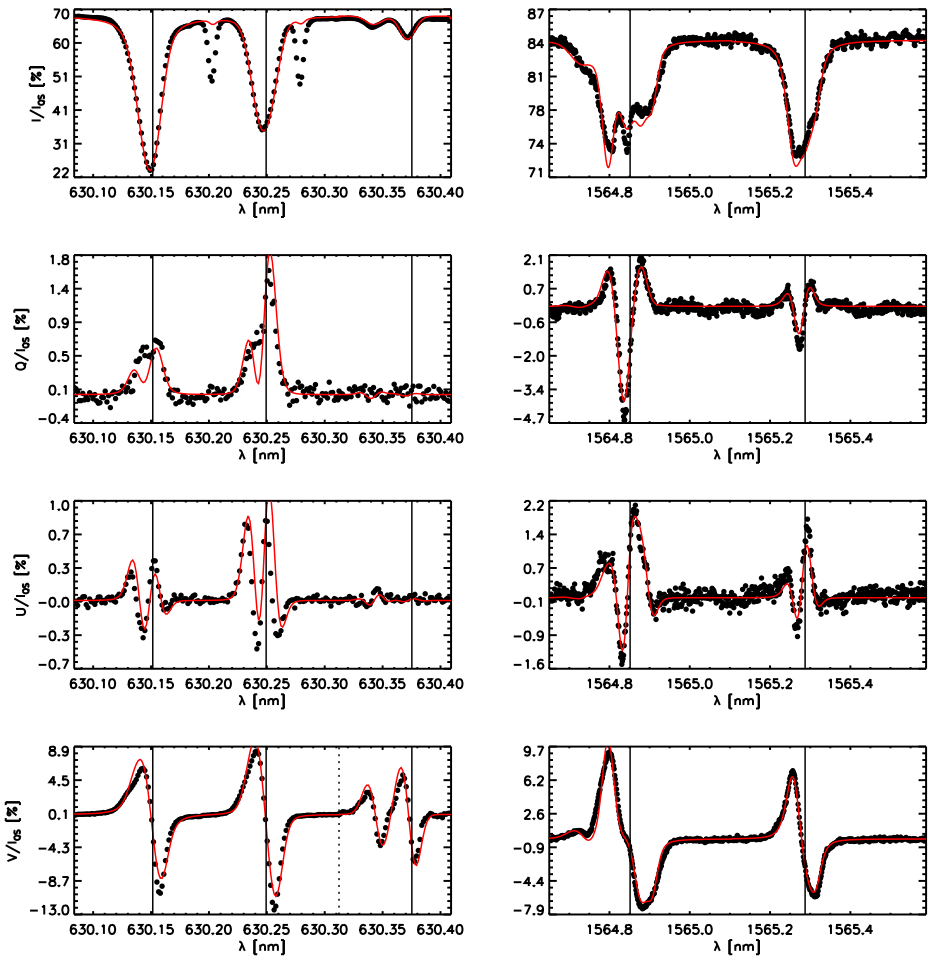

FIGURE 9.3:— Example of observed (dots) and best-fit (red lines) Stokes profiles obtained by means of the 2C inversion for a pixel at $r \sim 0.3$ displaying abnormal linear polarization profiles. For better visibility, the Stokes V signal around Ti I 630.38 nm has been multiplied by six.

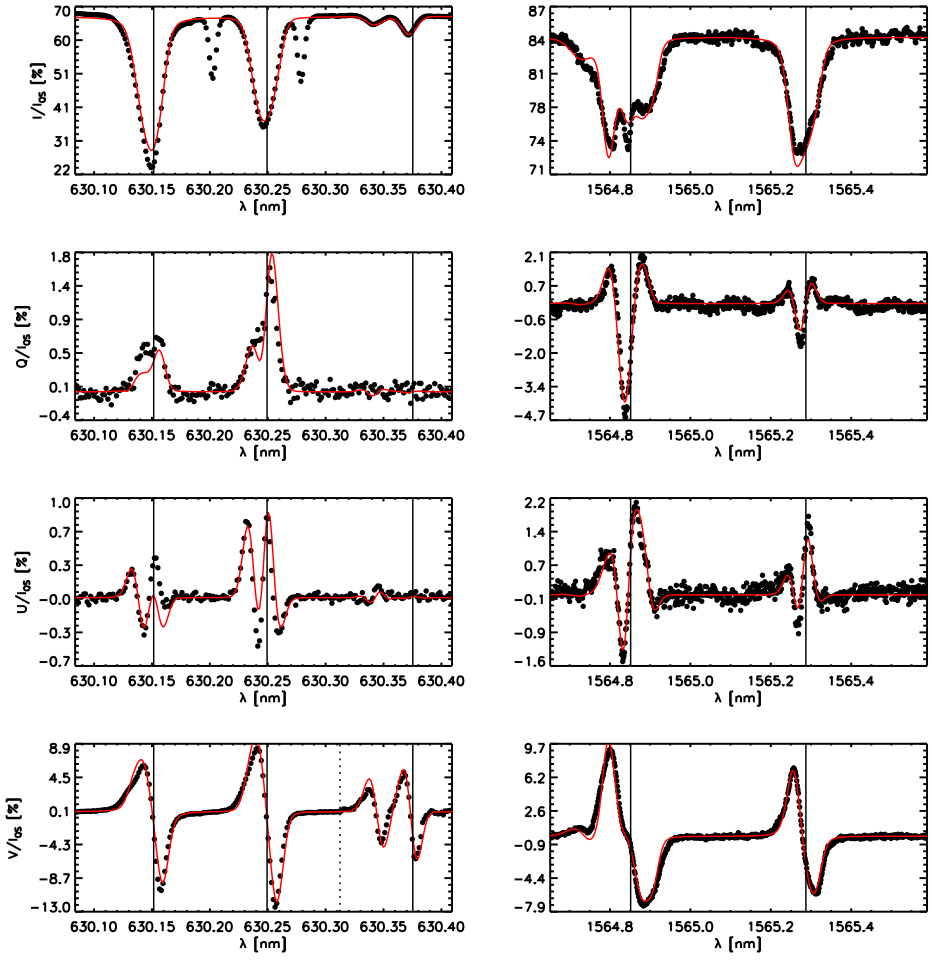

FIGURE 9.4:— Same as Fig. 9.3 for the gaussian inversion.

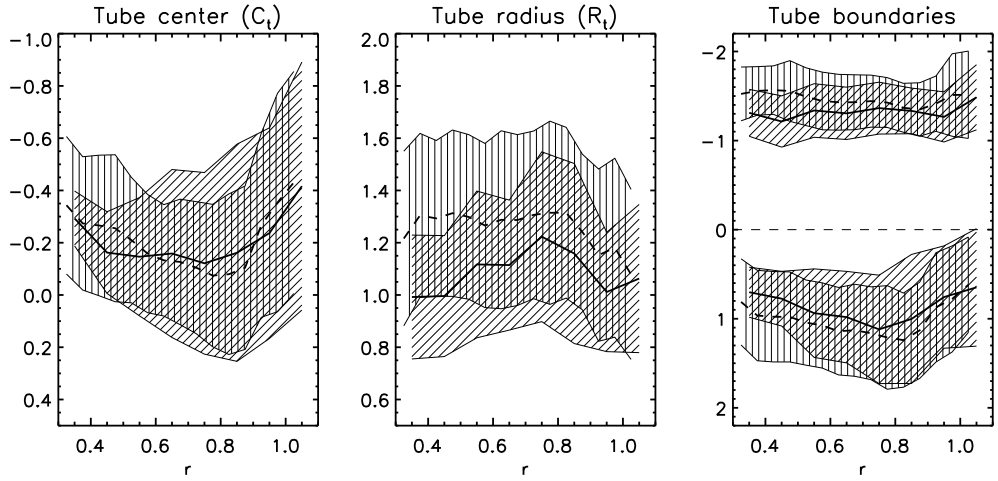

FIGURE 9.5:— Tube center (C_t), radius (R_t), and boundaries of the tube/s of the ECs (solid lines) and the intra-spines (dashed lines). The quantities are given in units of the logarithm of the optical depth. The shadows are the standard deviations of the quantities.

interface between tubes and background when comparing the ECs with the intra-spines.

9.5 Comparison of the two magnetic components inside the ECs

In this section we compare the atmospheric parameters of the background and tube atmospheres derived from 2C and gaussian inversions. In the case of the gaussian inversions, the atmospheric parameters of the tube are constructed taking the values at C_t, while the temperatures correspond to $\log\tau = 0$. Since most of the tubes are located above $\log\tau = 0$, the atmospheric parameters calculated in such way are a good approximation of the atmospheric conditions of the medium inside the tube. Figures 9.9−9.11 display the magnetic field strength, field inclination, temperature at $\log\tau = 0$, LOS velocity, and filling factor of the tube atmosphere calculate in this way for the time sequence observed on 30 June while the corresponding results for the data set taken on 1 July are displayed in Figs. Apendice?.

Figures 9.9, 9.10, and 9.11 show the radial evolution of the field strengths, inclinations, azimuths, modulus of the velocities, and temperatures at $\log\tau = 0$ in the tube (solid line) and background (dashed line) inside the ECs as derived from 2C (red) and gaussian (blue) inversions. As can be seen, both the results derived from the 2C and the gaussian inversions show that the field strengths in

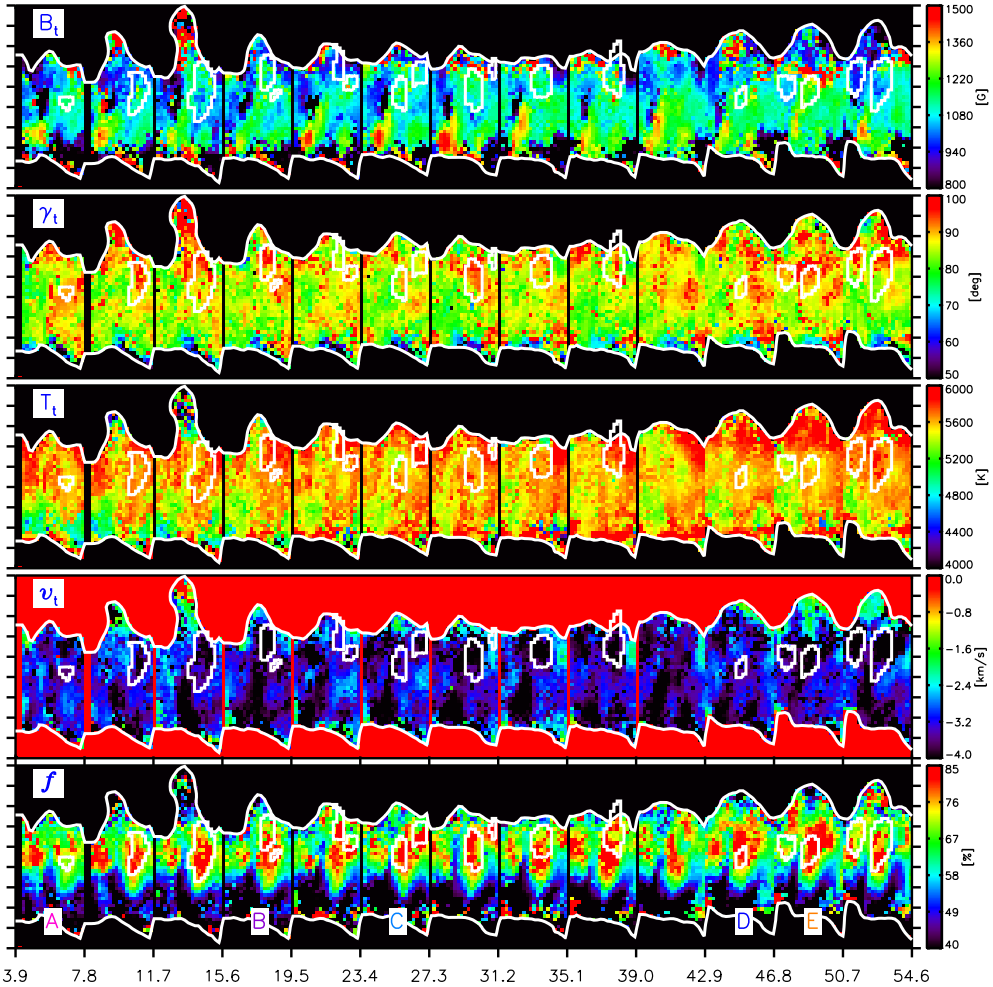

FIGURE 9.6:— From *Top* to *bottom*: Magnetic field strength, field inclination, temperature at $\log \tau = 0$, LOS velocity, and filling factor of the tube atmosphere retrieved from the gaussian inversion. White contours outline the ECs and the inner and outer penumbral boundaries. The letters at the bottom of the last panel label each EC.

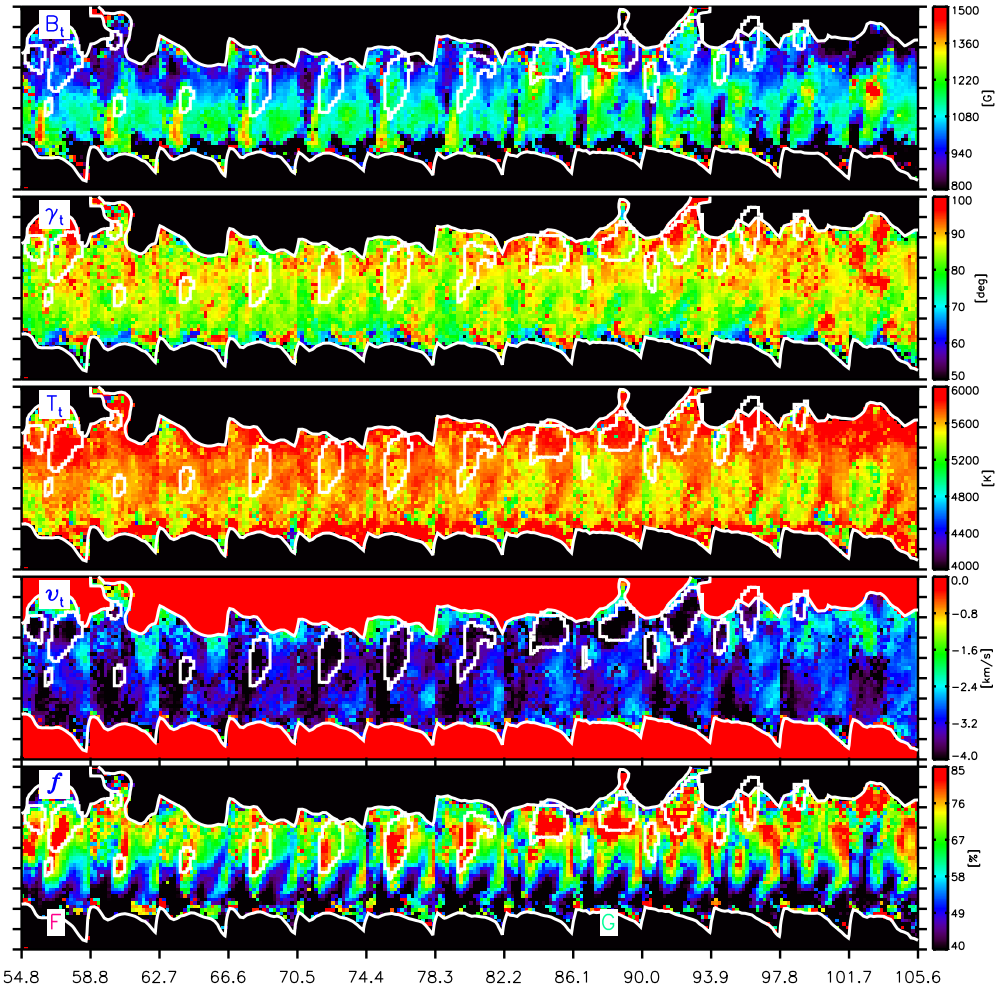

FIGURE 9.7:— Same as Fig. 9.6 from t=54.8 to t=105.5 min.

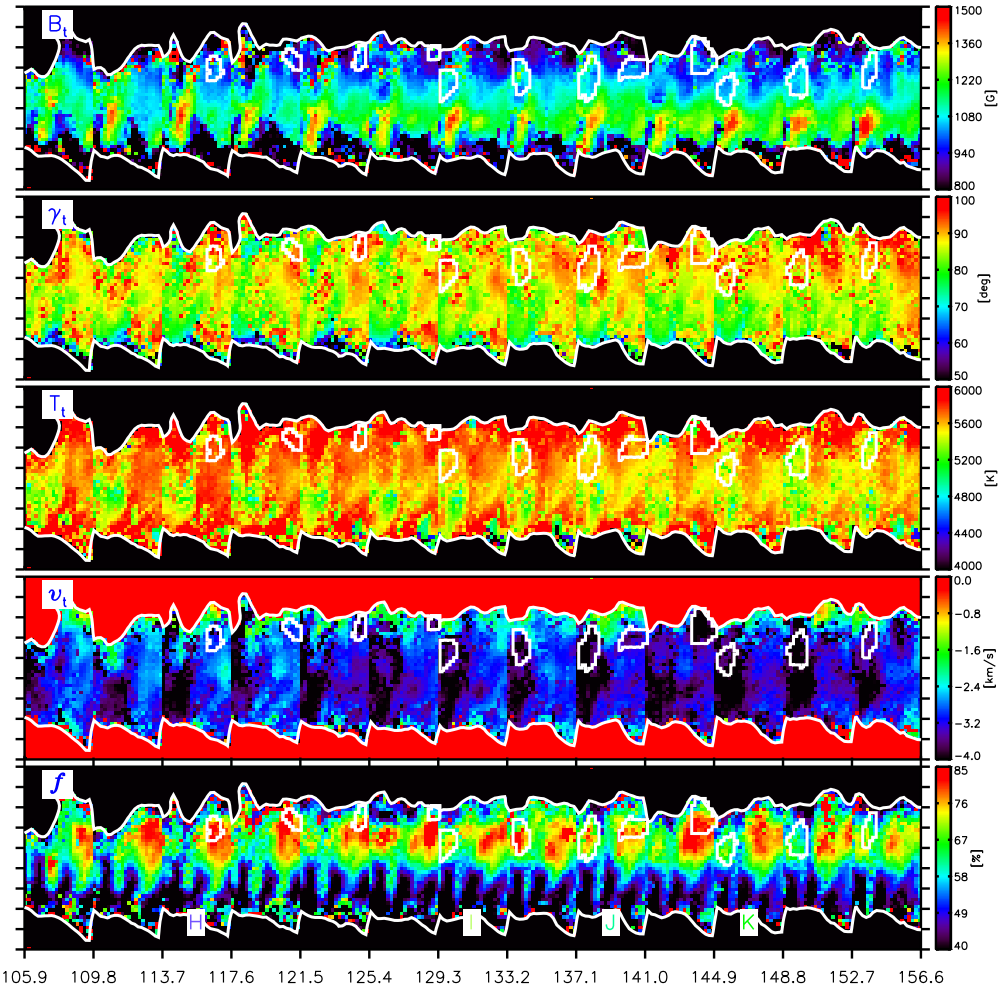

FIGURE 9.8:— Same as Fig. 9.6 from t=105.7 to t=156.4 min.

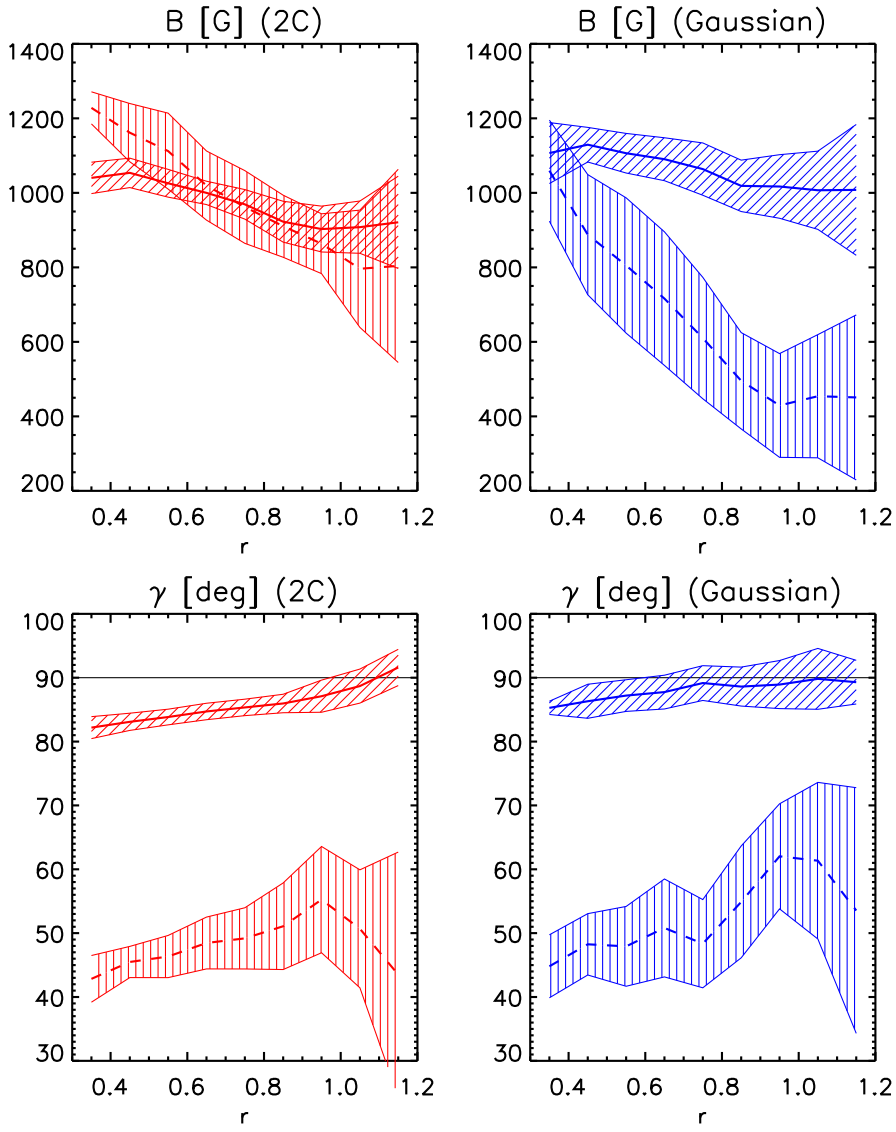

FIGURE 9.9:— Radial evolution of the magnetic field strength and inclination of the tube (solid) and background (dashed) components for the ECs as derived from 2C (red) and gaussian (blue) inversions. Shaded areas represent the rms variation of the atmospheric quantities at a given radial distance.

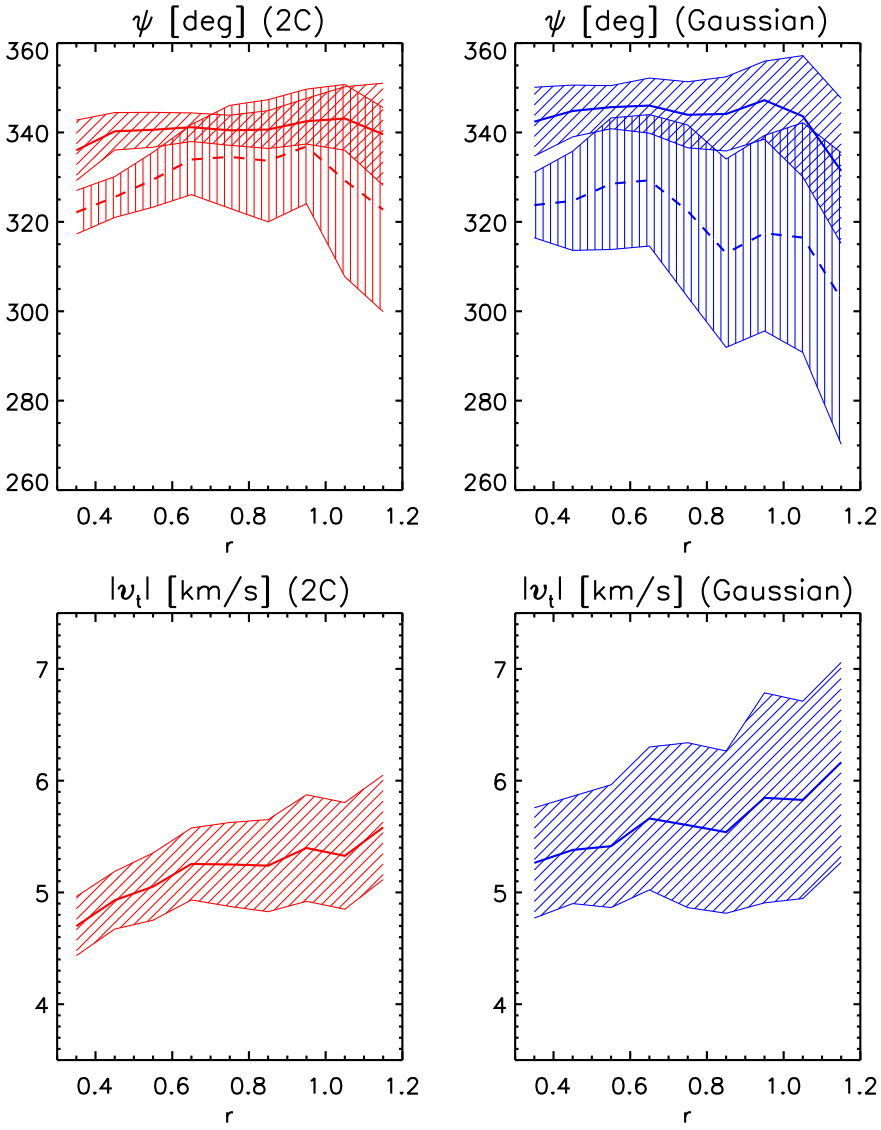

FIGURE 9.10:— Same as Fig. 9.9 for the azimuth and velocity modulus.

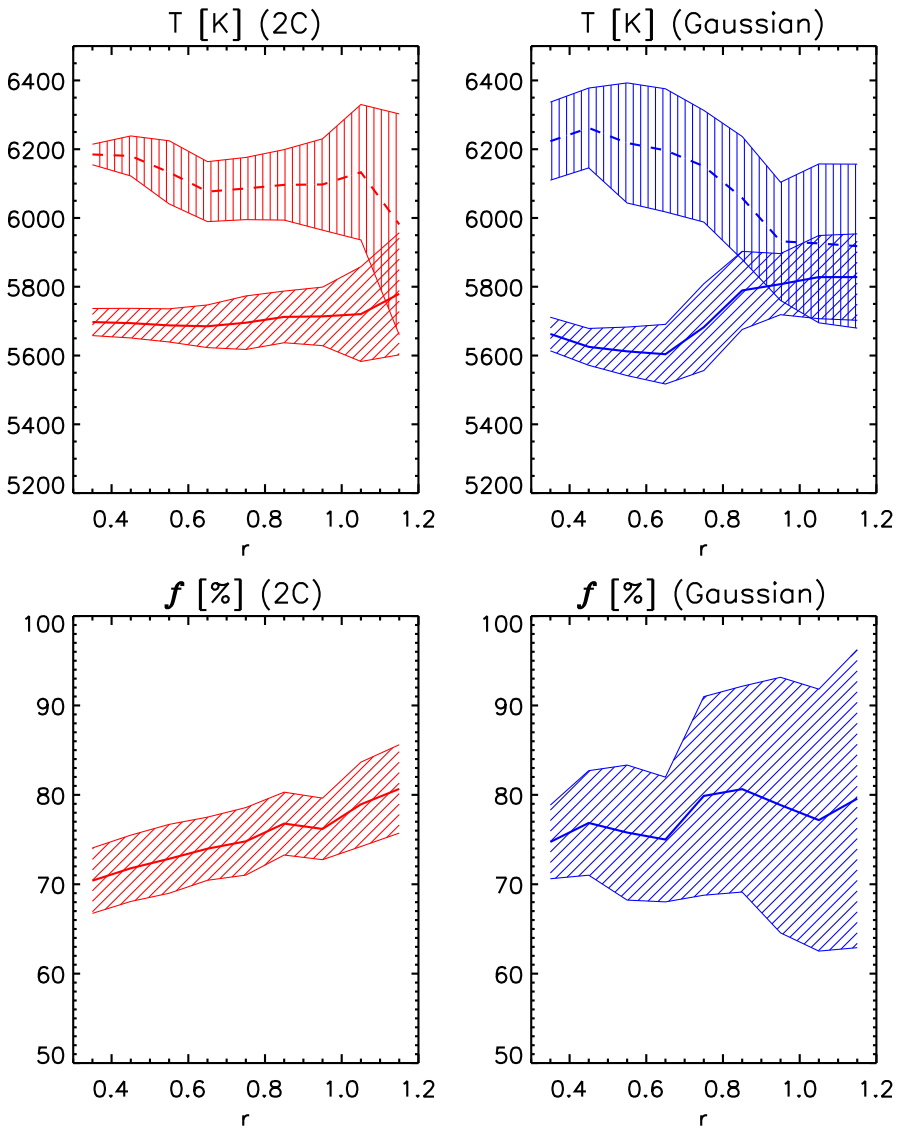

FIGURE 9.11:— Same as Fig. 9.9 for the temperature at $\log\tau = 0$ and the filling factor.

the tube (top panels of Fig. 9.9) display greater values in the inner penumbra for the two components. This result is one of the major problems that the theoretical models have to face. Both the moving tube model (Schlichenmaier 2002; Schlichenmaier et al. 1998b,a) and the siphon flow (Meyer & Schmidt 1968; Degenhardt 1989; Thomas & Montesinos 1991; Montesinos & Thomas 1997) predict greater fields of the tube at the outer penumbra. Montesinos & Thomas (1997) pointed out that the differences in the geometrical height at which the magnetic field is measured could explain this contradiction between the models and the results derived from the inversions. In fact, the radial variation of the field strengths of the tube component is much smaller than the derived for the background in agreement with the results of Borrero et al. (2005). On the other hand, if one compares the field strength of the two components the behavior derived from 2C and gaussian inversions is different. In terms of 2C, the field strength in the tube is weaker than in the background from the inner to the mid-penumbra which is agreement with the results of the moving tube of Schlichenmaier et al. (1998b). A greater field implies higher magnetic pressure and, consequently, a smaller gas pressure and temperature to maintain the horizontal total pressure balance. Hence, the radial behavior of the field strength has been interpreted as the cooling of the plasma as it flows along the tubes (Schlichenmaier et al. 1999) which has been first reported by Borrero et al. (2005). For the gaussian inversions, the field strength is always greater inside the tube. This behavior is surprising and the opposite to the inferred from the theoretical predictions given by Schlichenmaier et al. (1998b,a) and the results of the uncombed inversions of Borrero et al. (2005, 2006).

The field inclinations and azimuths derived from 2C and gaussian inversions display similar trends. As expected, the tube components display greater inclinations (bottom panels of Fig. 9.9) than the backgrounds in all radial distances. In agreement with previous investigations (Westendorp Plaza et al. 1997, 2001b; Schlichenmaier & Schmidt 2000; Mathew et al. 2003; Bellot Rubio et al. 2004; Borrero et al. 2004, 2005, 2006), field lines diving back to the solar interior ($\gamma_t > 90^\circ$) are found in the outer penumbra. On the other hand, the tube and background fields display differences in azimuth ($\leq 20^\circ$). This result is in disagreement with the radially oriented fields found for the tube and background components by Bellot Rubio et al. (2004). The reason could be the different way in which the radial curves are calculated. We construct the curves with the pixels of the ECs which only propagate along the intra-spines while Bellot Rubio et al. (2004) average the atmospheric parameters along azimuthal paths centered on the spot. This means that they derive the average behavior produced by both the spines and intra-spines.

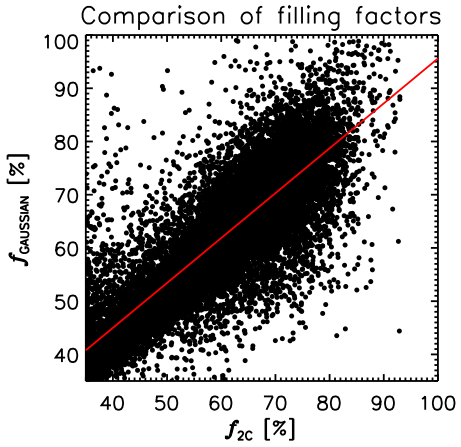

FIGURE 9.12:— Filling factors inferred from gaussian inversions against the ones retrieved from 2C inversions. Red line indicates the best fit assuming a first degree polynomial.

The velocity modulus of the tube as derived from 2C inversions (bottom panels of Fig. 9.10) increases monotonically towards the outer penumbral boundary. Its variation from the inner to the outer penumbra is ~ 1 km s^{-1} and ~ 0.7 km s^{-1} as derived from the 2C and gaussian inversions.

The radial evolution of the temperatures at $\log\tau \sim 0$ of the two components for the ECs are shown in the top panels of Fig. 9.11. As can be seen the temperatures inside the tube are smaller than in the background at all radial distances. This behavior is found in the outer penumbra by Borrero et al. (2005, 2006).

The evolution of the filling factors of the tube with radial distance are plotted in the bottom panels of Fig. 9.11. They display a monotonically increasing behavior with radial distance (Borrero et al. 2005). Since the vertical extension of the tubes do not significantly change along the penumbra (cf. Fig. 9.5), the behavior could be produced by either an increase of the number of tubes or an increase in the horizontal cross section of the tubes.

Excepting for the field strength, the values of the atmospheric parameters obtained by means of the 2C and gaussian inversions are comparable. As shown in the left panel of Fig. 9.5, the tubes extend beyond the maximum of sensitivity of the line forming region ($\log\tau \in [-0.5, -1.0]$). This together with the fact that the filling factors derived from 2C and gaussian inversions are comparable (see Fig. 9.12) explain the similarities on the values of the parameters derived from the two different geometrical models.

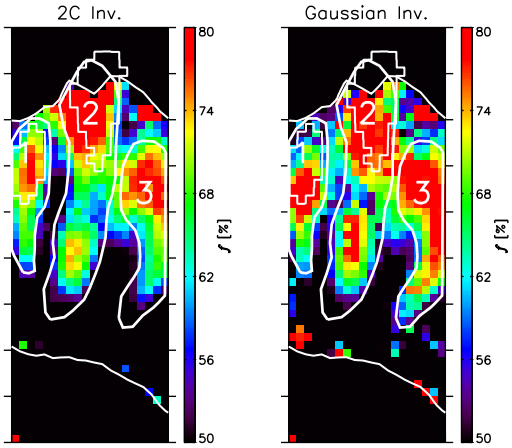

FIGURE 9.13:— Maps of the filling factor of the tube component at $t = 93.8$ min derived from 2C (*left*) and gaussian (*right*) inversions. Intra-spines are enclosed by the white lines.

9.6 ECs as structures of increased filling factor and velocity modulus

The spine/intra-spine organization of the penumbra can be interpreted as the azimuthal variation of the filling factors of two components whose properties remain relatively constant at a given radial distance (Bellot Rubio et al. 2004). In fact, spines and intra-spines can be considered as regions of the penumbra mainly filled by the tube and background components (see Fig. 9.13), respectively. Taking into account that in terms of one magnetic component the ECs can be seen as perturbations of the physical quantities propagating along the intra-spines (see Sect. 8.7), are they somehow related with variations of the filling factor?

Figure 9.14 blows up the filling factor of the tube (f) derived from 2C (top) and gaussian (bottom) for the maps where EC A is seen[3]. As can be seen, *ECs are regions of increased filling factor*. This is also shown in the left panel of Fig. 9.15 where the radial evolution[4] of f derived from gaussian inversions for the pixels of EC A and the rest of pixels of the intra-spine are plotted. As can be seen in the right panel of the same figure, the velocity modulus is also higher in the EC compared with the filament.

The differences of the filling factor of the tube (Δf) and the velocity modulus ($\Delta|v_t|$) between the ECs and the intra-spines as derived from the gaussian inversions are showed in Fig. 9.16. As can be seen, Δf is around 10 %, while $\Delta|v_t|$ is 0.7 km s^{-1}. The same plots for the differences of the field strength,

[3]This general behavior is only illustrated for the EC A

[4]The curves are constructed in a similar way than the radial curves displayed in the previous chapters.

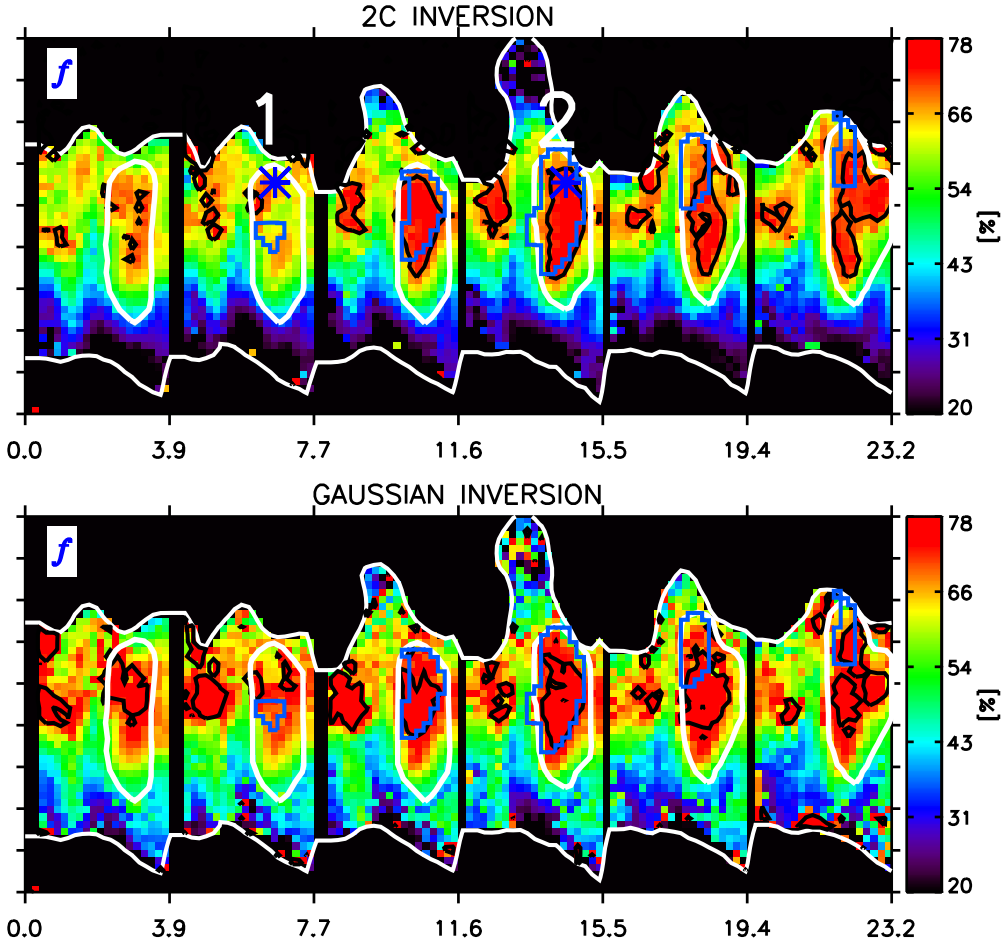

FIGURE 9.14:— Maps of the filling factor of the tube (f) derived from 2C (*top*) and gaussian (*bottom*) inversions. White contours mark the intra-spine and the boundaries of the penumbra. EC A is outlined with blue contours. Black contours delimit pixels having f larger than 70.5% (*top*) and 77% (*bottom*). Blue Asterisks and numbers on the top panel indicate the position of a pixel before and during the passage of the EC.

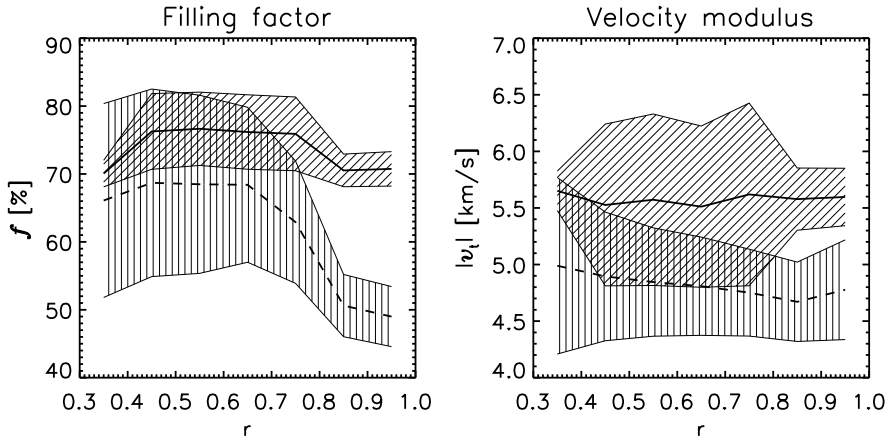

FIGURE 9.15:— *Left*: Radial evolution of the filling factor inside the EC A (solid line) and the intra-spine (dashed line). *Right*: Radial evolution of the velocity modulus of the pixels of EC A (solid line) and the intra-spine (dashed line).

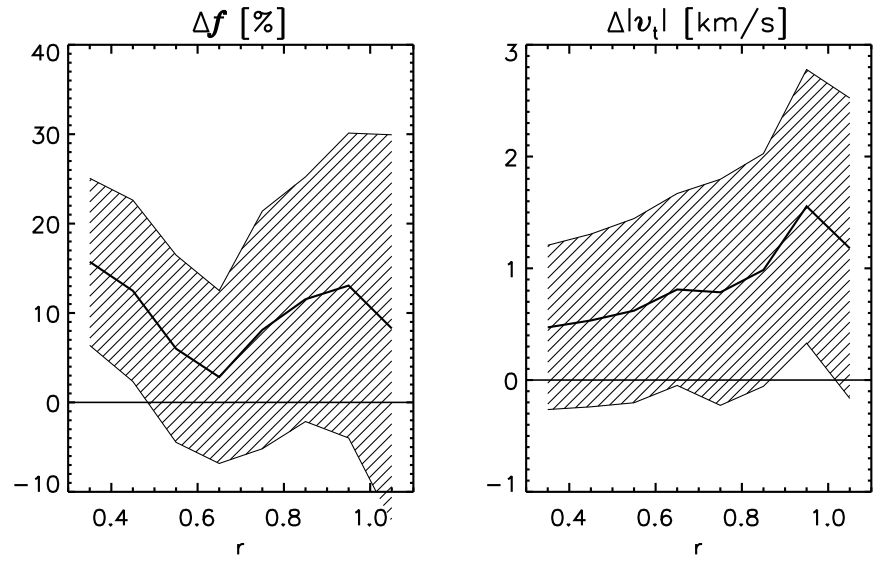

FIGURE 9.16:— Differences between the filling factor (left) and modulus of the flow velocities (right) inside the ECs and the intra-spines for the atmospheric quantities derived from gaussian inversions. The shadows are the rms variations of the differences.

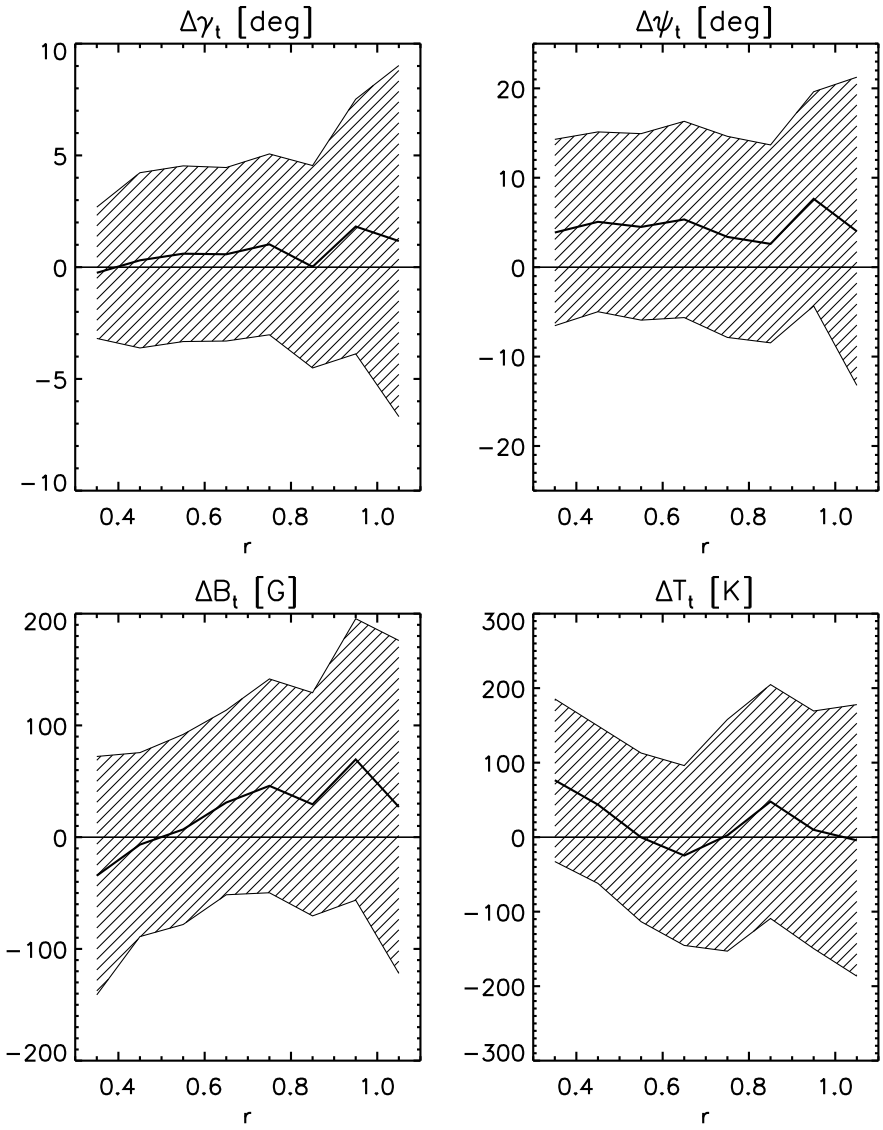

FIGURE 9.17:— Same as Fig. 9.16 for the field strength, inclination, azimuth, and temperatures at $\log\tau = 0$ of the tube.

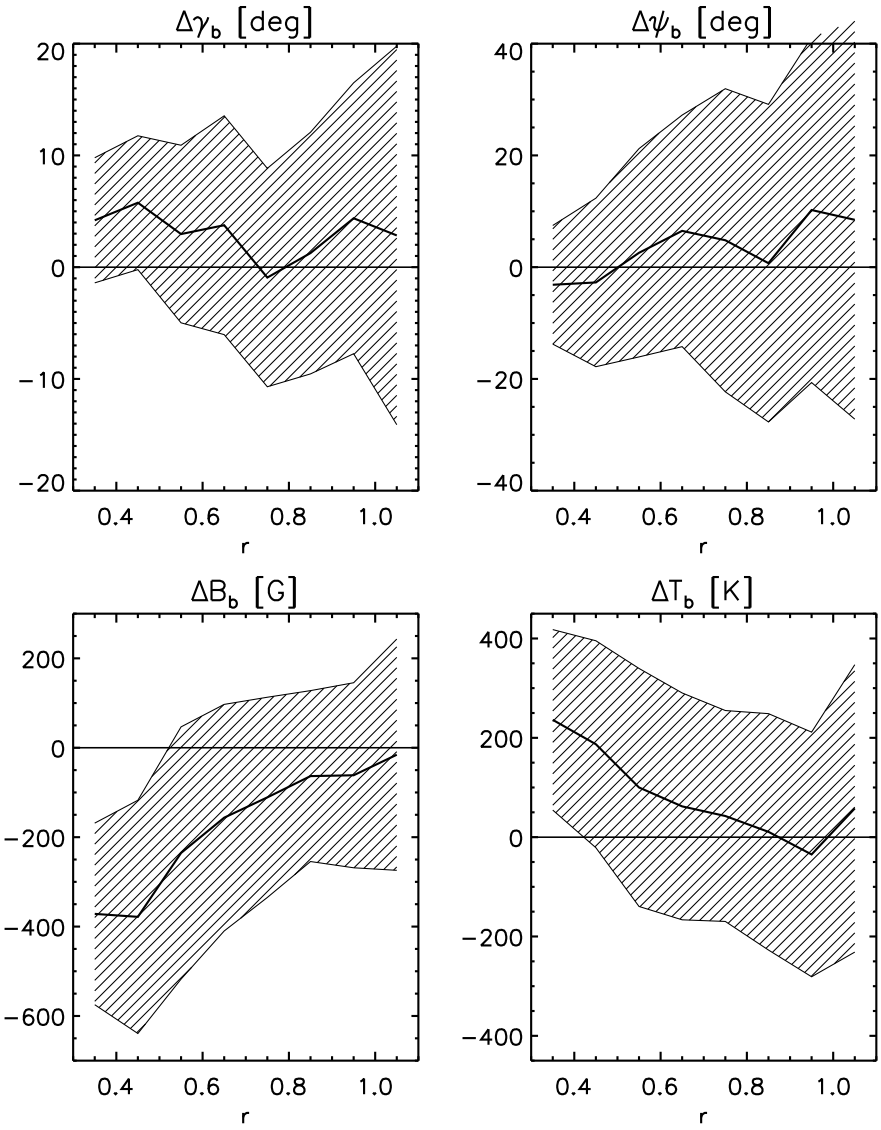

FIGURE 9.18:— Same as Fig. 9.16 for the field strength, inclination, azimuth, and temperatures at $\log\tau = 0$ of the background.

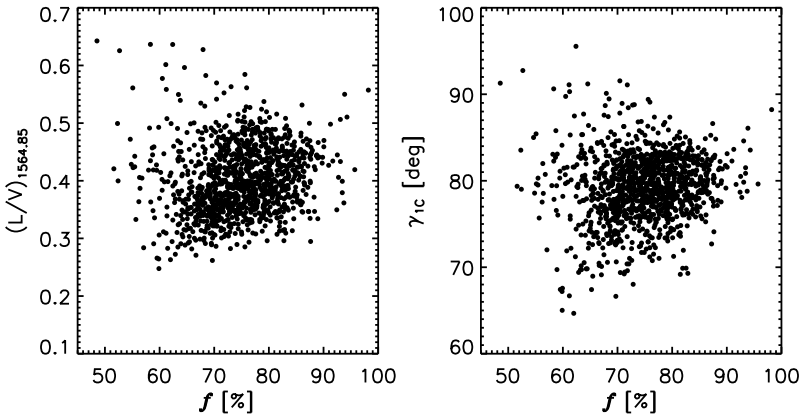

FIGURE 9.19:— *left:* Linear-to-circular polarization ratios of Fe I 1564.85 nm versus the filling factor of the tube for the pixels of the ECs. *Right:* Inclinations derived from 1C inversions against the filling factors of the tube for the ECs.

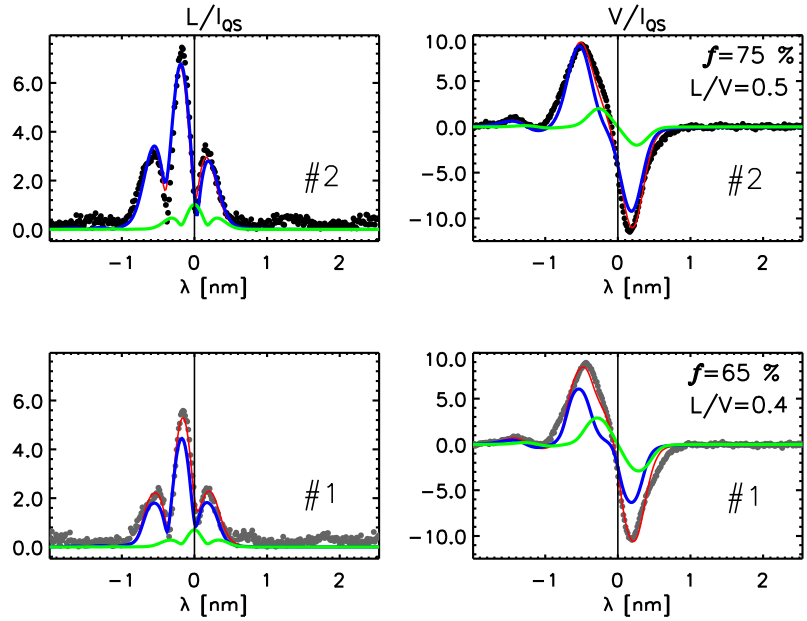

FIGURE 9.20:— Observed (dots) linear (left) and circular (right) polarization profiles of Fe I 1564.85 nm emerging from a pixel before (#1) and during the passage of EC A (#2). The pixel is marked by the asterisks and the corresponding numbers on the top panel of Fig. 9.14. Blue and green profiles represent the contributions of the tube and background components to the best-fit (red lines).

inclination, azimuth, and temperatures at $\log\tau = 0$ retrieved from gaussian inversions are shown in Fig. 9.17. The values of $\gamma_{\rm t}$ and $\psi_{\rm t}$ inside the ECs do not stand out compared with those of the intra-spines. Except for the inner penumbra, the same happens with $B_{\rm t}$ and $T_{\rm t}$. This proves that when one takes into account the uncombed structure of the penumbra, ECs do not modify the magnetic structure of the intra-spines. The same quantities for the background atmosphere are plotted in Fig. 9.18. As shown, the passage of the ECs do not modify $\gamma_{\rm b}$ and $\psi_{\rm b}$ while $B_{\rm b}$ and $T_{\rm b}$ decrease and increase in the inner penumbra, respectively.

The origin of the enhancement of f inside the ECs is shown in the left panel of Fig. 9.19 where the linear-to-circular polarization ratios of Fe I 1564.85 nm are plotted against the filling factors derived from the gaussian inversions for the pixels of the ECs. As can be seen, a larger L/V implies greater values of f. Logically, the same relation is observed between the inclinations derived from 1C inversions and f.

The former behavior is illustrated in Figure 9.20 where the observed (dots) and fitted linear and circular polarization profiles (red lines) of a pixel before (#1) and during (#2) the passage of the EC A (cf. Fig. 9.14) are shown. The contributions to the emerging profiles of the background (green lines) and tube (blue lines) atmospheres are also displayed. As can be seen, the linear polarization profiles are mainly fitted by the contribution of the tube component. When the linear-to-circular polarization ratios increase, as in the case of the ECs, the code fits the observed profiles enhancing the values of the filling factor of the tube.

9.7 Origin of the increased filling factor: variation of the thermodynamical properties

The origin of the increased filling factor of the ECs can be due to reasons of different nature: (a) an increment in the number of tubes; and (b) a greater fraction of the flux tube cross section inside the line forming region.

Since ECs propagate radially outwards along intra-spines, an organized increase in the number of tubes migrating outwards in a similar way than the ECs seems difficult. For this reason, we consider this option quite unlikely. A greater fraction of the cross section of the flux tubes inside the line forming region could be produced by different reasons: (a) movements of the tube that preserve its radius and put it nearer to the maximum of sensitivity of the line forming region; (b) an increment in the radius of the tubes; and (c) a variation of thermodynamic properties of the tube atmosphere which leads to a greater contribution of the tube. The two first possibilities are ruled out by the fact

that the positions and radius of the tubes do not change significantly with the passage of the ECs. Moreover, option (b) would imply that the field strength of the tube inside the ECs should be lower than in the intra-spines at all radial distances and this is not observed (see lower left panel of Fig. 9.17).

Therefore, we consider that a *perturbation of the thermodynamic properties* of the tubes propagating along the field lines is more feasible as the source of the enhancement of the filling factor of the ECs and, consequently, as the origin of the EC phenomenon.

9.7.1 Numerical test

We have carried out simple numerical experiments to examine whether or not larger linear-to-circular polarization ratios and, consequently, an enhancement of f, may result from the variation of thermodynamical properties inside the tube. To this end we use the model of penumbral flux tubes in mechanical equilibrium with a potential background atmosphere (Borrero 2007). In this model the flux tubes are not necessarily thin, i.e. the physical properties can change over the cross section of the tube.

We assume two different equilibrium configurations modelling the conditions of the tube and background atmospheres before and during the passage of the EC. In order to emulate the conditions before the EC passage we consider a horizontal ($\gamma_{\rm t} = 90^\circ$) flux tube driving an Evershed flow of $|v_{\rm t}| = 4.5$ km s^{-1} with a field strength of 1000 G located at the heliocentric angle of our observations (i.e. 43° on 30 June) with its axis pointing along the LS[5]. The tube have a radius of 100 km and it is surrounded by a background atmosphere with $\gamma_{\rm b} = 60^\circ$ and $B_{\rm b} = 450$ G. Figure 9.21 shows the temperature, pressure, and density conditions of the atmospheres filling the resolution element. The x and z-axes represent the horizontal and vertical directions inside the resolution element (cf. Fig. 9.1). The conditions during the EC passage are modeled by increasing the flow velocity in 1 km s^{-1} and assuming the same magnetic configuration for the flux tube. We found that an increase of the linear-to-circular polarization of the two lines is only compatible with a decrease of the temperature and pressure inside the tube (cf. bottom panels of Fig. 9.21). In order to maintain the mechanical equilibrium, the density decreases in the upper part of the tube and increases in the lower part while the field strength of the background atmosphere has to decrease[6] in 100 G. The temperature and density variations produced by the EC modify the optical

[5]Similar results are found with the tube's axis pointing 19° off of the LS.

[6]This is consistent with the lower field strength derived from the inversions for the ECs (cf. Fig. 9.18).

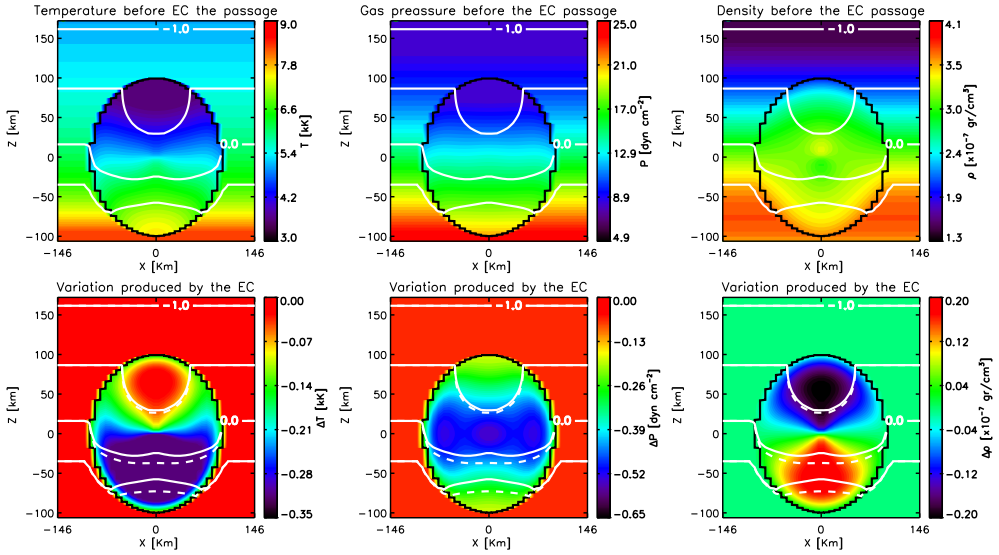

FIGURE 9.21:— *Top panels:* Temperature, gas pressure, and density in the tube and their surroundings simulating the conditions before the EC passage inside the resolution element. *Bottom panels:* Variation of the temperature, gas pressure, and density produced by the EC. The tube is enclosed by the black lines. Solid and dashed white lines indicate the $\log\tau = -1, -0.5, 0, 0.5$ before and during the EC passage.

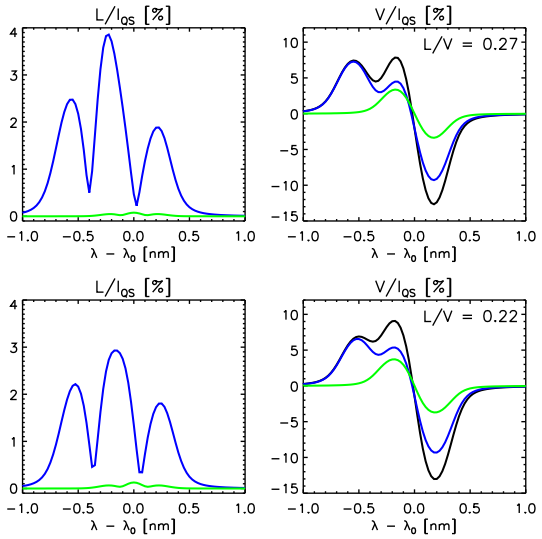

FIGURE 9.22:— Synthetic linear and circular polarization profiles simulating the conditions before (bottom) and during (top) the EC passage. Blue and green profiles represent the contributions of the tube (blue) and background (green) to the emergent profiles (black).

depth scale increasing the fraction of the tube inside the line forming region (cf. solid and dashed white lines in the bottom panels of Fig. 9.21). It is important to note that the variation of the optical depth is neglected in the upper half of the tube becoming significant near the lower half of the tube. This would explains why the upper boundary of the tube derived from the inversions do not change with the EC passage (cf. Fig. 9.5). On the other hand, the temperature variations at $\log\tau = 0$ are around of 280 K. Such differences should be detected from the inversions. Anyway, we stress that the numerical test does not pretend to provide accurate numbers but illustrates the right tendencies producing the increment in L/V.

In order to simulate the real observing conditions, the emergent Stokes profiles of the IR Fe I line at 1564.85 nm and the VIS Fe I line at 630.25 nm are calculated by averaging the synthetic profiles emerging from the resolution element. Figure 9.22 displays the emergent linear and circular polarization profiles before (bottom panels) and during (top panels) the EC passage. The contributions of the tube and background to the emergent profiles (black lines) are outlined by blue and green lines, respectively. As in the case of the observed profiles (cf. Fig. 9.20) the linear polarization profiles arise from the tube and the increment of the linear-to-circular polarization ratios is produced by an increase of the contribution of the tube to the emergent Stokes profiles. The same effect is observed in the polarization profiles of the Fe I line at 630.25 nm but in this case L/V only increases in 0.01 units.

9.8 Tube geometry inside the penumbra

In view of the increased values of f displayed by the intra-spines (cf. Fig. 9.13) one could think that they are the manifestation of individual flux tubes embedded in a more horizontal background as proposed by Solanki & Montavon (1993). As pointed by Bellot Rubio et al. (2004), one of the problems that this consideration has to face is the fact that the horizontal size of the intra-spines (0.″8-1.″5) is much greater than the typical size of the filamentary structure of the penumbra derived at very high resolution. Most of the filaments at the center side penumbra are known to have sizes around 0.″2 and display a Dark Core[7] (DC) (Scharmer et al. 2002) along them. If one considers that the typical diameter of the flux tubes coincides with the horizontal size of the DCs (0.″2 $\sim$ 150 km), an intra-spine would be filled by at least four tubes in the

[7]Numerical simulations performed by Ruiz Cobo & Bellot Rubio (2007) and Borrero (2007) indicate that those entities could be originated by flux tubes with weaker and more inclined magnetic fields. The problem is that their magnetic configuration is poorly known: there is only evidence that DC posses weaker fields than their surroundings (Bellot Rubio et al. 2005)

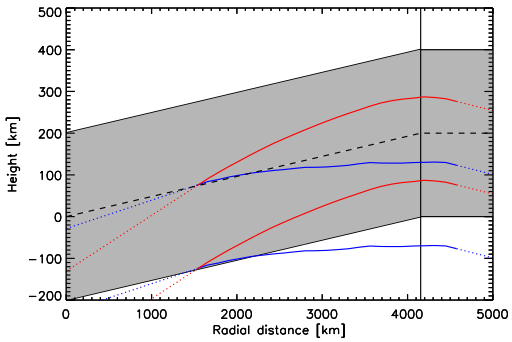

FIGURE 9.23:— Flux tube reconstructed by means of the averaged inclinations of the ECs for the tube component (see bottom panels of Fig. 9.9) as derived from 2C (red) and gaussian (blue) inversions. The dotted lines represent the extrapolation of the tube. The tube is assumed to have a radius of 200 km. The shaded area represents the line forming region ($\sim$ 400 km). A Wilson depression of $\sim$ 200 km has been assumed from the inner (i.e. $r = 0$) to the outer (vertical line) penumbra.

horizontal direction. We note that the width of the intra-spines changes along the sequence. Since the observational conditions were quite stable, this could indicate that the number of flux tubes filling the intra-spines changes with time.

On the other hand, one could also wonder whether the inclinations of the tube component inside the intra-spines are compatible with tubes extending along the penumbra in the vertical direction. Should this be the case, the tubes would not move outside of the line forming region. Since ECs propagate along the intra-spines and have the largest values of f (cf. bottom panels of Fig. 9.11) inside the penumbra, they should accurately sample the conditions of the tube. Hence, it seems suitable to construct the mean trajectory of the tubes from the average inclinations of the ECs along the penumbra ,$\langle\gamma_{\rm t}(r)\rangle$ (cf. bottom panels of Fig. 9.9). This trajectory is characterized by the elevation of the tube (Schlichenmaier & Schmidt 2000) given by:

$$h(r) = \int_0^r \tan\langle\alpha(r')\rangle dr', \tag{9.2}$$

where $\langle\alpha(r')\rangle = 90^\circ - \langle\gamma_{\rm t}(r)\rangle$ and r is the average penumbral radial distance. Fig. 9.23 displays the resulting geometry of the tube with a radius of 200 km for the results inferred from the 2c (red) and gaussian (blue) inversions. The shaded area represents the line forming region ($\sim$ 400 km). A Wilson depression of $\sim$ 200 km is assumed from the inner to the outer penumbra. As shown, the tubes are almost horizontal until the outer penumbra where they return to the solar interior. This produce a maximum elevation around 300 km (2C) and 90 km (gaussian) above the bottom of the quiet photosphere level ($h \sim 0$). This geometry is in disagreement with the *thin elevated tube* proposed proposed by Rimmele (1995). Basically, the geometry inferred from Fig. 9.23 suggests that the intra-spines could be produced by an ensemble of *low lying tubes* extending along the penumbra. If the flow is directed along the field lines, this would

explains why the Evershed flow is more conspicuous at deep atmospheric layers (see Sect. 7.7).

9.9 A qualitative geometrical model

Figure 9.24 summarizes our interpretation of the type I ECs. ECs appear quasi-periodically and propagate along the flux tubes which drive the Evershed flow. These tubes return to the solar interior at the outer penumbral boundary where the ECs dive into the photosphere and go out of the line-forming region. This scenario fits with our results and explains the disappearance of type I ECs in a natural way.

9.10 Summary and conclusions

- The atmospheric quantities of the tube and the background components inside the ECs have the following properties:
  - The field strength of the tube component is greater than the penumbral average as inferred from the gaussian inversions, while for the 2C displays smaller values in the inner and equal in the outer penumbra.
  - The tube component has greater inclinations than the background displaying field lines pointing to the solar interior ($\gamma_{\rm t} > 90^\circ$) at the outer penumbra.
  - The azimuths of the background and tube components display differences as large as 20°.
  - The velocity modulus increase from 4.7 km s^{-1} to 5.5 km s^{-1} from the inner to the outer penumbra as inferred from 2C, and from 5.3 km s^{-1} to 6.2 km s^{-1} as derived from gaussian inversions.
  - The temperature of the tube at $\log\tau \sim 0$ is smaller than the background at all radial distances.
- Except for the magnetic field strength, the values of the atmospheric parameters retrieved from 2C and gaussian inversions are compatible.
- ECs display the largest values of f and $|v_{\rm t}|$ at a given radial distance.
- The perturbations produced by the ECs along the intra-spines (cf. Sect. 8.7) have their origin on the increased values of f displayed by the ECs.

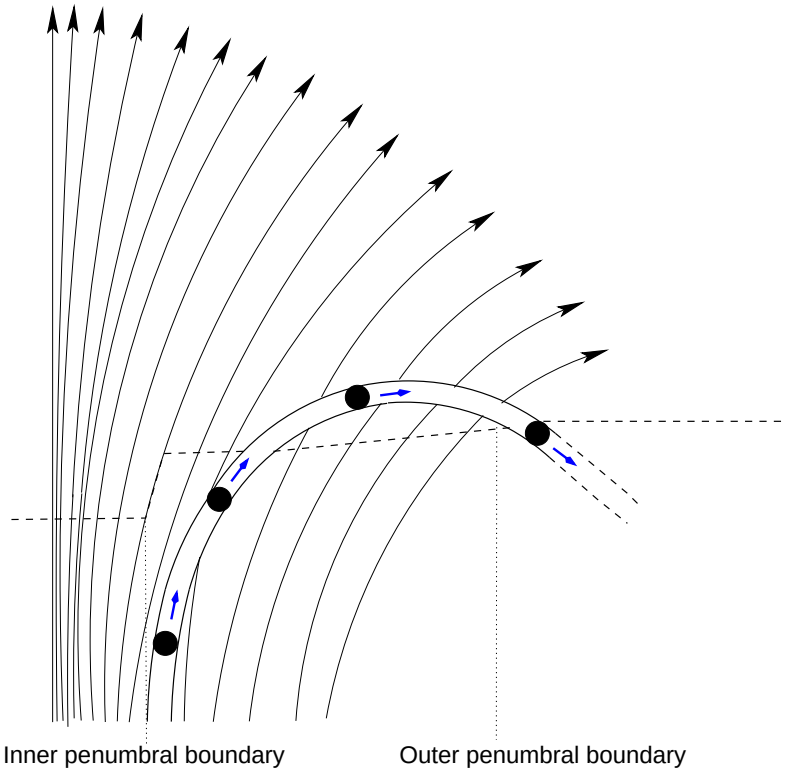

FIGURE 9.24:— Illustration of type I ECs propagating along a penumbral flux tube. ECs are represented by the black circles. The background field is outlined by the black arrows. Dashed line marks $\tau = 1$ while the vertical dotted lines indicate the penumbral boundaries.

- The tubes derived from the gaussian inversions are optically thick and/or low-lying in agreement with the results of Beck & Bellot Rubio (2007), Ruiz Cobo & Bellot Rubio (2007), and Borrero (2007).

- The increased filling factor displayed by the ECs could be produced by a a greater contribution of the tube in the deep atmospheric layers. This situation is originated by a decrease of the temperature and pressure inside the tube, while the density has to decreases in the the upper part of the tube and the opposite in the bottom.

- Intra-spines could be the manifestation of an ensemble of flux tubes extending along the penumbra. In this scenario, ECs would propagate along these tubes diving to the solar interior at the outer penumbral boundary. This would explain their disappearance.

The nature of the physical mechanism that produces the EC phenomenon has been constrained taking into the account the uncombed structure of the penumbra. As discussed in Sect. 7.2, four ECs are seen to leave the sunspot. In the next Chapter we investigate the evolution of these ECs in the moat.

10

Origin and nature of Moving Magnetic Features around sunspots

10.1 Introduction

Moving magnetic features (MMFs) are small flux concentrations observed in the moat surrounding sunspots. They were discovered by Sheeley (1969). Not surprisingly, a connection between MMFs and the magnetic field of sunspots was proposed a few years later by Harvey & Harvey (1973). The phenomenological properties of MMFs are relatively well known by now (Shine et al. 2000), but their origin and magnetic structure remain a mystery. Some investigators have pointed out the possible link between MMFs and the penumbral component carrying the Evershed flow (Martínez Pillet 2002; Schlichenmaier 2002; Thomas et al. 2002). In fact, recent observations support this idea. Using MDI magnetograms, Sainz Dalda & Martínez Pillet (2005) discovered magnetic filaments extending from the mid penumbra into the moat. Several bipolar MMFs were observed to leave the sunspot following the paths traced by these filaments. Zhang et al. (2003) and Penn et al. (2006) also detected the passage of MMFs through the outer penumbral boundary and their subsequent evolution across the moat. Bonet et al. (2004) applied a phase diversity restoration to G-band filtergrams of a sunspot. They concluded that most G-band bright points, which are associated with MMFs (Beck et al. 2007), are born close to the continuation of dark penumbral filaments. Hence, they pointed out the possible relationship between G-band bright points (or MMFs) and the more horizontal component of the penumbra. Finally, Kubo et al. (2007) analyzed Advanced

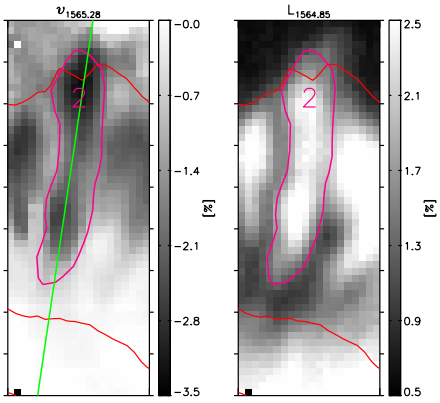

FIGURE 10.1:— Pink contours mark filament (i.e. intra-spine) #2. The green line represents a cut along the intra-spine.

Stokes Polarimeter measurements. He found significant correspondence between the magnetic field of MMFs and the penumbral uncombed structure.

In this Chapter, we study the relation between the Evershed flow, the magnetic field of the sunspot penumbrae, and the MMFs. The Chapter is structured as follows. We describe how the type II ECs modify the outer penumbral boundary when they cross it (Sect. 10.2). Their evolution beyond the outer penumbral boundary is studied in Sect. 10.3 where their disappearance into the moat (Sect. 10.3.1) and conversion to MMFs (Sect. 10.3.2) is investigated. In Section 10.4, the relation between the MMFs and the uncombed structure of the penumbra is establish. Our findings are summarized in Sect. 10.6.

10.2 Modification of the outer penumbral boundary by ECs

As mentioned in Sect. 7.2, type II ECs are seen to leave the sunspot and enter the moat. ECs D and F crossed the outer border of the spot on June 30. The relation between the arrival of these ECs to the quiet photosphere and the modification of the outer penumbral boundary is studied in this Section[1].

Figure 10.1 shows maps of the LOS velocity and the total linear polarization of filament # 2 as measured with Fe I lines at 1564.85 nm and 1565.28 nm. In Fig. 10.2 the temporal evolution of the velocity, the continuum intensity, and the total linear polarization as a function of the mean radial distance[2] are displayed for a cut along this filament (green line in Fig. 10.1). The three signals are strongly correlated at the outer penumbral boundary, which becomes more evident when an EC reaches the quiet photosphere. This happens at $t =$ 58.7 min for EC D and $t = 97.7$ min for EC F. When an EC penetrates further

[1]The results for the July 1 data set are equivalent.
[2]The radial scale is calculated as explained in Sect. 7.2

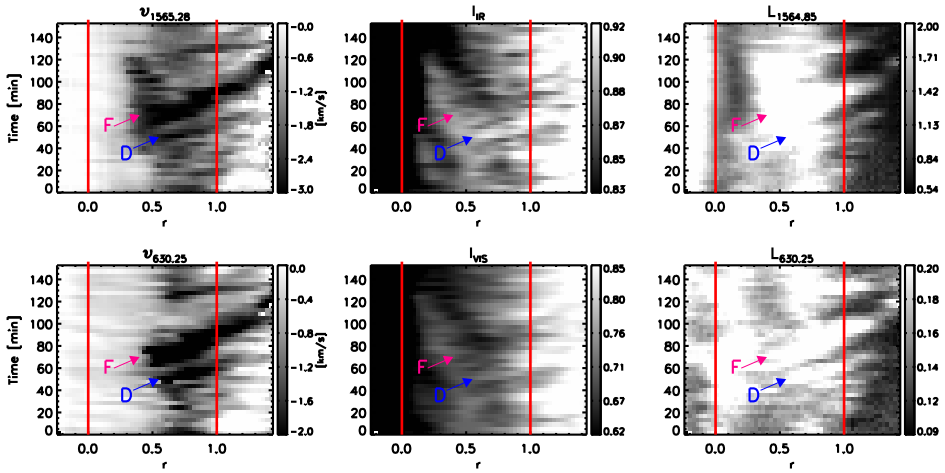

FIGURE 10.2:— Temporal evolution of line parameters along filament #2. *Top:* Stokes V zero-crossing velocity of Fe I 1565.28 nm (left), continuum intensity at 1565 nm (center), and total linear polarization of Fe I 1564.85 nm (right) for the radial cut shown in Fig. 10.1. *Bottom:* Stokes V zero-crossing velocity of Fe I 630.25 nm (left), continuum intensity at 6302 nm (center), and total linear polarization of Fe I 630.25 nm (right) for the same cut. The x-axis gives the average penumbral radial distance, r, and the y-axis displays time. The arrows indicate the positions of ECs D and F.

into the quiet photosphere, the outer penumbra does the same: an increase of the velocity and linear polarization produces a decrease of the continuum intensity in the quiet photosphere and, hence, an enlargement of the penumbra. This behavior has been already reported by Shine et al. (1994) for the intensity and velocity signals.

10.3 Evolution of type II ECs beyond the outer penumbral boundary

Both Shine et al. (1994) and Rimmele (1994) reported that some ECs penetrate slightly beyond of the outer penumbral boundary where they dissolve. In the next sections, we describe in detail the evolution of these (type II) ECs outside the spot.

10.3.1 Disappearance of the ECs into the moat

The evolution of ECs D and F in the moat can be followed in Fig. 10.3. In the top panels, EC D (blue contours) crosses the outer boundary of the spot at $t = 58.7$ min. Once in the moat region, its average propagation speed is

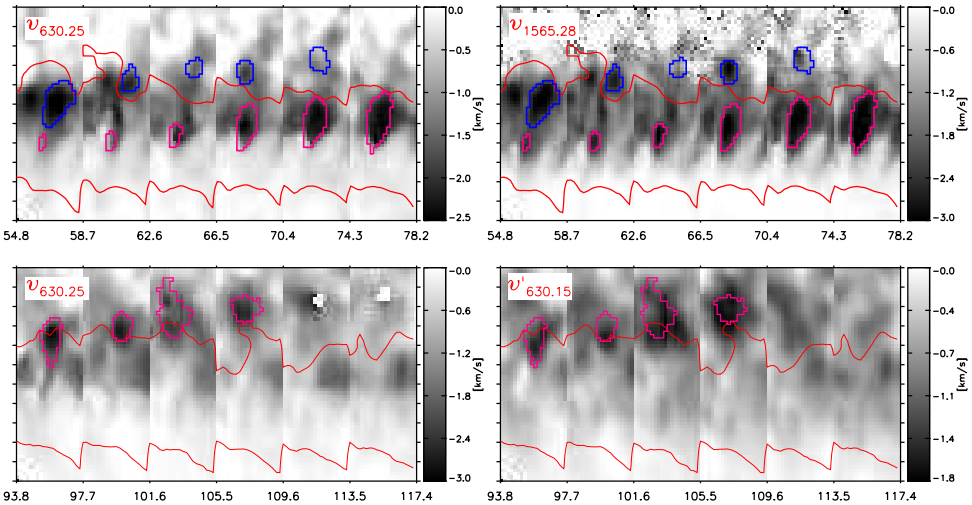

FIGURE 10.3:— *Top:* Velocities calculated by means of the Stokes V zero-crossing of Fe I 630.25 nm (*left*) and Fe I 1565.28 nm (*right*). *Bottom:* Velocities computed from the Stokes V zero-crossing of Fe I 630.25 nm (*left*) and the Doppler shifts of Stokes I of Fe I 630.15 nm. ECs D and F are outlined with blue and pink contours respectively.

~ 1.8 km s^{-1} and it is still observed until $t = 74.3$ min when it disappears at 1.″8 from the outer penumbral boundary. Then, it only survives ~ 15.6 min outside the spot.

The first map in the top panels of Fig. 10.3 demonstrates that EC F (pink contours) moves radially outward following the very same intra-spine as feature D (i.e. filament #2). The Evershed cloud crosses the penumbral boundary between $t = 93.8$ and $t = 97.7$ min and its proper motion outside the spot is ~ 1.9 km s^{-1}. Abnormal Stokes V profiles[3] appear in the positions where one would locate the EC at $t = 109.6$ (left panel). For this reason we also plot the velocities inferred from the Doppler shifts of Stokes I, $v'_{630.15}$ (right panel). As shown, the evolution of EC F can be tracked in both panels until $t = 109.6$ when EC F disappears 11.9 min after crossing the spot boundary.

The evolution of ECs M and N outside the spot is shown in Fig. 10.4 where the intensities at 1565 nm, the logarithm of the total circular polarization of Fe I 1564.85 nm, the magnetogram of Fe I 630.25 nm, and the Stokes-V zero-crossing shifts of Fe I 1565.28 nm and Fe I 630.25 nm are plotted from top to bottom. As can be seen, EC M is only visible in two maps, while EC N is seen

[3]Stokes V zero-crossing velocities can only be calculated for regular profiles. The pixels with abnormal profiles appear in blank in the velocity maps calculated by means of Stokes V profiles.

TABLE 10.1:— Phenomenological and morphological properties of type II ECs in the moat. The time and distance from the outer penumbral boundary where the ECs are seen to vanish are given in the second and third columns. The fourth column displays the time each EC survives in the quiet photosphere. The proper motions of each EC in the moat are given in the fifth column. The last two columns display the maximum lengths and widths reached by each EC, corrected for LOS effects, outside the penumbra. The last row shows the mean values of the quantities. The parentheses indicate that EC M leaves the FOV before disappearing.

EC	$t_{\rm dis}$ [min]	$d_{\rm dis}$ [arcsec]	$\tau_{\rm ph}$ [min]	$v_{\rm prop}$ [km s^{-1}]	$\mathcal{L}$ [km]	$\mathcal{W}$ [km]
D	74.3	1.8	15.6	0.6 ± 0.3	1300	700
F	109.6	1.8	11.9	1.9 ± 0.4	1000	1200
(M)				3.5 ± 0.0	900	400
N	57.8	2.1	14.0	1.3 ± 0.1	900	600
Mean		**1.9**	**13.8**	**1.8**	**1000**	**700**

to disappear at 2.″1 from the spot boundary.

The main phenomenological and morphological properties of ECs D, F, M, and N in the moat are summarized in Table 10.1. As shown in the third and fourth columns, the behavior of type II ECs in the moat is very similar: they quickly dissolve ($\sim$ 13.8 min) fairly near the outer penumbral boundary ($\sim$1.″9).

As discussed in Sect. 7.2, the two types of ECs show up as elongated structures inside the spot. Once type II ECs enter the moat, their lengths and widths are comparable (cf. the two last columns of Table 10.1) adopting a roundish shape. Moreover, their proper motions are reduced: one can see that the propagation velocities of the type II ECs in the moat (the fourth column of Table 10.1) are always smaller than their corresponding values inside the penumbra (the seventh column of Table 7.1).

10.3.2 Type II ECs as precursors of MMFs

In Fig. 10.5 we show part of the temporal evolution of the penumbra observed on 30 June when ECs D (blue) and F (pink) are seen to propagate outwards. We plot the velocities derived from Fe I 1565.28 nm and Fe I 630.25 nm, and the total linear polarization of the Fe I line at 1564.85 nm, besides the magnetograms constructed by means of the Stokes V signal of Fe I 630.25 nm at $\Delta\lambda = +10$ from line center, $\mathrm{M}_{630.25}$.

In the magnetograms one can see that, once ECs D (t = 74.3 min) and F (t = 109.6 min) vanish into the quiet photosphere, they become MMFs with positive and negative polarities respectively. The opposite-polarity flux patches are observed to move away from the spot in the moat region (cf. the

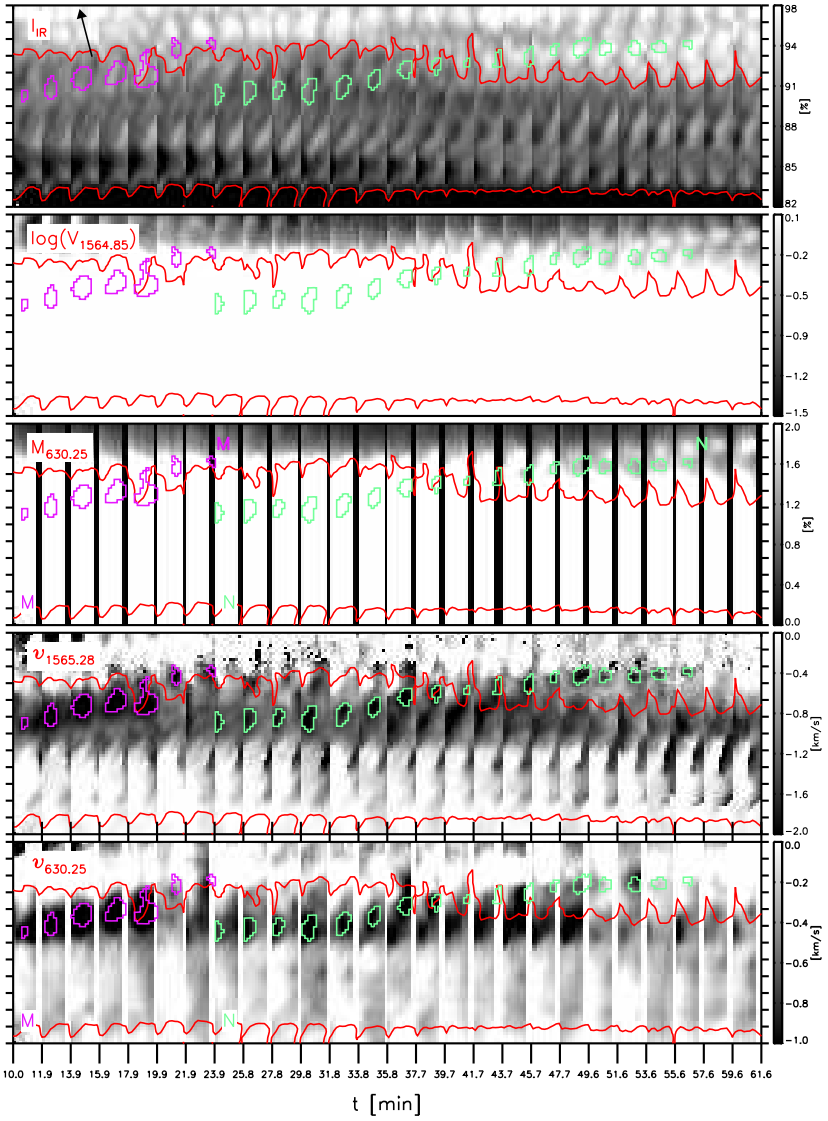

FIGURE 10.4:— From *top* to *bottom*: Continuum intensity at 1565 nm, logarithm of the total circular polarization of Fe I 1564.85 nm, magnetogram signal from Fe I 630.25 nm, logarithm of the total linear polarization of Fe I 1564.85 nm, Stokes V zero-crossing velocity of Fe I 1565.28 nm, and Stokes V zero-crossing velocity of Fe I 630.25 nm. Negative velocities are blueshifts. Pink and green contours delimit features M and N, respectively. Red lines indicate the inner and outer penumbral boundaries. Each tickmark in the y-axis represents $1''$. The arrow marks the direction to disk center. $t = 0$ min corresponds to July 1, 9:31 UT.

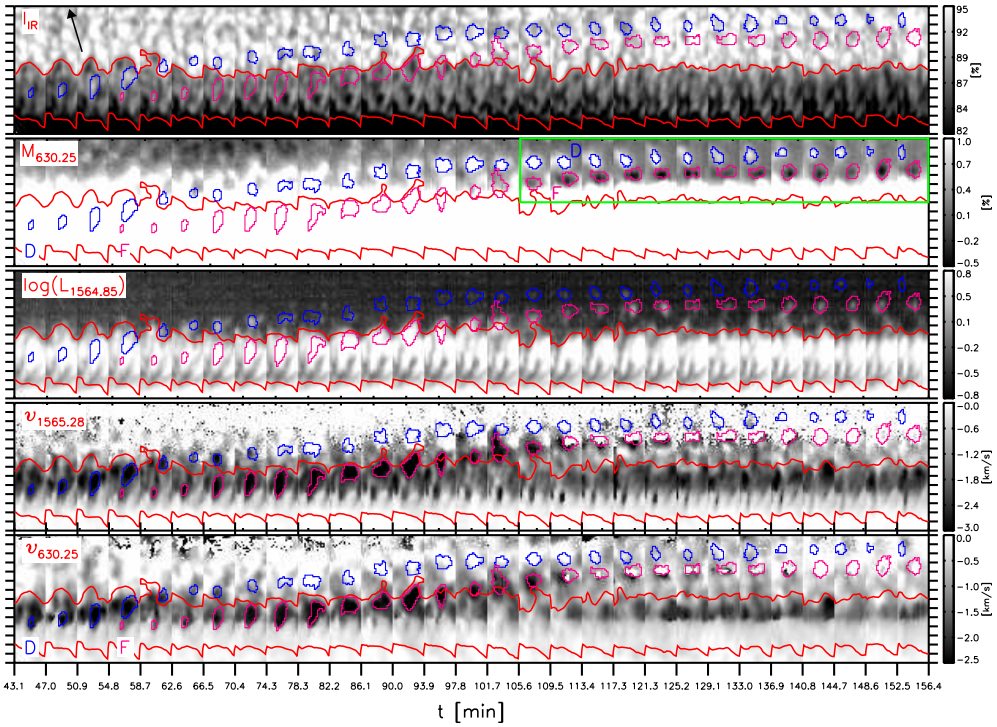

FIGURE 10.5:— From *top* to *bottom*: Continuum intensity at 1565 nm, magnetogram signal from Fe I 630.25 nm, logarithm of the total linear polarization of Fe I 1564.85 nm, Stokes V zero-crossing velocity of Fe I 1565.28 nm, and Stokes V zero-crossing velocity of Fe I 630.25 nm. Negative velocities are blueshifts. Pink and blue contours delimit features D and F, respectively. Red lines indicate the inner and outer penumbral boundaries. Each tickmark in the y-axis represents $1''$. The arrow marks the direction to disk center. $t = 0$ min corresponds to June 30, 8:47 UT.

area enclosed by the green box in the magnetograms of Fig. 10.5). Hereafter, the positive and negative flux patches are called features D and F respectively for obvious reasons. The properties of this pair are similar to those of bipolar MMFs: the separation between the two polarities is around $2''$ (Zhang et al. 2003), the magnetic patch having the same polarity as the sunspot is located farther from the spot (Lee 1992; Yurchyshyn et al. 2001; Zhang et al. 2003), and the average proper motion, corrected for the viewing angle, is around 0.5 km s^{-1} (Nye et al. 1984; Zhang et al. 2003). Hence, features D and F could be classified as a bipolar MMF or, according to Shine et al. (2000), as a type I MMF. However, from the magnetogram data alone we cannot rule out the possibility that D and F are two unrelated MMFs of type II and III. The conclusion that *MMFs can be traced back to Evershed clouds* appearing

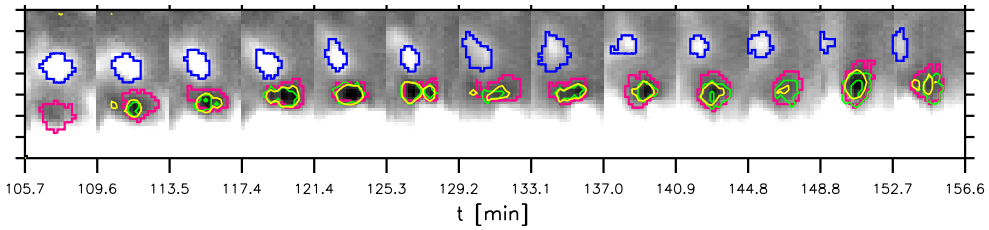

FIGURE 10.6:— Magnetograms showing the evolution of the bipolar MMF in the sunspot moat. The gray scale ranges from −0.5% to +1%. Pink and blue contours represent features D and F. Yellow contours delimit pixels having negative polarity, while green contours outline pixels with abnormal Stokes V profiles.

in the mid-penumbra is nevertheless a solid result that does not depend in any way on the exact nature of the flux concentrations. The second and third panels of Fig. 10.5 demonstrate that the two flux patches possess different field inclinations. While feature F shows up in both L and M, feature D is observed mainly in M. This indicates that feature F has more inclined magnetic fields to the LOS than feature D. Also interesting is that feature F seems to be connected to intra-spine #2 at $t = 133.1$ min (cf. third panel of Fig. 10.5).

In Fig. 10.4 we plot the maps where ECs M (purple) and N (green) are seen to leave the penumbra observed on 1 July. As can be seen, EC M is only visible in two maps in the moat (between $t = 19.9$ min and $t = 23.9$ min). On the other hand, EC N does not show up conspicuously in either the magnetogram or total circular polarization outside the spot (between $t = 43.8$ min and $t = 57.8$ min) compared with its surroundings. Also interesting is the presence of an MMF which propagates parallel to EC N outside the spot. It does not seem to be preceded by any EC and, according to Shine et al. (2000), would be classified as type II MMF.

Abnormal profiles inside MMFs

Anomalous Stokes V profiles with three or four lobes occur frequently in MMFs. This is demonstrated for the first time by our observations. Figure 10.6 blows up the magnetograms derived from Fe I 630.25 nm inside the green box of Fig. 10.5. The yellow contours outline areas where the polarity is opposite to that of the spot. The green contours mark the areas where we detect abnormal profiles. As can be seen, these pixels coincide quite precisely with positions of negative polarity in the magnetograms.

In Figs. 10.8–10.10 we show examples of co-spatial Stokes I and V profiles of Fe I 630.15 nm, Fe I 630.25 nm, Fe I 1564.85 nm, and Fe I 1565.2 nm. The positions where the profiles emerged from are marked with crosses and

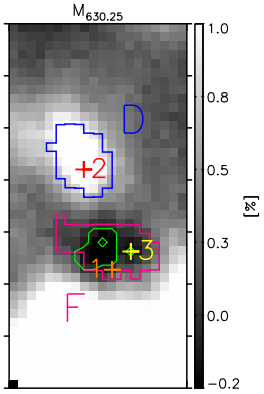

FIGURE 10.7:— Magnetogram of Fig. 10.6 at t=117.4 min. The crosses and numbers indicate the positions inside the MMFs corresponding to the co-spatial profiles shown in Figs. 10.8, 10.9, and 10.10.

numbers in Fig. 10.7. The two first examples correspond to regular Stokes V profiles. These profiles display asymmetries which can be explained in terms of gradients of the physical quantities along the LOS. The last figure displays an example of abnormal Stokes V profiles emerging from a pixel inside feature F. Such very complex profiles could be caused by the presence of several magnetic components in the resolution element. In fact, two magnetic components coexisting inside the resolution elements with different inclinations are enough to produce the mixed polarities displayed by the abnormal Stokes V profiles. This motivate us to speculate that the abnormal profiles could be the signature of the tube and background components described in Sect. 9.5. On the other hand, the anomalous profiles could be also caused by strong gradients of the atmospheric parameters along the LOS. These gradients could be produced by the interaction between the magnetic field and the convective motions of the plasma outside the spot. Such motions of material could drag the field lines producing a complex topology of the magnetic field that would lead to the emerging abnormal Stokes V profiles.

The problem with abnormal Stokes V profiles is that the meaning of polarity looses its sense, as both positive and negative polarities can be assigned to the same pixel depending on the exact wavelength(s) used to construct the magnetogram. It is not surprising that the existence of abnormal profiles has gone unnoticed: most of what we know today about MMFs has been learnt from magnetograph observations that cannot reveal this kind of spectral subtleties. One should realize, however, that gross errors may result from direct interpretations of magnetograms when abnormal profiles exist, simply because even the polarity of the field would be an ill-defined quantity.

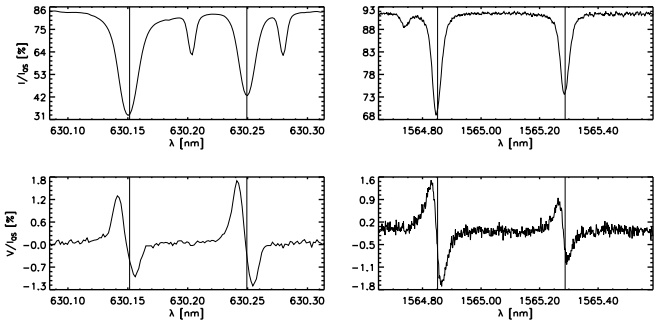

FIGURE 10.8:— Cospatial Stokes I (*top*) and V (*bottom*) profiles of Fe I 630.15 nm, Fe I 630.25 nm, Fe I 1564.85 nm, and Fe I 1565.2 nm emerging from pixel #1 inside feature F (see Fig. 10.7) with normal circular polarization signals. The vertical solid lines represent the rest wavelengths of the spectral lines.

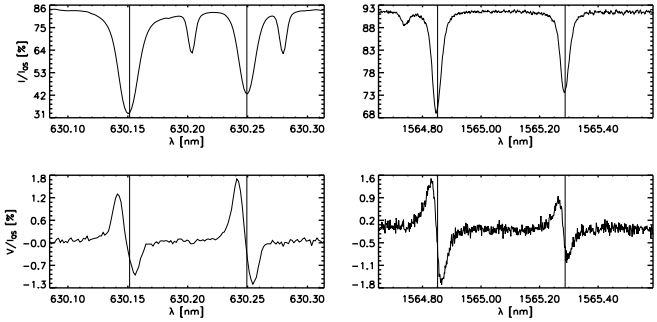

FIGURE 10.9:— Same as Fig. 10.8 for pixel #2 inside feature D with normal circular polarization signals.

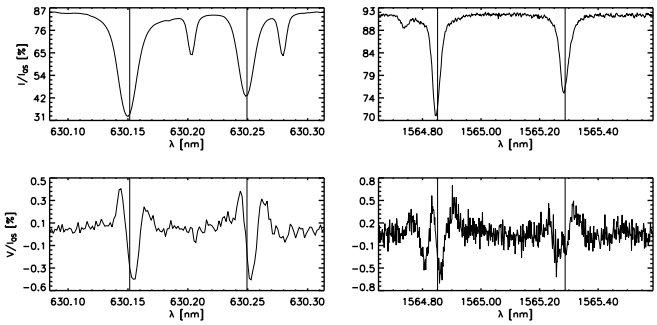

FIGURE 10.10:— Same as Fig. 10.8 for pixel #3 inside feature F with anomalous circular polarization signals.

10.4 Nature of MMFs and their relation with the uncombed structure of the penumbra

In this section we study the physical origin of the MMFs by analyzing the atmospheric parameters derived from the one-magnetic-component inversions (cf. Sect. 8.2). This allow us to find a new type of MMFs which are not preceded by ECs and appear inside the spines. Hence, we characterize the physical properties of two different types of MMFs: (a) MMFs originating from intra-spines (cf. Sect. 10.3.2); and (b) MMFs originating from spines. Hereafter, we call them i-MMFs and s-MMFs, respectively. Our results establish a link between the apparition of MMFs around sunspots and the uncombed structure of the penumbra. We anticipate that our findings are in agreement with the results of Kubo et al. (2007) who found a correspondence between the magnetic configuration of the MMFs located along the lines extrapolated from the spines and intra-spines and the uncombed structure of the penumbra.

10.4.1 MMFs originating inside intra-spines (i-MMFs)

The evolution of the field strength (B), LRF inclination (γ), magnetic flux (Φ), and velocity modulus ($|v|$) of ECs D (blue contours) and F (pink contours) when they become MMFs propagating in the moat is shown in Fig. 10.11. The magnetic flux is calculated as $\Phi = fB\cos\gamma A$ where f and A are the fractional area filled by the magnetic atmosphere and the pixel area, respectively. As can be seen, once EC D enters the moat ($t = 58.7$ min) it displays higher field strengths than its surroundings. This is the origin of the increased values in the magnetogram signal[4] (cf. Fig. 10.5) and allow us to detect the MMF when the EC disappears. For MMF F the situation is more complicated as the presence of abnormal circular polarization profiles does not allow us to invert most of the pixels inside it[5]. Hence, we only study the evolution of its physical properties until the appearance of abnormal Stokes profiles ($t = 109.5$ min).

Bipolar MMF: Sea-serpent scenario

As shown in Fig. 10.5, MMFs D and F appear in the magnetograms as a bipolar MMF. Three different geometries of the magnetic field have been proposed to originate such MMFs. Harvey & Harvey (1973) suggested that bipolar MMFs could be produced by the intersection of the same field lines forming Ω-loops

[4]The magnetogram signal is proportional to $f\cos\gamma_{\rm LOS}B$.

[5]If one wants to reproduce the abnormal profiles, at least, two magnetic components have to be taken into account. In the moat one should also consider the effect of the non-magnetic atmosphere.

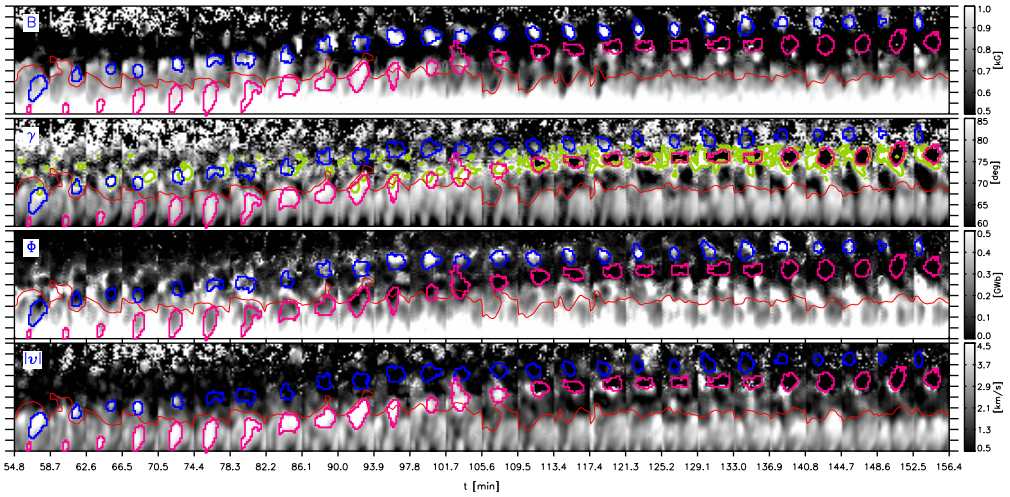

FIGURE 10.11:— From *top* to *bottom*: Field strength, inclination, magnetic flux, and flow velocity derived from 1C inversions. Blue and pink contours outline MMFs D and F in the moat and their precursors (i.e. ECs D and F) inside the spot. Green contours outline inclinations larger than 90° in the second panel. $t = 0$ min corresponds to June 30, 8:47 UT. Each tickmark in the y-axis represents 1″.

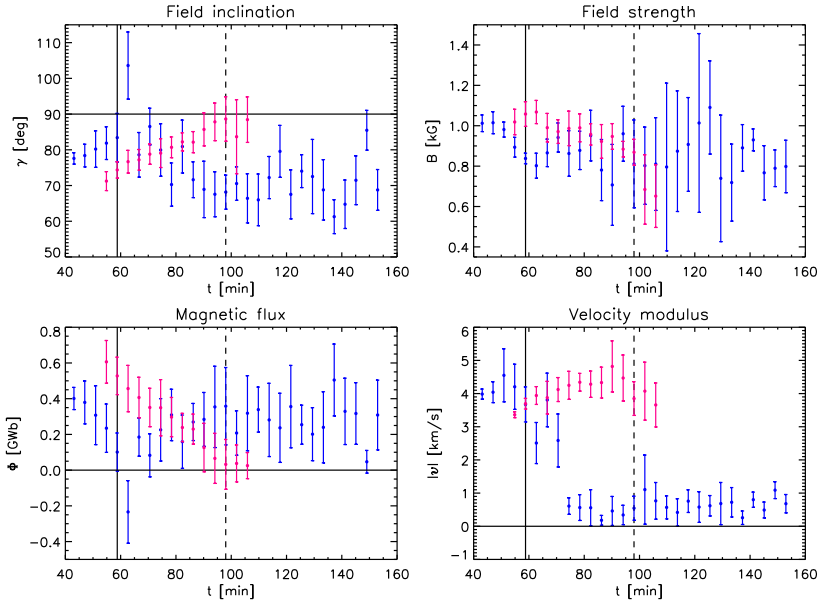

FIGURE 10.12:— Evolution of average field inclination, field strength, magnetic flux, and flow velocity in features D (blue) and F (pink). Dots represent the mean values inside the contours and the bars their standard deviations. Vertical solid and dashed lines mark the times when ECs D and F reach the moat.

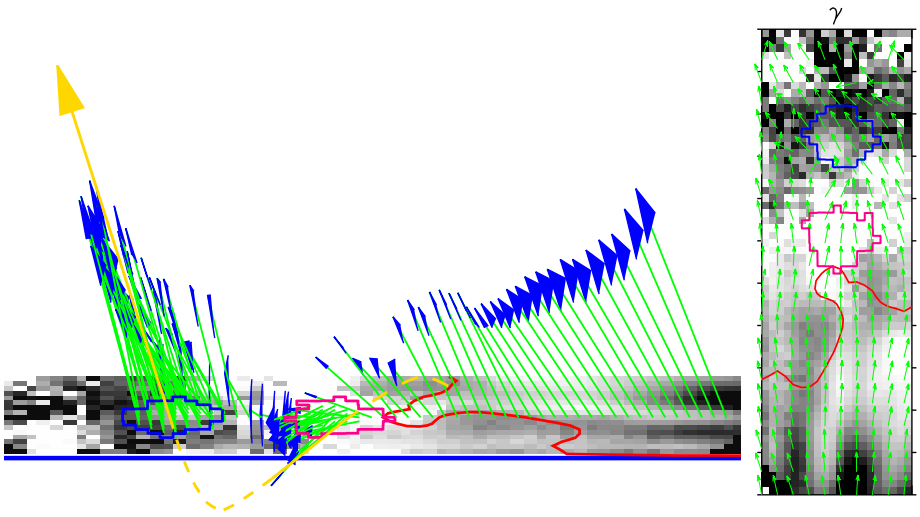

FIGURE 10.13:— Inclinations inside MMFs D and F at $t = 105.6$ min. Blue and pink contours enclose MMFs D and F. Each arrow indicates the orientation of the magnetic field in the LRF. Green and red arrows outline inclinations smaller and larger than 90°, respectively. The gray scale ranges from 50°(black) to 80°(white). The yellow line illustrates the geometry of a field line connecting the fields of the two MMFs. For MMF F only arrows with inclinations larger than 90° are showed.

with the solar photosphere while Zhang et al. (2003) proposed ℧-loops. This is the well known sea-serpent scenario. On the other hand, Wilson (1986) suggested closed field lines in the form of O-loops. In this section we study which of these models fits our observations of MMFs D and F.

Figure 10.12 quantifies the evolution with time of γ, B, Φ, and $|v|$ inside features D and F. We plot their average values for each contour of the features from the moment when they appear as ECs inside the penumbra. The vertical lines mark the times when EC D (solid line) and F (dashed line) reach the quiet photosphere. As can be seen in the top left panel of Fig. 10.12, the two ECs leave the spot with pixels displaying inclinations[6] greater than 90°. When EC D reaches the moat ($t = 58.7$ min), EC F is still inside the penumbra and displays inclinations smaller than 90°. When EC F leaves the spot ($t = 97.8$ min) and becomes an MMF, its magnetic field is already pointing downwards. This result

[6]Since the two ECs are structures extending from the mid to the outer penumbra, inclinations greater than 90° are only found in pixels at the outer boundary of the penumbra. This is the reason because the mean inclination of ECs D and F at the outer boundary of the spot are lower than 90°(cf. green contours at the second panel of Fig. 10.11 at $t = 54.8$ min (EC D) and $t = 93.9$ min (EC F)).

suggests that *the two MMFs could be the manifestation of the same field lines passing through them.* Figure 10.13 shows the orientation of the magnetic field for the pixels inside the MMFs. The yellow line illustrate a field line emerging from the spot that cross the two MMFs following the inferred geometry of the MMFs' magnetic field. This indicates that the two MMFs could be caused by a sea-serpent-like flux tube. In fact, only a $\mho$-loop could originated the geometry of the magnetic field inferred from the two MMFs. O and Ω-loops imply fields with $\gamma < 90^\circ$ at the outer penumbra in one of the two MMFs and this is not observed.

As shown in the upper right panel of Fig. 10.12, B decreases with radial distance for the two ECs inside the penumbra. Once they are in the moat ($t > 97.8$ min), MMF D displays stronger fields ($B \sim 0.85$ kG) than MMF F ($B \sim 0.7$ kG). Should the two MMFs be the manifestation of the same field lines, the predictions for higher field strengths at larger radial distances of the theoretical models (Schlichenmaier et al. 1998b; Meyer & Schmidt 1968) would be fulfilled. On the other hand, if the MMFs were produced by the same field lines, the magnetic flux inside the areas enclosed by them should be conserved. In other words, the magnetic flux across MMF F should be the same in magnitude and opposite in sign as the flux inside the area enclosed by MMF D. As shown in the lower left panel of Fig. 10.12, MMF F displays negatives values of Φ in the moat ($t \in [97.8, 105.6]$ min) but these values do not cancel the positive values of MMF D. This indicates that the magnetic flux across the two MMFs is not conserved. Anyway, we note that after taking into account the difficulties in the measurements and the arbitrary definition of the area delimiting each MMF, we do not consider this apparent disagreement a major obstacle to the sea-serpent scenario.

The bottom right panel of Fig. 10.12 shows the flow velocity. $|v|$ increases within the penumbra inside the two features. Once they reach the moat, their flow velocity decreases. In fact, when EC D disappears (cf. Sect. 10.3.1) and becomes an MMF at $t \sim 74.4$ min, it exhibits flow velocities generally smaller than 1 km s^{-1}.

Do all the ECs become MMFs in the moat?

In this section we study the physical properties of ECs M and N which are not detected as MMFs in the moat. Figure 10.14 shows B, γ, Φ, and $|v|$ for the sequence observed on 1 July from $t = 10.0$ min to $t = 61.6$ min. ECs M and N are outlined with purple and green contours, respectively. EC N does not display larger field strengths than its surroundings in the quiet photosphere ($t > 43.7$ min). This is the main reason why it is not seen as an MMF in the

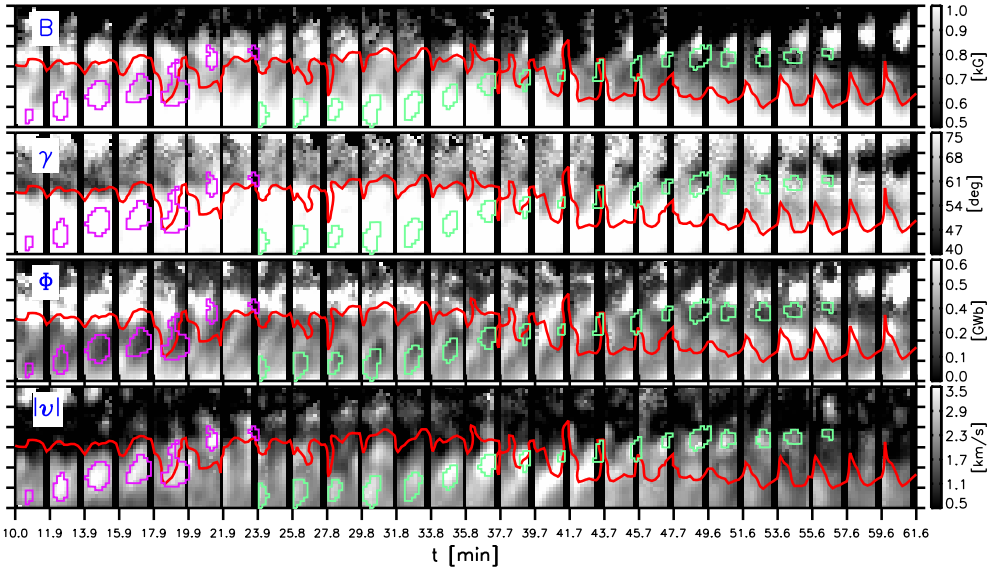

FIGURE 10.14:— Same as Fig. 10.11 for the time sequence observed on 1 July from t = 10.0 min to t = 61.6 min. Purple and green contours outline ECs M and N. t = 0 min corresponds to July 1, 9:31 UT.

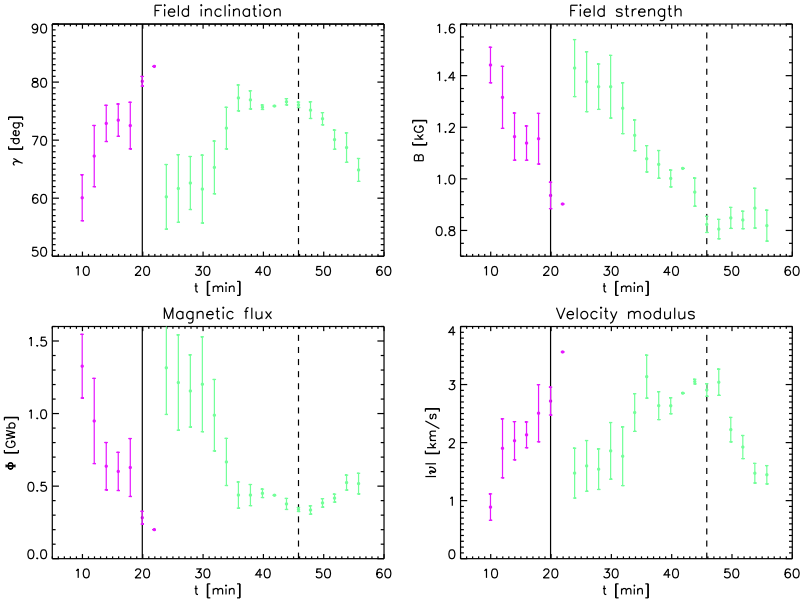

FIGURE 10.15:— Same as Fig. 10.12 for ECs M (pink) and N (green). Vertical solid and dashed lines mark the times when ECs M and N reach the moat.

magnetograms (cf. Fig. 10.4). In contrast, there is an MMF with stronger and less inclined fields than the surroundings propagating parallel to EC N. The possible origin of this type of MMFs will be discussed in the next section.

The evolution of γ, B, Φ, and $|v|$ inside the two ECs is summarized in Fig. 10.15. As can be seen, γ increases until the ECs enter the the moat where it begins to decreases. ECs M and N do not display field inclinations larger than 90° in the outer penumbra. This result is a consequence of the use of one magnetic component. As pointed by Bellot Rubio et al. (2003), one-component atmospheres deliver more vertical fields than those retrieved if one takes into account two magnetic components. In fact, with 2C and Gaussian inversions, we recover inclinations greater than 90° for the two ECs in the outer penumbra for the tube atmosphere. The field strength of ECs M and N decreases until the outer penumbra, reaching values around $B \sim 0.9$ G and $B \sim 0.85$ G in the moat. *These values are similar to those displayed by the MMFs of the former section.* The fact that the EC N is not detected as an MMF in the magnetograms is due to the stronger signal of the canopy of the spot for this day. This does not allow us to detect the EC as an isolated MMF. On the other hand, $|v|$ behaves in the same way as for the ECs of the former section: $|v|$ increases inside the spot and decreases in the moat until the EC vanishes.

10.4.2 MMFs originating inside spines (s-MMFs)

Figure 10.16 shows the evolution of two structures which are seen to appear along the spines. We have outlined them with orange and green contours and refer to them as features O and P, respectively. Feature O is first detected at $t = 105.7$ min as a structure with more vertical fields than its surroundings (cf. second panel of Fig. 10.16). It propagates with an average speed, corrected for the viewing angle, of 0.9 km s^{-1}. At $t = 121.3$ min feature O is also observed as an increased field strength structure (cf. first panel of Fig. 10.16). This happens at only $1''$ from the outer penumbral boundary. Near the spot, the polarization signal of the canopy is strong. *This is the reason why is hard to detect this MMF in the magnetograms.* Feature O propagates in the moat until $t = 140.8$ min, so it disappears 35 min after its apparition at $\sim 2''$ from the outer boundary of the spot.

Feature P appears at $t = 125.2$ min displaying more vertical fields than its surroundings (cf. second panel of Fig. 10.16). It propagates with an average speed of 1.1 km s^{-1}. At $t = 140.8$ min it shows up as an increased field strength structure. The second and third panel demonstrate that the feature also appears inside a spine.

Figure 10.17 shows the evolution of γ, B, Φ, and $|v|$ of the two features

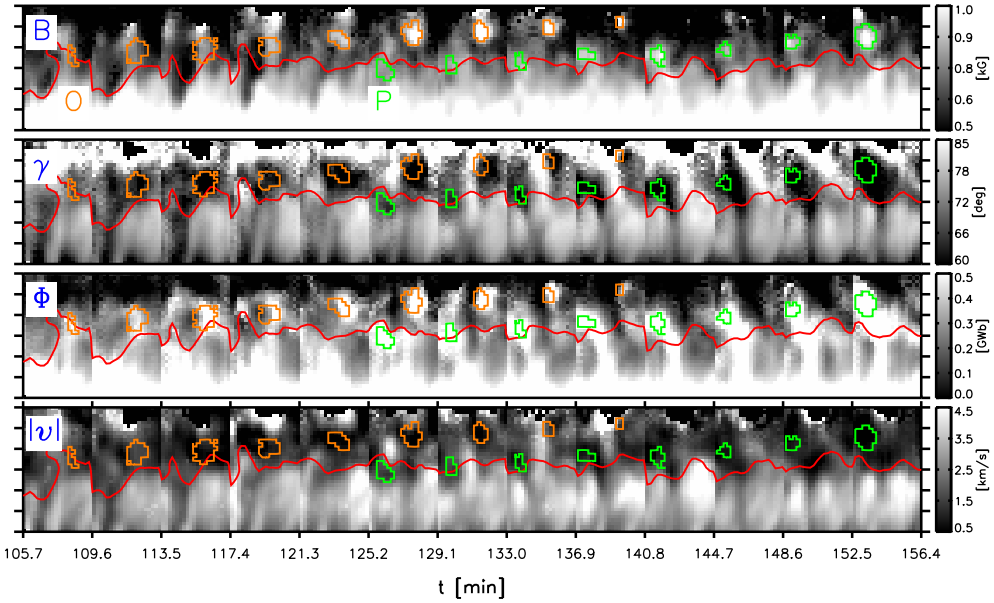

FIGURE 10.16:— Same as Fig. 10.11 from $t = 105.7$ min to $t = 156.4$ min. Orange and green contours enclosed pixels of MMFs O and P. Vertical solid and dashed lines mark the times when features O and P reach the moat.

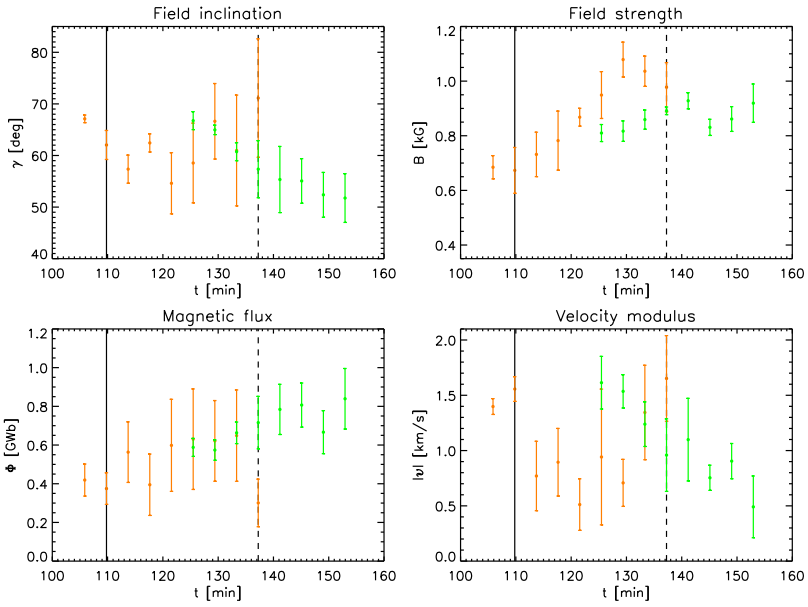

FIGURE 10.17:— Same as Fig. 10.12 for features O (orange) and P (green). Vertical solid and dashed lines mark the times when features O and P reach the moat.

with time. As can be seen, they share some common properties:

- They have inclinations around 60°.
- They display field strength around 0.9 kG.
- $\Phi \sim 0.7$ GWb.
- The flow Velocity is around 1km s^{-1}.

Since s-MMFs display relatively vertical fields, they could influence on the physical properties at chromospheric layers (Lin et al. 2006). The characteristics of these s-MMFs are certainly associated with those of the penumbral structures (spines) they come from in much the same way as i-MMFs. Their magnetic parameters are reminiscent of their respective origins. At this point, we note that if one takes into account the results of the uncombed inversions, the precursors of i-MMFs and s-MMFs are characterized by large and small values of the filling factor of the tube. This means that the precursors of i-MMFs and s-MMFs are representative of the conditions of the tube and background atmospheres, respectively. One can then speculate that s-MMFs are background field lines detached from the spot. As such, they may contribute to the sunspot decay by carrying away flux from it.

10.5 Qualitative geometrical models of MMFs

In this section we propose geometrical models for the formation of MMFs that are suggested by our results. As discussed in Sec. 9.9, type I ECs could be propagating along the tubes driving the Evershed flow. For type II ECs (cf. top panel of Fig. 10.18) the situation would be the same until the EC reach the outer penumbral boundary where the tube would move together with the EC beyond the outer penumbral boundary (cf. center panel of Fig. 10.18). This behavior could be produced by the transfer of linear momentum from the EC to the tube. Then the EC start to return to the solar atmosphere and leave the line forming region (cf. bottom panel of Fig. 10.18). Since this moment one can only see the intersection of the flux tube with the atmosphere that originates the i-MMF. As discussed in Sec. 10.4.1, this process could happen between two consecutives ECs producing the sea-serpent-like flux tube (cf. Fig. 10.19). Figure 10.20 shows the formation of s-MMFs. In this case, field lines of the background propagate outwards originating the s-MMFs in the moat.

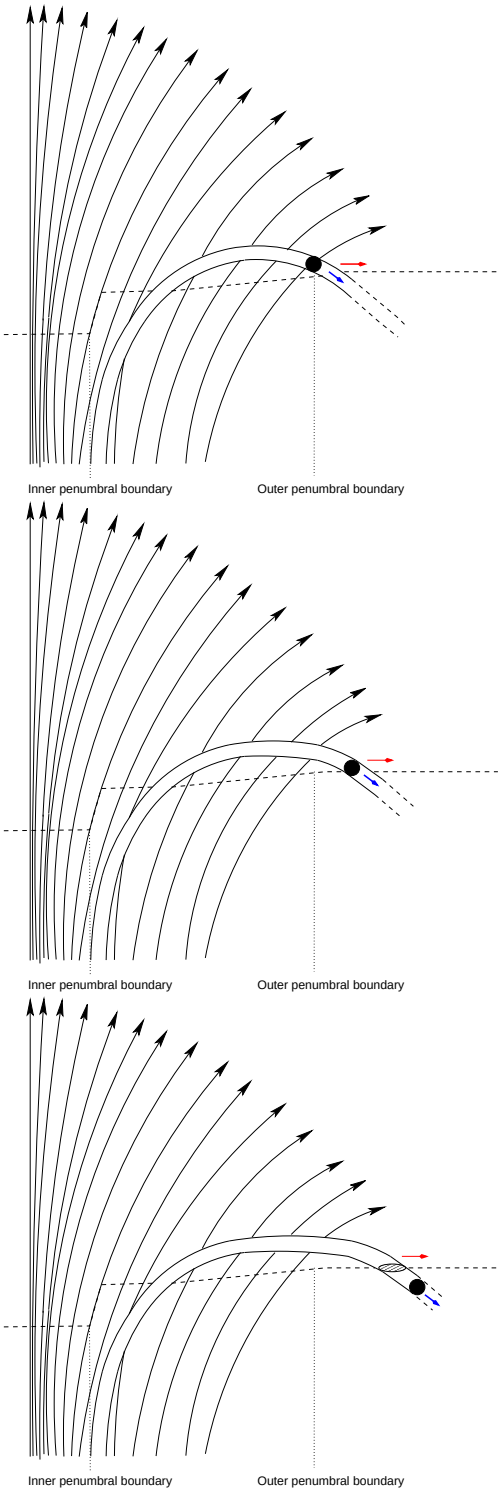

FIGURE 10.18:— Sketch that illustrates the formation of i-MMFs and the disappearance of type II ECs in the moat. Time is different in each snapshot increasing from top to bottom. The EC is represented by the circle while the i-MMF is produced by the intersection of the flux tube with the solar surface.

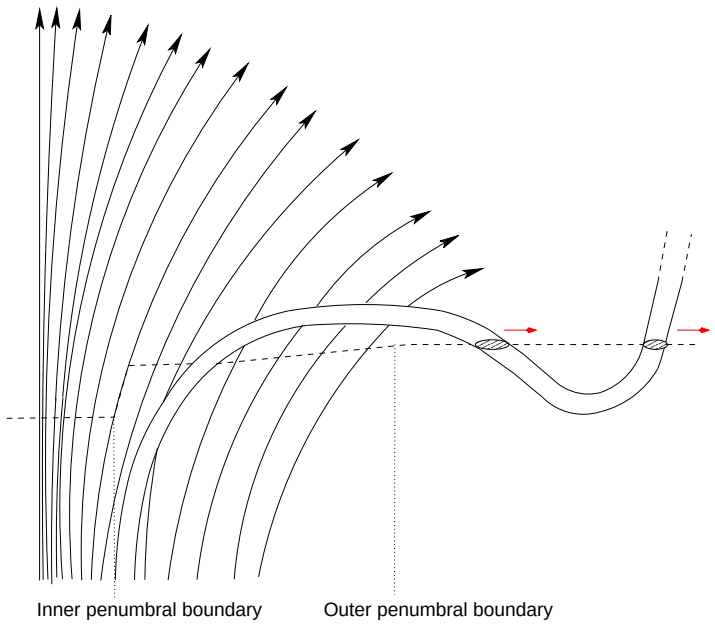

FIGURE 10.19:— Illustration of a bipolar MMF produced by a sea-serpent-like flux tube compatible with our observations.

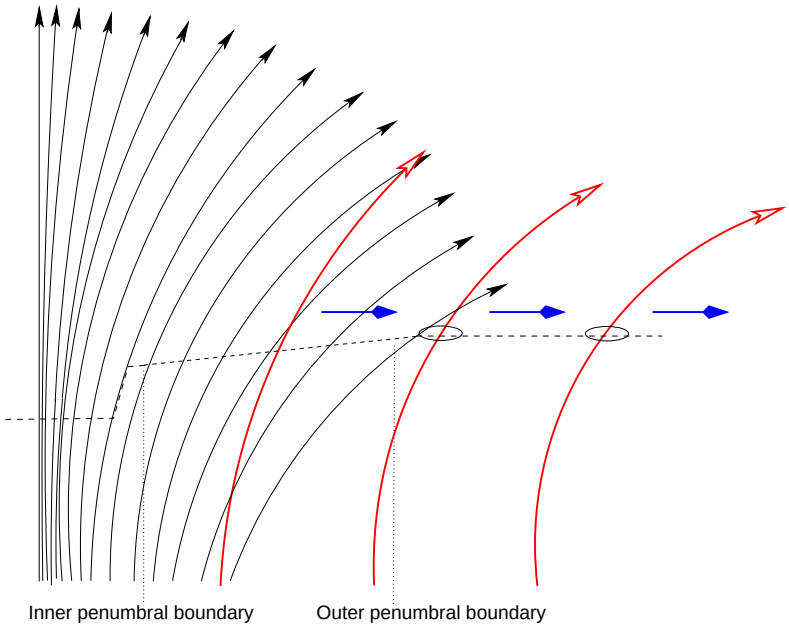

FIGURE 10.20:— Cartoon illustrating the formation of s-MMFs. Red arrows indicate a field line of the background propagating outwards and producing a s-MMF in the moat.

10.6 Summary and conclusions

1. The outer penumbral boundary is modified by the passage of the ECs that reach the quiet photosphere. When an EC penetrates into the quiet photosphere, the outer penumbral boundary does the same and the intensity decrease in the quiet photosphere.

2. Four ECs are seen to cross the visible border of the spot. Once they enter the the moat: (a) their propagation velocities ($v_{\rm prop} \sim 0.9$ km s^{-1}) are smaller than inside the penumbra ($v_{\rm prop} \sim 2.6$ km s^{-1}); (b) they adopt a roundish shape, in contrast to their previous elongation; and (c) their blueshifts quickly decrease until they vanish.

3. Two ECs that reach the moat become MMFs after they vanish. These ECs are seen to move outwards along the same intra-spine and reach the moat one after the other. The MMF farther from the spot displays larger magnetic fields than its surroundings (0.85 kG) and a flow velocity smaller than 1 km s^{-1}, while the other MMF possesses weaker fields than the former (0.7 kG) when it leaves the spot and displays abnormal circular polarization profiles. The geometry of the magnetic field inside the two MMFs is compatible with a $\mho$-loop, although magnetic flux conservation cannot be confirmed. Since the precursors of this type of MMFs (i.e. ECs) appear along the intra-spines, we call them i-MMFs.

4. Two ECs that reach the moat are not detected as MMFs. One of the them is only visible into maps until it seems to leave the FOV. The other EC displays similar field strength than those detected as MMFs (0.85 kG). The EC is not detected as a MMF because of the strong polarization signal of the sunspot canopy which hide the signal coming from the EC.

5. We find two MMFs which originate inside spines. They are detected inside the penumbra as structures with more vertical magnetic fields ($\gamma \sim 60$ °) than their surroundings and small flow velocities ($|v| \sim 1$ km s^{-1}). They could be the MMFs displaying brightenings at the transition region and chromospheric layers found by Lin et al. (2006). We refer to these MMFs s-MMFs.

6. Our results establish the relation between the apparition of MMFs around the spots and the uncombed structure of the penumbra. According to the results of uncombed inversions, the precursors of i-MMFs and s-MMFs posses large and small values of the filling factor of the tube atmosphere,

respectively. This implies that they are mainly characterized by the conditions of the tube (i-MMFs) and background atmospheres (s-MMFs). Our findings are in agreement with the results of Kubo et al. (2007).

7. Our results, in turn, give support to earlier results about the magnetic connection between the MMFs and the penumbra (e.g. Zhang et al. (2003); Sainz Dalda & Martínez Pillet (2005); Kubo et al. (2007)). In particular, we provide strong evidence for some MMFs to be a continuation of the penumbral Evershed flow into the moat and for some other to have their origin inside spines, where the Evershed effect is less conspicuous.

8. Magnetograms provide very little information on the magnetic structure of MMFs for two reasons. First, the observed polarities do not reflect true *field inclinations* because of projection effects. Second, and more important, abnormal Stokes V profiles with three or four lobes occur frequently in MMFs. When abnormal profiles exist, the polarity of the field is an ill-defined quantity.

9. Magnetograms are not suitable to study the formation of MMFs inside/around spots. In most cases, the strong polarization signal of the spot and the surrounding canopy hide the MMFs. This is the reason because the apparition of MMFs inside the penumbra have gone unnoticed until a few years ago (Sainz Dalda & Martínez Pillet 2005; Cabrera Solana et al. 2006; Ravindra 2006).

10. Inversions of full vector spectropolarimetric data are required to properly study the formation of MMFs around sunspots. The atmospheric properties derived from the inversions allow to detect the formation of s-MMFs and to properly characterize the different nature of i-MMFs and s-MMFs.

The evolution and nature of the ECs since they appear until become i-MMFs have been studied along this thesis. Moreover, we have found a new type of MMFs (s-MMFs) originated inside spines. In the next section, we summarizes the main results of this thesis and we propose qualitative geometrical models that explain the evolution of ECs (i.e. i-MMFs in the moat) and s-MMFs.

11

Conclusions

The main conclusions of this thesis and the new fields of research opened by our work are discussed in this chapter.

11.1 Sensitivity of spectral lines

The question still remains which lines are best suited to retrieve a given atmospheric parameter. This subject has been addressed by characterizing the sensitivities of weak spectral lines to magnetic field, velocity, and temperature by means of response functions to constant perturbations in Chapter 3. We have developed a simple phenomenological model capable of describing the response of any weak line in terms of simple line parameters such as the line width and depth. Thus, for the first time, we have at our disposal simple rules to select the most appropriate line for the problem we are interested in.

If the sensitivity is small, the changes in the emergent Stokes profiles are not detectable depending of the noise of the observations. Thus, it is always advisable to select lines having large sensitivities to a given parameter, in order to ensure that the subtle variations it produces in the spectrum are not buried by the noise. The sensitivities of the commonly used spectral lines in solar spectropolarimetry, like the visible Fe I line at 630.25 nm and the infrared Fe I line at 1564.85 nm, has been examined in detail as emerging from reference quiet Sun and sunspots models. Although is not possible to draw general conclusions about the differences between visible and infrared lines, there are some trends that can be ascribed to many spectral lines of the two regions:

- Due to the strong Zeeman splitting, changes in the magnetic field strength are much easier to detect in the infrared when the field is sufficiently large.
- In general visible lines show higher sensitivities to LOS velocities than infrared lines because their Stokes profiles are sharper.
- The excitation potential of the infrared lines is usually large. This implies that many infrared lines are not formed in the mid and upper atmosphere.
- Infrared lines display lower sensitivity to temperature. The reason is the smaller variation with temperature of the Planck function at longer wavelengths. However, the equivalent width of the infrared lines display a greater variation.

We have demonstrated that both visible and infrared lines have their advantages and limitations. Thus, it is desiderable to combine them in order to characterize the physical properties of the solar atmosphere more reliably.

The relations provided by our model are universal and can be used to decide which line is better suited to measuring a given atmospheric parameter. Our results are of practical interest for the design of new instruments and for a better exploitation of existing ones.

11.2 Inversion of visible and infrared sunspot Stokes profiles

We have inverted the Stokes parameters of the pair of visible Fe I lines at 630.25 nm and the pair of infrared Fe I lines at 1564.85 nm emerging from three sunspots located at different heliocentric angles. One-component models without gradients are used in order to compare the atmospheric quantities derived from the inversion of the two spectral ranges. Our results show that the inversions of the visible and infrared lines essentially lead to similar physical parameters for the sunspots demonstrating that inversion techniques provide unique results (cf. Chapter 6).

We found a cross-talk between temperature and stray light affecting the visible lines. This leads to systematic errors in the temperatures and magnetic fields determined from visible lines: due to their smaller Zeeman splitting, the code is not able to discriminate between enhancements of temperature and larger stray light contaminations. On the other hand, the SIR code only accounts for unpolarized stray light coming from the quiet Sun. However, it is known that there is polarized stray light from the surroundings into the resolution element. This emphasizes the need of a more realistic treatment of the stray light contamination.

The cross-talk can be minimized by inverting the lines of the two spectral ranges simultaneously. Hence, simultaneous inversions are desirable not only for the combination of spectral lines with different sensitivities but also for a more accurate determination of the stray light contamination. Thereby, simultaneous inversion of the visible and infrared spectral lines improve the diagnostic capabilities of a single spectral range alone and allows to characterize the physical properties of the solar atmosphere more reliably.

11.3 Temporal evolution of the Evershed flow

The temporal evolution of the Evershed flow has been studied, for the first time, by analyzing the polarization signals of visible (630 nm) and near infrared (1565 nm) lines taken during 236 min of observations at the VTT in Tenerife. The good seeing conditions together with the adaptative optic system of the telescope allowed us to reach diffraction-limited spatial resolution of the infrared observations ($0\farcs6$) which is one of the highest ever obtained in ground-based spectropolarimetry. Different levels of sophistication have been use in order to interpret the observations, since simple line parameters calculations (Chapter 7) to more complex one-component (Chapter 8) and uncombed inversions (Chapter 9). The evolution of the flow is mainly characterized by the quasi-periodic apparition of the ECs in the mid penumbra. They propagate outwards across the penumbra following penumbral intra-spines. The frequency of appearance of ECs varies between 14 and 40 minutes between different intra-spines. ECs exhibit the largest Doppler velocities and linear-to-circular polarization ratios of the whole penumbra. In addition, lines formed deeper in the atmosphere show larger Doppler velocities, much in the same way as the quiescent Eveshed flow. According to our observations, ECs can be classified in two groups: type I ECs, which vanish in the outer penumbra, and type II ECs, which cross the outer penumbral boundary and enter the sunspot moat. Most of the observed ECs belong to type I.

The fact that the ECs possess larger Doppler velocities and L/V ratios than the intra-spines where they are seen to propagate can be interpreted in different ways. If one assumes that the Stokes profiles emerging from the penumbra are produced by a single magnetic atmosphere, this signature in the polarization profiles of the ECs can only be interpreted as a perturbation of the magnetic and dynamic structure of the intra-spines producing larger inclinations and flow velocities. On the other hand, if one takes into account the fine structure of the penumbra and assumes two magnetic components horizontally and vertically interlaced filling the resolution element, the magnetic configuration of the intra-spines do not seem to be affected by the EC passage. These in-

versions suggest that ECs are the result of of enhancements of the visibility of penumbral flux tubes. The feasibility of this mechanism has been examined with simple numerical experiments that use penumbral flux tubes in mechanical equilibrium with a background field. We have been able to reproduce the increment of the L/V ratio produced by the ECs by modifying the thermodynamical structure of a penumbral flux tube in mechanical equilibrium with a background atmosphere. The increment of L/V is only compatible with a decrease of temperature and pressure in the tube while density has to decreases in the upper part of the tube and the opposite in the lower part. This modifies the optical depth scale in the deep layers allowing a higher contribution of the flux tube to the emergent Stokes profiles that produces the increment of L/V. Our results shed light about the physical mechanism producing the ECs and, consequently, about the nature of the Evershed flow.

We note that our results are consistent with the scenario where the penumbra is formed by thick and/or low lying horizontal flux tubes driving the Evershed flow embedded in a more vertical background magnetic field, as proposed by Solanki & Montavon (1993). In fact, the geometry of the magnetic field of the intra-spines is compatible with horizontal flux tubes extending along the penumbra and diving back to the solar interior in the outer boundary of the spot.

11.4 Origin and nature of MMFs around sunspots

We also investigated the evolution of type II ECs in the moat. In their passage the ECs modify the outer penumbral boundary: when an EC penetrates into the quiet photosphere, the outer penumbral boundary does the same and the intensity decreases in the quiet photosphere. Once the ECs enter the moat they behave in a similar way: they adopt a roundish shape and propagate with smaller velocities than inside the penumbra until they vanish near the boundary of the spot.

We follow the temporal evolution of two Evershed clouds that move radially outward along the same intra-spine and reach the moat one after other becoming MMFs with different polarity as measured by magnetograms. They display similar properties than those of bipolar MMFs. We detect the presence of abnormal circular polarization profiles inside the MMF which is nearer to the spot. Although the interpretation of such abnormal profiles is not straightforward, two magnetic components with different inclinations filling the resolution element are enough to produce the mixed polarities displayed by the Stokes profiles. The magnetic field vector inside the two MMFs is derived in terms of one-magnetic component. Until the apparition of the abnormal Stokes

profiles, the geometry of the magnetic field inside the two MMFs is compatible with υ-loop. If this would be the case, the two MMFs would not contribute to the sunspot decay process. The MMF further from the spot display stronger fields than their surroundings and flow velocities smaller than 1 km s^{-1}, while the other MMF possess weaker fields than the former when it leaves the spot. Hence, if the two MMFs would be the manifestation of the same field lines, the theoretical predictions of higher magnetic field at larger radial distances would be fulfilled.

The analysis of the inversions leaded us to find another type of MMF that originate along the spines. They display more vertical and smaller flows than their surroundings. When they are far enough from the spot, they possess stronger fields than their surroundings. As in the case of the ECs that are not detected as MMFs, this moving features are not seen as MMFs in the magnetograms.

Our results provide strong evidence for some MMFs to be a continuation of the penumbral Evershed flow into the moat and for some other to have their origin inside the spines where the Evershed flow is less conspicuous. Since the precursors of the two types of MMFs are originated inside the intra-spines and spines, we decided to call them i-MMFs and s-MMFs, respectively. For first time the formation process of MMFs around sunspots and its relation with the uncombed structure of the penumbra have been observed. According to the results of the uncombed inversions, the precursors of i-MMFs and s-MMFs possess large and small values of the filling factor of the tube atmosphere implying that they are representatives of the conditions of the tube and background atmosphere, respectively. In this context, one can speculate that s-MMFs are background field lines detached from the spot that could contribute to the removal of the flux that produces the decay of the spot, while i-MMFs could be produced by the intersection of the flux tubes driving the Evershed flow with the solar atmosphere.

Finally, we would like to stress that due to the strong polarization signal of the spot and the surrounding canopy, many MMFs originated inside the penumbra with the same polarity of the spot are not observed. This outline the need of full vector spectropolarimetric observations in order to properly study the formation of MMFs by means of their physical properties.

11.5 Future work

Despite the Evershed flow is a dynamical phenomenon, most of what we know has been learned from observations that do not reflect its temporal evolution. The advent of adaptive optics systems together multiwavelength spectropo-

larimetry capabilities at ground based observatories allow, for first time, the investigation of the time evolution of the physical processes taking place in the sunspots with a high degree of sophistication. The results of this thesis outline the importance of such type of studies. Although, the spatial resolution of spectropolarimetric observations from the ground have been improved, they are limited by the distorting effect of turbulence in the atmosphere. Fortunately we are now able to put spectropolarimeters in space. In this context, HINODE's spectropolarimeter represents the first opportunity to obtain uninterrupted full vector spectropolarimetric observations with very high spatial resolution ($0\farcs3$). The data provided by HINODE and future missions together high resolution ground based spectropolarimetric observations will provide a wealth of information about the evolution of the physical properties of the sunspot penumbra. Concerning to the analysis of those type of data we outline some lines of research that we consider of interest:

- The horizontal and vertical thermal, magnetic, and dynamical structure of the penumbra should be clarified. DC penumbral filaments are the most promising candidates to be isolated flux tubes. We think that those structures must be somehow related with the intra-spines on ground based spectropolarimetric observations. Taking into account that ECs propagate along intra-spines, ECs could propagate synchronized along several DC penumbral filaments at the same time. We think that those questions should be investigated in detail.

- Since our investigation is the first study of the temporal evolution of the physical properties of MMFs. The study of MMFs on longer spectropolarimetric sequences with higher spatial resolution is warranted. In fact, we expect a considerable progress in this field during the next years.

- We found the presence of abnormal polarization profiles inside the MMF of the bipolar pair which is nearer to the spot. An uncombed inversion of such profiles would help us to confirm if the geometry of the magnetic field of the two components is in agreement with the uncombed view of the penumbra. In order to perform those inversions, at least three different components have to be taken into account: two magnetics representing the background and tube contributions and one non-magnetic representing the quiet atmosphere contribution.

- Theoretical models reproducing the observational properties of the temporal evolution of the Evershed flow would be more than welcome. To this aim, we think that the study of the evolution of thick flux tubes as

the proposed by Ruiz Cobo & Bellot Rubio (2007) and Borrero (2007) is the next logical step.

- Our results outline the need of more refine semiempirical models implemented in the inversion codes. The fact that the ECs are characterized as structures of increased filling factor indicates that our modelling of the fine structure of the penumbra is insufficient. For this reason, we consider that the next logical step is to include models with flux tubes in mechanical equilibrium with their surroundings. This will allow to check if the ECs are produced by variations of the thermodynamical properties in the flux tube as suggested by our numerical tests.

A

Tables

Species	λ_0 [nm]	A_0	A_1 [pm]	A_2	$\partial A_0/\partial T$ [K^{-1}]	$\partial A_1/\partial T$ [pm/K]	$\partial A_2/\partial T$ [K^{-1}]	A_0^V	A_1^V [pm]	A_0^*	A_1^* [pm]
Ni I	491.20	0.54	2.72	1.00	$+1.26\times10^{-4}$	-5.27×10^{-4}	6.95×10^{-4}	0	0	0	0
Fe I	524.71	0.79	3.13	1.00	$+6.73\times10^{-5}$	-1.16×10^{-3}	6.70×10^{-4}	0.39	3.12	0.76	3.17
Fe I	525.02	0.78	3.11	1.00	$+5.12\times10^{-5}$	-1.13×10^{-3}	6.70×10^{-4}	0.39	3.10	0.76	3.20
Fe I	537.96	0.63	3.17	1.00	$+1.04\times10^{-4}$	-7.39×10^{-4}	6.61×10^{-4}	0.26	2.47	0.63	3.18
Ti II	538.10	0.57	3.21	1.00	$+5.36\times10^{-4}$	$+1.24\times10^{-4}$	6.61×10^{-4}	0.22	2.45	0.56	3.23
Fe I	557.61	0.80	5.32	1.00	$+4.52\times10^{-4}$	-4.78×10^{-3}	6.62×10^{-4}	0	0	0	0
Fe I	569.15	0.47	3.24	1.00	$+2.23\times10^{-5}$	-7.80×10^{-4}	6.40×10^{-4}	0	0	0	0
Fe II	614.93	0.41	3.70	1.00	$+5.70\times10^{-4}$	-7.80×10^{-5}	6.09×10^{-4}	0.19	3.23	0.40	3.74
Fe I	617.33	0.65	3.61	1.00	$+9.69\times10^{-6}$	-8.85×10^{-4}	6.08×10^{-4}	0.32	3.59	0.63	3.71
Fe I	630.25	0.68	4.61	1.00	$+2.10\times10^{-4}$	-2.44×10^{-3}	6.06×10^{-4}	0.33	4.40	0.66	4.72
Fe I	630.35	0.06	3.17	1.00	-2.57×10^{-5}	-3.59×10^{-4}	5.99×10^{-4}	0.03	2.97	0.06	3.22
Ti I	630.38	0.09	3.13	1.00	-1.54×10^{-4}	-5.92×10^{-5}	5.99×10^{-4}	0.03	3.03	0.09	3.16
Ni I	676.78	0.72	4.49	1.00	$+1.79\times10^{-4}$	-1.16×10^{-3}	5.74×10^{-4}	0.35	4.15	0.7	4.53
Fe I	709.04	0.50	4.17	1.00	$+2.59\times10^{-5}$	-9.06×10^{-4}	5.54×10^{-4}	0	0	0	0
Fe II	722.45	0.15	3.83	1.00	$+3.15\times10^{-4}$	-2.99×10^{-4}	5.45×10^{-4}	0	0	0	0
Si I	1062.76	0.44	11.24	1.00	$+2.54\times10^{-4}$	-6.55×10^{-3}	4.24×10^{-4}	0.21	10.89	0.43	11.45
Fe I	1089.63	0.31	5.74	1.00	-1.91×10^{-4}	-8.52×10^{-4}	3.96×10^{-4}	0.15	5.72	0.29	5.99
Fe I	1142.23	0.54	7.42	1.00	-5.95×10^{-5}	-2.44×10^{-3}	3.77×10^{-4}	0.27	8.42	0.51	7.81
Fe I	1221.33	0.12	6.77	1.00	-4.59×10^{-5}	-1.84×10^{-3}	3.39×10^{-4}	0.06	6.74	0.10	7.84
Fe I	1558.83	0.31	11.66	1.00	$+3.87\times10^{-6}$	-8.36×10^{-3}	1.89×10^{-4}	0.16	11.33	0.30	12.32
Fe I	1564.85	0.31	10.95	1.00	-5.26×10^{-5}	-6.85×10^{-3}	1.84×10^{-4}	0.16	10.83	0.26	13.80

TABLE A.1:— Weak line model parameters and their derivatives for the quiet Sun model. A_0 and A_1 are the residual intensity and the width of Stokes I in the absence of magnetic fields, while A_2 is the continuum intensity. A_0^V and A_1^V are the amplitude and width of the Stokes V lobes in the strong field regime. A_0^* and A_1^* are the depth and the width of Stokes I in the weak field approximation ($B = 200$G).

Species	λ_0 [nm]	A_0	A_1 [pm]	A_2	$\partial A_0/\partial T$ [K^{-1}]	$\partial A_1/\partial T$ [pm/K]	$\partial A_2/\partial T$ [K^{-1}]	A_0^V	A_1^V [pm]	A_0^*	A_1^* [pm]
Ni I	491.20	0.46	2.49	0.83	$+1.74\times10^{-4}$	-4.88×10^{-4}	6.34×10^{-4}	0	0	0	0
Fe I	524.71	0.70	3.00	0.85	$+1.74\times10^{-4}$	-1.27×10^{-3}	6.20×10^{-4}	0.14	2.00	0.69	3.04
Fe I	525.02	0.69	2.98	0.85	$+1.62\times10^{-4}$	-1.25×10^{-3}	6.20×10^{-4}	0.18	2.14	0.67	3.06
Fe I	537.96	0.56	2.95	0.86	$+1.50\times10^{-4}$	-7.25×10^{-4}	6.16×10^{-4}	0.07	2.00	0.56	2.96
Ti II	538.10	0.48	2.94	0.86	$+4.99\times10^{-4}$	$+2.18\times10^{-4}$	6.15×10^{-4}	0.06	2,04	0.48	2.95
Fe I	557.61	0.68	5.21	0.86	$+4.51\times10^{-4}$	-4.42×10^{-3}	6.25×10^{-4}	0	0	0	0
Fe I	569.15	0.43	2.98	0.87	$+6.58\times10^{-5}$	-7.25×10^{-4}	6.02×10^{-4}	0	0	0	0
Fe II	614.93	0.34	3.34	0.88	$+5.49\times10^{-4}$	$+7.38\times10^{-5}$	5.80×10^{-4}	0.04	2.81	0.33	3.38
Fe I	617.33	0.60	3.40	0.88	$+7.87\times10^{-5}$	-9.41×10^{-4}	5.80×10^{-4}	0.15	2.56	0.58	3.50
Fe I	630.25	0.61	4.41	0.88	$+2.44\times10^{-4}$	-2.24×10^{-3}	5.82×10^{-4}	0.14	2.89	0.60	4.53
Fe I	630.35	0.06	2.82	0.89	-1.85×10^{-5}	-3.09×10^{-4}	5.72×10^{-4}	0.01	2.53	0.05	2.88
Ti I	630.38	0.10	2.80	0.89	-1.59×10^{-4}	-5.93×10^{-5}	5.72×10^{-4}	0.01	2.42	0.10	2.82
Ni I	676.78	0.66	4.32	0.90	$+2.18\times10^{-4}$	-1.11×10^{-3}	5.55×10^{-4}	0.10	2.57	0.65	4.36
Fe I	709.04	0.47	3.87	0.90	$+6.79\times10^{-5}$	-8.43×10^{-4}	5.38×10^{-4}	0	0	0	0
Fe II	722.45	0.12	3.43	0.91	$+2.87\times10^{-4}$	-2.28×10^{-4}	5.30×10^{-4}	0	0	0	0
Si I	1062.76	0.39	10.60	0.92	$+2.62\times10^{-4}$	-4.36×10^{-3}	4.21×10^{-4}	0.07	7.27	0.39	11.03
Fe I	1089.63	0.31	5.25	0.93	-1.56×10^{-4}	-8.98×10^{-4}	3.92×10^{-4}	0.07	4.72	0.29	5.52
Fe I	1142.23	0.51	7.13	0.93	-6.35×10^{-6}	-2.49×10^{-3}	3.78×10^{-4}	0.14	5.73	0.48	7.53
Fe I	1221.33	0.11	6.14	0.93	-3.06×10^{-5}	-1.61×10^{-3}	3.44×10^{-4}	0.02	5.98	0.10	7.37
Fe I	1558.83	0.26	11.07	0.91	$+5.16\times10^{-5}$	-7.21×10^{-3}	2.25×10^{-4}	0.06	8.98	0.26	12.01
Fe I	1564.85	0.28	10.41	0.92	$+4.04\times10^{-7}$	-6.22×10^{-3}	2.21×10^{-4}	0.06	9.58	0.22	13.67

TABLE A.2:— Same as Table A.1, for the penumbral model.

Species	λ_0 [nm]	A_0	A_1 [pm]	A_2	$\partial A_0/\partial T$ [K^{-1}]	$\partial A_1/\partial T$ [pm/K]	$\partial A_2/\partial T$ [K^{-1}]	A_0^V	A_1^V [pm]	A_0^*	A_1^* [pm]
Ni I	491.20	0.18	2.90	0.30	$+3.02\times10^{-4}$	-7.37×10^{-4}	3.24×10^{-4}	0	0	0	0
Fe I	524.71	0.33	4.53	0.32	$+3.73\times10^{-4}$	-3.26×10^{-3}	3.34×10^{-4}	0.15	3.56	0.33	4.56
Fe I	525.02	0.33	4.46	0.32	$+3.71\times10^{-4}$	-3.09×10^{-3}	3.34×10^{-4}	0.16	3.96	0.33	4.53
Fe I	537.96	0.25	3.64	0.33	$+3.28\times10^{-4}$	-1.22×10^{-3}	3.34×10^{-4}	0.09	2.55	0.25	3.65
Ti II	538.10	0.16	2.94	0.33	$+3.44\times10^{-4}$	-2.38×10^{-4}	3.33×10^{-4}	0.07	2.21	0.16	2.95
Fe I	557.61	0.26	10.31	0.33	$+3.15\times10^{-4}$	-1.07×10^{-2}	3.37×10^{-4}	0	0	0	0
Fe I	569.15	0.19	3.69	0.34	$+3.13\times10^{-4}$	-1.66×10^{-3}	3.39×10^{-4}	0	0	0	0
Fe II	614.93	0.04	3.45	0.36	$+1.65\times10^{-4}$	-9.09×10^{-4}	3.43×10^{-4}	0.02	2.96	0.04	3.49
Fe I	617.33	0.31	4.23	0.36	$+3.37\times10^{-4}$	-1.20×10^{-3}	3.45×10^{-4}	0.15	3.98	0.31	4.32
Fe I	630.25	0.27	6.66	0.37	$+3.41\times10^{-4}$	-5.50×10^{-3}	3.45×10^{-4}	0.12	5.20	0.26	6.76
Fe I	630.35	0.04	3.08	0.37	$+8.68\times10^{-5}$	-1.36×10^{-3}	3.45×10^{-4}	0.02	2.89	0.04	3.14
Ti I	630.38	0.29	3.29	0.37	$+1.35\times10^{-4}$	-1.62×10^{-3}	3.46×10^{-4}	0.12	2.96	0.29	3.31
Ni I	676.78	0.34	5.15	0.39	$+3.41\times10^{-4}$	-1.58×10^{-3}	3.50×10^{-4}	0.15	4.21	0.34	5.19
Fe I	709.04	0.23	4.54	0.40	$+3.21\times10^{-4}$	-1.43×10^{-3}	3.49×10^{-4}	0	0	0	0
Fe II	722.45	0.01	3.88	0.41	$+4.83\times10^{-5}$	-1.22×10^{-3}	3.48×10^{-4}	0	0	0	0
Si I	1062.76	0.14	12.94	0.52	$+2.94\times10^{-4}$	-9.31×10^{-3}	3.18×10^{-4}	0.06	10.84	0.13	13.06
Fe I	1089.63	0.25	6.13	0.53	$+2.67\times10^{-4}$	-1.43×10^{-3}	3.20×10^{-4}	0.12	5.97	0.24	6.37
Fe I	1142.23	0.38	9.47	0.54	$+2.99\times10^{-4}$	-5.69×10^{-3}	3.18×10^{-4}	0.19	9.70	0.36	9.89
Fe I	1221.33	0.08	7.78	0.57	$+1.89\times10^{-4}$	-7.02×10^{-3}	2.98×10^{-4}	0.04	7.61	0.07	8.89
Fe I	1558.83	0.21	17.75	0.70	$+2.71\times10^{-4}$	-1.92×10^{-2}	2.00×10^{-4}	0.10	14.94	0.20	18.10
Fe I	1564.85	0.24	17.14	0.70	$+2.89\times10^{-4}$	-1.88×10^{-2}	1.98×10^{-4}	0.12	15.99	0.21	19.31

TABLE A.3:— Same as Table A.1, for the umbral model.

B

Sunspots A and C

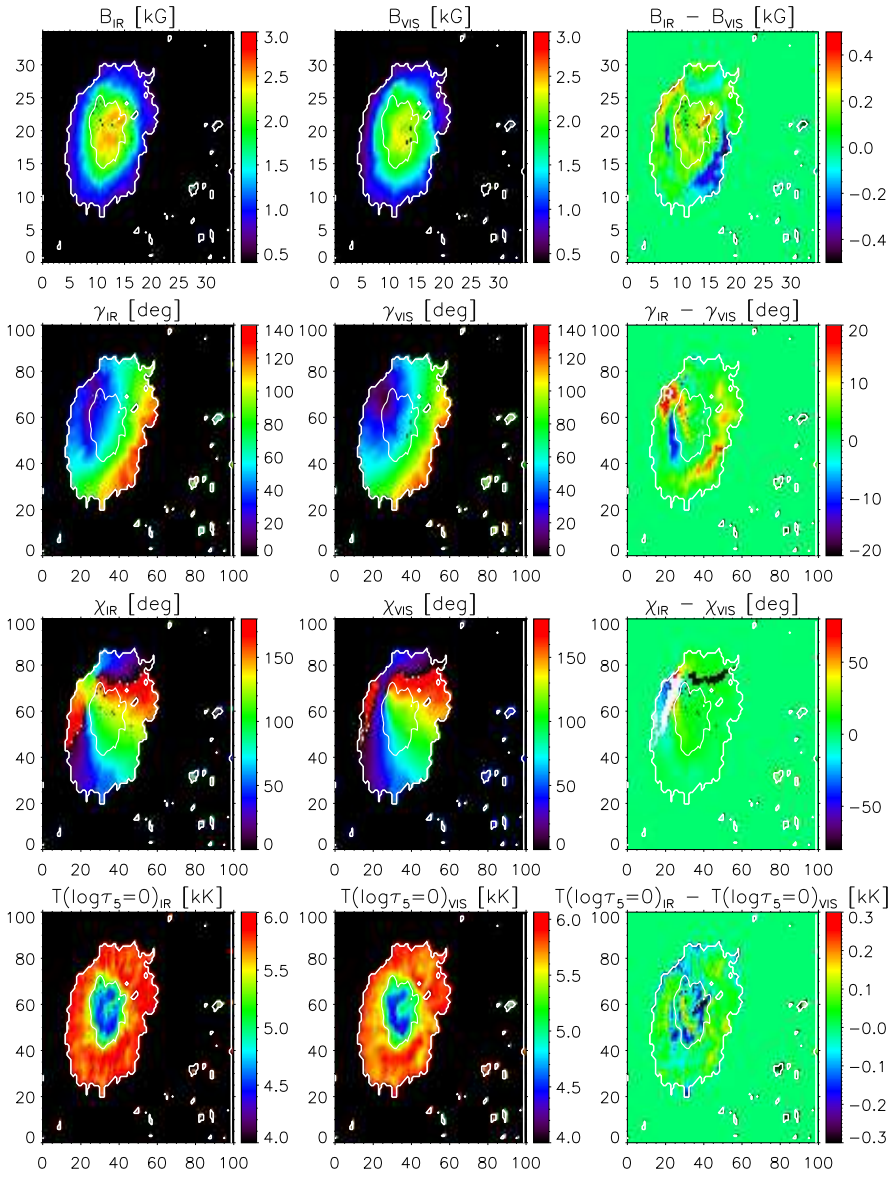

FIGURE B.1:— From *top* to *bottom*: Maps of the magnetic field strength, LOS inclination, LOS azimuth, and temperatures at $\log\tau = 0$ derived for sunspot A. The *left* and *center* panels show the quantities derived from IR and VIS lines, while the *right* panels displays the differences between them. Numbers on x and y-axis are given in arcseconds.

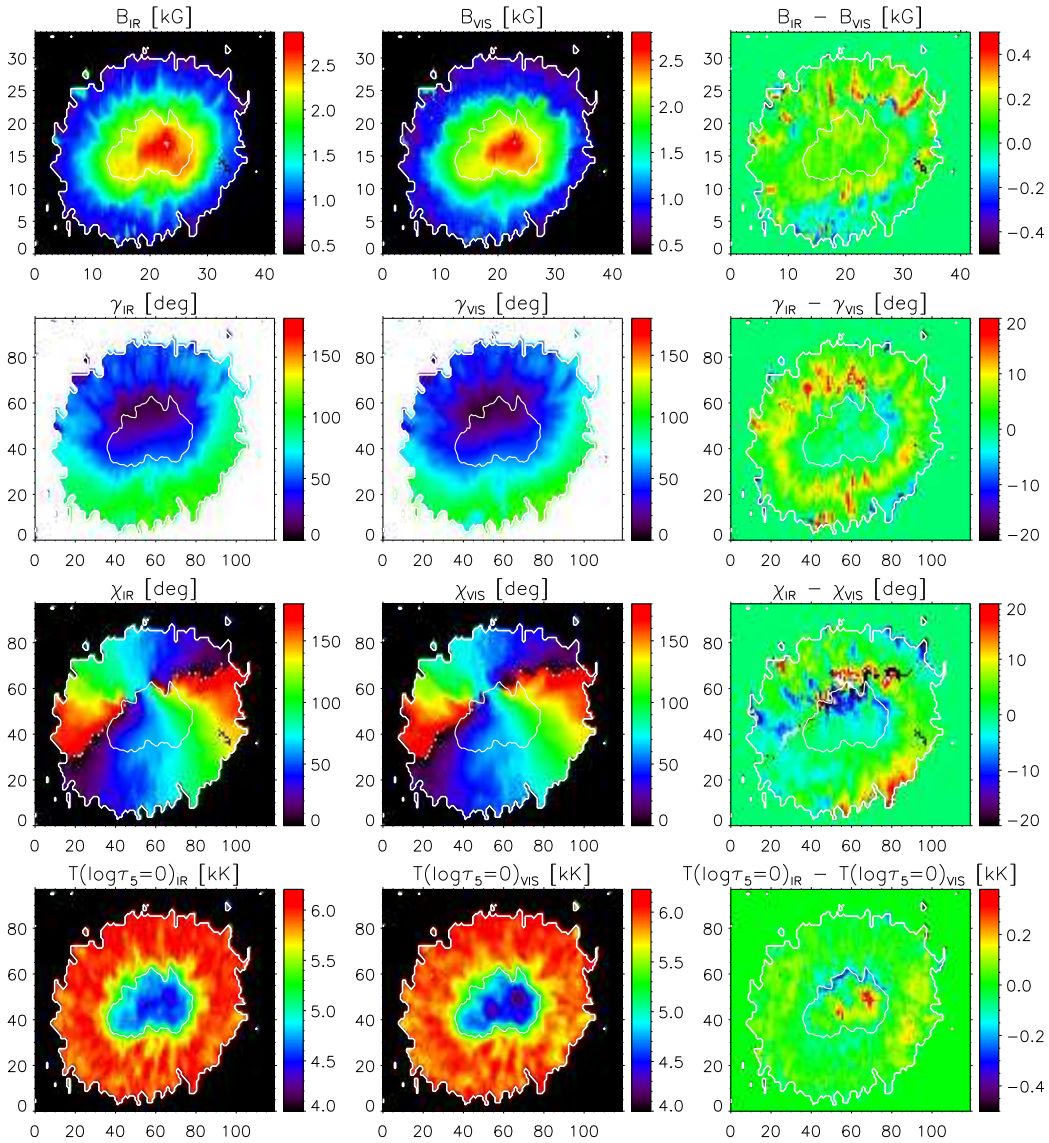

FIGURE B.2:— Same as Fig.B.1 for sunspot C.

C

1 July observations

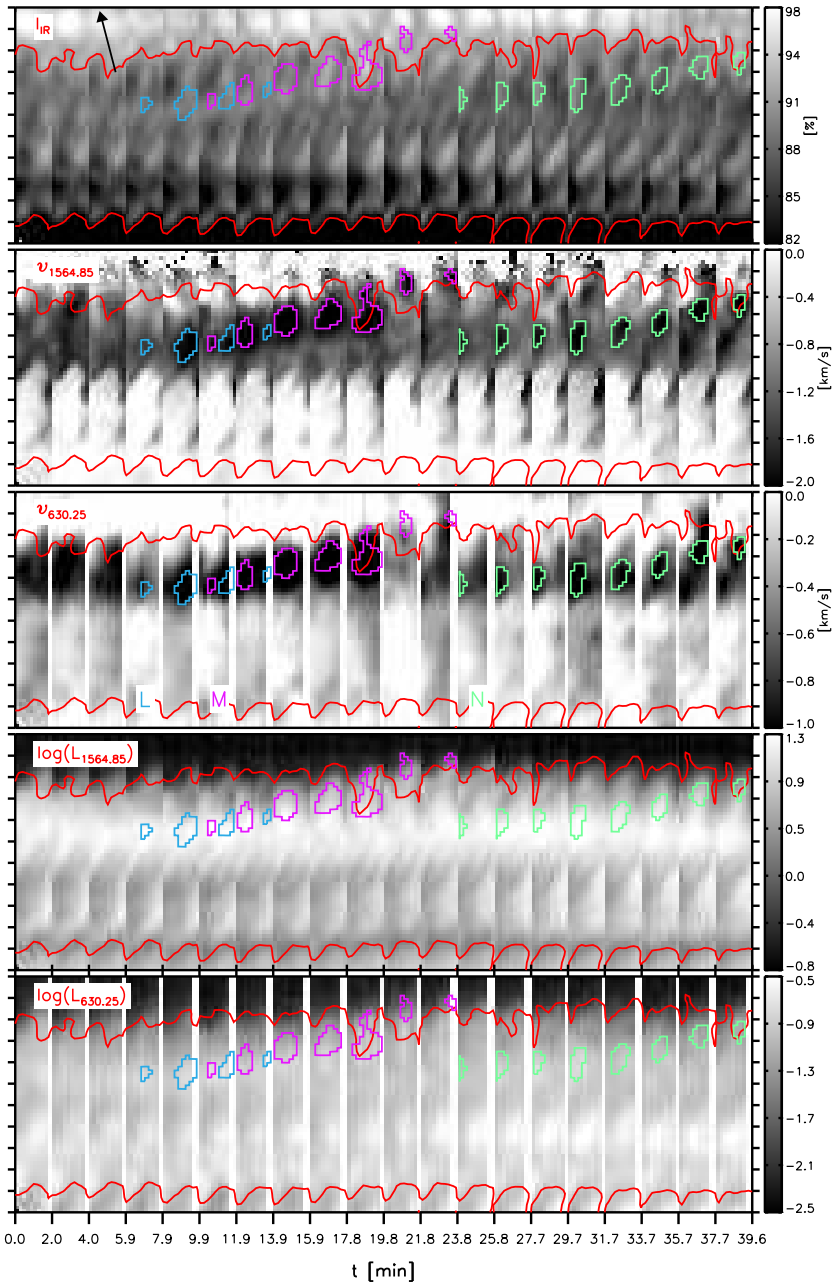

FIGURE C.1:— Same as Fig. 7.1 for the time sequence observed on 1 July, from t=0 to t=39.6 min.

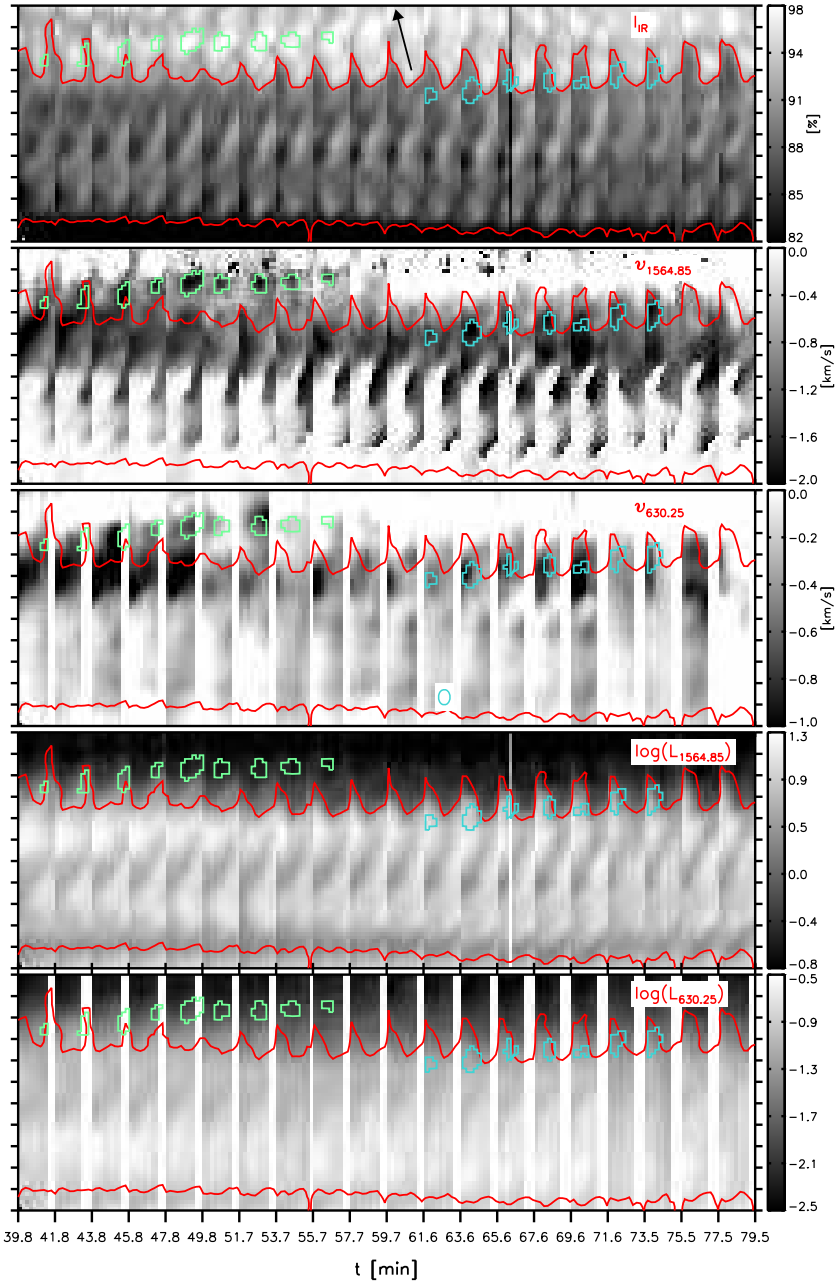

FIGURE C.2:— Same as Fig. C.1 from t=39.8 to t=79.5 min.

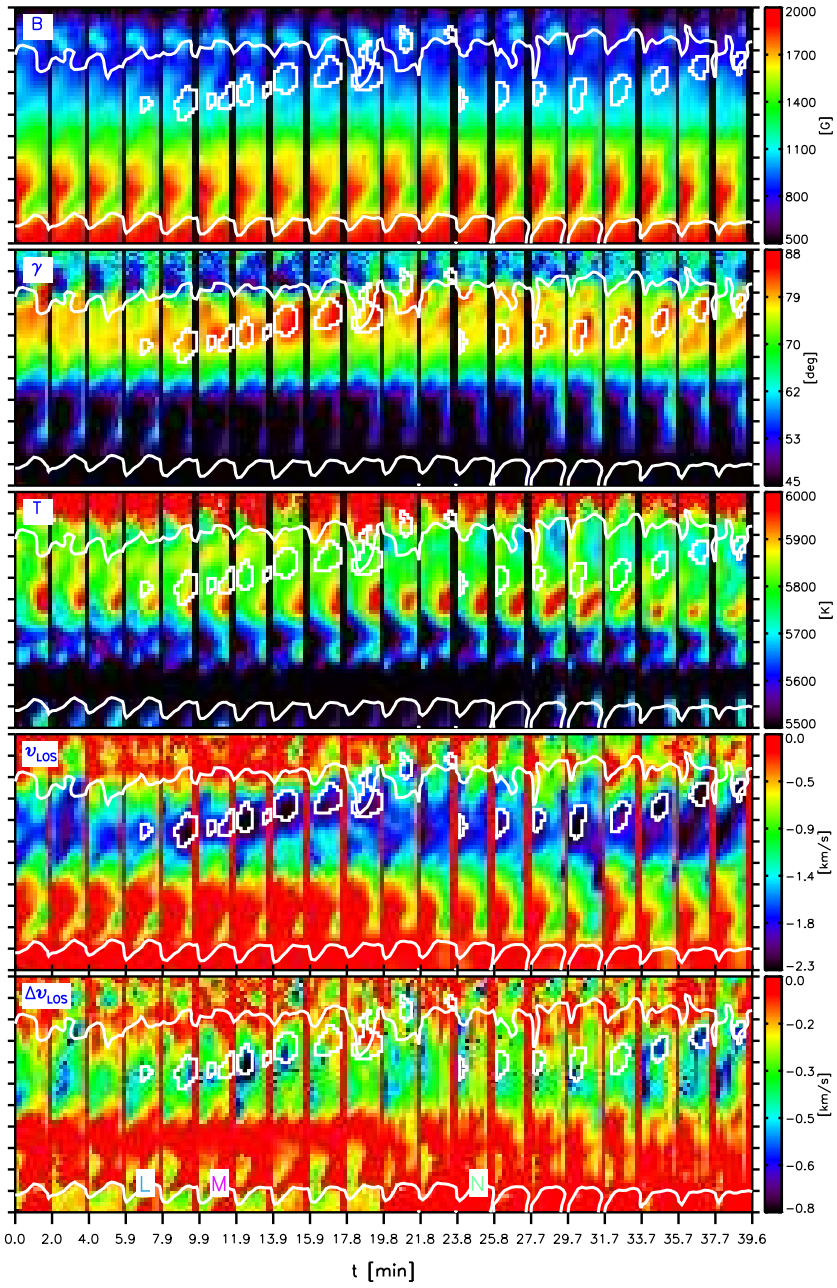

FIGURE C.3:— Same as Fig. 8.3 for the time sequence observed on 1 July, from t=0 to t=39.6 min.

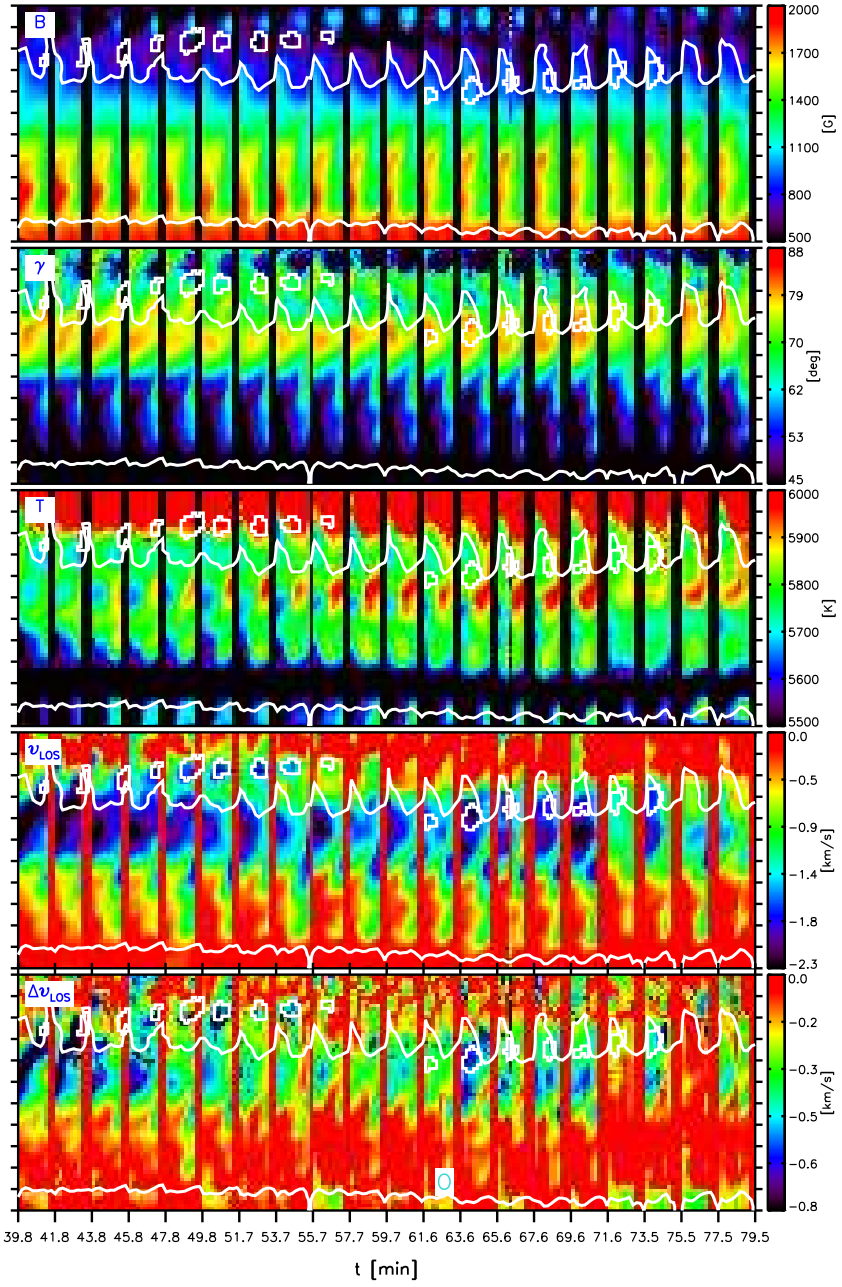

FIGURE C.4:— Same as Fig. C.3 from t=39.8 to t=79.5 min.

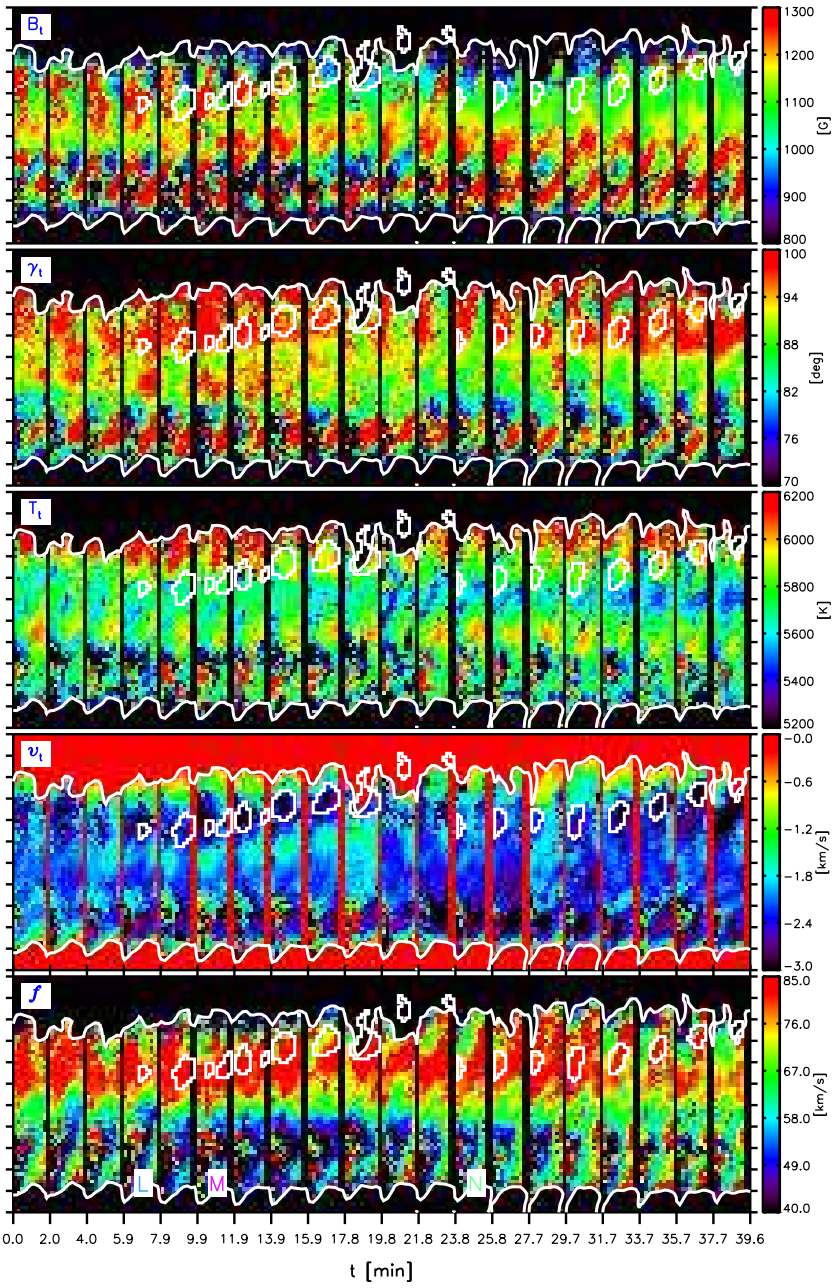

FIGURE C.5:— Same as Fig. 9.6 for the time sequence observed on 1 July, from t=0 to t=39.6 min.

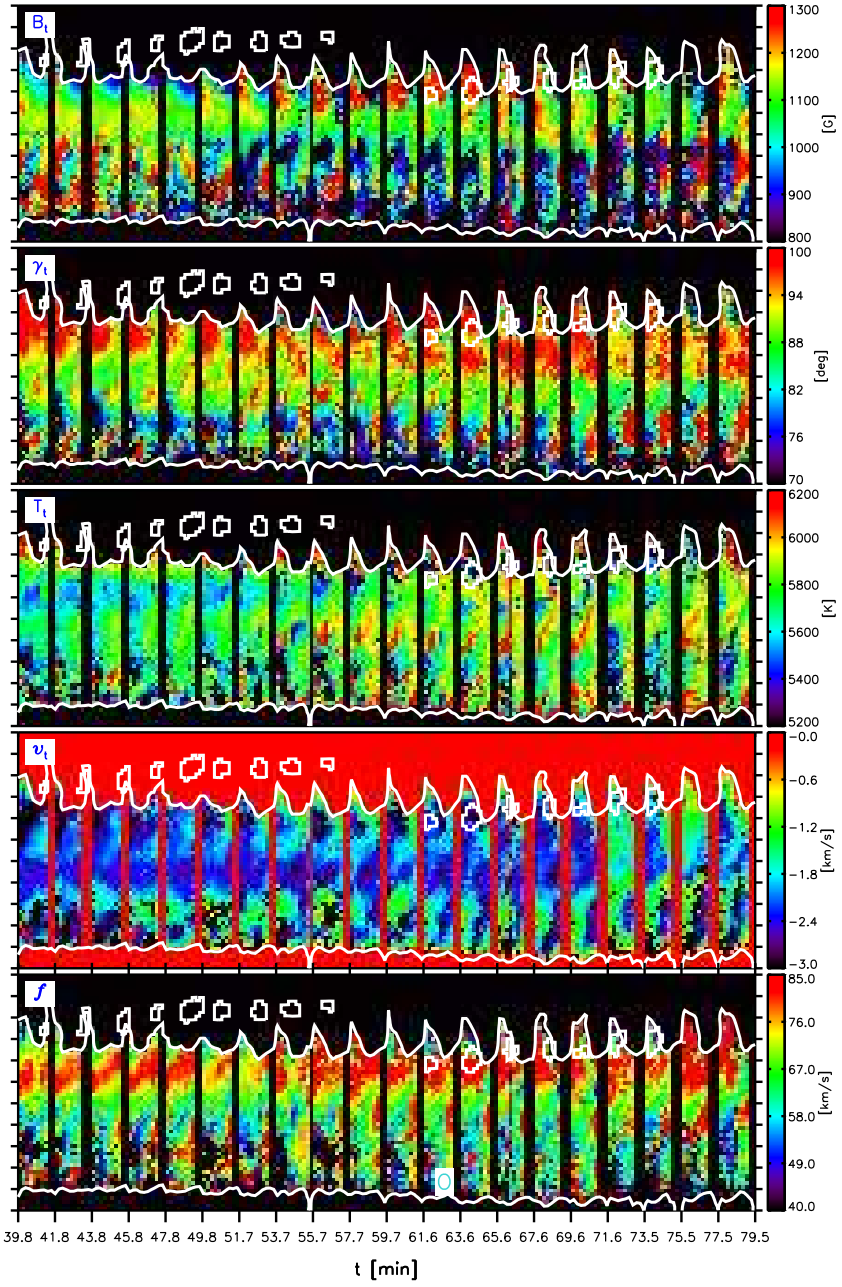

FIGURE C.6:— Same as Fig. C.5 from t=39.8 to t=79.5 min.

Bibliography

Allende Prieto, C., Asplund, M., & Fabiani Bendicho, P. 2004, A&A, 423, 1109

Auer, L. H. & Heasley, J. N. 1978, A&A, 64, 67

Ballesteros, E., Collados, M., Bonet, J. A., et al. 1996, A&AS, 115, 353

Battrick, B. & Sawaya-Lacoste, H., eds. 2001, Solar Orbiter Workshop (1st: 2001: Puerto de la Cruz, Tenerife, Spain) Proceedings of the first Solar Orbiter Workshop: solar encounter, Puerto de la Cruz, Tenerife, 14-18 May 2001

Beck, C. & Bellot Rubio. 2007, A&A, (in preparation)

Beck, C., Bellot Rubio, L., Schlichenmaier, R., & Sütterlin, P. 2007, A&A, (accepted)

Beck, C., Schlichenmaier, R., Collados, M., Bellot Rubio, L., & Kentischer, T. 2005a, A&A, 443, 1047

Beck, C., Schmidt, W., Kentischer, T., & Elmore, D. 2005b, A&A, 437, 1159

Beckers, J. M. 1968, Sol. Phys., 3, 258

Beckers, J. M. 1977, ApJ, 213, 900

Bellot Rubio, L. 2004, Reviews in Modern Astronomy, 17, 21

Bellot Rubio, L. 2006, in Solar polarization 4, ed. R. Casini & B. W. Lites, ASP Conf. Ser. (San Francisco: ASP), in press

Bellot Rubio, L. R., Balthasar, H., & Collados, M. 2004, A&A, 427, 319

Bellot Rubio, L. R., Balthasar, H., Collados, M., & Schlichenmaier, R. 2003, A&A, 403, L47

Bellot Rubio, L. R., Langhans, K., & Schlichenmaier, R. 2005, A&A, 443, L7

Bellot Rubio, L. R., Ruiz Cobo, B., & Collados, M. 1998, ApJ, 506, 805

Bellot Rubio, L. R., Schlichenmaier, R., & Tritschler, A. 2006, A&A, 453, 1117

Biermann, L. 1941, Astron. Ges. 76, 248

Blandford, R., Agol, E., Broderick, A., et al. 2002, in Astrophysical Spectropolarimetry, ed. J. Trujillo-Bueno, F. Moreno-Insertis, & F. Sánchez, 177–223

Bonet, J. A., Márquez, I., Muller, R., Sobotka, M., & Tritschler, A. 2004, A&A, 423, 737

Borrero, J. M. 2007, A&A, (accepted)

Borrero, J. M. & Bellot Rubio, L. R. 2002, A&A, 385, 1056

Borrero, J. M., Bellot Rubio, L. R., Barklem, P. S., & del Toro Iniesta, J. C. 2003, A&A, 404, 749

Borrero, J. M., Lagg, A., Solanki, S. K., & Collados, M. 2005, A&A, 436, 333

Borrero, J. M., Solanki, S. K., Bellot Rubio, L. R., Lagg, A., & Mathew, S. K. 2004, A&A, 422, 1093

Borrero, J. M., Solanki, S. K., Lagg, A., Socas-Navarro, H., & Lites, B. 2006, A&A, 450, 383

Buente, M. & Solanki, S. K. 1995, A&A, 297, 861

Bunte, M., Darconza, G., & Solanki, S. K. 1993, A&A, 274, 478

Cabrera Solana, D., Bellot Rubio, L. R., Beck, C., & del Toro Iniesta, J. C. 2006, ApJ, 649, L41

Cabrera Solana, D., Bellot Rubio, L. R., & del Toro Iniesta, J. C. 2005, A&A, 439, 687

Collados, M., Martínez Pillet, V., Ruiz Cobo, B., del Toro Iniesta, J. C., & Vazquez, M. 1994, A&A, 291, 622

Collados, M., Rodríguez Hidalgo, I., Bellot Rubio, L., Ruiz Cobo, B., & Soltau, D. 1999, in Astronomische Gesellschaft Meeting Abstracts, ed. R. E. Schielicke, 13–+

Degenhardt, D. 1989, A&A, 222, 297

del Toro Iniesta & Ruiz Cobo, B. 1997, in Forum THEMIS: the science with THEMIS, ed. N. Mein & S. Sahal-Bréchot, (Paris: Obs. de Paris), 93

del Toro Iniesta, J. C. 1996, Vistas in Astronomy, 40, 241

del Toro Iniesta, J. C. 2003a, Astronomische Nachrichten, 324, 383

del Toro Iniesta, J. C. 2003b, Introduction to Spectropolarimetry (Introduction to Spectropolarimetry, by Jose Carlos del Toro Iniesta, pp. 244. ISBN 0521818273. Cambridge, UK: Cambridge University Press, April 2003.)

del Toro Iniesta, J. C., Bellot Rubio, L. R., & Collados, M. 2001, ApJ, 549, L139

del Toro Iniesta, J. C. & Ruiz Cobo, B. 1996, Sol. Phys., 164, 169

del Toro Iniesta, J. C., Tarbell, T. D., & Ruiz Cobo, B. 1994, ApJ, 436, 400

Domingo, V., Fleck, B., & Poland, A. I. 1995, Sol. Phys., 162, 1

Elmore, D. F., Lites, B. W., Tomczyk, S., et al. 1992, in Polarization analysis and measurement; Proceedings of the Meeting, San Diego, CA, July 19-21, 1992 (A93-33401 12-35), p. 22-33., ed. D. H. Goldstein & R. A. Chipman, 22–33

Evershed, J. 1909, MNRAS, 69, 454

Ferriz-Mas, A. 1988, Physics of Fluids, 31, 2583

Ferriz-Mas, A. & Moreno-Insertis, F. 1987, A&A, 179, 268

Frutiger, C. 2000, Ph.D. Thesis, Institute of Astronomy, ETH Zrich, No. 13896

Gandorfer, A. M., Solanki, S. K., Schüssler, M., et al. 2004, in Ground-based Telescopes. Edited by Oschmann, Jacobus M., Jr. Proceedings of the SPIE, Volume 5489, pp. 732-741 (2004)., ed. J. M. Oschmann, Jr., 732–741

Georgakilas, A. A. & Christopoulou, E. B. 2003, ApJ, 584, 509

Gingerich, O., Noyes, R. W., Kalkofen, W., & Cuny, Y. 1971, Sol. Phys., 18, 347

Gray, D. F. 1992, The observation and analysis of stellar photospheres (Cambridge ; New York : Cambridge University Press, 1992. 2nd ed.)

Handy, B. N., Acton, L. W., Kankelborg, C. C., et al. 1999, Sol. Phys., 187, 229

Harvey, K. & Harvey, J. 1973, Sol. Phys., 28, 61

Hirzberger, J. & Kneer, F. 2001, A&A, 378, 1078

Illing, R. M. E., Landman, D. A., & Mickey, D. L. 1974a, A&A, 35, 327

Illing, R. M. E., Landman, D. A., & Mickey, D. L. 1974b, A&A, 37, 97

Illing, R. M. E., Landman, D. A., & Mickey, D. L. 1975, A&A, 41, 183

Jahn, K. & Schmidt, H. U. 1994, A&A, 290, 295

Kemp, J. C. & Henson, G. D. 1983, ApJ, 266, L69

Khomenko, E. V., Collados, M., Solanki, S. K., Lagg, A., & Trujillo Bueno, J. 2003, A&A, 408, 1115

Koch, A. 1984, Sol. Phys., 93, 53

Kubo, M., Shimizu, T., & Tsuneta, S. 2007, ApJ, 659, 812

Landi degl'Innocenti, E. 1992, Magnetic field measurements (Solar Observations: Techniques and Interpretation), 71–+

Landi Deglinnocenti, E. & Landi Deglinnocenti, M. 1977, A&A, 56, 111

Landi degl'Innocenti, E. & Landolfi, M. 2004, Physics of Solids and Liquids

Landolfi, M. & Deglinnocenti, E. L. 1982, Sol. Phys., 78, 355

Landolfi, M. & Landi degl'Innocenti, E. 1996, Sol. Phys., 164, 191

Langhans, K., Scharmer, G. B., Kiselman, D., & Löfdahl, M. G. 2007, A&A, 464, 763

Langhans, K., Scharmer, G. B., Kiselman, D., Löfdahl, M. G., & Berger, T. E. 2005, A&A, 436, 1087

Lee, J. W. 1992, Sol. Phys., 139, 267

Leka, K. D. 1997, ApJ, 484, 900

Leka, K. D., van Driel-Gesztelyi, L., Nitta, N., et al. 1994, Sol. Phys., 155, 301

Lin, C.-H., Banerjee, D., O'Shea, E., & Doyle, J. G. 2006, A&A, 460, 597

Lites, B. W. 1987, Appl. Opt., 26, 3838

Lites, B. W., Elmore, D. F., Seagraves, P., & Skumanich, A. P. 1993, ApJ, 418, 928

Lites, B. W., Elmore, D. F., & Streander, K. V. 2001, in ASP Conf. Ser. 236: Advanced Solar Polarimetry – Theory, Observation, and Instrumentation, ed. M. Sigwarth, 33–+

Lites, B. W. & Skumanich, A. 1990, ApJ, 348, 747

Lites, B. W., Skumanich, A., & Scharmer, G. B. 1990, ApJ, 355, 329

Makita, M. 1986, Sol. Phys., 106, 269

Marsch, E., Antonucci, E., Bochsler, P., et al. 2002, Advances in Space Research, 29, 2027

Martínez González, M. J., Collados, M., & Ruiz Cobo, B. 2006, A&A, 456, 1159

Martínez Pillet, V. 1992, Sol. Phys., 140, 207

Martínez Pillet, V. 2000, A&A, 361, 734

Martínez Pillet, V. 2002, Astronomische Nachrichten, 323, 342

Martínez Pillet, V., Collados, M., Sánchez Almeida, J., et al. 1999, in ASP Conf. Ser. 183: High Resolution Solar Physics: Theory, Observations, and Techniques, ed. T. R. Rimmele, K. S. Balasubramaniam, & R. R. Radick, 264–+

Martínez Pillet, V., Lites, B. W., & Skumanich, A. 1997, ApJ, 474, 810

Mathew, S. K., Lagg, A., Solanki, S. K., et al. 2003, A&A, 410, 695

Mein, P. 1971, Sol. Phys., 20, 3

Meyer, F. & Schmidt, H. U. 1968, Mitteilungen der Astronomischen Gesellschaft Hamburg, 25, 194

Montesinos, B. & Thomas, J. H. 1989, ApJ, 337, 977

Montesinos, B. & Thomas, J. H. 1997, Nature, 390, 485

Moore, C., Minnaert, M., & Houtgast, J. 1966, The Solar Spectrum from 2935 Å to 8770 Å, National Bureau of Standards Monograph, (Washington: US Government Printing Office)

Müller, D. A. N., Schlichenmaier, R., Fritz, G., & Beck, C. 2006, A&A, 460, 925

Müller, D. A. N., Schlichenmaier, R., Steiner, O., & Stix, M. 2002, A&A, 393, 305

Nave, G., Johansson, S., Learner, R. C. M., Thorne, A. P., & Brault, J. W. 1994, ApJS, 94, 221

Nye, A. H., Thomas, J. H., & Cram, L. E. 1984, ApJ, 285, 381

Orozco Suárez, D. & Del Toro Iniesta, J. C. 2007, A&A, 462, 1137

Penn, M. J., Jaeggli, S. A., Henney, C. J., Walton, S. R., & Luszcz, S. 2006, in 4th Solar Polarization Workshop, ed. R. Casini & B. W. Lites (San Francisco: ASP), (in press)

Pierce, A. K. & Breckenridge, J. B. 1974, The Kitt Peak table of photographic solar spectrum wavelengths (Kitt Peak National Observatory Contribution, Tucson: Kitt Peak National Observatory, 1973-1974)

Priest, E. R. 1982, Solar magneto-hydrodynamics (Dordrecht, Holland ; Boston : D. Reidel Pub. Co. ; Hingham,), 74P–+

Ravindra, B. 2006, Sol. Phys., 237, 297

Rees, D. E. 1987, A Gentle Introduction to Polarized Radiative Transfer (Numerical Radiative Transfer), 213–+

Rezaei, R., Schlichenmaier, R., Beck, C., & Bellot Rubio, L. R. 2006, A&A, 454, 975

Rimmele, T. & Marino, J. 2006, ApJ, 646, 593

Rimmele, T. R. 1994, A&A, 290, 972

Rimmele, T. R. 1995, A&A, 298, 260

Rouppe van der Voort, L. H. M. 2003, A&A, 397, 757

Rouppe van der Voort, L. H. M., Löfdahl, M. G., Kiselman, D., & Scharmer, G. B. 2004, A&A, 414, 717

Rueedi, I., Solanki, S. K., Keller, C. U., & Frutiger, C. 1998, A&A, 338, 1089

Rueedi, I., Solanki, S. K., Livingston, W., & Harvey, J. 1995, A&AS, 113, 91

Ruiz Cobo, B. & Bellot Rubio, L. R. 2007, A&A, (submitted)

Ruiz Cobo, B. & del Toro Iniesta, J. C. 1992, ApJ, 398, 375

Ruiz Cobo, B. & del Toro Iniesta, J. C. 1994, A&A, 283, 129

Ryutova, M., Shine, R., Title, A., & Sakai, J. I. 1998, ApJ, 492, 402

Ryutova, M. P., Hagenaar, H., & Title, A. 2007, ApJ, 656, L45

Sainz Dalda, A. & Martínez Pillet, V. 2005, ApJ, 632, 1176

Sánchez Almeida, J. & Lites, B. W. 1992, ApJ, 398, 359

Sánchez Cuberes, M., Puschmann, K. G., & Wiehr, E. 2005, A&A, 440, 345

Scharmer, G. B., Gudiksen, B. V., Kiselman, D., Löfdahl, M. G., & Rouppe van der Voort, L. H. M. 2002, Nature, 420, 151

Scherrer, P. H., Bogart, R. S., Bush, R. I., et al. 1995, Sol. Phys., 162, 129

Scherrer, P. H. & SDO/HMI Team. 2002, in Bulletin of the American Astronomical Society, 735–+

Schlichenmaier, R. 2002, Astronomische Nachrichten, 323, 303

Schlichenmaier, R., Bellot Rubio, L. R., & Tritschler, A. 2005, Astronomische Nachrichten, 326, 301

Schlichenmaier, R., Bruls, J. H. M. J., & Schüssler, M. 1999, A&A, 349, 961

Schlichenmaier, R. & Collados, M. 2002, A&A, 381, 668

Schlichenmaier, R., Jahn, K., & Schmidt, H. U. 1998a, ApJ, 493, L121+

Schlichenmaier, R., Jahn, K., & Schmidt, H. U. 1998b, A&A, 337, 897

Schlichenmaier, R., Müller, D. A. N., Steiner, O., & Stix, M. 2002, A&A, 381, L77

Schlichenmaier, R. & Schmidt, W. 2000, A&A, 358, 1122

Schmidt, W., Beck, C., Kentischer, T., Elmore, D., & Lites, B. 2003, Astronomische Nachrichten, 324, 300

Schmidt, W. & Kentischer, T. 1995, A&AS, 113, 363

Schröter, E. H. 1965, Zeitschrift fur Astrophysik, 62, 228

Schüssler, M. 2002, Astronomische Nachrichten, 323, 377

Shchukina, N. G., Trujillo Bueno, J., & Kostik, R. I. 1997, Sol. Phys., 172, 117

Sheeley, Jr., N. R. 1969, Sol. Phys., 9, 347

Shine, R., Title, A., & Murdin, P. 2000, Encyclopedia of Astronomy and Astrophysics

Shine, R. A., Title, A. M., Tarbell, T. D., et al. 1994, ApJ, 430, 413

Socas-Navarro, H. 2001, in ASP Conf. Ser. 236: Advanced Solar Polarimetry – Theory, Observation, and Instrumentation, ed. M. Sigwarth, 487–+

Socas-Navarro, H., Elmore, D., Pietarila, A., et al. 2006, Sol. Phys., 235, 55

Socas-Navarro, H., Pillet, V. M., Sobotka, M., & Vázquez, M. 2004, ApJ, 614, 448

Solanki, S. K. 1993, Space Science Reviews, 63, 1

Solanki, S. K. 2003, A&A Rev., 11, 153

Solanki, S. K., Biemont, E., & Muerset, U. 1990, A&AS, 83, 307

Solanki, S. K., Gandorfer, A. M., Schuessler, M., et al. 2003, in Innovative Telescopes and Instrumentation for Solar Astrophysics. Edited by Stephen L. Keil, Sergey V. Avakyan . Proceedings of the SPIE, Volume 4853, pp. 129-139 (2003)., ed. S. L. Keil & S. V. Avakyan, 129–139

Solanki, S. K., Inhester, B., & Schuessler, M. 2006, Rep. Prog. Phys., 69, 563-668

Solanki, S. K. & Montavon, C. A. P. 1993, A&A, 275, 283

Solanki, S. K., Montavon, C. A. P., & Livingston, W. 1994, A&A, 283, 221

Solanki, S. K., Pantellini, F. G. E., & Stenflo, J. O. 1987, Sol. Phys., 107, 57

Solanki, S. K., Rueedi, I. K., & Livingston, W. 1992, A&A, 263, 312

Soltau, D., Berkefeld, T., von der Lühe, O., Wöger, F., & Schelenz, T. 2002, Astronomische Nachrichten, 323, 236

Spruit, H. C. 1982, Sol. Phys., 75, 3

Spruit, H. C. & Scharmer, G. B. 2006, A&A, 447, 343

St. John, C. E. 1913a, ApJ, 37, 322

St. John, C. E. 1913b, ApJ, 38, 341

Stanchfield, II, D. C. H., Thomas, J. H., & Lites, B. W. 1997, ApJ, 477, 485

Sütterlin, P., Bellot Rubio, L. R., & Schlichenmaier, R. 2004, A&A, 424, 1049

Thomas, J. H. 1988, ApJ, 333, 407

Thomas, J. H. & Montesinos, B. 1991, ApJ, 375, 404

Thomas, J. H., Weiss, N. O., Tobias, S. M., & Brummell, N. H. 2002, Nature, 420, 390

Title, A. M., Frank, Z. A., Shine, R. A., et al. 1993, ApJ, 403, 780

Tritschler, A., Schlichenmaier, R., Bellot Rubio, L. R., et al. 2004, A&A, 415, 717

Unno, W. 1956, PASJ, 8, 108

Vela Villahoz, E., Sanchez Almeida, J., & Wittmann, A. D. 1994, A&AS, 103, 293

Vernin, J. & Muñoz-Tuñón, C. 1992, A&A, 257, 811

von Klüber, H. 1948, Zeitschrift fur Astrophysik, 24, 121

Westendorp Plaza, C., del Toro Iniesta, J. C., Ruiz Cobo, B., et al. 1997, Nature, 389, 47

Westendorp Plaza, C., del Toro Iniesta, J. C., Ruiz Cobo, B., & Pillet, V. M. 2001a, ApJ, 547, 1148

Westendorp Plaza, C., del Toro Iniesta, J. C., Ruiz Cobo, B., et al. 2001b, ApJ, 547, 1130

Wiehr, E. & Degenhardt, D. 1992, A&A, 259, 313

Wiehr, E. & Degenhardt, D. 1994, A&A, 287, 625

Wiehr, E. & Stellmacher, G. 1989, A&A, 225, 528

Wilson, P. R. 1986, Sol. Phys., 106, 1

Yurchyshyn, V. B., Wang, H., & Goode, P. R. 2001, ApJ, 550, 470

Zhang, J., Solanki, S. K., & Wang, J. 2003, A&A, 399, 755

Zhang, J. & Wang, J. 2002, ApJ, 566, L117